Equilibrium and Stability of Magnetically Confined Plasmas

by

Gabriel Shane Woodbury Saudeau

A dissertation submitted to the Graduate Faculty of
Auburn University
in partial fulfillment of the
requirements for the Degree of
Doctor of Philosophy

Auburn, Alabama
August 8, 2026

Keywords: plasma, fusion, equilibrium, stability, tokamak, stellarator

Approved by

Luca Guazzotto, Chair, Professor of Physics
David A. Maurer, Professor of Physics
Evdokiya Kostadinova, Assistant Professor of Physics
Guillaume M. Laurent, Professor of Physics
Andrew S. Ware, Affiliate Professor of Physics
Joseph Majdalani, Professor of Aerospace Engineering

Abstract

The equilibrium and stability of physical systems are fundamental topics with applications throughout physics. To realize a practical magnetically confined fusion power plant, it is essential to establish and maintain plasma equilibrium during periods of operation required for energy production. Moreover, this equilibrium must remain stable in the presence of perturbations. The work presented here is framed around the two leading magnetic confinement concepts: stellarators and tokamaks. Within this dissertation, the stellarator studies focus primarily on equilibrium, whereas the tokamak studies focus on plasma stability. These topics were chosen to address research questions of particular interest for each confinement concept.

For the equilibrium studies, we investigate three-dimensional plasma confined in stellarators. To this end, two projects were undertaken. The first was a verification study of equilibrium solvers, while the second was an in-depth investigation of a particular aspect of one equilibrium solver. In the former, we investigated whether several different three-dimensional (3D) magnetohydrodynamic (MHD) equilibrium codes, DESC, SIESTA, SPEC, and VMEC, a would arrive at the same equilibrium given the same physical system. Although the codes employ different numerical formulations, they are all based on the same MHD equations and should therefore converge to the same equilibrium solution. This expectation was confirmed. The latter project examined how SIESTA modeled magnetic islands, an important aspect of 3D equilibria. This study sought to better understand the mechanism by which the code introduces perturbations that generate magnetic islands. We show that increasing the magnitude of the perturbation parameter, which allows the islands to form, enlarges them and shifts their radial location in the plasma. Furthermore, a relationship between the location of the island relative to the edge and its size was identified and investigated.

Regarding stability, motivated by previous tokamak equilibrium research, we investigated how a simplified version of this system of interest would respond to perturbations. The initial sys-

tem, containing discontinuities in both velocity and pressure, is susceptible to instability growth. The former would lead to the development of a Kelvin-Helmholtz instability, and the latter could be modeled as a Rayleigh-Taylor instability. Dispersion relations and asymptotic expressions for the growth rates were derived for compressible fluids subject to both instabilities, showing the instability persists beyond where the classical compressible Kelvin-Helmholtz instability would stabilize. In the presence of flow-aligned magnetic fields, an approximate expression for the field strength required to suppress the instabilities was also obtained.

Artificial Intelligence (AI) Use Disclosure Statement

In the preparation of this dissertation, the following Artificial Intelligence (AI) tool was used: ChatGPT, Copilot. ChatGPT was used to check grammar and improve word choice, while Copilot was used to generate alt text. The author acknowledges full responsibility for the intellectual content of this work and has ensured that all AI-assisted sections have been reviewed and revised for accuracy and appropriate academic style. All AI-generated content was reviewed and validated for relevance, appropriateness, and accuracy before incorporation into the final document to maintain scholarly integrity of this research.

Digital Accessibility Disclosure Statement

In the preparation of this dissertation, the following digital accessibility tools were used to ensure this document complies with federal requirements: Adobe Acrobat, PAC, and veraPDF. The author acknowledges full responsibility for the intellectual content of this work and has made a good faith effort to comply with digital accessibility requirements in publishing, wherein the nature of the content does not significantly change in order to do so. Furthermore, all content has been reviewed and revised to meet these requirements prior to final publication.

Acknowledgments

This dissertation is dedicated to my parents. I am ever thankful for their support throughout my life. I would not have made it this far without their help.

Contents

List of Tables

List of Figures

Chapter 1

Introduction

According to the U.S. Energy Information Administration's 2026 Annual Energy Outlook, the U.S.'s electricity demand has increased by 2.1% per year, on average, over the last five years, and the overall electricity demand is expected to grow by between 25% and 50% by 2050. [1] A variety of sources will be required to meet these future energy needs. Options such as coal, oil, and natural gas are cheap sources but are limited in quantity and will eventually run out. Others, such as wind and solar, are contributing more electricity to the grid as time goes on, and while technically limitless have their own problems, mainly the lack of consistent power generation due to external factors such as lack of wind, or lack of sunshine due to clouds or at night. Nuclear fission generates approximately 17% of all electricity in the country, but is not expected to increase in the coming decades. [1] One of the main problems with it is the public distrust in nuclear energy due to disasters such as those which occurred at Chernobyl and most recently in Fukushima.

This thesis focuses on nuclear fusion - a promising energy option that could contribute significantly to resolving the increasing energy demand. Fusion energy offers many benefits over the previously mentioned energy sources. Nuclear fusion typically is proposed to be performed using deuterium, which is abundant and cheap to extract, and tritium, which is not easy to collect, but can potentially be bread self-consistently inside working fusion reactors. As such there should be no problem supplying fuel over the decades as opposed to fossil fuels. Fusion reactors also could be run continuously, supplying power to the grid as needed, resolving the issue of consistency found with renewables such as solar and wind power. Lastly, nuclear fusion is safer than fission as it is not prone to massive accident due to reactor meltdown. At any point in time inside a fusion device the fuel should only amount to the mass of a few postage stamps, and as such lacks the ability to allow for anything significant such as a meltdown to occur. [2]

That is not to say nuclear fusion is without issues. The science of fusion is quite complex from both a theoretical and engineering standpoint. From a theory perspective, we are required to find a configuration to confine on the order of 10^{20} particles per cubic meter to temperatures beyond 10^{8}K. These configurations must also be able to sustain these conditions for lengthy periods of time to generate electricity. As we have found over decades of research, these are no easy feats. From the engineering side, there are also several challenges which must be overcome, such as superconducting magnet development and construction, material design to handle neutron and heat loads, and technologies to provide heating power to raise plasma temperatures. [2] Lastly, one must also consider the financial cost to build such a complicated device, as we have seen with devices such as W7-X and ITER which cost billions of dollars.

1.1 The Fusion Reaction

The most commonly sought after nuclear reaction for a fusion power plant is the Deuterium-Tritium reaction. This is so because it is the easiest of all fusion reactions to initiate. [3] The reaction of interest can be written as,

$$\mathrm{D} + \mathrm{T} \rightarrow \alpha + \mathrm{n} + 17.6\ \mathrm{MeV}. \tag{1.1}$$

In Eq. (1.1) a Deuterium atom, an isotope of hydrogen with one neutron, D, collides with a Tritium atom, an isotope of hydrogen with two neutrons, T, and the byproducts are a helium nucleus, or alpha particle, α, a neutron, and 17.6 MeV of excess energy. Macroscopically the energy given off by the reaction is equivalent to 3.38×10^{8} MJ/kg of combined D-T fuel. In comparison, one of the standard reactions which occurs in a fission plant using uranium yields approximately 8.4×10^{7} MJ/kg of fuel, and the standard reaction of burning gasoline yields approximately 40 MJ/kg of gasoline. This shows how little fuel is required for fusion relative to some of the other standard energy generation methods.

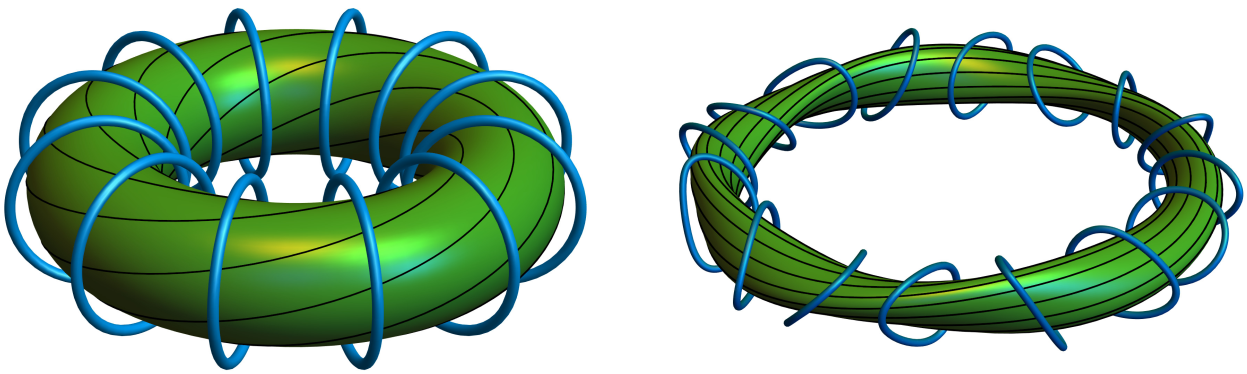

Figure 1.1: Sample schematics illustrating the general shape and configuration of a tokamak (left image) and a stellarator (right image). The green represents the plasma, the black lines represent magnetic field lines, and the blue rings are the toroidal field coils.

1.2 Fusion Devices of Interest

Although several approaches to achieving fusion have been proposed, including magnetic confinement fusion (MCF), which uses magnetic fields to confine the plasma, and inertial confinement fusion (ICF), which uses lasers to compress and heat a fuel pellet, this thesis focuses exclusively on MCF. Furthermore, while there are several proposed MCF designs, those relevant to the projects presented herein are the tokamak and stellarator designs. We will proceed to briefly describe both.

1.2.1 Tokamak

A tokamak is an axisymmetric toroidal device which aims to magnetically confine plasma. It uses toroidal magnetic field coils to produce toroidal fields, and a transformer to induce a toroidal current in the plasma to produce poloidal magnetic fields. A simple schematic of the plasma and coil shapes are presented in Fig. 1.1. It is presently the most popular kind of MCF device due to historical performance.

With the tokamak design there are both advantages and disadvantages. Some of the advantages are related to good physics performance. Large toroidal magnetic fields are readily achievable which allows for improved plasma confinement. The symmetry of the design guarantees certain beneficial plasma properties which improve performance as well. Also from an engineering and cost standpoint, the design of the magnets are relatively simple, and since they are all the same, it becomes cost-effective to produce many. On the other hand, there are two main problems associated with tokamaks.

The first problem is related to the stability of the plasma inside a reactor. Tokamak plasmas can be subject to various instabilities which can then lead to the catastrophic loss of plasma containment, an event typically known as a disruption. One method of suppressing these instabilities is through the use of stronger confining magnetic fields. However, this approach incurs substantial costs and relies on advances in materials technology to produce magnets capable of generating stronger magnetic fields. The other issue is related to the fact that a toroidal current is induced into the plasma, as one cannot inductively drive a current for an indefinite period of time. Ideally a fusion power plant would be run as a steady state device so that it would continuously generate energy. As such other methods of external current drive are required, and generally they are complex and costly.

1.2.2 Stellarator

The stellarator is a non-axisymmetric toroidal device with helical symmetry. Similar to the tokamak it uses toroidal magnetic field coils to generate toroidal fields, but unlike the tokamak, these field coils are designed in such a way that they also produce a poloidal field. As a result of this distinction, it is not necessary to drive any current in a stellarator to ensure plasma confinement. A sample schematic of a stellarator plasma and coils can be seen in Fig. 1.1.

As with the tokamak design there are benefits and disadvantages to using a stellarator. As previously mentioned, since an externally driven current is not required for confinement, stellarators generally do not experience disruptions. Furthermore, this allows for the device to be run in steady state, without the need for current drive, which is necessary for a power plant.

However, these welcomed advantages come at a cost, namely poor confinement properties, and costly magnet designs. Unless the magnetic fields are optimized, a stellarator's magnetic field can lead to a rapid loss of particles. This is mainly due to the system no longer being axisymmetric. As such, a great deal of optimizations must be performed to construct fields which will perform well, a task which can be computationally expensive and time-consuming. Also, the magnets used in stellarators are not all identical and can have complex shapes, further complicating the manufacturing process.

1.2.3 Interest In Each Device

This dissertation focuses on two core research topics, each one focusing on a different problem each device faces, but still linked by the model used to study them. Our interest lie in two fundamental aspects of physics, equilibrium and stability, and each device motivates the study of one. In the case of stellarators, the study of 3D equilibria and the subtleties involved are key aspects of designing a functional power plant Having a solid understanding of the tools available to perform these calculations is vital for future work. In the case of tokamaks, instabilities are abundant, and developing methods to control them will allow for better operation of such devices in the future.

1.3 The Magnetohydrodynamics Model

To perform the studies we are interested in, a choice must be made regarding the physical model which will be used. One could, for instance, think about looking at a system in terms of single particle motion. While this could give insight to the kind of motion a particle would undertake in a fusion device, attempting to model on the order of 10^{20} particles per cubic meter in a device whose plasma volume will be on the order of 10^2 cubic meters and all the interactions between each particle is quite daunting computationally. Other methods look to study the average behaviors of the particles, calculating distribution functions forming a kinetic model. While a valid choice to make, it is still quite complex and computationally challenging.

A simplification can be made, where one takes fluid moments of the distribution functions, to derive a fluid description of the plasma. Then a number of assumptions can be made to obtain closure of the system of equations. This leaves one with a model such as the one used predominantly herein, the magnetohydrodynamics (MHD) model, and its variations, such as ideal MHD.

The MHD model, and especially the ideal MHD model, are some of the simplest models that describe the macroscopic equilibrium and stability properties of a plasma. [3] We say "simplest" because the model neglects a great deal of physics, such as electromagnetic wave propagation, relativity, and quantum mechanics. Furthermore, effects such as radiation, radio frequency (RF) heating and current drive, plasma-wall interactions, and resistive instabilities are not adequately described by ideal MHD. [3] Even with such a simplified system, the models are still quite difficult to solve analytically or computationally, especially with the geometries being studied. Chapter 2 provides a more detailed discussion of the model, its derivation, and several calculations based on it.

1.4 The Study of Plasma Equilibrium

With the MHD model, it is possible to describe and investigate global behavior of fusion plasmas. An important area of study related to the successful operation of any MFE device is its ability to generate a plasma which is in equilibrium. In simple terms, an equilibrium is a state in which all forces acting on the plasma are balanced, resulting in a configuration that does not change with time. Ideally, a fusion device is able to bring a plasma to an equilibrium, which is continuously allowing for fusion reactions to occur. If the system was not in a steady state, then the plasma would be ever-changing and possibly not reaching the required temperatures needed for the fusion events to take place. These considerations make the study of plasma equilibria a critical area of research.

Regarding the tokamak, the problem is simplified because of its axisymmetric geometry. Due to this, the system essentially become two-dimensional, and other beneficial confinement properties arise. A notable one is that in a tokamak, magnetic surfaces, also known as flux surfaces, are guaranteed to exist. As will be further explained in Chapter 2 these are essentially surfaces formed by magnetic field lines which lie on tubes of constant pressure. As charged particles will tend to move along magnetic field lines, being ensured that the field lines will be confined to the plasma volume is quite desirable.

On the other hand because stellarators are not axisymmetric, nested surfaces are not guaranteed to occur in the equilibrium. Rather, phenomena known as magnetic islands can form, and these can lead to rapid transport of particles from the hot core to the cooler edge, which is the opposite of what one is attempting to accomplish. The optimal design of the stellarator and its coils is then of great importance, because if the equilibrium generated cannot confine the plasma properly, then the device will not function as intended. Due to the complexity of the three-dimensional system, numerical codes are required to calculate stellarator equilibria. In Chapter 3 we discuss two stellarator equilibrium projects which were performed. The former is a verification study, comparing some of the different equilibrium solvers to investigate if they would arrive at the same equilibrium given the same system. The latter is an in-depth study of how one of the codes resolves magnetic islands, along with related calculations.

1.5 Linear Stability Studies

Once satisfactory equilibria have been found, it becomes necessary to perform stability studies. These stability studies are meant to determine how the equilibria respond to small perturbations. If the system is stable, it will either oscillate around the equilibrium or return to its initial state. If the system is unstable it will move away from the initial equilibrium, possibly leading to decreased plasma performance or worse, disruptions.

Unfortunately, historically experiments have shown that tokamak equilibria are not stable. [4–6] Tokamak discharges are susceptible to a plethora of instabilities with space-time scales varying greatly as well as the physical quantities which characterize the configuration. For this reason, the study of plasma instabilities, and methods to suppress or mitigate them is vital to tokamak research. Chapter 4 examines a stability problem motivated by previous work that presented an equilibrium susceptible to both Kelvin–Helmholtz [7, 8] and Rayleigh–Taylor [9, 10] modes, the latter arising from a pressure discontinuity. The former is driven by velocity shear, whereas the latter is driven by gravity or an analogous force.

1.6 Outline

The dissertation is structured as follows. In Chapter 2, we present the theoretical background knowledge required to understand the work performed. Chapter 3 then discusses the two equilibrium projects previously mentioned, a free-boundary verification study, and a study on magnetic islands. This is followed by Chapter 4 which details the stability analysis performed for a Kelvin-Helmholtz Rayleigh-Taylor unstable system. Then in Chapter 5, we summarize the presented research and propose possible future research avenues which build upon what was presented.

Chapter 2

Magnetohydrodynamics Theory

2.1 Introduction

To achieve a functional fusion power plant, it is widely accepted that the plasma will need to be in Magnetohydrodynamic (MHD) equilibrium and MHD stable. As such, it is vital that we understand the model and the physics involved so that we can design and operate a reactor that will become a viable source of energy for the future. The majority of the projects discussed in this thesis were undertaken with one of the models of MHD, and as such this chapter will provide an introduction on the model, how it is derived, and important aspects and consequences of the different variations of the model. There are various forms of the MHD model, but the ones that will be discussed in this thesis are the following:

1. Ideal MHD – The ”simplest” form of the model, where the plasma is assumed to have infinite electrical conductivity.
2. Resistive MHD – Similar to ideal MHD, but it includes finite resistivity so that certain effects, such as magnetic islands, can occur.
3. Multi Region Relaxed MHD (MRxMHD) – A variation of MHD where the plasma is broken into various regions of constant pressure to avoid certain mathematical inconsistencies that occur in ideal MHD.

The chapter is organized as follows. In Sec. 2.2, we derive the MHD model from the two fluid equations. Section 2.4 discusses some basic background on curvilinear coordinate systems, as well as its applications to magnetic fields seen in 3D geometries. In Sec. 2.5, one-dimensional MHD equilibria are investigated, and the same is done for two-dimensional equilibria in Sec. 2.6. We finish our discussion on equilibria in Sec. 2.7 where we thoroughly describe how 3D equilibria are calculated, as well as some of the issues that are associated with them. We finish the chapter in Sec. 2.8 with an introduction to linear stability theory.

It also bears mentioning that many of the derivations present here originate from the following sources; J. Freidberg's *Plasma Physics and Fusion Energy* [2], and *Ideal MHD* [3]; P. Helander's review article [11]; the text *An introduction to Stellarators*[12] by L. Imbert-Gérard et al.; and D'haeseleer et al.'s text *Flux Coordinates and Magnetic Field Structure* [13]. If further detail is desired on any of the topics presented in this chapter, please reference any of the listed sources. They are all well written and good sources to be aware of and are readily available as reference texts.

2.2 Magnetohydrodynamics Model

2.2.1 Derivation of Magnetohydrodynamics

We will now proceed to give an abbreviated derivation of the MHD model. The derivation will begin from the two-fluid equations and from there attain the MHD equations. To arrive at the two-fluid equations one would typically begin with a kinetic model where the goal is to determine the particle distribution functions of the different quantities. The kinetic model is more accurate and contains a greater amount of physics, but as a result is much more complicated. Regardless, the MHD model is adequate in capturing global plasma dynamics, which is the essential physics studied here. Taking the velocity moments of the kinetic model will allow one to arrive at the two-fluid equations, where quantities have now lost their velocity dependence and are now only functions of space and time. The following are the two-fluid equations as well as Maxwell's equations as found in J. Freidberg's book Plasma Physics and Fusion Energy [2].

Conservation of mass:

$$\begin{aligned} \frac{\partial n_e}{\partial t} + \nabla \cdot (n_e \mathbf{u}_e) = 0 \\ \frac{\partial n_i}{\partial t} + \nabla \cdot (n_i \mathbf{u}_i) = 0 \end{aligned} \tag{2.1}$$

Conservation of momentum:

$$
\begin{aligned}
m_e n_e \left(\frac{\partial}{\partial t} + \mathbf{u}_e \cdot \nabla\right) \mathbf{u}_e &= -e n_e \left(\mathbf{E} + \mathbf{u}_e \times \mathbf{B}\right) - \nabla p_e - m_e n_e \bar{\upsilon}_{ei} \left(\mathbf{u}_e - \mathbf{u}_i\right) \\
m_i n_i \left(\frac{\partial}{\partial t} + \mathbf{u}_i \cdot \nabla\right) \mathbf{u}_i &= e n_i \left(\mathbf{E} + \mathbf{u}_i \times \mathbf{B}\right) - \nabla p_i - m_e n_e \bar{\upsilon}_{ei} \left(\mathbf{u}_i - \mathbf{u}_e\right)
\end{aligned}
\tag{2.2}
$$

Conservation of energy:

$$
\begin{aligned}
\frac{3}{2} n_e \left(\frac{\partial}{\partial t} + \mathbf{u}_e \cdot \nabla\right) T_e + p_e \nabla \cdot \mathbf{u}_e + \nabla \cdot \mathbf{q}_e &= S_e \\
\frac{3}{2} n_i \left(\frac{\partial}{\partial t} + \mathbf{u}_i \cdot \nabla\right) T_i + p_i \nabla \cdot \mathbf{u}_i + \nabla \cdot \mathbf{q}_i &= S_i
\end{aligned}
\tag{2.3}
$$

Maxwell's equations

$$
\begin{aligned}
\nabla \times \mathbf{E} &= -\frac{\partial \mathbf{B}}{\partial t} \\
\nabla \times \mathbf{B} &= \mu_0 e \left(n_i \mathbf{u}_i - n_e \mathbf{u}_e\right) + \frac{1}{c^2} \frac{\partial \mathbf{E}}{\partial t} \\
\nabla \cdot \mathbf{E} &= \frac{e}{\varepsilon_0} \left(n_i - n_e\right) \\
\nabla \cdot \mathbf{B} &= 0
\end{aligned}
\tag{2.4}
$$

Where n_e, n_i are the electron and ion number densities, $\mathbf{u}_e, \mathbf{u}_i$ are the electron and ion flow velocities, m_e, m_i are the electron and ion masses, p_e, p_i are the electron and ion pressures, $\bar{\upsilon}_{ei}$ is the frequency of electron and ion collisions, T_e, T_i are the electron and ion temperatures, q_e, q_i are the electron and ion heat fluxes, and S_e, S_i are sink and source functions with other physics effects contained in them.

With the two-fluid model defined we proceed to derive the MHD model. The first step is to define the length and time scales of interest, which we can then use to compare the magnitudes of the different terms in the two-fluid equations. Then, we eliminate terms in the model as a result of scaling arguments. Finally, we introduce single fluid variables, ignoring terms that are small, to arrive at the MHD equations.

In the MHD model, the characteristic length is the plasma radius, $L \sim a$, the characteristic time is the ion thermal transit time, $\tau \sim a/\upsilon_{Ti}$, which leads to the characteristic velocity, the ion thermal velocity, $u \sim L/\tau \sim v_{Ti}$. Since the plasma scale length satisfies the inequality $a \gg \lambda_{De}$, where λ_{De} is the Debye length, the plasma is quasineutral. This allows for the $\nabla \cdot \mathbf{E}$ term in Poisson's equation to be dropped. The MHD frequency, $\omega \sim 1/\tau$ is small when compared to the electron cyclotron frequency. This implies that the electron inertia term in the momentum equation can be neglected. Finally, since the ion thermal velocity is much smaller than the speed of light, we are able to ignore the displacement current term in the Maxwell-Ampére equation.

Now we proceed to define the single fluid variables. We begin with the density, $\rho \equiv m_i n$, where the electron mass is neglected since $m_i \gg m_e$, and from quasi-neutrality the number densities, $n_e = n_i = n$, are the same. Since m_i/ggm_e the momentum of the fluid is carried by the ions, and we define the fluid velocity, $\mathbf{v} \equiv \mathbf{u}_i$. The electron velocity can then be defined in terms of the current density and fluid velocity, $\mathbf{u}_e = \mathbf{v} - \mathbf{J}/en$. The last quantity is the pressure, where we define it as the total electron and ion pressure, $p \equiv p_e + p_i$. We can now manipulate the two-fluid equations to reduce them to single-fluid form.

Starting with the conservation of mass, multiplying the ion equation by the ion mass yields,

$$\frac{\partial \rho}{\partial t} + \nabla \cdot (\rho \mathbf{v}) = 0. \tag{2.5}$$

We skip over the electron equation as no new information will be gained from it. Next adding the two momentum equations together and substituting the single fluid variables gives,

$$\rho \left(\frac{\partial}{\partial t} + \mathbf{v} \cdot \nabla \right) \mathbf{v} = \mathbf{J} \times \mathbf{B} - \nabla p. \tag{2.6}$$

The above equation describes the force balance of the plasma, and is central to equilibrium calculations. Another piece of information can be found by looking solely at the electron momentum equation. Substituting the single fluid variables where possible and setting the resistivity, $\eta = m_e \bar{v}_{ei}/e^2 n$, gives after rearranging terms,

$$\mathbf{E} + \mathbf{v} \times \mathbf{B} = \frac{1}{en}(\mathbf{J} \times \mathbf{B} - \nabla p_e) + \eta \mathbf{J}. \tag{2.7}$$

The terms in the parenthesis on the right are the Hall term and electron diamagnetic term respectively, while the last term on the right corresponds to the plasma resistivity. Both terms in the parenthesis are small relative to the rest and can be ignored, while choosing to neglect the resistivity depends on the MHD model you are using. Resistive MHD will keep the term, whereas ideal MHD will not. The energy conservation equations simplify in the MHD regime, with the source, sink and heat flux terms all vanishing due to their time scales being much larger than the MHD one. This reduces the ion energy equation to,

$$\frac{3}{2}n\left(\frac{\partial}{\partial t} + \mathbf{v} \cdot \nabla\right) T_i + p_i \nabla \cdot \mathbf{v} = 0. \tag{2.8}$$

Using the conservation of mass equation to eliminate the divergence term, and remembering that $p_i = nT_i$, after rearranging and simplifying one gets,

$$\frac{d}{dt}\left(\frac{p_i}{\rho^\Gamma}\right) = 0$$

where $\Gamma = 5/3$ is the adiabatic index. The electrons have a similar relation, and adding the two together yields the single-fluid energy equation,

$$\frac{d}{dt}\left(\frac{p}{\rho^\Gamma}\right) = 0. \tag{2.9}$$

With this we have successfully derived the single-fluid MHD equations and repeat them below,

$$
\begin{aligned}
&\text{mass}: && \frac{\partial \rho}{\partial t} + \nabla \cdot (\rho \mathbf{v}) = 0 \\
&\text{momentum}: && \rho \left(\frac{\partial}{\partial t} + \mathbf{v} \cdot \nabla \right) \mathbf{v} = \mathbf{J} \times \mathbf{B} - \nabla p \\
&\text{Ohm's law}: && \mathbf{E} + \mathbf{v} \times \mathbf{B} = \eta \mathbf{J} \\
&\text{energy}: && \frac{d}{dt} \left(\frac{p}{\rho^{\Gamma}} \right) = 0 \\
&\text{Maxwell}: && \nabla \times \mathbf{E} = -\frac{\partial \mathbf{B}}{\partial t} \\
& && \nabla \times \mathbf{B} = \mu_0 \mathbf{J} \\
& && \nabla \cdot \mathbf{B} = 0
\end{aligned}
\tag{2.10}
$$

2.2.2 Frozen-in Flux

One of the important consequences of the ideal MHD formulation is the frozen-in flux theorem. First, note that the magnetic flux ψ passing through a surface S in the plasma is,

$$\psi = \int_S \mathbf{B} \cdot \mathbf{n} \, \mathrm{d}S. \tag{2.11}$$

Now let us assume that the plasma contained in the surface is moving with a velocity $\mathbf{v}$. This movement of the surface will cause the flux passing through it to change in time,

$$\frac{d\psi}{dt} = \int_S \frac{\partial \mathbf{B}}{\partial t} \cdot \mathbf{n} \, \mathrm{d}S - \oint \mathbf{v} \times \mathbf{B} \cdot \mathrm{d}\mathbf{l} \tag{2.12}$$

where $d\mathbf{l}$ is the arc length along the perimeter of the surface. There is some subtlety in how the line integral term is obtained. Appendix C of Freidberg's Ideal MHD book shows a thorough derivation of how it comes about if the reader is interested. We can then use Faraday's law to eliminate the partial time derivative and then use Stoke's theorem to convert the surface integral into a loop integral, giving,

$$\frac{d\psi}{dt} = -\oint (\mathbf{E} + \mathbf{v} \times \mathbf{B}) \cdot d\mathbf{l}. \tag{2.13}$$

From the ideal Ohm's law we know that the integrand is zero and thus,

$$\frac{d\psi}{dt} = 0. \tag{2.14}$$

Since the surface was chosen arbitrarily setting it to be the plasma cross section implies that the total flux in an ideal MHD plasma is conserved. This also works in the opposite manner, whereby setting the surface to be arbitrarily small to only "contain" a magnetic field line, we see that the field line must move with the plasma and is "frozen" into the fluid. This then implies that topological changes to the magnetic field are not allowed. Thus, phenomena, such as field line reconnection, are not allowed under the ideal MHD model. For that to occur, resistive effects must be included, for they permit the magnetic field to diffuse and change topology.

2.3 Magnetohydrodynamics Equilibrium

With a model that can describe the behavior of a plasma, we are now interested in finding configurations where the plasma is in equilibrium, as these would be necessary for a potential fusion reactor. To study an equilibrium, we assume the system is in steady-state, meaning all quantities are time independent. Another assumption that can be made is whether the system is static, $\mathbf{v} = 0$, or stationary, $\mathbf{v} \neq 0$. The former is the one that we will use in this chapter, as well as Chapter 3, whereas the latter will be used for the equilibrium studied in Chapter 4. While the equilibria to be discussed presently are magnetohydrostatic equilibria, for the sake of simplicity they will still be referred to as MHD equilibria. We then have that the MHD equilibrium equations are:

$$\begin{gathered} \mathbf{J} \times \mathbf{B} = \nabla p \\ \nabla \times \mathbf{B} = \mu_0 \mathbf{J} \\ \nabla \cdot \mathbf{B} = 0. \end{gathered} \tag{2.15}$$

For this system, an equilibrium is achieved when the magnetic force, $\mathbf{J} \times \mathbf{B}$, balances the pressure gradient force, ∇p. There are two mechanisms through which the magnetic field keeps the system in force balance. This can be shown by using Ampére's law to eliminate $\mathbf{J}$ in the pressure balance equation and and making use of the identity $\nabla(B^2/2) = \mathbf{B} \times (\nabla \times \mathbf{B}) + (\mathbf{B} \cdot \nabla)\mathbf{B}$ to obtain the following,

$$\nabla_{\perp}\left(p + \frac{B^2}{2\mu_0}\right) - \frac{B^2}{\mu_0}\kappa = 0 \tag{2.16}$$

where $\nabla_{\perp} = \nabla - \mathbf{b}(\mathbf{b} \cdot \nabla)$ is the component of the gradient perpendicular to, $\mathbf{b} = \mathbf{B}/B$, and $\kappa = \mathbf{b} \cdot \nabla \mathbf{b}$ is the curvature vector. In Eq. (2.16), the $B^2/2\mu_0$ term represents the magnetic pressure, and the $(B^2/\mu_0)\kappa$ term represents the magnetic tension created by the curvature of the magnetic field lines.

2.3.1 Flux Surfaces

Note that if you take the dot product of the pressure balance equation with the magnetic field vector one gets,

$$\mathbf{B} \cdot \nabla p = 0. \tag{2.17}$$

Typical equilibrium pressure profiles will peak near the center of the poloidal cross section and decrease radially outwards. This combined with the above equation implies that magnetic field lines must lie on surfaces of constant pressure. These surfaces are known as flux surfaces. The surface which all other standard flux surfaces are centered around is known as the magnetic axis. Rather than a surface,it is a line where the pressure is a maximum. There is a similar relation for the current density, where you can dot the momentum equation with the current density to get,

$$\mathbf{J} \cdot \nabla p = 0. \tag{2.18}$$

Thus, current lines must also lie on surfaces of constant pressure. Another point of interest are the trajectories of the magnetic field lines on these surfaces. These can be classified as one of three types: rational, ergodic, and stochastic. Rational field lines close on themselves on a constant pressure contour after a finite number of toroidal revolutions. Ergodic field lines instead trace out the entirety of the contour never closing in on itself. Lastly stochastic field lines are those which wander and trace a volume of space rather than a closed contour. The later case is the most undesirable as it is associated with poor confinement properties, mostly due to significant thermal transport. These stochastic field lines can only be found in systems that lack geometric symmetry, such as 3D magnetic fields found in a stellarator.

2.3.2 Rotational Transform

Returning to the other two kinds of field lines, the way we characterize them as either rational or ergodic is by looking at their rotational transform. The rotational transform angle, ι, is defined as the average change in poloidal angle of a field line after an infinite number of toroidal revolutions. Written out as an equation we have,

$$\iota = \lim_{N \to \infty} \frac{1}{N} \sum_{n=1}^{N} \Delta\theta_n. \tag{2.19}$$

Here $\Delta\theta_n$ represents the rotation angle from the n^{th} toroidal revolution. Typically, one does not work with ι, but rather, $\iota\!\!\!-$, which is defined as,

$$\iota\!\!\!- \equiv \frac{\iota}{2\pi}. \tag{2.20}$$

The quantity $\iota\!\!\!-$ is known as the rotational transform, and represents the average number of poloidal transits a magnetic field line makes per toroidal transit. In the tokamak community rather than working with the rotational transform, the safety factor is used, which is defined as, $q \equiv 1/\iota\!\!\!-$. If the rotational transform of a field line is an irrational number, then it is ergodic, whereas if it were rational then the field line is rational and closes on itself. Ergodic field lines will trace out torus shaped tubes in a Poincaré, or puncture, plot, whereas rational field lines will appear as dashed lines.

2.4 Magnetic Coordinates

Before beginning the deeper discussion on equilibrium it is helpful, especially for the 3D case, to introduce magnetic coordinates. This is because by using the right coordinate system we can simplify a great deal of the mathematics involved as well as easily observe global properties of the system. An example of a set of magnetic coordinates is a system where one coordinate is constant on the flux surfaces and the magnetic field lines are straight in terms of the other two. In this section, we will assume the system is given by a torus and the surfaces of constant pressure are nested, meaning they lie inside each other. Let the coordinate system be set by (p, ϑ, φ), representing the pressure, an angle measured along the short way of a torus, the poloidal direction, increasing by 2π after a full rotation, and an angle measured along the long way of a torus, the toroidal direction, increasing by 2π after a full rotation. In this coordinate system the magnetic field, **B** can be written in terms of its contravariant components as,

$$\mathbf{B} = B^p \mathbf{e}_p + B^\vartheta \mathbf{e}_\vartheta + B^\varphi \mathbf{e}_\varphi \tag{2.21}$$

or in terms of its covariant components,

$$\mathbf{B} = B_p \nabla p + B_\vartheta \nabla \vartheta + B_\varphi \nabla \varphi \tag{2.22}$$

where $\nabla u^i = \mathbf{e}^i$, $B^i = \mathbf{B} \cdot \nabla u^i$, $B_i = \mathbf{B} \cdot \mathbf{e}_i$, and the u^i are the coordinates of the system. Before going further into the discussion of the magnetic coordinates, a brief discussion on curvilinear coordinates is required.

2.4.1 Curvilinear Coordinates

The metric coefficients, $g_{ij} = \mathbf{e}_i \cdot \mathbf{e}_j$ and $g^{ij} = \nabla u^i \cdot \nabla u^j$ can be used to convert between the two vector representations $\mathbf{e}_i = g_{ij} \nabla u^j$ and $\nabla u^i = g^{ij} \mathbf{e}_j$, where Einstein summation notation is used. It is important to make the distinction that the vectors $\mathbf{e}_i$ are not unit vectors. Rather, the unit vector is instead defined as $\hat{\mathbf{e}}_i = \mathbf{e}_i / \sqrt{g_{ii}} = \mathbf{e}_i / h_i$, where the h_i terms are scale factors. The metric coefficient is related to the Jacobian, $\mathcal{J}$, of the coordinate system. We can construct a three by three matrix populated by the metric coefficients called the metric matrix. The determinant of said matrix, g, is equal to the square of the Jacobian. The Jacobian itself has other equivalent definitions, such as,

$$\mathcal{J} = \mathbf{e}_1 \cdot \mathbf{e}_2 \times \mathbf{e}_3 = h_1 h_2 h_3 \tag{2.23}$$

or the inverse Jacobian,

$$\mathcal{J}^{-1} = \nabla u^1 \cdot \nabla u^2 \times \nabla u^3. \tag{2.24}$$

Converting between the contravariant and covariant forms can also be done using the Jacobian,

$$\mathbf{e}_i = \mathcal{J}(\nabla u^j \times \nabla u^k) \tag{2.25}$$

and

$$\nabla u^i = \frac{1}{\mathcal{J}}(u_j \times u_k) \tag{2.26}$$

where only cyclical combinations of i, j, k are allowed, i.e. (1,2,3), (3,1,2), and (2,3,1). With the Jacobian and metric coefficients one is also able to define the differential arc length, area, and volume elements. The differential arc length is given by,

$$\mathrm{d}l(\text{along } u^i) = h_i.\, \mathrm{d}u^i \quad \text{no summation} \tag{2.27}$$

The differential area element vector is,

$$\mathrm{d}\mathbf{S}(\text{in } u^i = \text{constant}) = \frac{\nabla u^i}{|\nabla u^i|}\,\mathrm{d}S = \pm\mathcal{J}\,\mathrm{d}u^j\,\mathrm{d}u^k \nabla u^i \tag{2.28}$$

where the sign must be assigned according to the convention chosen for the vector normal to the surface. The scalar differential area element is,

$$\mathrm{d}S = h_j h_k \,\mathrm{d}u^j \,\mathrm{d}u^k. \quad \text{no summation} \tag{2.29}$$

The differential volume element is,

$$\mathrm{d}^3R = \mathcal{J} \,\mathrm{d}u^1 \,\mathrm{d}u^2 \,\mathrm{d}u^3. \tag{2.30}$$

It can be convenient to rewrite the above expression by combining Eqs. (2.28) and (2.30) to obtain

$$\mathrm{d}^3R = \frac{\mathrm{d}u^i}{|\nabla u^i|}\mathrm{d}S. \tag{2.31}$$

Lastly, we give the definition of a gradient,

$$\nabla A = \sum_i \nabla u^i \frac{\partial A}{\partial u^i}. \tag{2.32}$$

2.4.2 Equations of a Field Line

With the curvilinear coordinate discussion finished, it is beneficial to discuss the equation of a magnetic field line. A magnetic field line is a curve that is at all points parallel to the magnetic field vector. In mathematical terms this can be expressed as,

$$\mathbf{B} = c \,\mathrm{d}\mathbf{R} \tag{2.33}$$

where c is a proportionality constant and d**R** is a differential vector tangent to the field line, and **R** is the position vector from the coordinate system origin to any point in space. Solving the above equation for the contravariant components of both $\mathbf{B}(B^1, B^2, B^3)$ and $\mathrm{d}\mathbf{R}(du^1, du^2, du^3)$ gives,

$$\frac{B^1}{du^1} = \frac{B^2}{du^2} = \frac{B^3}{du^3} = c.$$

Recalling that $B^i = \mathbf{B} \cdot \nabla u^i$ allows us to rewrite the above equation as,

$$\frac{\mathbf{B} \cdot \nabla u^1}{du^1} = \frac{\mathbf{B} \cdot \nabla u^2}{du^2} = \frac{\mathbf{B} \cdot \nabla u^3}{du^3}.$$

Lastly, we can parameterize the field line curve by the arc length l, then the ensuing vector, $\mathrm{d}\mathbf{R}/\mathrm{d}l$ is a unit vector, which then gives,

$$\frac{\mathbf{B}}{B} = \frac{\mathrm{d}\mathbf{R}}{\mathrm{d}l}. \tag{2.34}$$

From Eq. (2.33), we note that the constant c must equal $B/\mathrm{d}l$, and thus the magnetic field line equations are,

$$\frac{B}{\mathrm{d}l} = \frac{\mathbf{B} \cdot \nabla u^1}{\mathrm{d}u^1} = \frac{\mathbf{B} \cdot \nabla u^2}{\mathrm{d}u^2} = \frac{\mathbf{B} \cdot \nabla u^3}{\mathrm{d}u^3}. \tag{2.35}$$

2.4.3 Magnetic Field in Magnetic Coordinates

From Eq. (2.17) the first term in Eq. (2.21) is eliminated. Then using Eq. (2.25) the magnetic field can be written as,

$$\mathbf{B} = \mathcal{B}^{\vartheta}(\nabla\varphi \times \nabla p) + \mathcal{B}^{\varphi}(\nabla p \times \nabla\vartheta) \tag{2.36}$$

where the $\mathcal{B}$ terms have absorbed the Jacobian factor. Since the magnetic field is divergenceless, taking the divergence of the above equation gives,

$$\nabla\mathcal{B}^{\vartheta} \cdot (\nabla\varphi \times \nabla p) + \nabla\mathcal{B}^{\varphi} \cdot (\nabla p \times \nabla\vartheta) = 0.$$

Using Eqs. (2.32),(2.24) the above equation simplifies to,

$$\frac{1}{\mathcal{J}}\left(\frac{\partial \mathcal{B}^{\vartheta}}{\partial \vartheta}+\frac{\partial \mathcal{B}^{\varphi}}{\partial \varphi}\right)=0 \tag{2.37}$$

thus implying that the terms inside the parenthesis add to zero. Integrating over ϑ yields,

$$\frac{\partial}{\partial \varphi}\int_0^{2\pi}\mathcal{B}^{\varphi}\,\mathrm{d}\vartheta=0$$

for all values of p and φ. Integrating over φ gives,

$$\int_0^{2\pi}\mathcal{B}^{\varphi}\,\mathrm{d}\vartheta=g(p)$$

where $g(p)$ is some arbitrary function. A similar relation can be obtained for $\mathcal{B}^{\vartheta}$. This implies that $\mathcal{B}^{\varphi}$ and $\mathcal{B}^{\vartheta}$ can be written as,

$$\begin{aligned}\mathcal{B}^{\varphi}&=\frac{\partial f}{\partial \varphi}+\frac{g(p)}{2\pi}\\ \mathcal{B}^{\vartheta}&=\frac{\partial f}{\partial \vartheta}+\frac{h(p)}{2\pi}\end{aligned} \tag{2.38}$$

for some function $f(p,\vartheta,\varphi)$ and $h(p)$. The functions f, g, and h, can be redefined as $\psi'(p)=g(p)/2\pi$, $\chi'(p)=h(p)/2\pi$, and $\lambda(p,\vartheta,\varphi)=f(p,\vartheta,\varphi)/\psi'(p)$, where primes are derivatives with respect to p. Substituting the new definitions in the above equations gives,

$$\begin{aligned}\mathcal{B}^{\varphi}&=\psi'(p)\left(1+\frac{\partial \lambda}{\partial \vartheta}\right)\\ \mathcal{B}^{\vartheta}&=\chi'(p)-\psi'(p)\frac{\partial \lambda}{\partial \varphi}.\end{aligned}$$

Then the expression for the magnetic field, **B** becomes,

$$\mathbf{B}=\left(1+\frac{\partial \lambda}{\partial \vartheta}\right)\nabla\psi\times\nabla\vartheta+\nabla\varphi\times\nabla\chi-\frac{\partial \lambda}{\partial \varphi}\nabla\varphi\times\nabla\psi$$

or more compactly,

$$\mathbf{B} = \nabla\psi \times \nabla\theta + \nabla\varphi \times \nabla\chi \tag{2.39}$$

where $\theta = \vartheta + \lambda$. This is $\mathbf{B}$ in magnetic coordinates, (ψ, θ, φ) where the first term corresponds to the toroidal component and the second term corresponds to the poloidal component. It is important to note that both ψ and χ have physical meaning as they are related to the toroidal and poloidal magnetic flux, respectively. To demonstrate this, note that both ψ and χ are constant on surfaces of constant pressure and are set to vanish at the magnetic axis. First, we calculate the toroidal flux, which is found by calculating the amount of magnetic field passing through a surface of constant φ between the magnetic axis and some surface $\psi =$constant. The toroidal flux given by,

$$\Psi_T = \iint_S \mathcal{J}\,\mathbf{B} \cdot \nabla\varphi \,\mathrm{d}\psi\,\mathrm{d}\theta \tag{2.40}$$

where Eq. (2.28) has been used to replace the area element vector. Recalling the definition of the inverse Jacobian in Eq. (2.24), the integral becomes

$$\begin{aligned}
\Psi_T &= \int_0^{\psi} \mathrm{d}\psi' \int_0^{2\pi} \frac{\mathbf{B} \cdot \nabla\varphi}{\nabla\psi' \cdot (\nabla\theta \times \nabla\varphi)}\,\mathrm{d}\theta \\
&= \int_0^{\psi} \mathrm{d}\psi' \int_0^{2\pi} \frac{(\nabla\psi' \times \nabla\theta) \cdot \nabla\varphi}{\nabla\psi' \cdot (\nabla\theta \times \nabla\varphi)}\,\mathrm{d}\theta \\
&= 2\pi\psi.
\end{aligned} \tag{2.41}$$

The poloidal flux is found by calculating the amount of magnetic field which passes through a surface of constant θ between the magnetic axis and some surface $\psi =$constant. The poloidal flux is given by,

$$\Psi_P = \iint_S \mathcal{J}\,\mathbf{B} \cdot \nabla\theta \,\mathrm{d}\psi\,\mathrm{d}\varphi. \tag{2.42}$$

Similarly as before we have,

$$
\begin{aligned}
\Psi_P &= \int_0^{\psi} \mathrm{d}\psi' \int_0^{2\pi} \frac{\mathbf{B}\cdot\nabla\theta}{\nabla\psi'\cdot(\nabla\theta\times\nabla\varphi)}\,\mathrm{d}\varphi \\
&= \int_0^{\psi} \mathrm{d}\psi' \int_0^{2\pi} \frac{(\nabla\varphi\times\nabla\chi)\cdot\nabla\theta}{\nabla\psi'\cdot(\nabla\theta\times\nabla\varphi)}\,\mathrm{d}\varphi \\
&= \int_0^{\psi} \mathrm{d}\psi' \int_0^{2\pi} \frac{d\chi}{d\psi'}\frac{(\nabla\varphi\times\nabla\psi')\cdot\nabla\theta}{\nabla\psi'\cdot(\nabla\theta\times\nabla\varphi)}\,\mathrm{d}\varphi \\
&= 2\pi\chi(\psi).
\end{aligned} \tag{2.43}
$$

We can gain further insight into χ by returning to the field line equations. Rearranging terms gives,

$$
\frac{\mathrm{d}\theta}{\mathrm{d}\varphi} = \frac{\mathbf{B}\cdot\nabla\theta}{\mathbf{B}\cdot\nabla\varphi} = \frac{(\nabla\varphi\times\nabla\chi)\cdot\nabla\theta}{(\nabla\psi\times\nabla\theta)\cdot\nabla\varphi} = \frac{\mathrm{d}\chi}{\mathrm{d}\psi}. \tag{2.44}
$$

Recalling that the rotational transform is a measure of the change in poloidal angle relative to the change in toroidal angle as it transits a torus, we have that,

$$
\frac{\mathrm{d}\theta}{\mathrm{d}\varphi} = \frac{\mathrm{d}\chi}{\mathrm{d}\psi} = \iota(\psi). \tag{2.45}
$$

The above equation also shows that magnetic field lines draw out straight lines in the (θ,φ) plane. It must be emphasized that the equality is only true in these straight field line coordinates, otherwise the previous definition of the rotational transform is required. Furthermore, with the above definition, we are able to write Eq. (2.39) is a more compact way known as the Clebsch representation. First we rearrange some terms to obtain,

$$
\begin{aligned}
\mathbf{B} &= \nabla\psi\times\nabla\theta + \nabla\varphi\times\iota\nabla\psi \\
&= \nabla\psi\times\nabla\theta - \nabla\psi\times\iota\nabla\varphi.
\end{aligned}
$$

Then we define $\alpha = \theta - \iota\varphi$ so we may write,

$$
\mathbf{B} = \nabla\psi\times\nabla\alpha \tag{2.46}
$$

which will be used in Sec. 2.7.

2.5 One Dimensional Equilibria

With the ideal MHD equilibrium defined, we can now study different configurations and the associated equilibria. This begins with looking at a one dimensional cylindrical system, where quantities only have a dependence on the radial coordinate, r. The configuration presented below is known as the screw pinch, where in a cylinder of arbitrary length current is driven into the plasma such that it has components in the poloidal direction and the z direction. The magnetic field lines in this configuration twist around the surface, similar to the threads in a screw, hence the name.

To begin the analysis, we must make an accounting of the unknowns of the problem to know what we need to solve for. Those unknowns are: $p, \mathbf{B} = B_\theta \mathbf{e}_\theta + B_z \mathbf{e}_\mathbf{z}$, and $\mathbf{J} = J_\theta \mathbf{e}_\theta + J_z \mathbf{e}_z$. The first and easiest equation to address is the solenoidal condition, $\nabla \cdot \mathbf{B} = 0$, which is satisfied automatically since the two components of the magnetic field are only dependent on the radial coordinate. Ampére's law gives,

$$\mu_0 \mathbf{J} = -\frac{dB_z}{dr}\mathbf{e}_\theta + \frac{1}{r}\frac{d}{dr}(rB_\theta)\mathbf{e}_z. \tag{2.47}$$

Then the current density can be substituted into the pressure balance equation,

$$p' = J_\theta B_z - J_z B_\theta \tag{2.48}$$

to get,

$$\frac{d}{dr}\left(p + \frac{B_\theta^2}{2\mu_0} + \frac{B_z^2}{2\mu_0}\right) + \frac{B_\theta^2}{\mu_0 r} = 0. \tag{2.49}$$

The system has now been reduced to one equation with three unknowns. As a result we are free to choose arbitrary functions for two of the unknowns, for example the components of the magnetic field, and determine the remaining one using the above equation. The arbitrary functions are typically known as free functions. While the above equilibrium is simple, it does not have the properties which would be required for a fusion power plant. The magnetic field lines all go through the vacuum vessel, since it is a straight cylinder, there will be significant energy loss rates as particles leave the plasma and collide with the walls. A solution to some of these issues is to add toroidicity and make the system doughnut-shaped rather than a cylinder.

2.6 Two-Dimensional Equilibria

By changing the system from a cylinder to a torus, an extra dimension is added to the problem. For this toroidal equilibrium we will use a standard cylindrical coordinate system, (R, ϕ, Z), shown in Fig. 2.1. In this configuration we will assume that there is toroidal axisymmetry, meaning that derivatives of any quantity in the toroidal direction is zero, or simply, $\partial_\phi F = 0$. The analysis of this 2D equilibrium will follow a similar structure as before, except the goal is to derive what is known as the Grad-Shafranov equation which describes axisymmetric toroidal equilibrium.

The divergence of **B** equation with the assumption of axisymmetry gives,

$$\frac{1}{R}\frac{\partial}{\partial R}(RB_R) + \frac{\partial B_Z}{\partial Z} = 0. \tag{2.50}$$

We can also express the magnetic field in terms of the vector potential, **A**. Since $\mathbf{B} = \nabla \times \mathbf{A}$ the components B_R and B_Z can be expressed as,

$$\begin{aligned} B_R &= -\frac{\partial A_\phi}{\partial Z} \\ B_Z &= \frac{1}{R}\frac{\partial}{\partial R}(RA_\phi). \end{aligned} \tag{2.51}$$

With the forms of Eqs. (2.50)-(2.51) a stream function, $\chi = RA_\phi$, can be defined which will facilitate the rest of the derivation. It is worth noting that this is the same χ we discussed

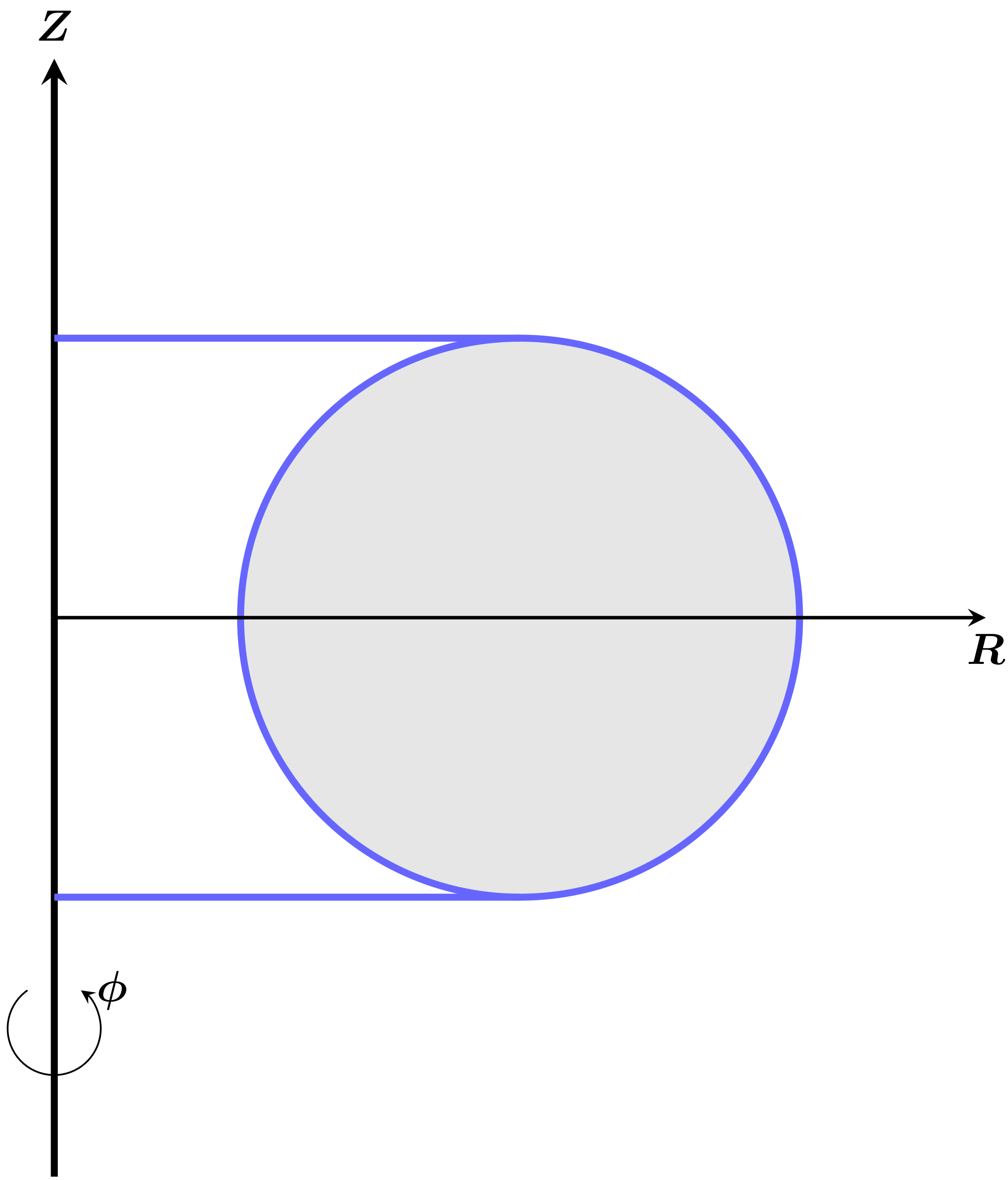

Figure 2.1: Geometry for axisymmetric equilibrium

previously. Now note that,

$$\mathbf{B} \cdot \nabla \chi = B_R \frac{\partial \chi}{\partial R} + B_Z \frac{\partial \chi}{\partial Z} = 0 \tag{2.52}$$

which can be shown by eliminating the partial derivatives using Eq. (2.51). This implies that magnetic field lines lie on surfaces of constant χ. It is also beneficial to recognize that the magnetic field can be rewritten in terms of its toroidal and poloidal components,

$$\mathbf{B} = B_\phi \mathbf{e}_\phi + \frac{1}{R} \nabla \chi \times \mathbf{e}_\phi. \tag{2.53}$$

Next we look at Ampére's law. Expanding $\nabla \times \mathbf{B}$ and using the previous results gives,

$$\begin{aligned} \mu_0 \mathbf{J} &= -\frac{\partial B_\phi}{\partial Z} \mathbf{e}_R + \left(\frac{\partial B_R}{\partial Z} - \frac{\partial B_Z}{\partial R} \right) \mathbf{e}_\phi + \frac{1}{R} \frac{\partial}{\partial R} (R B_\phi) \mathbf{e}_Z \\ &= \frac{1}{R} \nabla (R B_\phi) \times \mathbf{e}_\phi - \left(\frac{1}{R} \frac{\partial^2 \chi}{\partial Z^2} + \frac{\partial}{\partial R} \left(\frac{1}{R} \frac{\partial \chi}{\partial R} \right) \right) \mathbf{e}_\phi \\ &= \frac{1}{R} \nabla (R B_\phi) \times \mathbf{e}_\phi - \frac{1}{R} \Delta^* \chi \, \mathbf{e}_\phi \end{aligned} \tag{2.54}$$

where the operator Δ^* is defined as,

$$\Delta^* \equiv R \frac{\partial}{\partial R} \left(\frac{1}{R} \frac{\partial}{\partial R} \right) + \frac{\partial^2}{\partial Z^2}. \tag{2.55}$$

The last step is to substitute the expressions found above for **B** and **J** into the momentum equation. Before making the substitutions, it is helpful to take the dot product of the momentum equation with **B** and **J** and expand from there to make certain observations. Dotting the equation with **B** gives,

$$\begin{aligned} \mathbf{B} \cdot \nabla p &= \frac{1}{R} \nabla \chi \times \mathbf{e}_\phi \cdot \nabla p \\ &= \mathbf{e}_\phi \cdot \nabla \chi \times \nabla p = 0. \end{aligned} \tag{2.56}$$

This implies that $\nabla \chi \parallel \nabla p$. Since they are parallel, one can invoke the chain rule to make the transformation,

$$\nabla p = \nabla \chi \frac{dp}{d\chi} \tag{2.57}$$

which indicates that $p = p(\chi)$, and thus the pressure is a flux function. As before, the pressure is also a free function which the model itself cannot determine.

Taking the dot product of the momentum equation with **J** yields a similar result,

$$\begin{aligned} \mathbf{J} \cdot \nabla p &= \frac{1}{R} \nabla (RB_\phi) \times \mathbf{e}_\phi \cdot \nabla p \\ &= \mathbf{e}_\phi \cdot \nabla (RB_\phi) \times \nabla p = 0. \end{aligned} \tag{2.58}$$

Again, this indicates that RB_ϕ is also a flux function as well as a free function. Let us define the function, $F(\chi) = RB_\phi$ to be used in the ensuing steps. Now that the components of the momentum equation can all be represented in terms of flux functions or χ, we can substitute into the momentum equation,

$$\begin{aligned} \nabla p &= \mathbf{J} \times \mathbf{B} \\ \nabla \chi \frac{dp}{d\chi} &= \left(\frac{1}{\mu_0 R} \nabla F \times \mathbf{e}_\phi - \frac{1}{\mu_0 R} \Delta^* \chi \, \mathbf{e}_\phi \right) \times \left(\frac{F}{R} \mathbf{e}_\phi + \frac{1}{R} \nabla \chi \times \mathbf{e}_\phi \right) \\ \nabla \chi \frac{dp}{d\chi} &= -\frac{F}{\mu_0 R^2} \nabla F + \frac{1}{\mu_0 R^2} \Delta^* \chi \nabla \chi \\ \nabla \chi \frac{dp}{d\chi} &= -\frac{1}{2\mu_0 R^2} \nabla \chi \frac{dF^2}{d\chi} - \frac{1}{\mu_0 R^2} \Delta^* \chi \nabla \chi \end{aligned}$$

and solving for $\Delta^* \chi$,

$$\Delta^* \chi = -\mu_0 R^2 \frac{dp}{d\chi} - \frac{1}{2} \frac{dF^2}{d\chi} \tag{2.59}$$

which is the Grad-Shafranov equation. To solve the equation, one must set the profiles for $p(\chi)$ and $F(\chi)$, as well as boundary conditions, to then solve for χ. From there, one is able to calculate the functional forms of the magnetic field and the current density. In most circumstances, an analytic solution of Eq. (2.59) does not exist and it is instead solved numerically.

From a theoretical point of view, 2D axisymmetric equilibria are attractive because of their relative simplicity, which makes them easier to study. There are some practical challenges to the design though. A main driver of this is the fact that a net toroidal current is required to achieve force balance. In a tokamak, this is achieved by driving current into a plasma with a transformer. This leads to several problems. The first is that it is difficult to indefinitely drive DC current with a transformer, which makes a tokamak run as a pulsed device rather than a steady state one. This is undesirable as a fusion power plant would ideally be running continuously. It is worth noting that there are non-inductive methods to drive current in the plasma that are currently a subject of research. Another issue with driving current in the plasma is that this can lead to a variety of current-driven instabilities, which can lead to catastrophic losses of plasma confinement, known as disruptions. As a result, the study of instabilities and how to suppress them is a major area of interest in the field of tokamak physics.

2.7 Three-Dimensional Equilibria

Now we begin the discussion on 3D toroidal equilibria. The third dimension is added to the system by removing the toroidal symmetry assumed in the previous section. The loss of axisymmetry makes the problem of calculating the equilibrium more difficult, and as a result one cannot formulate a relation that is equivalent to the Grad-Shafranov equation for the 3D case. Thus, a method different from what was previously described must be used. Because most 3D equilibria must be calculated numerically, it is preferable to set up the force balance problem as a variational principle. What this means is that solutions of the equation $\nabla p = \mathbf{J} \times \mathbf{B}$ are in fact states of minimum MHD energy,

$$W = \int \left(\frac{p}{\Gamma - 1} + \frac{B^2}{2\mu_0} \right) \mathrm{d}V \tag{2.60}$$

under several constraints. In the above equation, Γ is the adiabatic index, the first term represents the plasma's thermal energy, and the second term represents the magnetic energy. The constraints are as follows, where they are listed as they are found in Ref [11].

1. ψ has nested toroidal flux surfaces ranging from the innermost one, $\psi = 0$, to $\psi = \psi_{max}$ on the boundary;

2. $\nabla \cdot \mathbf{B} = 0$;

3. $\mathbf{B} \cdot \nabla\psi = 0$;

4. The toroidal magnetic flux, seen in Eq. (2.41), inside the toroid defined by each level curve $\psi = \psi_0 \in [0, \psi_{max}]$ is equal to $2\pi\psi_0$;

5. The corresponding poloidal flux, seen in Eq. (2.43), is equal to $2\pi\chi(\psi)$;

6. $$\int_{\psi<\psi_0} p^{1/\Gamma}\,\mathrm{d}V = M(\psi_0).$$

Where the last constraint is stating that, since the entropy density, p/ρ^{Γ}, is conserved, the total mass inside each flux surface is constant, with that quantity being, $M(\psi_0)$. Among all choices of p, $\mathbf{B}$, and ψ, Eq. (2.60) is made stationary if, and only if, p is a function of ψ alone and $\mathbf{J} \times \mathbf{B} = \nabla p$, where $\mathbf{J} = \nabla \times \mathbf{B}/\mu_0$. The goal of this section is to prove the previous statement.

We begin this by varying the pressure. This gives,

$$\begin{aligned} 0 = \delta W &= \int_{\psi=\psi_0} \frac{\delta p}{\Gamma - 1}\mathrm{d}V \\ &= \frac{1}{\Gamma - 1}\int_0^{\psi_0} d\psi \int_{\psi=\psi_0} \frac{\delta p}{|\nabla\psi|}\mathrm{d}S \end{aligned} \tag{2.61}$$

where Eq. (2.31) was used to change the volume element. For the right-hand side to equal zero, we require that the surface integral be zero. To show this, we can first vary the pressure in constraint 6,

$$
\begin{aligned}
M(\psi_0) &= \int_{\psi<\psi_0} (p+\delta p)^{\frac{1}{\Gamma}} \frac{\mathrm{d}\psi}{|\nabla\psi|}\,\mathrm{d}S \\
&= \int_{\psi<\psi_0} \left(p^{\frac{1}{\Gamma}} + \frac{\delta p}{\Gamma} p^{\frac{1}{\Gamma}-1}\right) \frac{\mathrm{d}\psi}{|\nabla\psi|}\,\mathrm{d}S \\
&= \int_{\psi<\psi_0} p^{\frac{1}{\Gamma}} \frac{\mathrm{d}\psi}{|\nabla\psi|}\,\mathrm{d}S + \int_{\psi<\psi_0} \frac{\delta p}{\Gamma} p^{\frac{1}{\Gamma}-1} \frac{\mathrm{d}\psi}{|\nabla\psi|}\,\mathrm{d}S.
\end{aligned}
$$

Then, if we take the derivative of the above equation with respect to ψ, we obtain,

$$
M'(\psi_0) = \int_{\psi=\psi_0} \frac{p^{\frac{1}{\Gamma}}}{|\nabla\psi|}\,\mathrm{d}S \tag{2.62}
$$

and,

$$
0 = \int_{\psi=\psi_0} p^{\frac{1}{\Gamma}-1} \frac{\delta p}{|\nabla\psi|}\,\mathrm{d}S. \tag{2.63}
$$

Equation (2.63) restricts which variations are permitted. For example, if p_0 and p_1 are the pressures at two locations $\mathbf{r}_0$ and $\mathbf{r}_1$, respectively, on the same ψ surface, then

$$
\delta p = \left(p_0^{1-\frac{1}{\Gamma}} \delta(\mathbf{r}-\mathbf{r}_0) + p_1^{1-\frac{1}{\Gamma}} \delta(\mathbf{r}-\mathbf{r}_1) \right) |\nabla\psi| \tag{2.64}
$$

is an allowable variation. However, substituting this into Eq. (2.61) requires that $p_0 = p_1$ for the equality to be satisfied. Hence, the pressure must be constant on a flux surface, making it a flux function, and $\mathbf{B}\cdot\nabla p = 0$.

The next step is to vary the magnetic field. First, recall the formulation of the magnetic field found in Eq. (2.46),

$$
\mathbf{B} = \nabla\psi \times (\nabla\vartheta + \nabla\lambda - \iota\nabla\varphi).
$$

This representation of the magnetic field satisfies constraints (3)-(5), and $\mathbf{B}$ can be varied by varying λ and ψ separately. Varying λ gives,

$$\begin{aligned}
\mu_0(W + \delta W) &= \frac{1}{2}\int (\mathbf{B} + \delta\mathbf{B})^2 \, \mathrm{d}V \\
\mu_0 \delta W &= \int \mathbf{B} \cdot \delta\mathbf{B} \, \mathrm{d}V \\
&= \int \mathbf{B} \cdot (\nabla\psi \times \nabla\delta\lambda) \, \mathrm{d}V \\
&= \int \nabla(\delta\lambda) \cdot (\mathbf{B} \times \nabla\psi) \, \mathrm{d}V.
\end{aligned}$$

Then using the divergence theorem,

$$\begin{aligned}
\mu_0 \delta W &= \int \delta\lambda(\mathbf{B} \times \nabla\psi) \cdot \frac{\nabla\psi}{|\nabla\psi|} \, \mathrm{d}S - \int \delta\lambda \nabla \cdot (\mathbf{B} \times \nabla\psi) \, \mathrm{d}V \\
&= -\int \delta\lambda \, \nabla\psi \cdot (\nabla \times \mathbf{B}) \, \mathrm{d}V = 0.
\end{aligned} \tag{2.65}$$

Where the surface integral vanishes because of the dot product of two perpendicular vectors. Using Maxwell's equations this implies that $\mathbf{J} \cdot \nabla\psi = 0$.

Finally, we must vary ψ, remembering constraint (6). Varying ψ will change the shape of the flux surfaces. The volume of the flux surface at $\psi = c$ is given by,

$$V(c) = \int_0^c \mathrm{d}\psi \int \frac{\mathrm{d}S}{|\nabla\psi|}$$

and its variation is,

$$\delta V(c) = -\int_{\psi=c} \frac{\delta\psi}{|\nabla\psi|} \, \mathrm{d}S \tag{2.66}$$

from Eq. (2.62) the pressure can be written as,

$$p(\psi) = \left(\frac{M'(\psi)}{V'(\psi)}\right)^{\Gamma}$$

and its variation at constant ψ is,

$$\frac{\delta p(\psi)}{p(\psi)} = -\frac{\Gamma \delta V'(\psi)}{V'(\psi)}$$

thus giving that,

$$\int \delta p \, \mathrm{d}V = -\Gamma \int \frac{p \, \delta V'(\psi)}{V'(\psi)} \, \mathrm{d}V = -\Gamma \int p \, \delta V \, \mathrm{d}\psi. \tag{2.67}$$

Integrating by parts and using Eq. (2.66) one is able to show that,

$$\int \delta p \, \mathrm{d}V = \Gamma \int p'(\psi) \delta V \, \mathrm{d}\psi = -\Gamma \int p' \delta\psi \, \mathrm{d}V. \tag{2.68}$$

Finally, we can vary W with respect to ψ,

$$\begin{aligned} \delta W &= \int \left(\frac{p' \delta\psi + \delta p}{\Gamma - 1} + \frac{\mathbf{B} + \delta \mathbf{B}}{\mu_0} \right) \mathrm{d}V \\ &= \int \left(-p' \delta\psi + \frac{\mathbf{B} \cdot (\nabla \delta\psi \times \nabla \alpha)}{\mu_0} \right) \mathrm{d}V. \end{aligned}$$

Integrating by parts and noting that $\delta\psi = 0$ on the boundaries yields,

$$\delta W = \int \delta\psi \left(\frac{\nabla \cdot (\mathbf{B} \times \nabla \alpha)}{\mu_0} - p' \right) \mathrm{d}V. \tag{2.69}$$

Taking $\delta W = 0$ implies that,

$$(\nabla \times \mathbf{B}) \cdot \nabla \alpha = \mu_0 p'(\psi). \tag{2.70}$$

Since,

$$\mathbf{J} \times \mathbf{B} = \mathbf{J} \times (\nabla\psi \times \nabla\alpha) = (\mathbf{J} \cdot \nabla\alpha) \nabla\psi$$

we then conclude that $\mathbf{J} \times \mathbf{B} = \nabla p$. Thus, the proof is finished. This shows that the equilibrium for a 3D plasma is entirely determined by the last closed flux surface, and two profile functions. In this case we chose them to be $\chi(\psi)$ and $M(\psi)$, but there are different possible choices, such as $\iota(\psi)$ and $p(\psi)$.

2.7.1 Problems with 3D Ideal Equilibria

The above proof demonstrates the existence of 3D MHD equilibria, but it does not guarantee that the pressure profile and magnetic fields are physical and free of any singularities. This becomes most evident when one assumes all the magnetic surfaces in the equilibrium are perfect, closed, and continuously nested. By saying a perfect closed surface, we mean that the field lines are not stochastic, and by continuously nested we mean that the surfaces all surround the same central point, the magnetic axis. This assumption can result in the current density going to infinity at all surfaces where the rotational transform is rational. This is a problem because flux surfaces are generally required for good confinement properties, and two of the most commonly used stellarator equilibrium codes, VMEC [14] and DESC [15], assume the system has perfect nested flux surfaces. This can be shown in the following manner.

Consider an equilibrium with an arbitrary magnetic field and a pressure profile. We now undertake the task of computing the current density parallel to the magnetic field. The current density can be decomposed into a component parallel and perpendicular to the magnetic field,

$$\mathbf{J} = J_{\parallel}\mathbf{b} + \mathbf{J}_{\perp}.$$

Since $\nabla \cdot \mathbf{J} = 0$ from Eq. (2.15), taking the divergence of the above equation and rearranging terms gives,

$$\mathbf{B} \cdot \nabla \left(\frac{J_{\parallel}}{B} \right) = -\nabla \cdot \mathbf{J}_{\perp}. \tag{2.71}$$

Equations like the one above of the form,

$$\mathbf{B} \cdot \nabla f = S \tag{2.72}$$

are known as magnetic differential equations (MDE). The S is a source term, and f is an unknown single-valued function which we are solving for. In order for f to be single valued, there is a condition on S. Expanding Eq. (2.72),

$$\mathbf{B} \cdot \nabla f = B\frac{\partial f}{\partial l} = S$$

where the partial derivative is the derivative along the magnetic field line. Integrating over an arbitrary length L gives,

$$f(L) - f(0) = \int_0^L S\frac{\mathrm{d}l}{B}.$$

Then, if the curve being integrated along is a rational surface which closes on itself after a distance L, $f(0) - f(L) = 0$ and

$$\oint S\frac{\mathrm{d}l}{B} = 0. \tag{2.73}$$

It is now convenient to re-express $\mathbf{J}_\perp$ in terms of $\mathbf{B}$ and p. Note that,

$$\mathbf{J}_\perp = \mathbf{b} \times (\mathbf{J} \times \mathbf{b}).$$

Then crossing both sides of the momentum equation with $\mathbf{B}$ and dividing by B^2, we find that,

$$\mathbf{J}_\perp = \frac{\mathbf{B} \times \nabla p}{B^2}.$$

Taking the divergence and using some vector derivative identities gives,

$$\nabla \cdot \mathbf{J}_\perp = (\mathbf{B} \times \nabla p) \cdot \nabla\left(\frac{1}{B^2}\right) = p'(\psi)(\mathbf{B} \times \nabla\psi) \cdot \nabla\left(\frac{1}{B^2}\right). \tag{2.74}$$

For Eq. (2.71) to have a solution, the constraint in Eq. (2.73) must be satisfied. We can integrate the right side of the above equation, and simplifying gives,

$$p'(\psi)\frac{\partial}{\partial\alpha}\oint\frac{\mathrm{d}l}{B} = 0. \tag{2.75}$$

This constraint is satisfied if the pressure gradient, $p'(\psi)$, vanishes on every rational surface.

There are other ways to satisfy the above equation, but those are restrictive and will not be mentioned. Further discussion on this topic can be found in Sec. 10.3.2 in the Introduction to Stellarators textbook. [12] Now we return to solving Eq. (2.71).

Since we have that $\mathbf{B} \cdot \nabla\varphi = \mathcal{J}^{-1}$ and $\mathbf{B} \cdot \nabla\theta = \mathcal{J}^{-1}\iota(\psi)$ Eq. (2.71) can be expanded as,

$$\iota\frac{\partial}{\partial\theta}\left(\frac{J_{\|}}{B}\right) + \frac{\partial}{\partial\varphi}\left(\frac{J_{\|}}{B}\right) = -\mathcal{J}\nabla\cdot\left(\frac{\mathbf{B}\times\nabla p}{B^2}\right). \tag{2.76}$$

To solve this differential equation, we can express each of the terms as Fourier series which are periodic in their angular quantities, (see the next section for a discussion on this method)

$$\frac{J_{\|}}{B} = \sum_{m,n} a_{m,n}(\psi)e^{i(m\theta-n\varphi)} \tag{2.77}$$

$$-\mathcal{J}\nabla\cdot\left(\frac{\mathbf{B}\times\nabla p}{B^2}\right) = \sum_{m,n} b_{m,n}(\psi)e^{i(m\theta-n\varphi)}. \tag{2.78}$$

Inserting these into Eq. (2.76), taking derivatives, and eliminating the exponentials gives the following algebraic equation for the Fourier coefficients,

$$i(\iota(\psi)m - n)a_{m,n} = -b_{m,n}. \tag{2.79}$$

This implies that for all values of (m, n), $b_{m,n} = 0$ when $\iota = n/m$. The general solution to the differential equation is,

$$\frac{J_{\|}}{B} = \sum_{m,n} i\frac{b_{m,n}}{n-\iota(\psi)m}e^{i(m\theta-n\varphi)} + \Delta_{m,n}(\psi)\delta(\iota(\psi)m-n)e^{i(m\theta-n\varphi)}. \tag{2.80}$$

Note, that the solution to the equation $xf(x) = 0$ in the space of generalized functions $f(x)$ is not $f(x) = 0$, but $f(x) = c\delta(x)$, where c is an arbitrary constant. [11] Thus, there are two contributions with singularities to the parallel current, one in the form of a δ-function, and the other in the form of $1/x$. The δ-function term is responsible for the formation of current sheets around rational flux surfaces, and is not problematic computationally. The $1/x$ term, on the other hand, can become an issue. It contributes to the parallel current throughout the plasma and is dependent on the pressure gradient, thus sometimes referred to as the pressure gradient-driven current. [12] If one allows the pressure gradient to become non-zero on a rational surface, the constraint in Eq. (2.75) is no longer satisfied and the parallel current becomes infinite. This is precisely what is done in Equilibrium codes such as VMEC, [16] and DESC [15] which assume nested surfaces and continuous pressure profiles. Thus, it is arguable whether these solutions are strictly mathematically correct. There are several ways to enforce that the pressure gradient vanishes. One non-trivial way is to set the pressure gradient to zero everywhere except at certain irrational surfaces, giving a stepped pressure profile. The SPEC code implements this method, known as MRxMHD. The more general method to resolve this issue is to do away with the assumption of nested surfaces, and allow the formation of magnetic islands.

2.7.2 Magnetic Islands

To begin the discussion on magnetic islands, we note that we can represent the magnetic field in a general form which does not require the assumption of magnetic surfaces as in Sec. 2.4. Let our coordinates be (r, θ, φ), and

$$\mathbf{A} = A_r \nabla r + A_\theta \nabla \theta + A_\varphi \nabla \varphi$$

be the covariant representation of the vector potential. We can then introduce,

$$g(r, \theta, \varphi) = \int_{r_0}^{r} A_r(r', \theta, \varphi) dr'$$

$$\psi = A_\theta - \frac{\partial g}{\partial \theta}$$

$$\chi = -A_\varphi + \frac{\partial g}{\partial \varphi}$$

where r_0 is arbitrary. Making the proper substitutions we can re-express the vector potential as,

$$\mathbf{A} = \psi\nabla\theta - \chi\nabla\varphi + \nabla g \tag{2.81}$$

and the magnetic field is then,

$$\mathbf{B} = \nabla \times \mathbf{A} = \nabla\psi \times \nabla\theta + \nabla\varphi \times \nabla\chi. \tag{2.82}$$

The above equation is "equivalent" to the magnetic field in Eq. (2.39). They are technically not the same equations because the χ in the two equations are not the same. In Eq. (2.39), χ can be written as a function of ψ alone, which then implies the existence of nested magnetic surfaces, since then $\mathbf{B} \cdot \nabla\psi = 0$. Therefore, the representation in Eq. (2.82) is the more general formulation and holds even if magnetic surfaces do not exist. χ being a funtion of ψ alone also implies that the field line equations are a Hamiltonian system,

$$\frac{\mathrm{d}\psi}{\mathrm{d}\varphi} = \frac{\mathbf{B} \cdot \nabla\psi}{\mathbf{B} \cdot \nabla\varphi} = -\frac{\partial\chi}{\partial\theta}$$

$$\frac{\mathrm{d}\theta}{\mathrm{d}\varphi} = \frac{\mathbf{B} \cdot \nabla\theta}{\mathbf{B} \cdot \nabla\varphi} = \frac{\partial\chi}{\partial\psi}.$$

This can be proved by showing that the magnetic field lines satisfy a variational principle. The action of a moving charged particle is,

$$S = \int L_p \mathrm{d}t$$

where the Lagrangian, L is,

$$L_p = \frac{mv^2}{2} + Ze\mathbf{A} \cdot \mathbf{v} - Ze\phi \tag{2.83}$$

where Ze is the charge, m is the mass, v is the velocity, and ϕ is the electrostatic potential. In the limit where $m/Ze \to 0$ and $\phi = 0$, the particle exactly follows the magnetic field, and the action becomes,

$$S = Ze \int \mathbf{A} \cdot \mathrm{d}r = Ze \int (\psi \, \mathrm{d}\theta - \chi \, \mathrm{d}\varphi) \tag{2.84}$$

where Eq. (2.81) has been used to eliminate the vector potential, ignoring the ∇g, as it only contributes a constant to S and does not contribute to its variation δS, assuming the end points of the integral are fixed. Equation (2.84) is of the form,

$$S = \int (p \, \mathrm{d}q - H \, \mathrm{d}t)$$

showing that the field lines are Hamiltonian.

A byproduct of this is that since Hamiltonians are generally chaotic, the magnetic field lines are also chaotic if the "Hamiltonian", $\chi(\psi, \theta, \varphi)$, depends on all three coordinates. Assuming that χ is periodic in (θ, φ), χ can be Fourier decomposed as,

$$\chi(\psi, \theta, \varphi) = \chi_0(\psi) + \sum_{m,n \neq 0} \chi_{mn}(\psi) e^{i(m\theta - n\varphi)}.$$

We can then express the field-line equations as,

$$\frac{\mathrm{d}\theta}{\mathrm{d}\varphi} = \iota(\psi) + \sum_{m,n \neq 0} \chi'_{mn}(\psi) e^{i(m\theta - n\varphi)}$$

$$\frac{\mathrm{d}\psi}{\mathrm{d}\varphi} = -i \sum_{m,n \neq 0} m \chi_{mn}(\psi) e^{i(m\theta - n\varphi)}$$

with $\iota = \mathrm{d}\chi_0 / \mathrm{d}\psi$. If $\chi_0 \gg \chi_{mn}$, implying that the magnetic field consists almost entirely of nested flux surfaces, then the above equations can be integrated to give,

$$\theta = \theta_0 + \iota(\psi_0)\varphi$$

$$\psi = \psi_0 - \sum_{m,n} \frac{m \chi_{mn}(\psi_0)}{m\iota(\psi_0) - n} e^{i[m\theta_0 + (m\iota(\psi_0) - n)\varphi]}.$$

The above definition of ψ has a singularity at rational surfaces and indicates that Fourier components with $n/m = \iota(\psi)$ are dominant. Keeping only the dominant components gives the Hamiltonian,

$$\chi(\psi,\theta,\varphi) = \chi_0(\psi) + \sum_{n/m=\iota(\psi_0)} \chi_{mn}(\psi) e^{i(m\theta - n\varphi)}.$$

Rather than using (ψ,θ) as the canonical coordinates for the Hamiltonian, we can replace θ with $\alpha = \theta - \iota(\psi_0)\varphi$. This then allows for the Hamiltonian to be expressed as,

$$\begin{aligned} H(\psi,\alpha,\varphi) &= \chi(\psi,\theta,\varphi) - \iota(\psi_0)(\psi - \psi_0) \\ &= \chi_0(\psi) + f(\psi,\alpha) - \iota(\psi_0)(\psi - \psi_0) \end{aligned}$$

where, f is the summation term over $n/m = \iota$. This Hamiltonian is approximately equal to, (a non-important constant excluded)

$$H(\psi,\alpha,\varphi) = \frac{\chi_0''(\psi_0)(\psi - \psi_0)^2}{2} + f(\psi_0,\alpha)$$

where the above equation is obtained by expanding $\chi_0(\psi)$ about $\psi = \psi_0$. Since the right hand side is independent of the "time" coordinate, φ, the Hamiltonian is integrable and describes the formation of magnetic islands around resonant magnetic surfaces. The "potential" well, $f(\psi_0,\alpha)$ dictates the shape of the islands. Keeping only a single pair of harmonics makes the shape sinusoidal,

$$H(\psi,\alpha,\varphi) = \frac{\chi_0''(\psi_0)(\psi - \psi_0)^2}{2} + 2\chi_{mn}\cos(m\alpha).$$

The system the above equation describes is equivalent to that of an ordinary nonlinear pendulum. Each value of the Hamiltonian corresponds to a distinct magnetic field line. In particular, the magnetic island separatrix is defined by $H = 2\chi_{mn}$. Substituting this value into the above equation and solving for $\psi - \psi_0$ gives,

$$\psi - \psi_0 = \pm\sqrt{\frac{4\chi_{mn}(1 - \cos(m\alpha))}{\iota'(\psi_0)}}$$

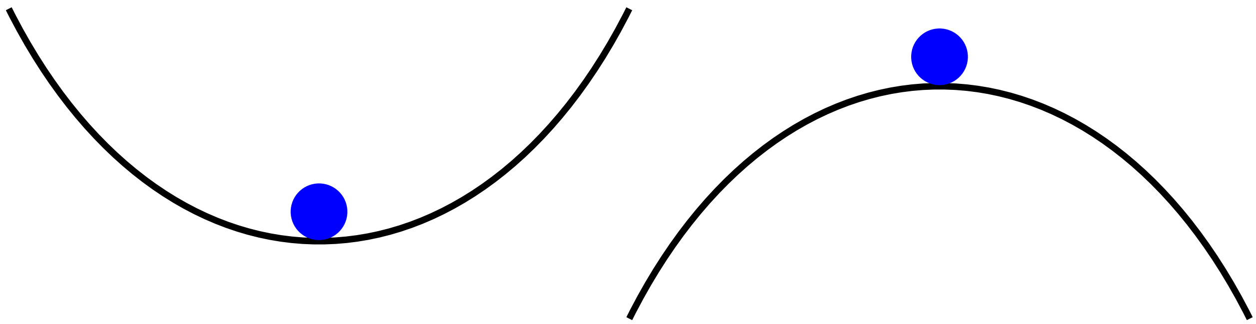

Figure 2.2: Two possible equilibria. The one on the left is stable, while the one on the right is unstable.

on the separatrix. The width of the island, $\Delta\psi = \psi_{\text{max}} - \psi_{\text{min}}$, is then,

$$\Delta\psi = \sqrt{\frac{32\chi mn}{\iota'(\psi_0)}}.$$

If this width is much smaller than the distance to the next island, then neglecting the non-resonant Fourier modes is justified. If that is not the case, then the method fails and coupling of the different Fourier harmonics arises as well tending to make the magnetic field lines chaotic.

2.8 Linear Stability Theory

Once a satisfactory equilibrium is found, it then becomes important to know if it is stable or unstable. By stable or unstable we mean whether the system will return to its initial state after being perturbed. An analogy for this is a ball in a valley or on the top of a hill, as depicted in Fig. 2.2. A stable equilibrium is similar to a ball in a valley, where any displacement or perturbation will result in a force acting in the opposite direction, bringing the ball back to its initial point to then oscillate around the equilibrium. An unstable equilibrium is similar to a ball on the top of a hill, where any displacement will cause the ball to continue in the direction of the displacement and away from the equilibrium.

There are various methods one can use to investigate the stability of a system. The method used later in this thesis is known as the method of normal modes, which will be described below. Before applying the method of normal modes, there are a few steps that must first be taken. First, it is necessary to linearize the equilibrium equations. This is done by expanding each quantity, such as densities, pressure, or magnetic field, into an equilibrium term and a small perturbation term, such as $p = p_0 + \delta p$. Then one substitutes the expanded term into the original equation and expands all terms. Components which only consists of equilibrium quantities will all cancel as they are the ones that must satisfy the equilibrium force balance being studied. Others, which are products of multiple perturbed quantities are assumed to be too small to make a significant contribution to the result, and thus are dropped. Thus, the only remaining terms will be those which are a mixture of equilibrium terms and a single perturbed quantity. This process is known as linearization.

Once the equations have been linearized we can use the method of normal modes to assume the form that the perturbations will take. To justify the form these functional forms will take consider the following PDE,

$$(A\,\partial_{xx} + B\,\partial_{yy} + C\,\partial_{tt} + D\,\partial_x + E\,\partial_y + F)\psi(x, y, t) = 0. \tag{2.85}$$

Where the coefficients can be of the form $A(x, y, t), ..., F(x, y, t)$. If the coefficients are independent of x and t, i.e. $\partial_x A = ... = \partial_t F = 0$, and the system is either infinite or periodic in x, then we can Fourier analyze in the x coordinate as well as Laplace transform in the time coordinate to take derivatives and reduce the complexity of the problem. We can do that by writing,

$$\psi(x, y, t) = K \iint \tilde{\psi}(k, y, \gamma) e^{ikx+\gamma t}\, \mathrm{d}k\, \mathrm{d}\gamma \tag{2.86}$$

which is the inverse Fourier transform in x as well as the inverse Laplace transform in time, where K contains the transform prefactors. Then substituting Eq. (2.86) into Eq. (2.85) and taking derivatives yields,

$$K \int \left(B\partial_{yy} + E\partial_y + \left(\gamma^2 C + F + \mathrm{i}kD - k^2 A\right)\right) \tilde{\psi}(k, y, \gamma)\mathrm{e}^{\mathrm{i}kx}\, \mathrm{d}k = 0. \tag{2.87}$$

And thus

$$\left(B\partial_{yy} + (E + \mathrm{i}kC)\partial_y + \left(F + \mathrm{i}kD - k^2A\right)\right)\tilde{\psi}(k, y, \gamma) = 0 \quad \forall\ k, \gamma. \tag{2.88}$$

Rather than studying all the modes, we can make the simplifying assumption that the function of interest is only a single mode. Then rather than using Eq. (2.86), we make the following definition,

$$\psi(x, y, t) = \tilde{\psi}(y)e^{ikx+\gamma t} \tag{2.89}$$

which is the normal mode method. The above equation is equivalent to having performed the transforms and assumed that the function's only dependence in k and γ are found in the exponential. One can substitute the above equation into Eq. (2.85) and one should recover Eq. (2.88), except it will be only for a single k and γ.

Once the perturbations are assumed to be of the form in Eq. (2.89) taking derivatives in the transformed coordinates becomes trivial. Once that is done one must solve the resulting system of equations, including the boundary conditions which also must be linearized and so forth, for γ which will be known as the growth rate. The stability of the equilibrium will depend on the sign of the real component of γ. If $\gamma > 0$ the system will be unstable as the perturbations will grow exponentially in time. If $\gamma = 0$ the system will be neutrally stable. If $\gamma < 0$ the system will be stable as the perturbations will decay exponentially in time.

To demonstrate the method described above a stability analysis will be performed on the following system,

$$\frac{\partial f}{\partial t} = f - f^2 + \frac{1}{\lambda}\frac{\partial^2 f}{\partial x^2}, \quad f(x = 0, t) = f(x = 1, t) = 0 \tag{2.90}$$

where, $\lambda =$ constant and is positive. Assuming a static equilibrium gives,

$$\frac{1}{\lambda}\frac{\partial^2 f}{\partial x^2} + f - f^2 = 0. \tag{2.91}$$

We take the equilibrium solution to be $f_0(x, t) = 0$. Now we add a perturbation to the equilibrium and substitute, $f = f_0 + \delta f$ in the original equation. This gives,

$$\frac{\partial(f_0 + \delta f)}{\partial t} = f_0 + \delta f - (f_0 + \delta f)^2 + \frac{1}{\lambda}\frac{\partial^2(f_0 + \delta f)}{\partial x^2}. \tag{2.92}$$

Linearizing according to the standard procedure gives,

$$\frac{\partial\, \delta f}{\partial t} = \delta f + \frac{1}{\lambda}\frac{\partial^2\, \delta f}{\partial x^2}. \tag{2.93}$$

Now we assume the perturbations are normal modes and thus have the form,

$$\delta f = Ae^{ikx+\gamma t} \tag{2.94}$$

where γ is the growth rate of the perturbation, k is the wave vector, and A is a constant. Substituting, taking the derivatives and solving for γ gives

$$\gamma = 1 - \frac{k^2}{\lambda}. \tag{2.95}$$

Therefore we have three regions of different stability. When $\lambda > k^2$, $\gamma > 0$, which makes the equilibrium unstable. When $\lambda = k^2$, $\gamma = 0$, which makes the equilibrium neutral. When $\lambda < k^2$, $\gamma < 0$, which makes the equilibrium stable. A similar linear stability analysis is presented in Chapter 4 to investigate a system subject to both the Kelvin–Helmholtz and Rayleigh–Taylor instabilities.

Chapter 3

3D Magnetohydrodynamics Equilibrium

Text and figures in this chapter are reproduced from:

S. R. Hudson, D. Panici, C. Zhu, G. S. Woodbury Saudeau, A. Baillod, M. Cianciosa, A. S. Ware; Verification of the Shafranov shift in free-boundary VMEC, DESC, and SPEC calculations with elliptical geometry. Phys. Plasmas 1 April 2025; 32 (4): 043906. `https://doi.org/10.1063/5.0253843`

G. S. Woodbury Saudeau, M. Cianciosa, D. A. Maurer, A. S. Ware; Modeling and Detecting Magnetic Islands in SIESTA. Phys. Plasmas 1 June 2026; 33 (6): 063902. `https://doi.org/10.1063/5.0330426`

with the permission of AIP Publishing.

3.1 Introduction

Fixed- and free-boundary three-dimensional (3D) magnetohydrodynamic (MHD) equilibrium calculations are required for the reconstruction of existing stellarator experiments. [17–35] With a known external field, the plasma pressure and current profiles are adjusted so that the corresponding equilibrium provides a best-fit to experimental measurements. [36–38] Reconstruction and analyses of observed experimental phenomena is essential for validation of theoretical models of plasma confinement, which in turn is essential for predictive design.

For both validating physical models and numerical codes against existing experiments and for designing future experiments, verification of the free-boundary equilibrium calculation is required. Verification calculations seek to confirm whether or not a given code is correctly solving the equations that it was built to solve, as opposed to validation which shows that the model accurately reproduces experimental behavior. [29, 39–42] The first portion of this chapter is dedicated to the presentation of verification calculations, both qualitative and quantitative, of equilibria calculated by the DESC, [15] SPEC, [43] SIESTA, [44] and VMEC [16] codes for the same system. The second portion will investigate a specific aspect of these kinds of equilibria, namely magnetic islands.

This chapter is organized as follows. In Sec. 3.2, we give brief descriptions of the equilibrium codes used to perform the equilibrium calculations. Section 3.3 discusses the work and results of the free-boundary equilibrium comparison project. Then Sec. 3.4 is dedicated to the investigation into modeling and detecting magnetic islands with SIESTA.

3.2 Plasma MHD Equilibrium Codes

3.2.1 Fixed vs Free-Boundary

Before delving into the details of the individual codes used in this chapter, it is important to discuss the two ways MHD equilibrium codes calculations are performed. These two run modes are known as fixed boundary and free-boundary. Fixed boundary calculations are performed by giving the equilibrium code the shape of the plasma boundary or last closed flux surface, keeping that curve fixed, and then solving the associated equilibrium with said boundary. This method of finding an equilibrium has the benefit of reducing the computational complexity of the problem, which in turn makes it more likely for the solver to find a solution. The downside of this kind of calculation is that it does not represent the most “accurate” solution, as it is not taking into account the impact of the external magnetic fields. Also, it forces a particular solution onto the plasma, which given a specific coil set, may not be correct. The free-boundary method resolves these issues. Typically, when one runs a free-boundary calculation, rather than provide the plasma boundary, one instead gives an initial guess for the boundary, as well as information about the vacuum magnetic fields which surround the plasma, and the vacuum region surrounding the plasma. The plasma is then allowed to move and deform as the solver seeks an equilibrium. Although one is able to achieve a higher physics fidelity with a free-boundary calculation, this increases the complexity of the problem, and thus it becomes that much more difficult for the equilibrium solver to find a solution. In the ensuing calculations VMEC, DESC, and SPEC were run as free-boundary calculations while SIESTA was run as a fixed boundary calculation.

3.2.2 VMEC

The Variational Moments Equilibrium code (VMEC) [16] is a 3D ideal MHD equilibrium solver that has been widely used in the field since the code's inception. The static ideal MHD equations that set the equilibrium are,

$$\mathbf{F} \equiv -\mathbf{J} \times \mathbf{B} + \nabla p = 0 \tag{3.1a}$$

$$\nabla \times \mathbf{B} = \mu_0 \mathbf{J} \tag{3.1b}$$

$$\nabla \cdot \mathbf{B} = 0 \tag{3.1c}$$

where $\mathbf{F}$ is the residual MHD force, which must vanish in equilibrium. The equilibrium computed by the code is required to consist of nested flux surfaces and is obtained by minimizing the energy functional

$$E \equiv \int_V \left(\frac{p}{\gamma - 1} + \frac{B^2}{2\mu_0} \right) \mathrm{d}v + \int_{\bar{V}} \frac{B^2}{2\mu_0} \mathrm{d}v \tag{3.2}$$

where V is the plasma domain and $\bar{V}$ is the vacuum region.

The coordinate system employed by the code is as follows. The radial coordinate is defined as the normalized toroidal flux, $s \equiv \psi/\psi_T$, where ψ_T is the total toroidal flux enclosed by the plasma. In this formulation, $s = 0$ is set to the magnetic axis, and $s = 1$ is the plasma boundary. The other two coordinates used are u, a poloidal angle measured the short way along the torus, and v the cylindrical toroidal angle.

In the described coordinate system, the magnetic field in VMEC is of the form,

$$\mathbf{B}_{\text{VMEC}} = B^u \mathbf{e}_u + B^v \mathbf{e}_v \tag{3.3}$$

where $\mathbf{e}_i$ represents the covariant basis vector. The current density will have the same form. We also have that the pressure is constant on a flux surface, or

$$\nabla P_{\text{VMEC}} \cdot \mathbf{e}^u = \nabla P_{\text{VMEC}} \cdot \mathbf{e}^v = 0 \tag{3.4}$$

where $\mathbf{e}^i$ represents the contravariant basis vector.

In the code angular quantities are decomposed into Fourier harmonics and radial quantities are finite differenced, resulting in them having the following form assuming stellarator symmetry, (which means quantities are up-down symmetric, or symmetric across the radial axis) [45]

$$C = \sum_{m=0}^{M} \sum_{n=-N}^{N} C_{mn}(s)\sin(mu - nN_{\text{fp}}v) \tag{3.5}$$

for quantities with sine parity, and

$$C = \sum_{m=0}^{M} \sum_{n=-N}^{N} C_{mn}(s)\cos(mu - nN_{\text{fp}}v) \tag{3.6}$$

for quantities with cosine parity. Above, C is an arbitrary quantity, m is the poloidal mode number, n is the toroidal mode number, N_{fp} is the number of field periods, and M and N are the number of poloidal and toroidal Fourier modes used in the calculation.

Calculating an equilibrium requires the pressure profile and either the current or rotational transform profile. If VMEC is run in fixed boundary mode, it also requires the last closed flux surface is expressed in Fourier amplitudes. If rather it is run in free-boundary mode, the code requires the vacuum magnetic field, typically provided in the form of an mgrid file. The boundary is then found when the total magnetic pressure combined with the plasma pressure is continuous across the last closed flux surface. In either fixed boundary or free-boundary mode, VMEC finds an equilibrium by minimizing the energy functional through a variational method.

3.2.3 SIESTA

The Scalable Iterative Equilibrium Solver for Toroidal Applications (SIESTA) [44] is a 3D ideal/resistive MHD equilibrium solver which does not assume nested flux surfaces. Removing the nested surface assumption allows the magnetic field and current density to have radial dependence, i.e.

$$\mathbf{B}_{\text{SIESTA}} = B^s\mathbf{e}_s + B^u\mathbf{e}_u + B^v\mathbf{e}_v. \tag{3.7}$$

A byproduct of this is that the pressure is no longer a constant on grid surfaces,

$$\nabla P_{\text{SIESTA}} \cdot \mathbf{e}^u \neq \nabla P_{\text{SIESTA}} \cdot \mathbf{e}^v \neq 0. \tag{3.8}$$

SIESTA begins its calculation from a VMEC equilibrium, using it to set up a computational grid as well as an initial guess for the equilibrium. The u and v coordinates used in SIESTA are the same ones used in VMEC, whereas the s coordinate is rescaled from the VMEC one. In SIESTA the radial coordinate is defined as, $s_{\text{SIESTA}} \equiv \sqrt{s_{\text{VMEC}}}$. This is done to have a more evenly spaced radial grid as well as to guarantee analyticity of the fields near the magnetic axis. [44] Quantities in SIESTA are stored in a similar fashion as VMEC quantities assuming stellarator symmetry, [45]

$$C = \sum_{m=0}^{M} \sum_{n=-N}^{N} C_{mn}(s)\sin(mu + nN_{\text{fp}}v) \tag{3.9}$$

for quantities with sine parity, and

$$C = \sum_{m=0}^{M} \sum_{n=-N}^{N} C_{mn}(s)\cos(mu + nN_{\text{fp}}v) \tag{3.10}$$

for quantities with cosine parity. Above, C is an arbitrary quantity, m is the poloidal mode number, and n is the toroidal mode number as before, N_{fp} is the number of field periods, and summed over the same values previously mentioned as well. To find an equilibrium, SIESTA displaces the fields and pressure in order to lower the MHD energy.

While SIESTA does not assume nested surfaces, magnetic islands are unable to form unless a seed perturbation is applied or resistivity is allowed to diffuse the magnetic field lines. The island seeding is performed by adding a parallel component to the vector potential around a resonant surface. This helical perturbation is then,

$$\delta \mathbf{B} = \nabla \times \left(\frac{A_{||} \mathbf{B}}{|\mathbf{B}|} \right) \tag{3.11}$$

$$A_{||} = a(s) \exp[i(m^* u + n^* N_{\text{fp}} v)] \tag{3.12}$$

where $a(s)$ is the amplitude of the perturbation and m^* and n^* specify the poloidal and toroidal mode numbers of the perturbation. This quantity has a direct impact on the size of the island that will be formed. As such, this leads to uncertainties in the equilibrium calculation, since the actual island size is generally unknown *a priori*. This is implemented in the code as follows.

To open an island, SIESTA must be given two input quantities, the poloidal mode of the resonance, as well as the amplitude of the magnetic perturbation, H_{pert}. It then searches for a compatible resonance which satisfies $m\iota\!\!\!-(s) + nN_{\text{fp}} = 0$. If a resonance is found a test perturbation is applied,

$$P = H_{\text{pert}} \cos(m_{\text{res}} u + n_{\text{res}} N_{\text{fp}} v)$$

which is then scaled by a profile given a width, w,

$$W(s) = \frac{1}{1 + \left(\frac{s - s_{\text{res}}}{w} \right)}.$$

SIESTA then scans the width of the helical perturbation for the lowest energy. Once found the helical perturbation is applied by modifying the electric field update. Using Ohm's law the electric field can be updated as,

$$\mathbf{E} = \mathbf{v} \times \mathbf{B} + \eta \mathbf{J}$$

where the resistivity, η is scaled as,

$$\eta(s) = s^2(1 - s)\eta_0.$$

The field update is set as,

$$\mathbf{E} = \mathbf{v} \times \mathbf{B} + \eta(s)W(s)P\mathcal{J}\mathbf{J} \tag{3.13}$$

where $\mathcal{J}$ is the Jacobian of the coordinate system. The magnetic field is then updated using a discrete form of Faraday's law.

A recent development in SIESTA has added extra versatility to this process. [46] Typically, SIESTA uses toroidal mode numbers that are multiples of the device's number of field periods. If the equilibrium has a resonance with a toroidal mode number not included in this list, a magnetic island would not form when the perturbation is applied. An example would be a five field period device with an $\iota = 1/4$ resonance. Telling the code to apply a perturbation with $m = 4$ would lead to no change because the $n = 1$ mode is not included. A workaround would be to set the number of field periods to 1 in the input, and then increase the number of toroidal modes used to include the ones that were originally desired. Doing this would lead to a multi-fold increase in computational complexity.

Currently, SIESTA can run with user specified toroidal mode numbers, known as "sparse mode". This allows the user to run using the usual toroidal mode numbers that are multiples of the number of field periods, as well as any other desired mode numbers. SIESTA is thus able to study field periodicity breaking islands for a marginal increase in computational cost. This is important for devices such as CTH, a five field period device, which regularly observes $1/2$ and $1/3$ resonant modes. [47]

3.2.4 DESC

The DESC stellarator equilibrium and optimization code [15, 48–50] solves the equilibrium problem in a manner similar to that of VMEC. The coordinate system and magnetic field representation is nearly identical to VMEC's, differing in the chosen radial coordinate, where DESC uses $r \equiv \sqrt{\psi/\psi_T}$, and in the radial discretization. The coordinate mapping in DESC uses a 3D Fourier-Zernike spectral basis, [51] [52]

$$R(r,\theta,\zeta) = \sum_{l,m,n} R_{l,m,n} \mathcal{Z}_l^m(r,\theta) Fo^n(\zeta), \tag{3.14}$$

where $l \in [0, L]$, $m \in [-M, M]$ and $n \in [-N, N]$ (with the radial mode numbers l coupled to the poloidal m such that $l \geq m$, and is dependent on the indexing scheme used, the "ANSI/standard" indexing was used here [53–55]) , and similarly for λ and Z, where $\mathcal{Z}_l^m$ is the Zernike polynomial of radial degree l and poloidal degree m, defined as

$$\mathcal{Z}_m^l(r,\theta) = \begin{cases} \mathcal{R}_l^{|m|}(r)\cos(|m|\theta), & \text{for } m \geq 0, \\ \mathcal{R}_l^{|m|}(r)\sin(|m|\theta), & \text{for } m < 0, \end{cases} \tag{3.15}$$

with the radial function $\mathcal{R}_l^{|m|}$ as the shifted Jacobi polynomial,

$$\mathcal{R}_l^{|m|}(r) = \sum_{s=0}^{(l-|m|)/2} \frac{(-1)^s (l-s)!}{s!\,[(l+|m|)/2 - s]!\,[(l-|m|)/2 + s]!} r^{l-2s} \tag{3.16}$$

and Fo is the typical Fourier series in ζ,

$$Fo^n(\zeta) = \begin{cases} \cos(|n| N_P \zeta), & \text{for } n \geq 0, \\ \sin(|n| N_P \zeta), & \text{for } n < 0. \end{cases} \tag{3.17}$$

To solve for ideal MHD equilibrium force balance, DESC uses a pseudospectral approach, minimizing the equilibrium force balance residuals. By weighting the force components by volume, one can obtain a system of nonlinear algebraic equations for the total MHD force balance error in the plasma volume [15] evaluated at collocations nodes in (r, θ, ζ). This system is then solved in a least-squares sense, with the residual minimized with respect to $R_{l,m,n}$, $Z_{l,m,n}$, and

$\lambda_{l,m,n}$. The poloidal angle, θ, in DESC is free to be varied (through variations of the spectral coefficients) in order to best reduce the force residual, and this has been shown to result in similarly condensed Fourier spectra as VMEC [49].

The free-boundary problem is approached as a minimization problem [48, 56], where the objective to minimize is the errors in the free-boundary equilibrium conditions:

$$
\begin{aligned}
\mathbf{B}_{out} \cdot \mathbf{n} &= 0, && (3.18)\\
\frac{B_{in}^2}{2\mu_0} + p_{in}^2 - \frac{B_{out}^2}{2\mu_0} &= 0, && (3.19)\\
\mathbf{n} \times (\mathbf{B}_{out} - \mathbf{B}_{in}) - \mu_0 \mathbf{K} &= 0, && (3.20)
\end{aligned}
$$

where $\mathbf{B}$ is the total magnetic field (from external coils and from the plasma currents), p_{in} is the plasma pressure at $r = 1$, and $\mathbf{K}$ is a possible sheet current which may exist on the plasma boundary, parameterized as another unknown in addition to the plasma shape as $\mathbf{K} = \mathbf{n} \times \nabla\Phi$ with Φ given as a Fourier series in (θ, ζ). The errors in satisfying these equations (after being multiplied by the appropriate surface Jacobian element, $|\mathbf{e}_\theta \times \mathbf{e}_\zeta|$) are minimized with respect to the plasma boundary shape and the Fourier coefficients describing the surface sheet current, all while under the constraint of MHD force balance in the volume, in order to obtain a free-boundary equilibrium solution. For vacuum equilibria, this sheet current is not a necessary degree of freedom, and for the nonzero β equilibria presented, the sheet current was found to be negligible, so the results shown are without sheet currents as a degree of freedom.

In DESC, the external field may be provided in a number of ways [56]: DESC can take an mgrid file as is used in VMEC, a representation using Dommaschk potentials [57], or DESC can take the coil geometry directly, and compute the field where it is needed using Biot-Savart calculations. The latter “direct-from-coil” calculation was employed for the DESC calculations presented herein.

3.2.5 SPEC

The Stepped Pressure Equilibrium Code (SPEC) [43] is a multi region relaxed MHD (MRxMHD) equilibrium solver which like SIESTA does not assume nested flux surfaces, and as the name implies, uses a stepped pressure profile rather than a continuous one. This unorthodox choice is motivated by the previously discussed singular currents in Sec. 2.7.1 that occur in ideal 3D MHD when assuming nested surfaces. Codes such as VMEC and DESC find solutions which can have these singular currents present, and thus are not entirely physical. [58] SPEC avoids this problem by splitting the plasma into a discrete set of nested regions, the number of which is set as an input parameter depending on the situation. In each of these regions the pressure is constant throughout and there is a pressure discontinuity at the interface between two regions. Across each interface the total pressure, $p + B^2/2\mu_0$, is continuous. Furthermore, the normal magnetic field on each interface is required to be zero. The choice of where to place these interfaces is also important. They cannot be located where the rotational transform is rational, as this will impact any magnetic island that may arise at said rational surface. Instead, they are chosen to lie where the rotational transform is irrational, to avoid this problem.

To find an equilibrium, SPEC seeks to minimize the MRxMHD functional,

$$F \equiv \sum_{i=1}^{N_V} \left[E_i - \frac{\mu_i}{2} \left(\int_{V_i} \mathbf{A}_i \cdot \mathbf{B}_i \, dv - K_i \right) \right] \tag{3.21}$$

where E_i is the plasma energy as given in Eq. 3.2 over the volume V_i, $\mathbf{A}_i$ is the magnetic vector potential, K_i is the prescribed helicity, N_V is the number of volumes, and μ_i is a Lagrange multiplier. Also in the limit where $N_V \to \infty$ MRxMHD recovers the ideal MHD equilibrium. [59] This can be understood in the following way. Each interface functions as a nested flux surface, and in the limit of infinitely many interfaces, the spacing between adjacent volumes tends to zero, thereby recovering the nested flux surface solution. Furthermore, in this limit, the stepped pressure profile becomes continuous, as in an ideal MHD equilibrium.

For free-boundary calculations, a computational boundary, D, is included. This must lie outside the plasma boundary and inside the external currents. In principle, the geometry of D is arbitrary; but, in practice, having a computational boundary with a geometry similar to the plasma boundary provides greater numerical accuracy. In the vacuum region between the plasma boundary and D, the magnetic field satisfies $\nabla \times \mathbf{B} = 0$. To compute the magnetic field in the vacuum region, the normal field on D is required as a boundary condition, but this is not known *apriori*.

3.3 Free-Boundary Equilibrium Comparisons

As is evident by the discussion in the previous section, there are several MHD equilibrium solvers that are used by the community, and they are all different from one another. These differences are quite significant, either assuming nested flux surfaces or allowing for magnetic islands to form, having a stepped pressure profile instead of a continuous one, or the chosen radial discretization. Regardless, the models are all based on the MHD model and if they are each given the same system to solve, the resulting equilibria should be identical, or near identical. As such, verification calculations are needed to prove the codes are solving the equations they claim to be solving.

When it is available, the numerical approximation can be compared against the exact solution. For free-boundary calculations, an exact solution is available for the so-called vacuum case, where the magnetic field is completely provided by the external coils and can be computed using the Biot-Savart law. For the non-zero pressure case, there are approximate analytic equilibria that are available, which are constructed via near-axis expansions [60–74]; but, for equilibria with arbitrary geometry and profiles, exact 3D equilibrium solutions are typically not available. In this case, we can compare one numerical approximation against one another.

The geometry of the flux surfaces determines the local stability and transport properties of the plasma. One particularly important effect induced by pressure is the global geometrical shift of the magnetic axis known as the Shafranov shift. [18, 75–80]. In this section, verification calculations as computed by the VMEC, DESC and SPEC free-boundary MHD equilibrium codes,

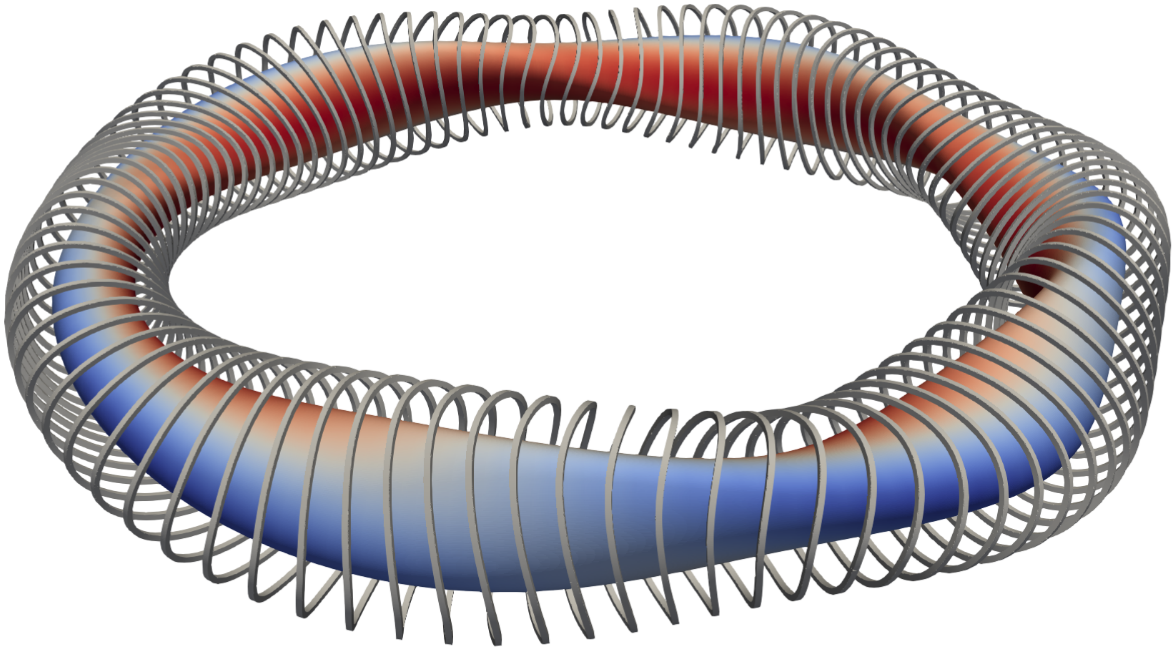

Figure 3.1: The target boundary, a 5 field-period rotating ellipse described by Eq. 3.22, and the coils represented by the gray loops.

and fixed-boundary SIESTA, as well as other more qualitative comparisons of the equilibria are presented. Even though SPEC is based on a different theoretical model, the codes have similar capabilities, and they should agree in certain limits. Biot-Savart calculations are performed using the FOCUS [81] code.

3.3.1 Rotating Ellipse Stellarator

For expedience, a rather simple configuration was chosen, for which the target boundary is a “rotating ellipse” defined by,

$$\begin{aligned} R &= R_0 + a\ \cos(\theta) + b\ \cos(\theta - N_P\,\phi), \\ Z &= -a\ \sin(\theta) + b\ \sin(\theta - N_P\,\phi). \end{aligned} \tag{3.22}$$

The major radius was set to be $R_0 = 10m$, the minor radius to be $a = 1m$, and $b = 0.25m$. The field periodicity is $N_P = 5$. The target surface and coil set are shown in Fig. 3.1.

Vacuum Quantity	VMEC	SPEC	SIESTA	DESC
Vol (m^3)	46.1555	46.1716	46.1555	46.1554
$\langle B \rangle$ (T)	1.9973	1.9960	1.9971	1.9967

Table 3.1: The macroscopic quantities from the different equilibria calculated by each code. All except the SIESTA result are from free-boundary calculations. Here $\langle B \rangle$ refers to the volume average magnetic field.

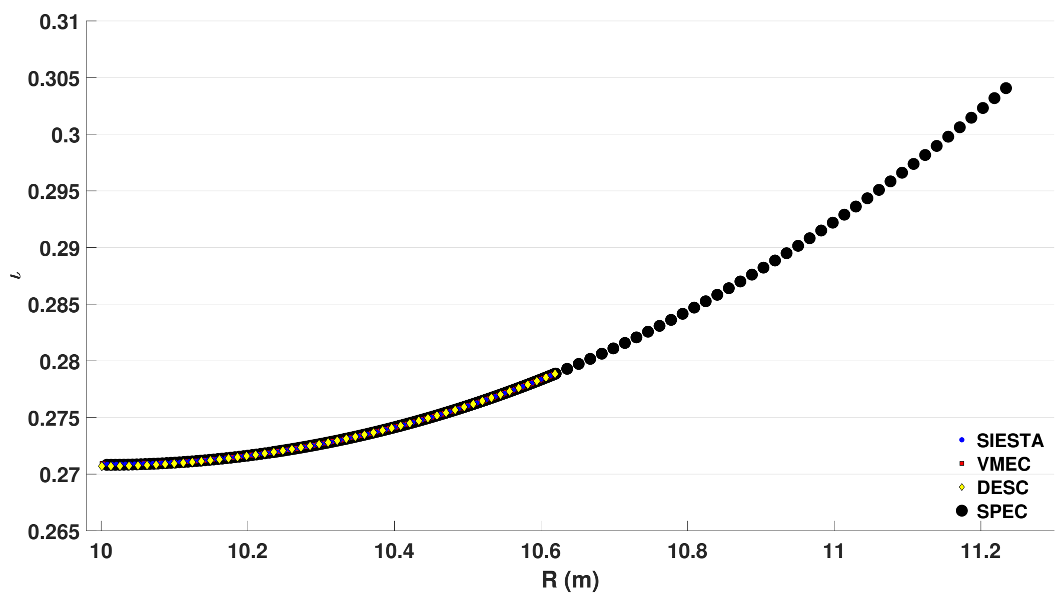

Figure 3.2: Rotational transform calculated from equilibria found by all four codes. The dotted line beyond approximately $R > 10.6$ corresponds to the vacuum region in the SPEC calculation.

3.3.2 Vacuum Equilibrium Comparison

We begin the equilibrium discussion with a qualitative comparison of the outputs from the different codes. This is meant to ensure that the equilibrium calculated by each code is the identical, or as close as possible to one another. This can be a difficult task as each code requires different inputs, and these inputs are not all in the same dimensions or units. This is not a problem with DESC, as it can use the same input as VMEC, and since SIESTA uses a VMEC output as part of its inputs, it should solve the same equilibrium. On the other hand, the SPEC inputs are vastly different, and conversions between the different input parameters of SPEC and VMEC were needed for this analysis. The transformation was recently implemented by Dr. Stuart Hudson as part of the work performed in [82]. The first equilibria we analyze is the vacuum case. For this comparison VMEC and SIESTA were run with 120 radial surfaces, and the Fourier harmonics, (m, n) were set to 12. For DESC the radial, poloidal and toroidal Fourier resolutions were set to 12. For SPEC the poloidal and toroidal Fourier harmonics were set to 12, and the plasma was split into 7 volumes. Table 3.1 shows that the plasma volume and volume averaged magnetic field are approximately the same across all cases. We can then look at the rotational transform to check if there is any variation. Figure 3.2 shows that in vacuum there is no discernible difference between the rotational transform profiles of the equilibria. Comparing the resulting flux surfaces for each equilibrium also shows good agreement between the codes.

The first case we consider is the comparison between DESC and VMEC. Since both codes assume nested surfaces and can take in the same inputs, the flux surfaces should be identical or near identical. Figure 3.3 shows that the flux surfaces are quite similar. Then, we examine the comparison between SPEC and VMEC presented in Fig. 3.4. We observe again good agreement in the shapes of the magnetic surfaces as well as the plasma boundary. Lastly, we have Fig. 3.5 which shows the SPEC and SIESTA surfaces. Once again we note good matching in the surfaces and boundary. Thus, our qualitative analysis concludes that the vacuum equilibria calculated by the codes are effectively the same.

It is desirable to also make comparisons between the codes that are more quantitative in nature. One particularly important effect induced by pressure is the global geometrical shift known as the Shafranov shift. [83, 84] In short, the Shafranov shift is an outward displacement of the magnetic axis due to the pressure and magnetic field. Certain codes, such as VMEC, calculate the location of the axis as part of its regular execution, while others, such as SPEC and SIESTA require it to be found afterwards. Since the magnetic axis is an order one fixed point, meaning it closes on itself after one toroidal rotation, one can locate the field line which satisfies this criteria using a 2D Newton's method. This process will be also needed for locating magnetic islands, another class of fixed points, in Sec. 3.4, and as such we will give a description of the method.

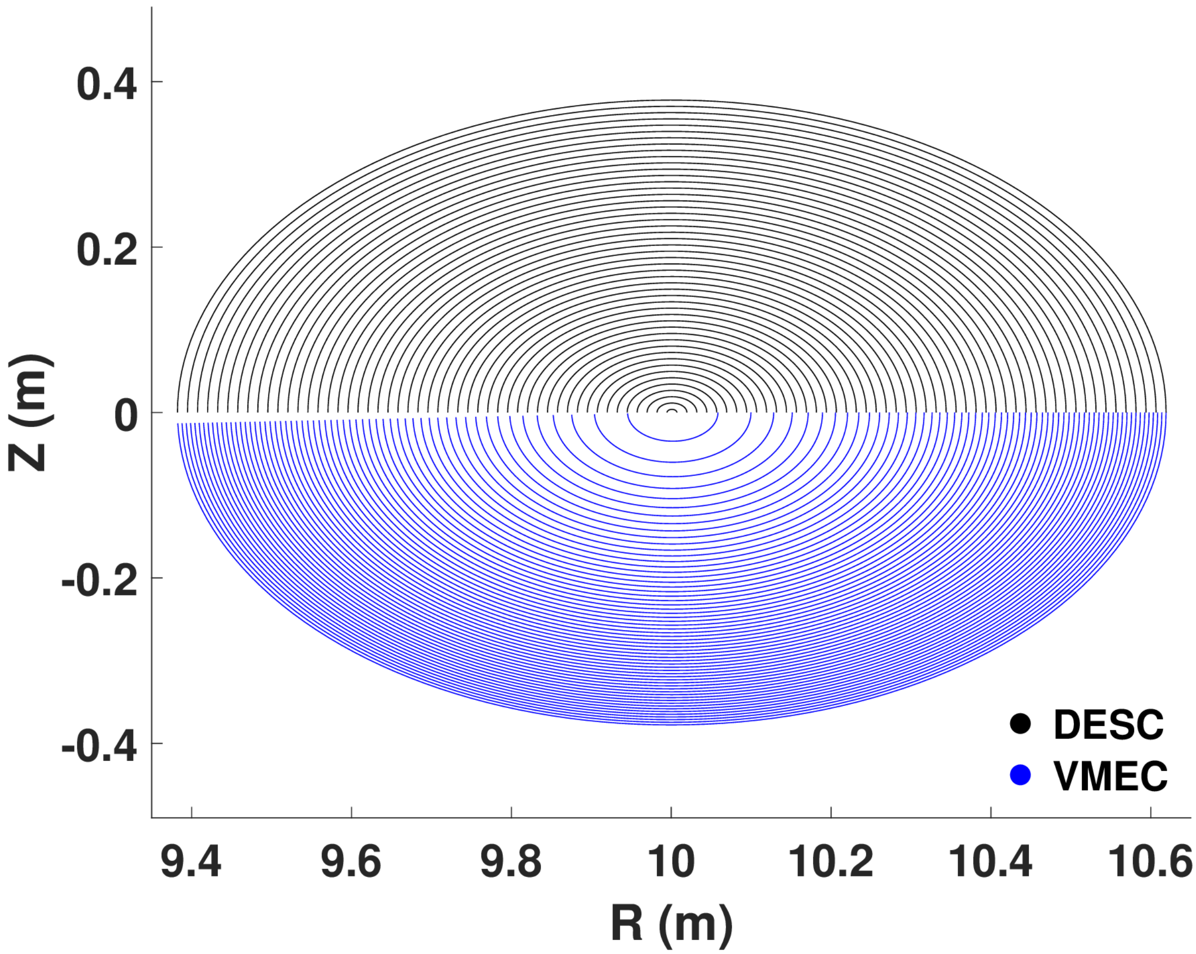

Figure 3.3: Comparison of flux surfaces from equilibria calculated with DESC and VMEC. The DESC flux surfaces are the black curves on the top and the VMEC surfaces are the blue curves on the bottom. Due to VMEC's formulation, there is a lower surface density near the axis as opposed to the edge, as opposed to DESC where the surfaces are evenly distributed.

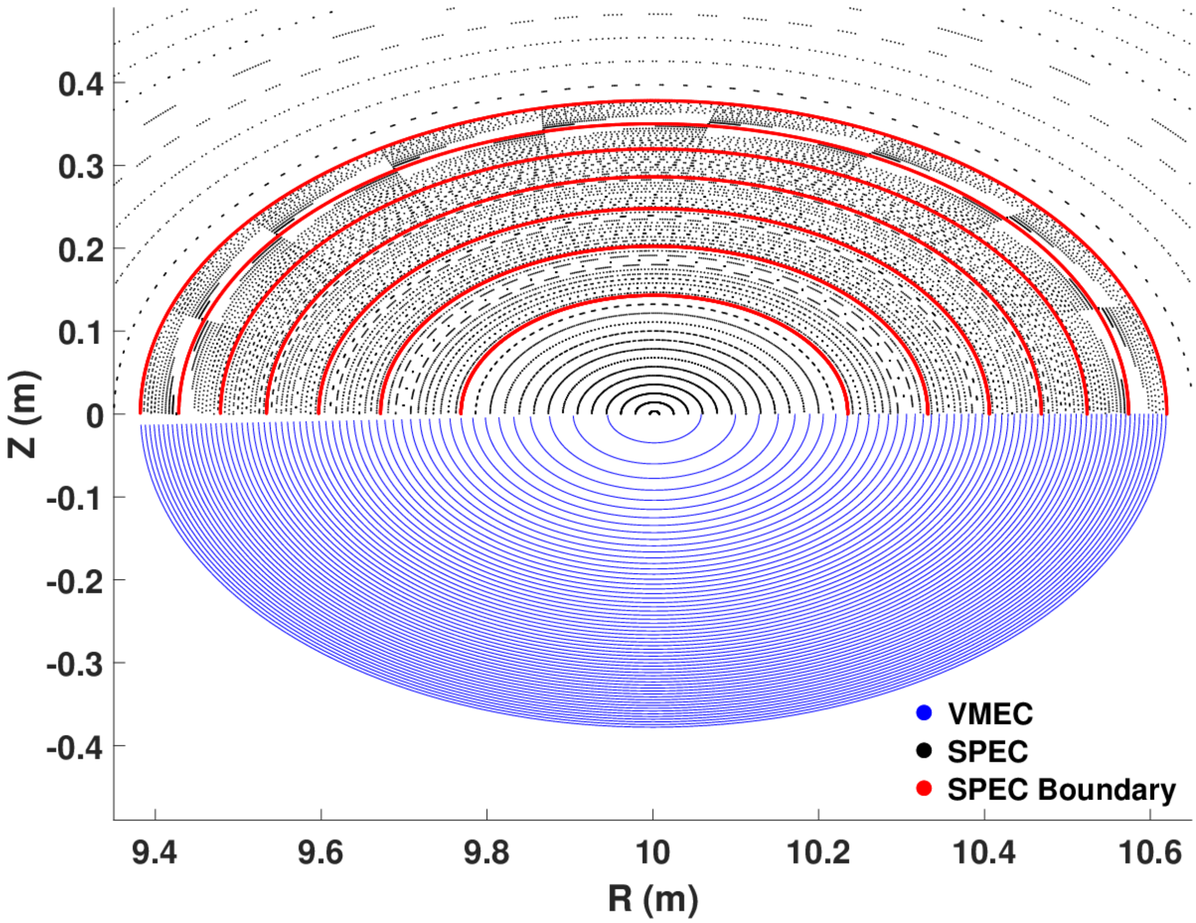

Figure 3.4: Comparison of flux surfaces from the equilibria calculated with SPEC and VMEC. The red curves represent the ideal interfaces which separate the plasma into seven volumes. The black lines within are the plasma flux surfaces, while the black lines outside represent the vacuum flux surfaces. The blue curves are the VMEC flux surfaces. The visual artifact occurring around the second to last ideal interface is a result of the rotational transform crossing some rational surface.

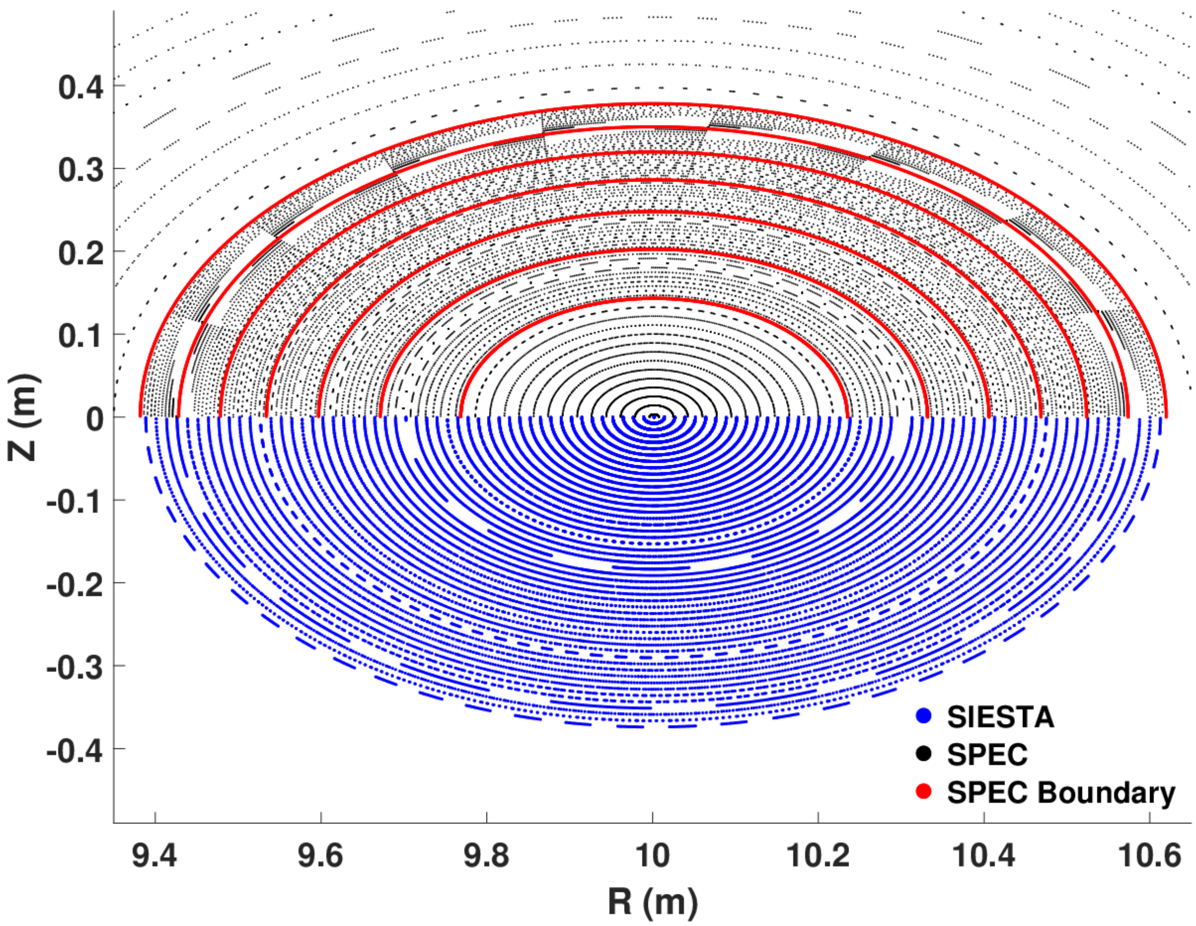

Figure 3.5: Comparison of flux surfaces from equilibria calculated with SIESTA and SPEC. The red curves represent the ideal interfaces which separate the plasma volumes. The black lines within are the plasma flux surfaces, while the black lines outside represent the vacuum flux surfaces. The blue curves are the SIESTA flux surfaces. The visual artifact occurring around the second to last ideal interface is a result of the rotational transform crossing some rational surface. The SIESTA curves that are dashed rather than continuous also correspond to flux surfaces with a rational rotational transform value.

3.3.3 Locating Fixed Points

As previously seen in Sec. 2.35, the magnetic field line of an arbitrary magnetic field, $\mathbf{B}(r, \theta, \varphi)$, can be parameterized as,

$$\dot{r} = \frac{\mathrm{d}r}{\mathrm{d}\varphi} = \frac{B^r}{B^\varphi} \tag{3.23}$$

$$\dot{\theta} = \frac{\mathrm{d}\theta}{\mathrm{d}\varphi} = \frac{B^\theta}{B^\varphi} \tag{3.24}$$

where r is a radial coordinate, θ is a poloidal angle, and φ is a toroidal angle. One can "follow" the field line by treating the above set of ordinary differential equations (ODE) as an initial value problem, treating the toroidal angle as the "time" variable, and typically traversing some multiple of 2π in φ. Since the fixed point we are currently interested in is the magnetic axis we need only follow the field line for one toroidal revolution. The initial value is the starting point in space you wish to begin following the field line from.

A fixed point of a function is one which satisfies the relation $f(\mathbf{x}) = \mathbf{x}$. In this case the function f is the set of ODEs in Eqs. (3.23)-(3.24). Rather than solve this as a traditional fixed point problem, we can instead reformulate it into a root finding problem, $g(\mathbf{x}) = f(\mathbf{x}) - \mathbf{x} = 0$. This is beneficial because Newton's method is especially good at solving these kinds of problems. The method is iterative and usually works as follows;

1. Supply an initial guess for $\mathbf{x}_i$.
2. Calculate $g(\mathbf{x}_i)$ and $g'(\mathbf{x}_i)$.
3. Set the next guess to $\mathbf{x}_{i+1} = \mathbf{x}_i - \dfrac{g(\mathbf{x}_i)}{g'(\mathbf{x}_i)}$.
4. Repeat above steps until the change in $\mathbf{x}$ is below a certain threshold.

A difficulty arises because in this particular case $g(\mathbf{x}_i)$ is a 2×1 matrix and $g'(\mathbf{x})$ is a 2×2 matrix. As such the correct way to express the division term would be $g'(\mathbf{x}_i)^{-1}g(\mathbf{x}_i)$. Furthermore, we have that, $g'(\mathbf{x}) = f'(\mathbf{x}) - \mathbb{I}$, and $f'(\mathbf{x})$ is the Jacobian matrix of $f(\mathbf{x})$, which will be set to $f'(\mathbf{x}) = \mathbf{S}(\mathbf{x})$ for future consistency, Sec. 3.4.3. To find $\mathbf{S}$, we must solve the following system,

$$\frac{\mathrm{d}}{\mathrm{d}\varphi}\mathbf{S} = \mathbf{C} \cdot \mathbf{S}, \quad \mathbf{S}(0) = \mathbb{I} \tag{3.25}$$

where the matrix $\mathbf{C}$ is defined as,

$$\mathbf{C} = \begin{pmatrix} \frac{\partial \dot{r}}{\partial r} & \frac{\partial \dot{r}}{\partial \theta} \\ \frac{\partial \dot{\theta}}{\partial r} & \frac{\partial \dot{\theta}}{\partial \theta} \end{pmatrix} \tag{3.26}$$

for added clarity the components of $\mathbf{C}$ are,

$$\mathbf{C}_{1,1} = \frac{\partial \dot{r}}{\partial r} = \frac{B^{\varphi}(\partial_r B^r) - B^r(\partial_r B^{\varphi})}{(B^{\varphi})^2}$$

$$\mathbf{C}_{1,2} = \frac{\partial \dot{r}}{\partial \theta} = \frac{B^{\varphi}(\partial_\theta B^r) - B^r(\partial_\theta B^{\varphi})}{(B^{\varphi})^2}$$

$$\mathbf{C}_{2,1} = \frac{\partial \dot{\theta}}{\partial r} = \frac{B^{\varphi}(\partial_r B^\theta) - B^\theta(\partial_r B^{\varphi})}{(B^{\varphi})^2}$$

$$\mathbf{C}_{2,2} = \frac{\partial \dot{\theta}}{\partial \theta} = \frac{B^{\varphi}(\partial_\theta B^\theta) - B^\theta(\partial_\theta B^{\varphi})}{(B^{\varphi})^2}$$

where $\partial_i = \partial/\partial i$. Thus, to be able to calculate the update quantity, Eq. 3.25 must also be solved numerically alongside the field line equations. The full Newton's method is then,

1. Supply an initial guess for $\mathbf{x}_i$.

2. Calculate $g(\mathbf{x}_i)$ and $\mathbf{S}(\mathbf{x}_i)$.

3. Solve the system $(\mathbf{S}(\mathbf{x}_i) - \mathbb{I})(\mathbf{x}_{i+1} - \mathbf{x}_i) = -g(\mathbf{x}_i)$ for $(\mathbf{x}_{i+1} - \mathbf{x}_i)$ to find $(\mathbf{S}(\mathbf{x}_i) - \mathbb{I})^{-1}g(\mathbf{x}_i)$. (This approach offers a computational advantage over the direct calculation of $(\mathbf{S}(\mathbf{x}_i) - \mathbb{I})^{-1}$.)

4. Set the next guess to $\mathbf{x}_{i+1} = \mathbf{x}_i - (\mathbf{S}(\mathbf{x}_i) - \mathbb{I})^{-1}g(\mathbf{x}_i)$.

Code	Axis R (m)	Axis Z (m)
VMEC	10.002	0
SPEC	10.002	0
SIESTA	10.000	0

Table 3.2: The location in real space of the magnetic axis at the $\varphi = 0$ toroidal cross section for the different codes.

Finite Pressure Quantity	VMEC	SPEC	SIESTA
Vol (m^3)	47.8482	47.8627	47.8482
$\langle B \rangle$ (T)	1.9600	1.9600	1.9600
$\langle \beta \rangle$	2.634×10^{-3}	2.675×10^{-3}	2.634×10^{-3}

Table 3.3: The macroscopic quantities from the different equilibria calculated by each code. All except the SIESTA result are from free-boundary calculations. Here $\langle B \rangle$ and $\langle \beta \rangle$ refer to the volume averaged magnetic field and volume averaged plasma beta respectively. The plasma beta is the ratio of the plasma pressure to the magnetic pressure.

5. Repeat above steps until the change in **x** is below a certain threshold.

Presented in Table 3.2 are real space location of the magnetic axis for each code's calculated equilibrium. It is important to mention that the axis locations are not "exactly" the same for the codes, as they begin to differ at decimal places not shown in the case of SPEC vs VMEC. Realistically these differences are so small that they would not be detectable/measurable experimentally. Nonetheless, the agreement between the codes is further indication that the solvers are calculating the "same" equilibrium.

3.3.4 Finite Pressure Equilibrium Comparison

We now move on to the more interesting and complicated case, equilibria with finite pressure. We describe it as such because by including finite pressure into the system, the required calculations become more complex and take into account a greater amount of physical effects. As a result, such calculations, especially when performed in free-boundary mode, present significant challenges for equilibrium solvers, and convergence to a fully resolved equilibrium cannot be

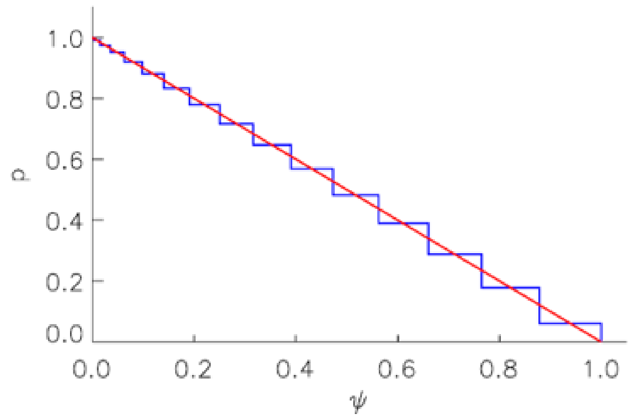

Figure 3.6: Normalized pressure profile plot. The x-axis is the normalized toroidal flux and the y-axis is the normalized pressure. The red curve is the VMEC pressure profile, while the blue curve is the SPEC pressure profile.

guaranteed. For this case we studied the same rotating ellipse configuration as before, except now a linear pressure profile was used, for simplicity, in VMEC and SIESTA and SPEC was solved with 16 volumes. See Fig. 3.6 which shows what these look like. All codes use the same Fourier resolution as before as well.

We begin the qualitative comparison of the different calculated equilibria with the resulting rotational transform profiles as seen in Fig. 3.7. Immediately we see the effect of SPEC's stepped pressure profile, as it has led to the equilibrium having a discontinuous iota profile. Since there is a pressure jump between each interface, to keep the total pressure across interfaces continuous, the magnetic field must adjust itself, changing the rotational transform, which then leads to the results shown. Therefore, the shown behavior is to be expected. It becomes clear when we compare the flux surfaces from the SPEC equilibrium to those found with SIESTA and VMEC, that this different iota profile does not produce surfaces which are qualitatively distinct.

When we compare the SPEC and VMEC surfaces in Fig. 3.8, they show very good agreement, with the surfaces looking almost identical. They seem to have settled on the same plasma boundary for this equilibrium, as well as a similar Shafranov shift. A similar result is shown in Fig. 3.9. There the SIESTA and SPEC surfaces also match well, with the axis location seeming to be located in approximately the same place, and the boundaries of the two agreeing as well. Thus, we see that given approximately the same system with finite pressure the three codes find

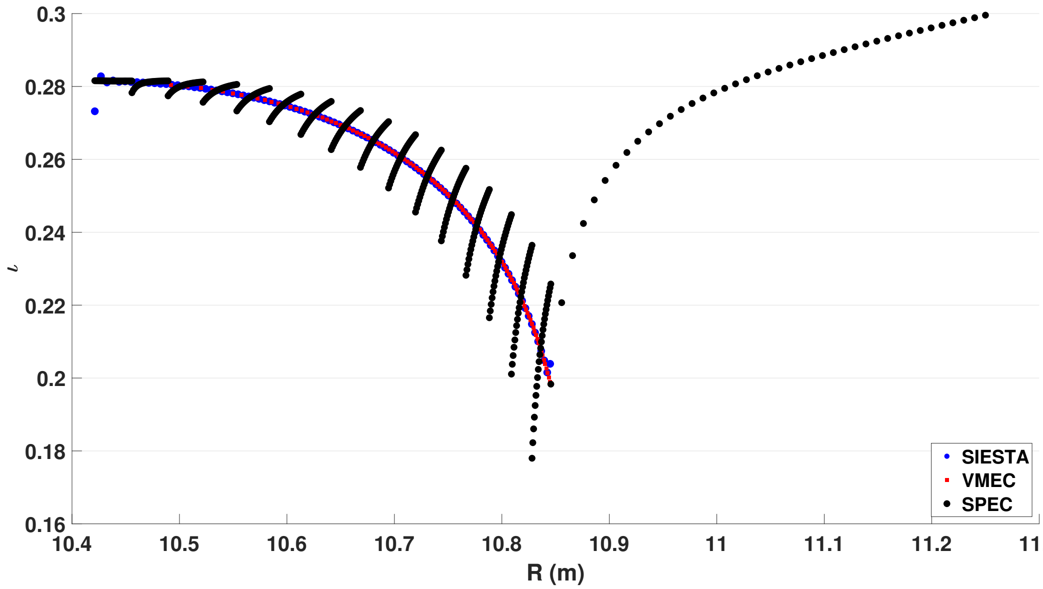

Figure 3.7: Rotational transform calculated from equilibria found by the three codes. The dotted line beyond approximately $R > 10.85$ corresponds to the vacuum region in the SPEC calculation. The SPEC rotational transform is discontinuous because of the pressure jumps between each interface. Since the total pressure is continuous across each interface, the magnetic field must adjust itself, changing the rotational transform.

equilibria that look quite similar to each other, even if the rotational transform profiles do not match.

We are now interested again in the quantitative comparisons between the calculated equilibria, and for this we again calculate the location of the magnetic axis in the three codes. From Table 3.4, we see that all three agree on their axis location to two decimal places, now with some variation at the third decimal place. Again, these differences would not be measurable experimentally, and as such are effectively the same. This further indicates that while SPEC uses

Code	Axis R (m)	Axis Z (m)
VMEC	10.421	0
SPEC	10.420	0
SIESTA	10.418	0

Table 3.4: The location in real space of the magnetic axis at the $\varphi = 0$ toroidal cross section for the different codes.

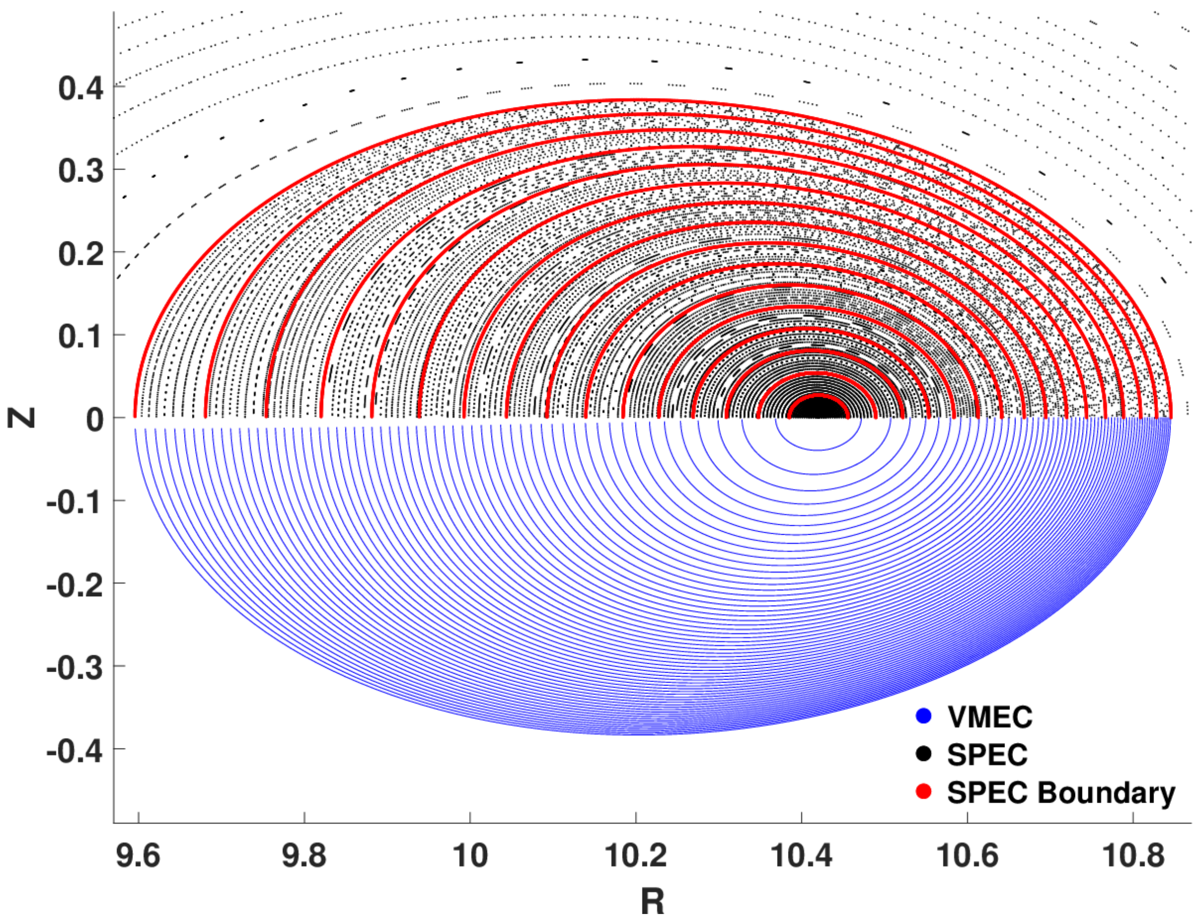

Figure 3.8: Comparison of flux surfaces from equilibria calculated with SPEC and VMEC. The red curves represent the ideal interfaces which separate the plasma into 16 volumes. The black lines within are the plasma flux surfaces, while the dashed lines outside represent the vacuum flux surfaces. The blue curves are the VMEC flux surfaces.

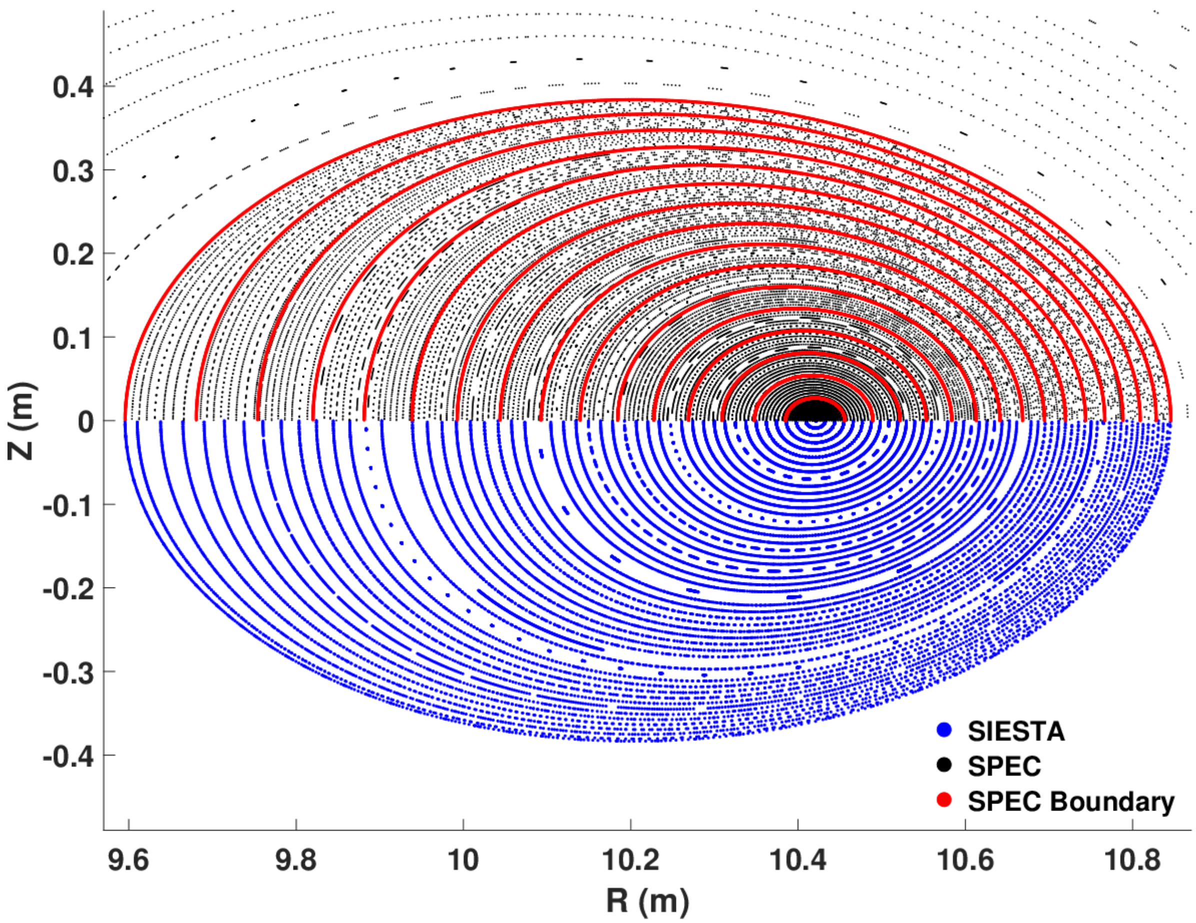

Figure 3.9: Comparison of flux surfaces from equilibria calculated with SIESTA and SPEC. The red curves represent the ideal interfaces which separate the plasma volumes. The black lines within are the plasma flux surfaces, while the black lines outside represent the vacuum flux surfaces. The blue curves are the SIESTA flux surfaces. The lines that are dashed rather than continuous also correspond to flux surfaces with a rational rotational transform value.

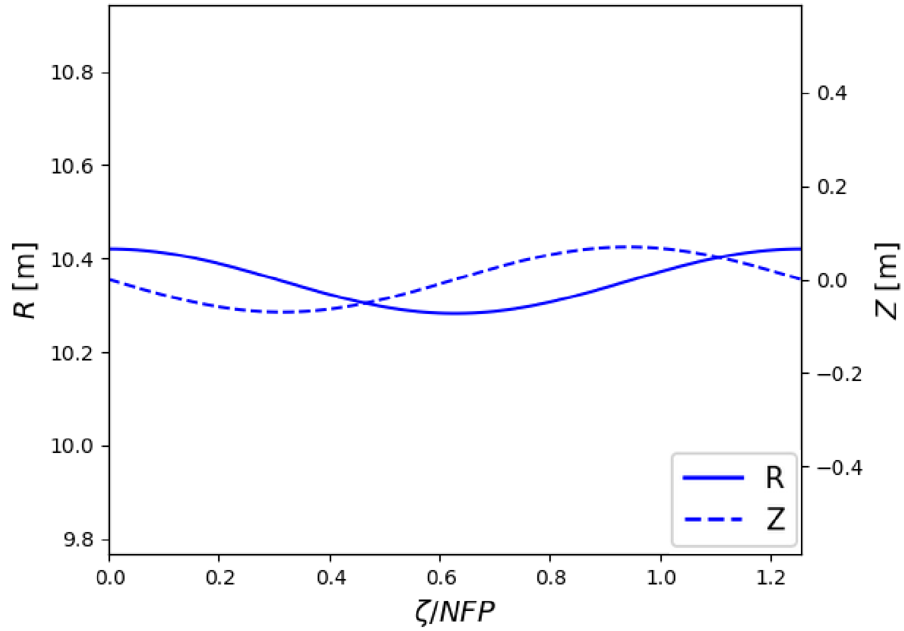

Figure 3.10: R and Z coordinates of magnetic axis from VMEC free-boundary finite pressure equilibrium as functions of the toroidal angle per field period. This is a five field period device, resulting in the toroidal angle ranging from $[0, 2\pi/5]$.

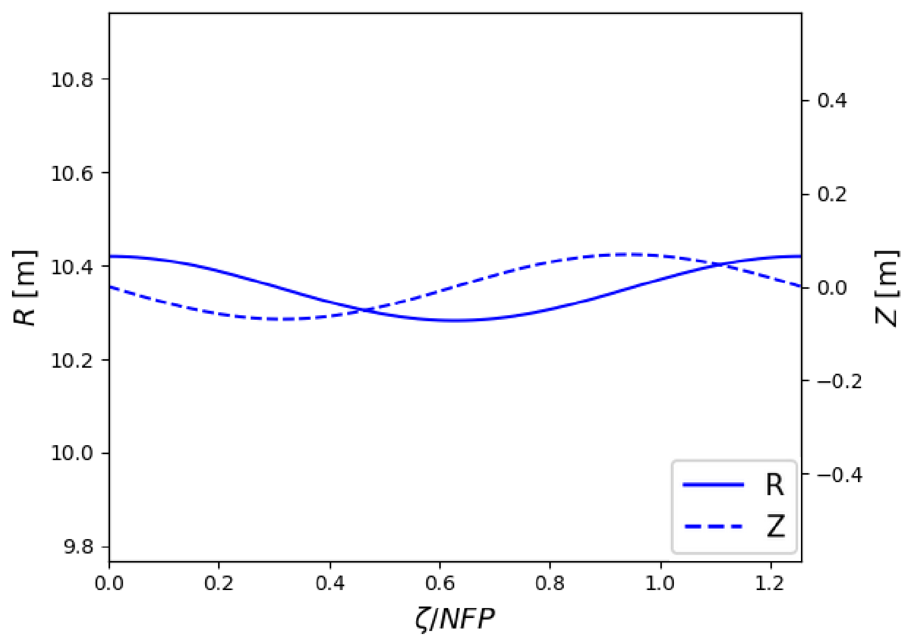

Figure 3.11: R and Z coordinates of magnetic axis from SPEC free-boundary finite pressure equilibrium as functions of the toroidal angle per field period. This is field period device, resulting in the toroidal angle ranging from $[0, 2\pi/5]$.

a different formulation of MHD, using many volumes, it is able to find a similar equilibrium as codes which use ideal MHD. We can also compare the location of the axis across the entire device rather than only one toroidal slice. Looking at Figs. 3.10-3.11 we see that for the present case the SPEC and VMEC magnetic axes match throughout the device as well. For a more thorough investigation on the error of the axis location between SPEC and both VMEC and DESC, see Ref. [82].

3.3.5 Conclusion

In this study we performed an investigation of free-boundary equilibria of the same system calculated with several codes. We show that for both the vacuum and finite pressure cases the resulting equilibria found all agree when subjected to a qualitative comparison. The flux surfaces in both cases and the rotational transform in the vacuum case were indistinguishable between the various cases. We also carried out quantitative comparisons based on the location of the magnetic axis. For both the vacuum and finite pressure systems the agreement on the axis location was very good, and any error found would not be measurable experimentally regardless.

3.4 Detecting and Measuring Magnetic Islands in SIESTA

3.4.1 Introduction

One of the current problems in 3D MHD equilibria is the presence of magnetic islands in the plasma. Ideally, toroidal plasmas will have nested flux surfaces as this would generally lead to the best confinement properties. Unfortunately, since 3D magnetic fields found in devices such as stellarators [85] are no longer axisymmetric, nested flux surfaces are no longer guaranteed. [11] Depending on the rotational transform profile of the device, islands can form in the plasma and bring with them undesirable results such as particle and heat transport from the core to the edge, among other things.

As such, the study of how to eliminate the occurrence of magnetic islands, or to minimize their size has been a long-term active research subject. [86–91] One avenue that has been explored to reduce the presence of magnetic islands is to have transform profiles that are flat and do not cross low order rationals. [92] The downside of this approach is that the confinement benefits of magnetic shear will not be available to this configuration. [92, 93] Another method, which this work builds towards, is to set up an optimization loop where one defines a parameter which quantifies the size of magnetic islands present in the equilibrium, and then proceeds to modify the configuration in an attempt to reduce or remove entirely the island. This latter method employs Greene's residue which gives a local measure of the stochasticity of a Hamiltonian system around a fixed point. [94, 95] Using the residue to reduce islands has been looked at previously with particular emphasis on the work by Cary and Hanson, [86, 87] which was the first to implement this approach for stellarator geometries, and most recently with the works by Baillod et al. [90] and Smiet et al. [91] who implemented this in SIMSOPT [96] with the Stepped Pressure Equilibrium Code (SPEC).[43]

If an actual measurement of the island size is desired, say to compare a computational model to experiment, the residue alone is not sufficient. Over the years several methods for calculating the width of magnetic islands have been developed. [97–99] The simplest, yet most time-consuming, method is to generate a Poincaré plot of the magnetic surfaces. From the graph one is able to visually measure the width of the island. An issue with this method arises with generating a puncture plot of sufficient resolution, given that following large numbers of field lines for hundreds of revolutions around the torus is a lengthy process, even when the computation is performed in parallel. Therefore, a more computationally efficient and robust method is required if these kinds of calculations need to be performed on a regular basis. The method derived by Cary and Hanson [98] has none of the above issues. It makes use of the previously mentioned residue as well as the shear of the unperturbed magnetic field at the island O-point to calculate the island width.

We use the Scalable Iterative Equilibrium Solver for Toroidal Applications (SIESTA) [44] to calculate the plasma equilibrium with magnetic islands. SIESTA is a 3D MHD equilibrium code that does not assume nested flux surfaces and can switch between using ideal and resistive

MHD in its calculation. As part of its inputs it takes an equilibrium calculated by the Variational Moments Equilibrium Code (VMEC)[16] to set up both the computational grid and the initial guess for the solver. Applying a helical magnetic perturbation coupled with the implemented resistivity, the code is able to resolve magnetic islands.

Several considerations motivate the use of SIESTA for this study, despite similar investigations having previously been conducted using SPEC. The first is that SIESTA is capable of converging to a solution for strongly shaped configurations. Another is related to recent developments in the SIESTA code that give it a functionality that other codes do not have. It is now able to work with toroidal mode numbers that do not match the field periodicity of the device without significantly increasing the problem size. This allows for the study of islands with toroidal mode number not matching the field periodicity of the device at a marginal increase in computational cost. [46] The inclusion of these asymmetric Fourier modes has been observed to have significant impact on SIESTA equilibria with islands. [100] Centurión and Martinell showed that by including the asymmetric low order Fourier modes the resulting magnetic islands were significantly larger than the case where only field periodic Fourier modes were included. Observing these islands in SPEC with similar low order Fourier modes would require a significant increase in computational complexity and would lead to an increased likelihood of non-convergence. The last reason we will mention is the integration of SIESTA into V3FIT, [101, 102] which allows for the reconstruction of experimental equilibria with islands. When reconstructing those equilibria both the size and phase of the island are unknowns and reconstructions will be required to determine them.

It is known that inaccuracies form in numerical MHD calculations when $\nabla \cdot \mathbf{B} \neq 0$. [103, 104] This likewise holds true with field line following and fixed point identification, as issues arose with initial calculations performed. Development of methods to guarantee divergence-free interpolation can be found in various publications over the years. [105–111] A standard method is to calculate the vector potential from the magnetic field data, interpolate it, then take the curl to find the magnetic field. One can use the equation $\nabla \cdot \mathbf{B} = 0$ to find two of the components of the magnetic field and use them to fix the third component. Also used are methods where the components are set to polynomial equations, and a system of equations is solved to assign the coefficients of each polynomial. In cases where quantities are represented as Fourier series, is it only necessary to interpolate in the radial coordinate as angular quantities are calculated analytically. To ensure that the magnetic field was kept divergence-free in our analysis, we developed an interpolation method which maintains the divergence-free quality of the magnetic field using a mixture of the above-mentioned techniques.

For this project, we apply a 2D Newton method to locate fixed points of the magnetic field line map in SIESTA equilibria with magnetic islands. These fixed points correspond to O-points and X-points. We then make use of the residue of the fixed points to characterize the island's size. We perform this analysis on two different V3FIT shot reconstructions of CTH [112] plasmas known to have islands present. A scan was performed in the perturbation magnitude given as an input to SIESTA to study its effect on the resulting equilibrium. We confirm expected behaviors of increased island size with increased perturbation size, as well as observe unexpected behavior of island width saturation and island displacement.

This section is organized as follows. The device used for the equilibrium calculations is reviewed in Sec. 3.4.2. Sections 3.4.3 and 3.4.4 summarize some of the key mathematics used in the analysis. Then Sections 3.4.5 and 3.4.6 go into the results of the analysis and expand on the findings. Lastly, the conclusions are presented in Section 3.4.7.

3.4.2 Compact Toroidal Hybrid

CTH is a torsatron-tokamak hybrid located in Auburn University's physics department. It is a five-field period device with a 0.75 m major radius, and a 0.29 m minor radius. [112] It has a central solenoid from which one can drive current in the plasma. An added benefit of this is that by varying the amount of current driven in the plasma, it is possible to vary the rotational transform profile to study different configurations. CTH flux surfaces from the equilibrium calculated using VMEC for the two shots studied can be seen in Figs. 3.12-3.13, and the corresponding rotational transform profiles can be found in Fig. 3.14. The Poincaré plots for some of the SIESTA equilibria

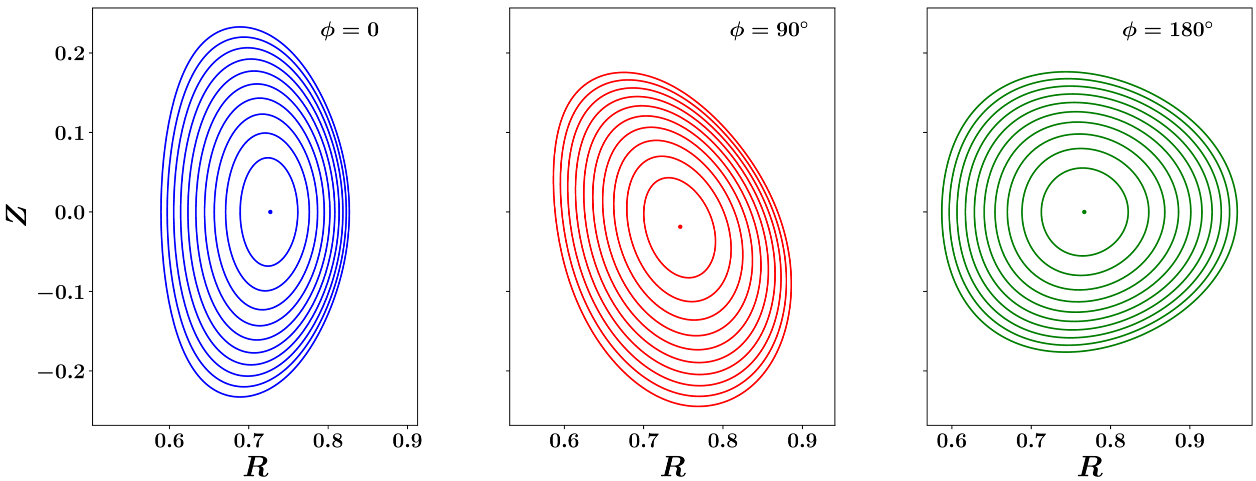

Figure 3.12: CTH Shot 12092031 flux surfaces from VMEC equilibrium at three toroidal slices, the initial point, the quarter field period and the half field period.

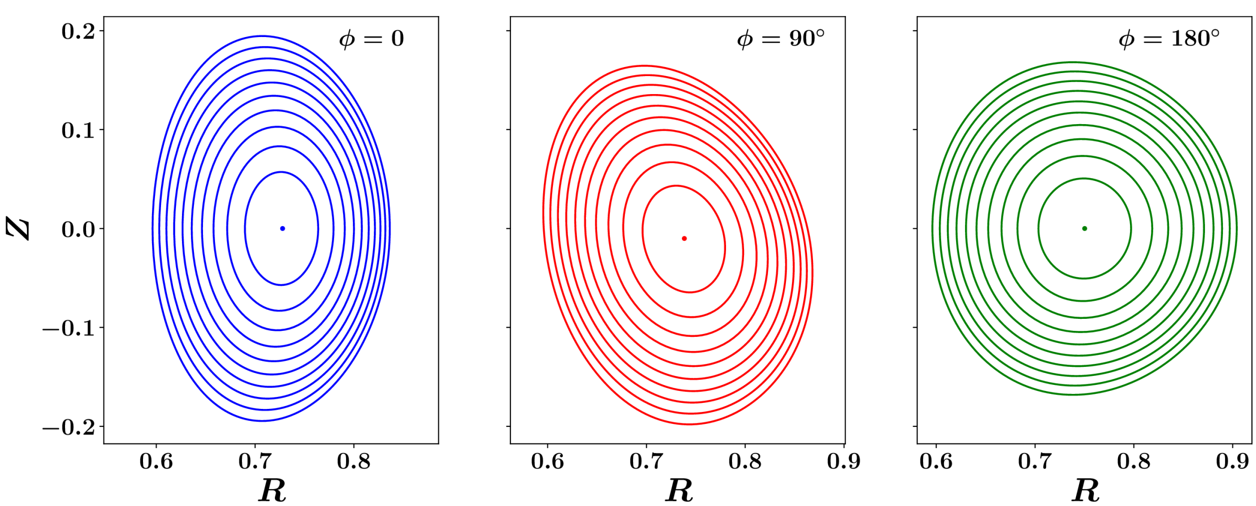

Figure 3.13: CTH Shot 14092626 flux surfaces from VMEC equilibrium at three toroidal slices, the initial point, the quarter field period and the half field period.

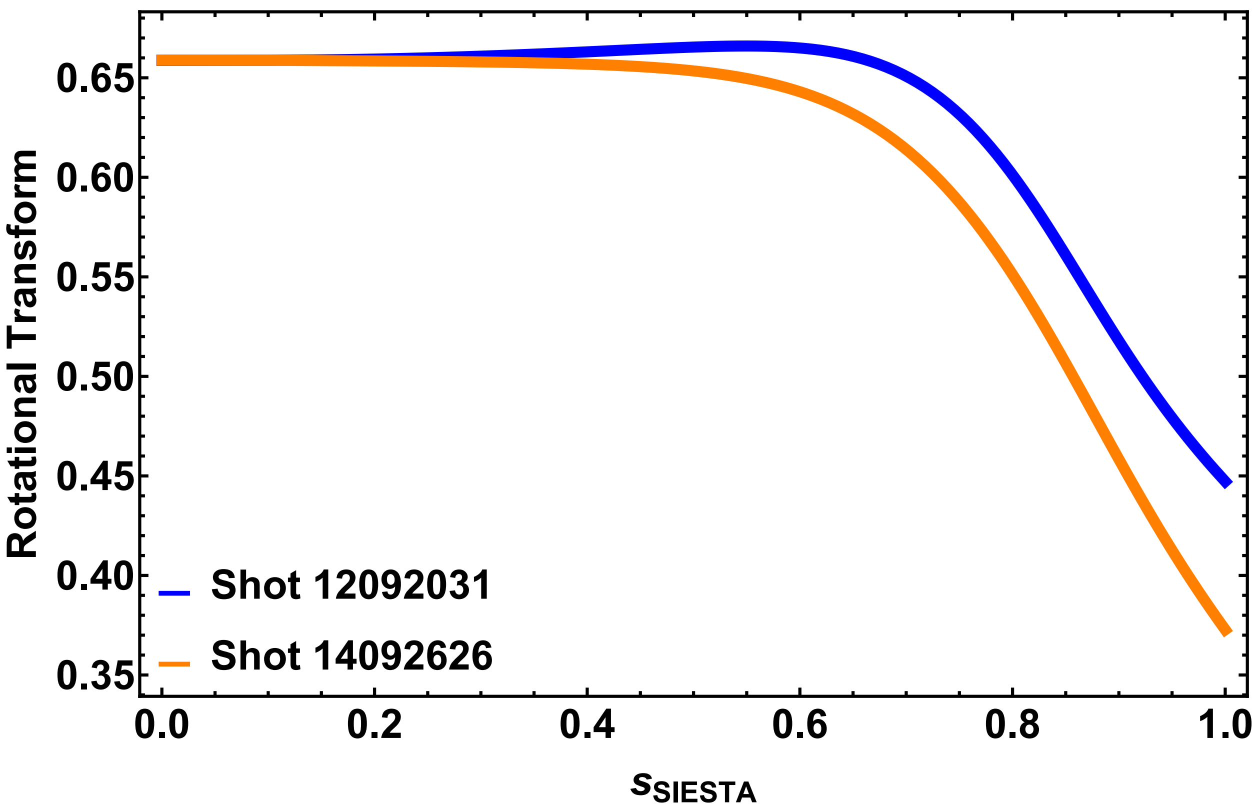

Figure 3.14: Iota profiles of the VMEC equilibrium for the two CTH shots. The horizontal axis is plotted using the SIESTA radial coordinate, s.

can be seen in Figs. 3.15-3.16.

3.4.3 Fixed Points and Island Size

We use the Cary-Hanson method [87, 98] to detect and measure magnetic island O-points and X-points in a plasma equilibrium. For convenience, we will give a brief summary below.

The following of magnetic field lines through a full toroidal loop can be treated as a mapping. [113] The system of equations we used in the SIESTA coordinate system are the following,

$$\frac{\partial s}{\partial v} = \frac{\mathcal{J}B^s}{\mathcal{J}B^v} \qquad \frac{\partial u}{\partial v} = \frac{\mathcal{J}B^u}{\mathcal{J}B^v}. \tag{3.27}$$

The Jacobian term has been kept because SIESTA uses the $\mathcal{J}B^i$ terms in its internal calculations and they will always cancel, thus having no impact on the results. Also keeping the Jacobian will be beneficial for the interpolation that will be explained in the next subsection.

Points that close on themselves after a fixed number of toroidal loops (they map onto themselves) are known as fixed points. In the presence of magnetic islands, the field-line flow map in a plasma equilibrium will always have multiple fixed points. One fixed point that is always present is the magnetic axis, as following the axis field line once around toroidally will map back to the initial point. A quantity that is closely related to the behavior of the other fixed points is the rotational transform, ι. In general, the rotational transform can be defined as,

$$\iota = \lim_{K\to\infty} \frac{\sum_{k=1}^{K} \Delta\theta_k}{\sum_{k=1}^{K} \Delta\phi_k} \tag{3.28}$$

where θ is an arbitrary poloidal angle, ϕ is an arbitrary toroidal angle, and the $\Delta\theta_k, \Delta\phi_k$ terms represent the change in the angle after the k^{th} toroidal transit.

Magnetic islands form at rational values of iota, $\iota = n/m$, where n is the toroidal mode number and m is the poloidal mode number. When iota is rational the field-line returns to its original location after m toroidal revolutions. Therefore, when looking for O-points and X-points, the fixed points must return the same point after making m toroidal revolutions corresponding

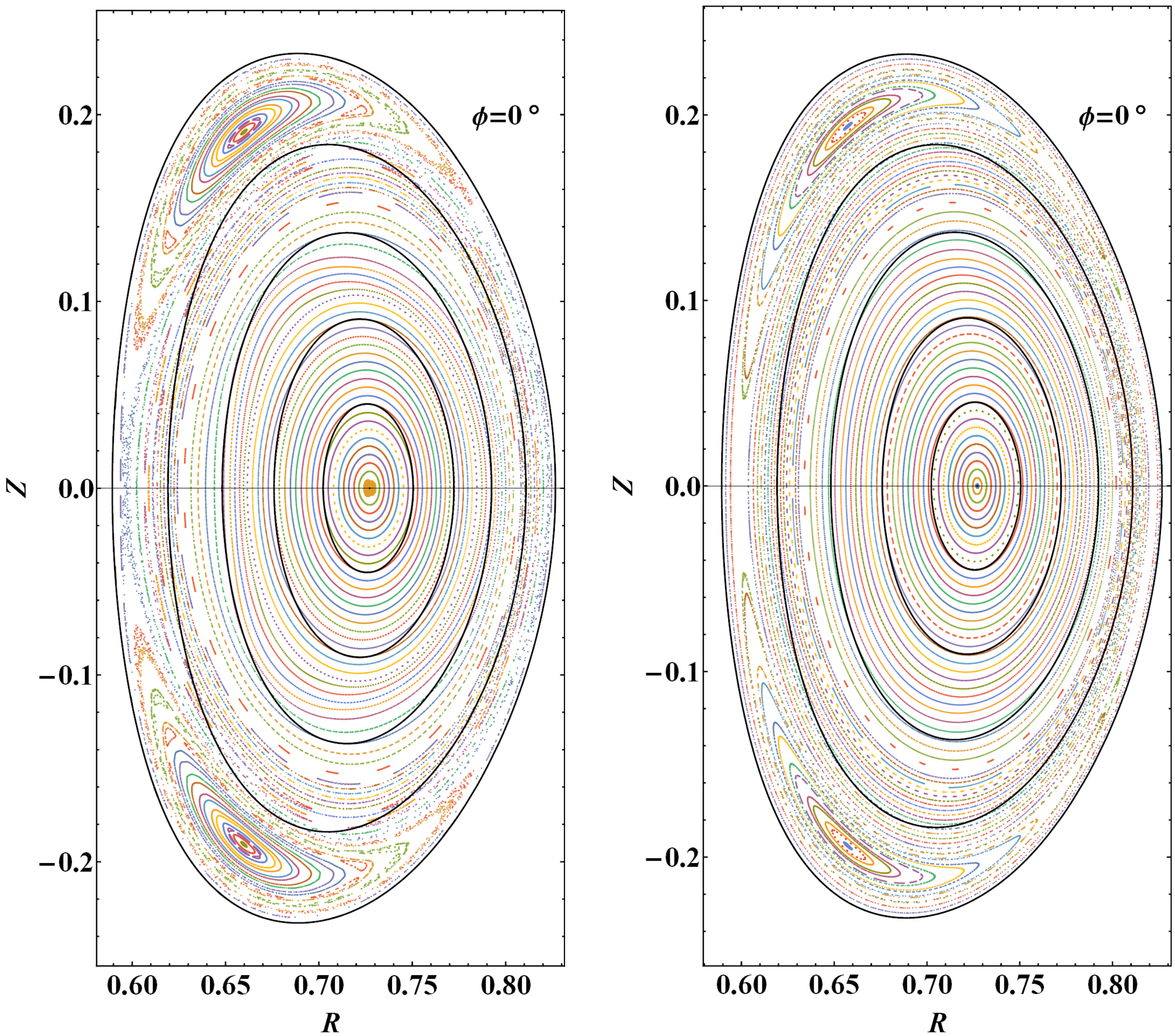

Figure 3.15: CTH Shot 12093031 flux surfaces from SIESTA equilibrium for two different perturbation magnitudes. The case on the left used a perturbation of 2.0×10^{-3}, whereas the case on the right used a perturbation of 1.0×10^{-3}. The black curves are lines of constant normalized toroidal flux, intended to represent VMEC surfaces. In the above plots, the core region is plotted with a lower flux surface density as opposed to around the island region for improved visual clarity.

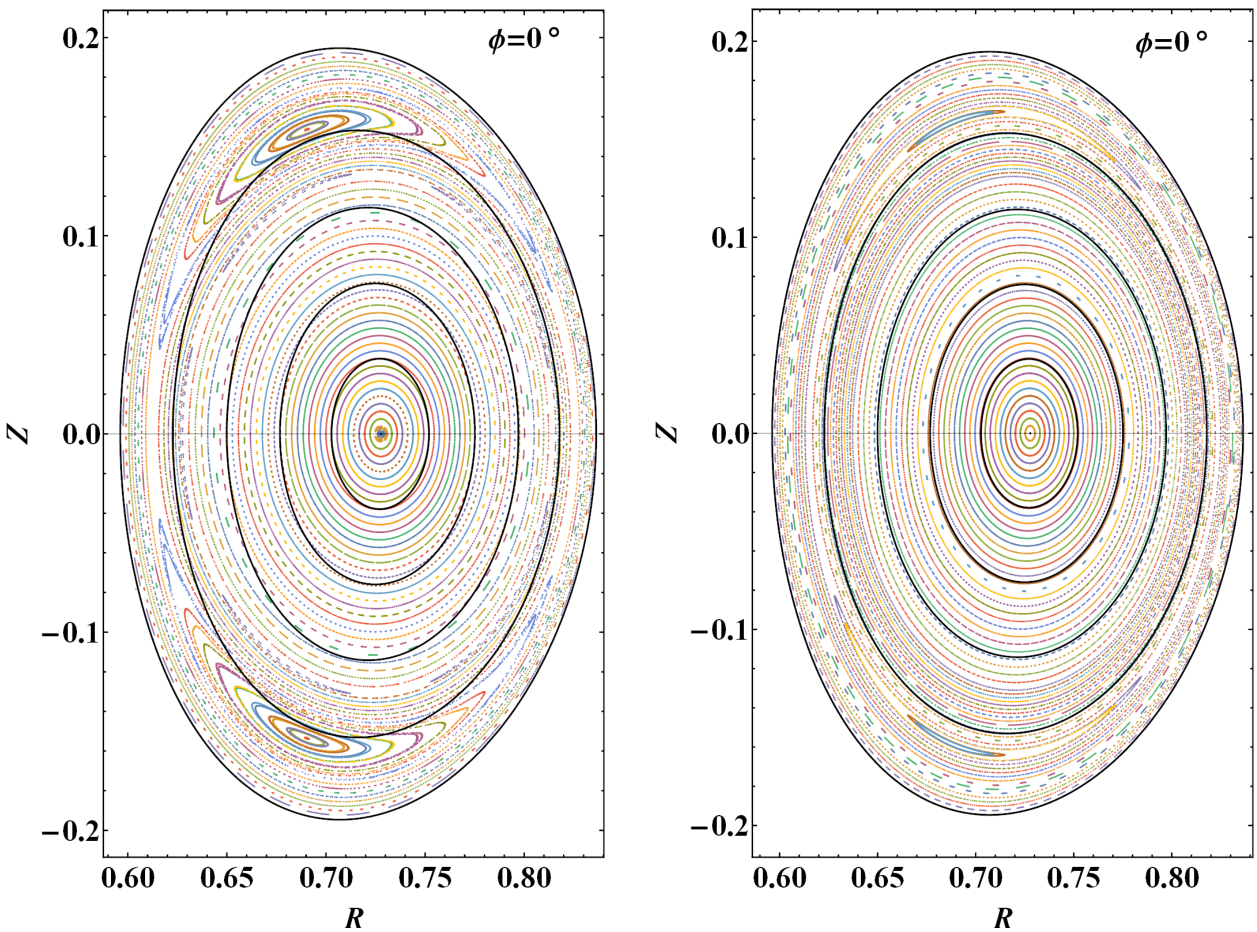

Figure 3.16: CTH Shot 14092626 flux surfaces from SIESTA equilibrium for two different perturbation magnitudes. The case on the left used a perturbation of 2.0×10^{-3}, whereas the case on the right used a perturbation of 2×10^{-4}. The black curves are lines of constant normalized toroidal flux, intended to represent VMEC surfaces. In the above plots, the core region is plotted with a lower flux surface density as opposed to around the island region for improved visual clarity.

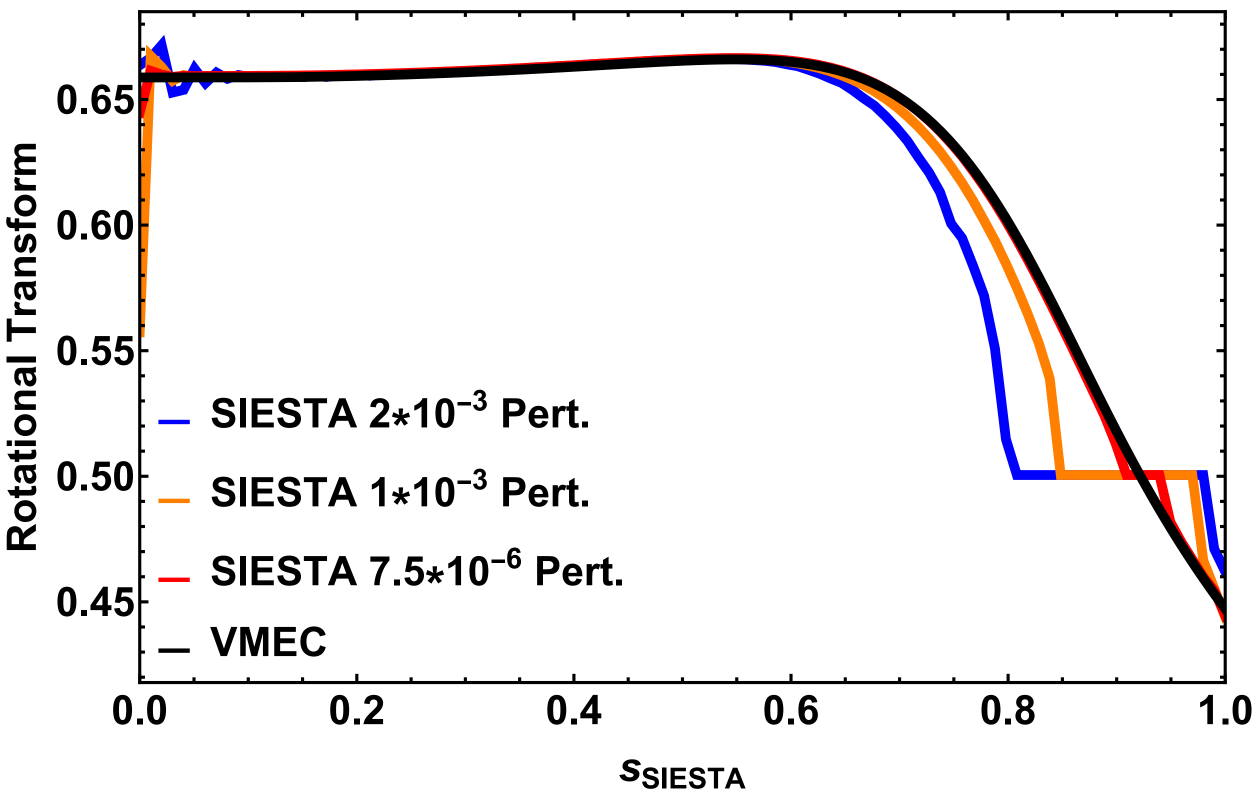

Figure 3.17: Rotational transform profiles of CTH shot 12093031 equilibria calculated with SIESTA for various perturbation magnitudes and the VMEC profile for comparison. Noise near the magnetic axis in the SIESTA profiles is a known issue with the code. ι is calculated using Eq. (3.28) for $K = 1000$.

to the resonant value of iota.

To locate these fixed points we implement a 2D Newton method to find the roots of the equation, $g(\mathbf{x}) = f(\mathbf{x}) - \mathbf{x} = \mathbf{0}$, where f is the flow map. A derivative of f is required to perform the Newton step, and this quantity proves to be the tangent map. This is convenient as the tangent map is required for the ensuing analysis.

Once the fixed points are found, we can get a measure of the size of the island. The first method is calculating the quantity known as the Greene's residue, [94, 95] defined as,

$$\mathcal{R} = \frac{1}{2} - \frac{1}{4}\mathrm{Tr}(\mathbf{S}) \tag{3.29}$$

where $\mathbf{S}$ is the Jacobian matrix, or the tangent map at the fixed point. For a more detailed discussion on how the tangent map is calculated, refer to Appendix 2. The residue itself gives a way to quantify the size of the island. When $0 < R < 1$, the residue is associated with an O-point, and when $R < 0$ or $R > 1$ the residue is associated with an X-point, the former being the more typical case.

To calculate the radial width of the magnetic island, we apply the formulas derived in Ref. [98], specifically Eqs. (44)-(45), which are the following,

$$\omega = \frac{\cos^{-1}(1 - 2\mathcal{R})}{2\pi m} \tag{3.30}$$

$$\Delta s = \frac{4\omega}{m\,|\iota'_{\mathrm{VMEC}}|} \tag{3.31}$$

where ω is the frequency of trajectories near the fixed point, Δs is the radial width, in s, of the island at its widest point, and $\iota'_{\mathrm{VMEC}} = d\iota_{\mathrm{VMEC}}/ds_{\mathrm{SIESTA}}$ is the shear of the unperturbed equilibrium. Note that in the original formulation, the shear is calculated in terms of the tangent map parameters, where it is calculated from the unperturbed flow. Since a VMEC equilibrium is required to calculate the corresponding SIESTA equilibrium, we already have the rotational transform of the case without any islands, and can easily calculate the shear from them.

The other method we use to calculate the size of the island is to measure the length of the portion of the rotational transform profile that is flat from the SIESTA equilibrium. In the region of an island, the value of iota stays fixed at the resonant rational value. As such, it is possible to estimate the radial width of the island in flux coordinate space in this manner. An example of island flattening of the ι profile is shown in Fig. 3.17.

The island measurement using the rotational transform, calculated from Eq. (3.28), is performed as follows. As the system has stellarator symmetry, and the fixed points are even order, because $m = 2$, there exists a plane at either $v = 0$ or $v = 2\pi/m$ where an O-point is located on the line $Z = 0$. [87] Choosing that plane and setting the initial poloidal angle ($u = 0$), the rotational transform is calculated for each s using 100 toroidal rotations ($K = 100$). For the s resolution, we choose the increment to be one fifth of the SIESTA grid size. The island width is the span in s for which the rotational transform values are within 2% of $1/2$. The percentage is chosen to account for any numerical error in the transform calculation.

3.4.4 Divergence-Free Interpolation

Here we present a simple analytic method developed to ensure the divergence of the magnetic field is effectively zero. All ensuing quantities will be assumed to be stellarator symmetric for simplicity.

The divergence of the magnetic field can be expressed as,

$$\mathcal{J}(\nabla \cdot \mathbf{B}) = \frac{\partial(\mathcal{J}B^s)}{\partial s} + \frac{\partial(\mathcal{J}B^u)}{\partial u} + \frac{\partial(\mathcal{J}B^v)}{\partial v}. \tag{3.32}$$

In the above case $\mathcal{J}B^s$ has sine parity, and both $\mathcal{J}B^u$ and $\mathcal{J}B^v$ have cosine parities due to the stellarator symmetry. Substituting the respective Fourier expansions using Eqs. (3.9)-(3.10) into Eq. (3.32), taking the poloidal and toroidal derivatives, and rearranging terms yields the condition for a divergence free magnetic field,

$$\frac{\partial}{\partial s}\mathcal{J}B^{s}_{mn}(s) = m\mathcal{J}B^{u}_{mn}(s) + n\mathcal{J}B^{v}_{mn}(s) \quad \forall\,(m,n). \tag{3.33}$$

The last step is to interpolate each Fourier coefficient, $\mathcal{J}B^{u}_{mn}$ and $\mathcal{J}B^{v}_{mn}$, as an order n spline, and then use Eq. (3.33) to set the coefficients of the $n+1$ order spline which interpolates the Fourier coefficients $\mathcal{J}B^{s}_{mn}$. Note that the coefficients without a radial term that would vanish after taking the radial derivative are set by the actual value of the quantity on the grid. We have used cubic polynomials to interpolate the poloidal and toroidal field terms, and quartic polynomials to interpolate the radial terms. Using this method the divergence of the magnetic field is on the order of machine precision on all points in the grid. It is worth noting that the method can easily be extended to stellarator asymmetric cases. Following the same process yields another condition necessary for divergence free fields that is entirely composed of the asymmetric terms. Equation (3.33) is derived and the method is discussed in more detail in Appendix 2.

3.4.5 Perturbation Magnitude Scan

We have studied V3FIT reconstructions of two CTH shots, numbers 12092031 and 14092626, which were known to have $\iota = 1/2$ islands. The reconstructions were rerun at higher resolution, specifically using 100 surfaces and setting both the number of poloidal and toroidal modes to six. VMEC was then run in free-boundary mode, assuming stellarator symmetry, until the square of each component of the force residual, **F**, was below 1×10^{-21}. Such a low VMEC force residual was chosen because it has been observed to improve convergence in SIESTA. Afterwards SIESTA was run with a fixed boundary in "sparse" mode until it obtained a squared force residual below 10^{-20}. The device was changed to only have a single field period, rather than five, and the toroidal modes $n = \{0, \pm1, \pm5, \pm10, \pm15, \pm20, \pm25, \pm30\}$ were chosen so that a perturbation with a poloidal mode number of $m = 2$ would open the island.

Finally, the equilibrium was calculated for various values of the helical perturbation input parameter, H_{pert}, with values ranging from 1×10^{-6} to 2×10^{-3}. The range of values was chosen by seeing what was the smallest value which allowed an island to form, and the largest value for which SIESTA could converge to the desired force residual. Plots of the equilibria with islands can be seen in Figs. 3.15-3.16. Because these cases were run assuming stellarator symmetry, the resulting equilibria had either the O-points or X-points at the line $Z = 0$, as one would expect. [87] In real space the islands were most visible when they were located on the top and bottom of the plasma with the X-points on the mid-plane.

It is clear from the plots that the larger perturbation results in larger islands. An interesting byproduct of the larger islands is the deformation of the flux surfaces. It is most easily seen when comparing the SIESTA surfaces to the surfaces of constant s. In the plot with the smallest perturbation the SIESTA surfaces appear to match the constant s surfaces well. In the case of the larger perturbations the islands deform the flux surfaces in the entire plasma, most significantly in the case of Shot 12093031 with the 2×10^{-3} perturbation. This indicates how inaccurate a VMEC solution could be in the presence of large islands, as well as how VMEC could still be reasonably accurate when small islands are present.

We now move our attention to the islands in the equilibrium and their response to the choice of perturbation value. This is shown in Figs. 3.18-3.19 where we have plotted the magnitudes of the residues found for both O-points and X-points as functions of the perturbation given to SIESTA. As expected, increasing the helical perturbation results in larger residues, which then implies larger magnetic islands. We observe that the magnitude of the residues for the O-points and X-points in each shot are roughly the same. The main exclusion from this behavior is the last point in Fig. 3.18 that is approximately three times larger in magnitude than the corresponding X-point. The two plots show different relationships between the residue and the perturbation. Shot 12092031 indicates an approximately linear relationship between the two parameters, the curve in Fig. 3.18 being $y = 81.3x$ is included to corroborate this. Shot 14092626 has an approximate quadratic relationship, the curve in Fig. 3.19 being $y = 38,000x^2 + 39x$ is included to show this. It is important to mention that the points on the left of both plots with constant residues were excluded in the curve fitting, as well as the outlier on the right in Fig. 3.18.

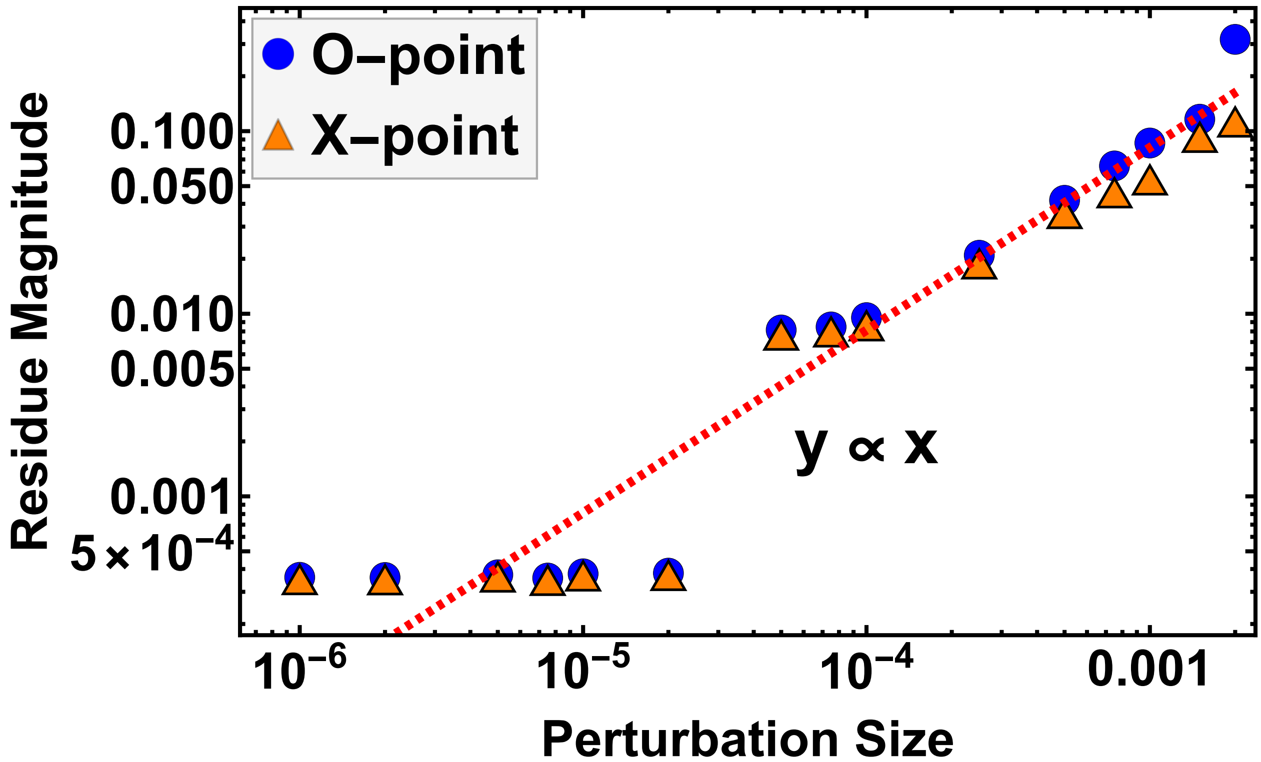

Figure 3.18: Residue as a function of the perturbation size for CTH shot 12092031. Both axes are set to a log scale.

Also, note that in both cases the residue is relatively constant until some threshold value is reached, upon which the residue increases from then on. The cause of this can be seen when looking at the island width calculation as a function of the perturbation size plotted for both shots in Figs. 3.20-3.21.

From these plots it becomes clear that for smaller residues SIESTA opens an island but is only able to resolve it to the resolution of the grid. A greater radial resolution is required to observe smaller islands, though they are so small at that perturbation magnitude one can ignore them. We will now discuss the overall behavior of the island widths for the two different shots

It is first worth noting the relative agreement between the two methods employed to calculate the magnetic island width, with most relative errors ranging between $1\% - 15\%$. If we Taylor expand Eq. (3.30) about $\mathcal{R} = 0$ we see that for small residues the Cary-Hanson island width is proportional to $\mathcal{R}^{1/2}$, to leading order. This then would imply that the island widths for shots 12092031 and 14092626 should be approximately proportional to the square root

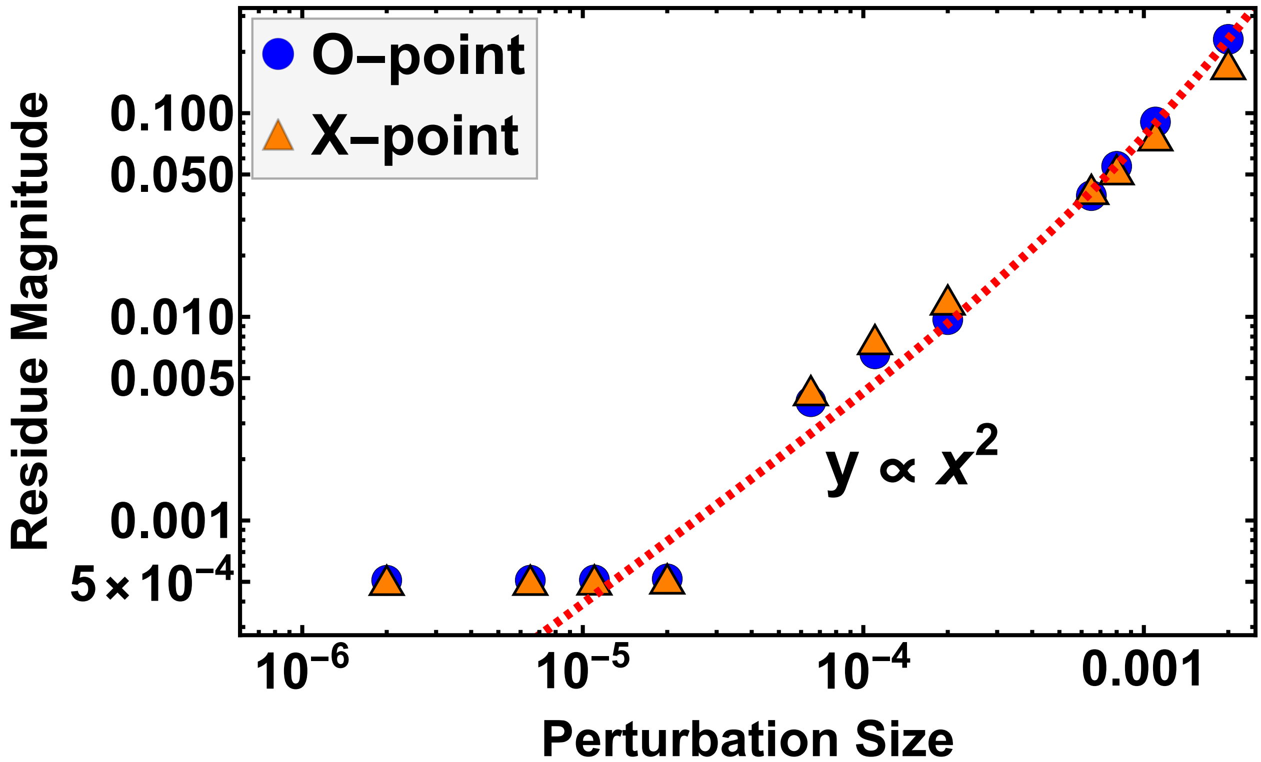

Figure 3.19: Residue as a function of the perturbation size for CTH shot 14092626. Both axes are set to a log scale.

of the perturbation size and the perturbation size, respectively. This behavior is seen in both Figs. 3.20-3.21, with the linear relationship being especially clear in shot 14092626. This calls into question why the islands in the two equilibria have differing dependencies on the helical perturbation. A possible explanation for this behavior is the coupling of the radial location of the resonance with the fact that SIESTA was run in fixed-boundary mode.

If we look at Figs. 3.22-3.23 we can see that the O-point in shot 12092031 is located further towards the edge of the plasma than in shot 14092626, with initial s values of approximately 0.922 and 0.857 respectively. In both cases as the perturbation size grows the O-points move inwards, while the X-points move outwards. Comparing the island width plots with the radial location plots, some inferences can be made.

Since SIESTA was run in fixed boundary mode, the last closed flux surface could not change from the initial VMEC solution. As the islands grow in size, they require more room to exist and will move inwards to gain this space to not affect the plasma edge. The issue is that the

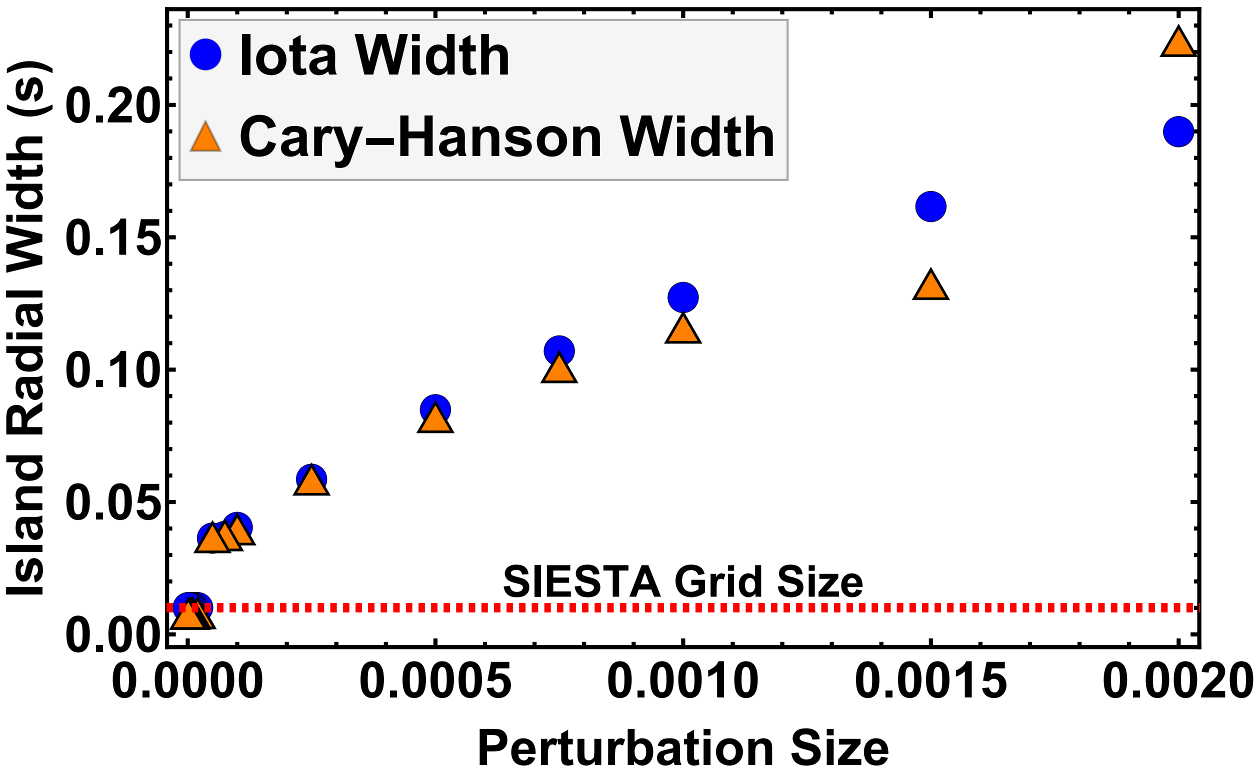

Figure 3.20: Island Width as a function of the perturbation size for CTH shot 12092031 for both prescribed calculation methods.

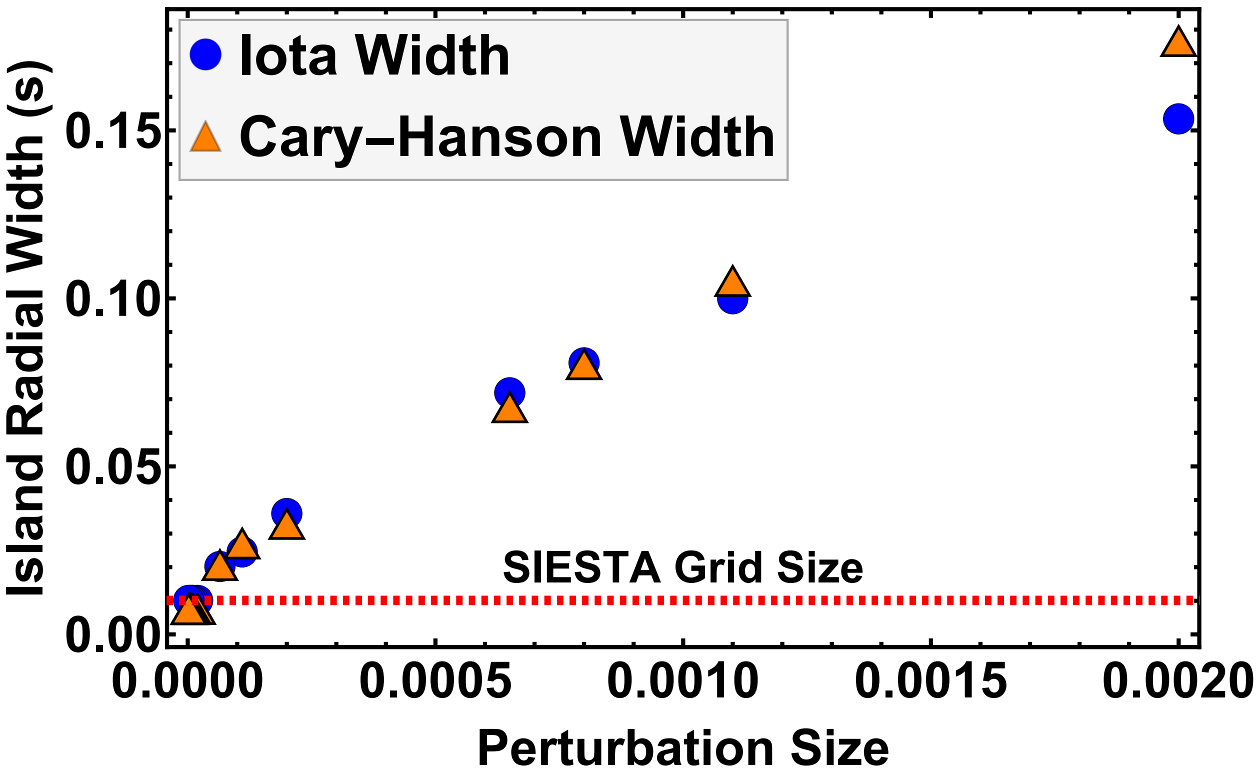

Figure 3.21: Island Width as a function of the perturbation size for CTH shot 14092626 for both prescribed calculation methods.

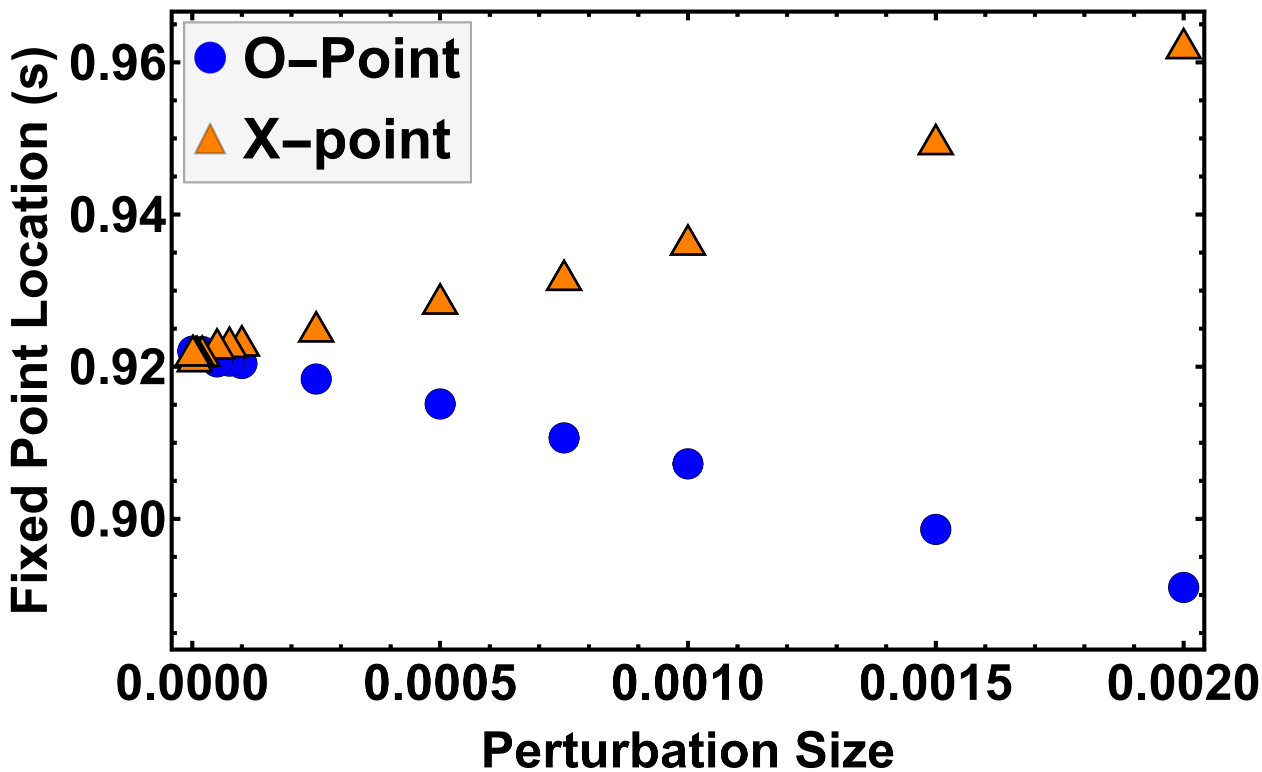

Figure 3.22: Radial location of fixed points as a function of the perturbation size for shot 12092031.

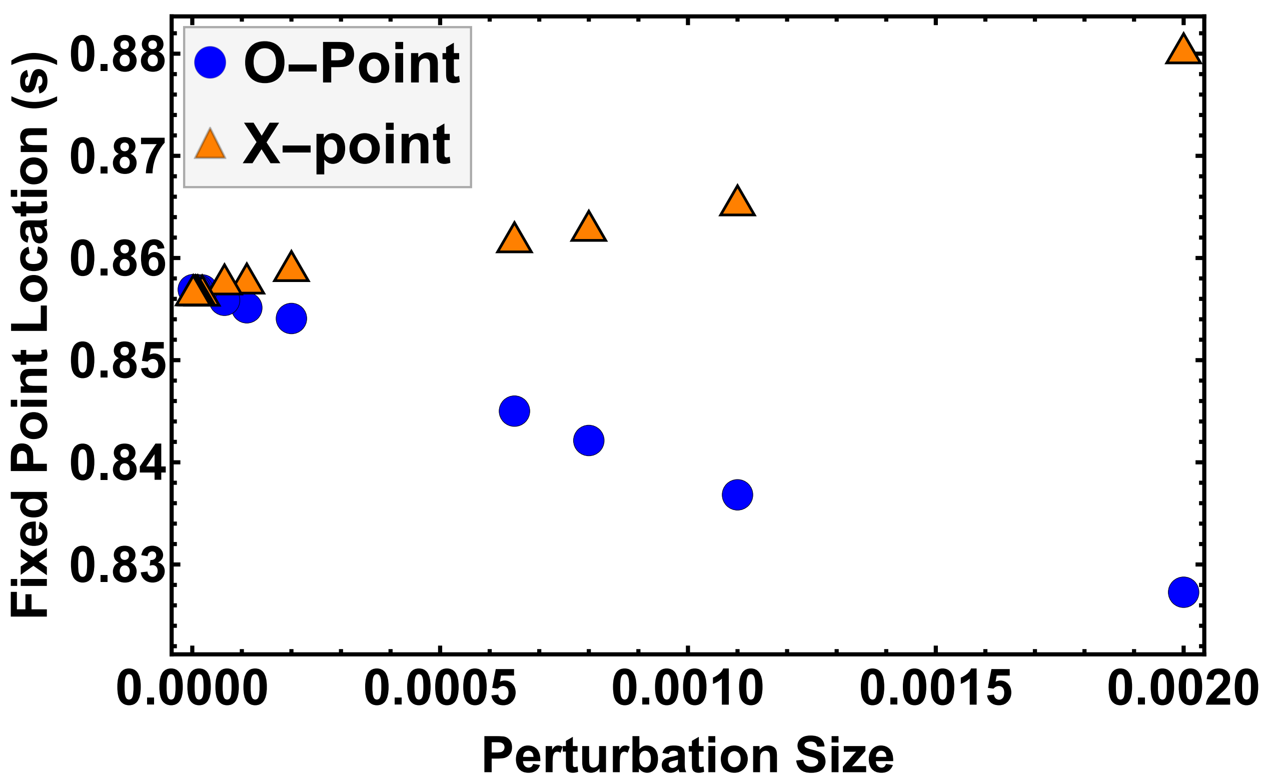

Figure 3.23: Radial location of fixed points as a function of the perturbation size for shot 14092626.

island grows much faster than it moves inwards, and as such it will no longer have the ability to expand without affecting the boundary. This may lead to solutions, that while possible according to the code, are not physical or an accurate response to the resonant perturbation applied. Free boundary runs may be required to study these larger islands located near the edge of the plasma.

3.4.6 Island-Plasma Boundary Interaction

The location of the resonance with respect to the boundary has an impact on the resulting island, as an H_{pert} value of 2×10^{-3} resulted in islands (O-points) with residues of approximately 0.23 for shot 14092626 and 0.32 for shot 12092031. To investigate this further, we performed a set of SIESTA runs where we varied the plasma boundary while keeping the perturbation value fixed. This was done by taking the VMEC equilibrium calculated for shot 14092626, running it for one iteration in SIESTA, converting all the VMEC quantities to the SIESTA grid, removing the data of the last few surfaces, and then running SIESTA like normal with this reduced case. This would give approximately the same equilibrium as before, but now the plasma edge is located closer to the resonant surface. For this study we chose to use $H_{\text{pert}} = 2 \times 10^{-4}$, as it resulted in a small, but still noticeable island, as seen in Fig. 3.16, which is not too close to the boundary, allowing us to remove several surfaces. The results of this investigation can be found in Table 3.5.

There are some limitations with the procedure that must be mentioned. While we are applying the same value of H_{pert} to each of the equilibria, we cannot fully control when it is applied. Before SIESTA applies the resonant perturbation, the squared force residuals must first reach values below a certain threshold, $\mathcal{O}(10^{-10})$, and thus it takes a few ideal iterations to achieve this. Sometimes the solver is able to achieve force residuals that are several orders of magnitude smaller than the threshold, and others it just passes it. This is important because of how the perturbation is applied in Eq. (3.13), where it is a scale factor applied to the currents. If the equilibrium is too well resolved before the perturbation is applied then the radial currents will be very small and the perturbation will not have the same effect as if it were applied at higher values. Therefore, we are not certain these perturbations are applied equally across the different

NS	O-point Res.	O-Point R (m)	Island Width (m)	Unpert. Energy (J)	ΔE_{pert}(J)
100	9.692×10^{-3}	0.8835	5.271×10^{-3}	37421.314	0.007
99	1.535×10^{-2}	0.8831	7.232×10^{-3}	37425.782	0.013
97	3.224×10^{-2}	0.8824	9.958×10^{-3}	37434.763	0.024
95	5.456×10^{-2}	0.8819	1.191×10^{-2}	37443.783	0.040
90	8.322×10^{-2}	0.8815	1.271×10^{-2}	37466.226	0.073

Table 3.5: Data from surface removal study. All fixed point data was taken from the toroidal plane where the O-point is located at $Z = 0$. Since each calculation in SIESTA is performed with the radial coordinate ranging from 0 to 1, and thus will be different for each case, we have used the cylindrical radial coordinate R for the spatial quantities. The unperturbed MHD energy is calculated for each equilibrium where no island was seeded, and the energy decrease was the change in MHD energy in the equilibrium which included the island.

configurations. This analysis does provide insight into the limitations of how SIESTA handles the relationship between island locations and the fixed boundary.

It is clear from these results that moving the resonance closer to the boundary has an effect when running fixed-boundary SIESTA. As we move the plasma edge closer to the resonant region, we see the residue and island width both increasing, as well as the O-point moving inwards. The increased island size can be observed in Fig. 3.24. This indicates that large islands near the plasma boundary should be studied with a free-boundary formulation in SIESTA, as this should eliminate any effects from the fixed boundary and allow the island to expand unopposed.

3.4.7 Conclusion

In this study we developed a method to locate and characterize magnetic islands from a SIESTA equilibrium, as well as an analytic method to ensure a divergence free interpolated magnetic field. Both were successfully implemented on two test cases, VMEC reconstructions of CTH equilibria with known $n = 1, m = 2$ islands present. This was done by studying the sensitivity of the magnetic island size with respect to the helical perturbation SIESTA input parameter. A scan was performed on helical perturbation values that ranged over several orders of magnitudes, and several trends were noted in the equilibrium calculated.

First, as the perturbation magnitude was increased, the island size increased as well. This

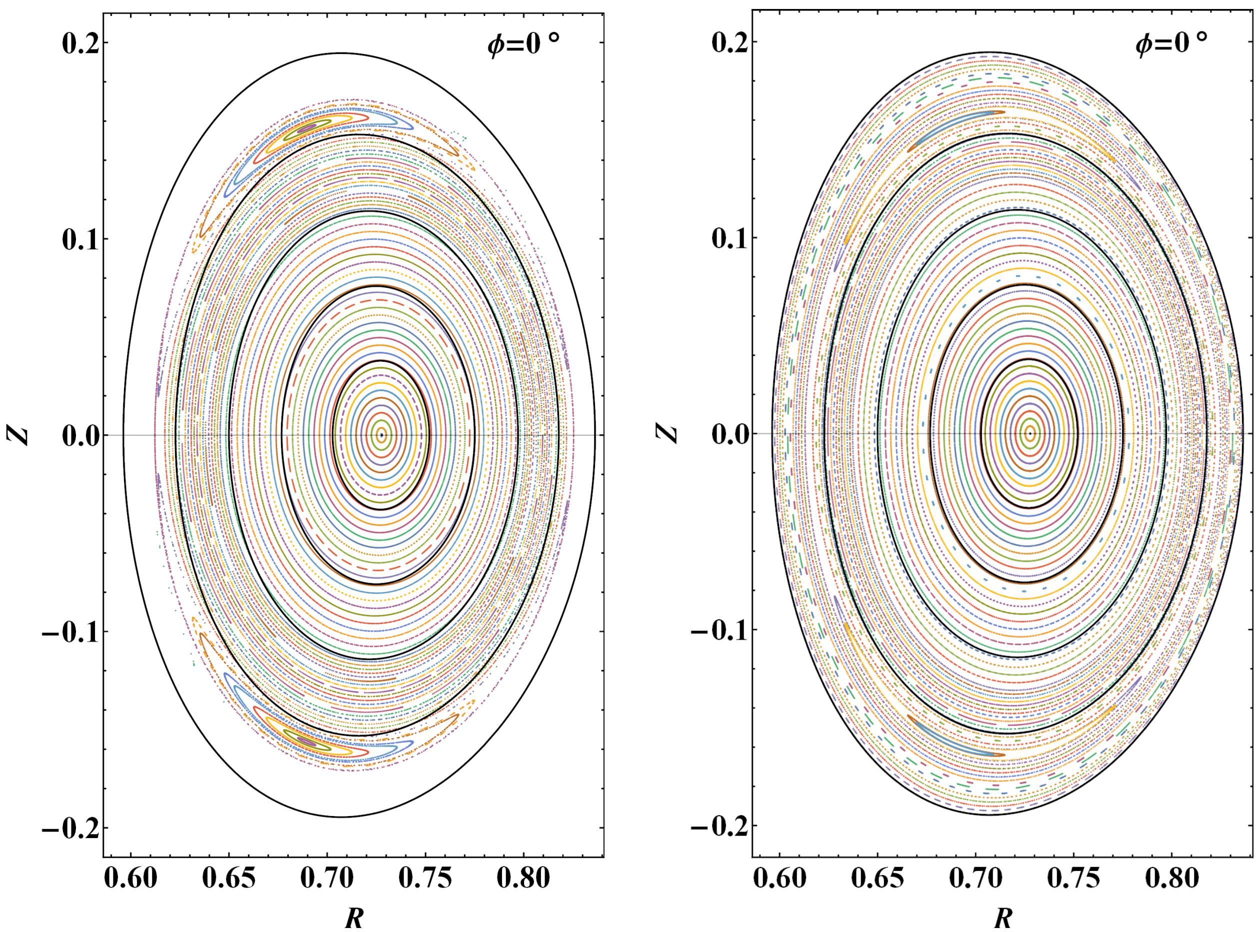

Figure 3.24: CTH Shot 14092626 flux surfaces from SIESTA equilibrium for two different number of SIESTA surfaces. Both cases on the used a perturbation of 2.0×10^{-4}. The plot on the left is from a SIESTA equilibrium with the last ten surfaces removed, (NS $= 90$), while the plot on the right is the same as in Fig. 3.16, repeated for the reader's convenience. The black curves are lines of constant normalized toroidal flux, intended to represent VMEC surfaces. The black lines on the left plot are the same as those in the right, to emphasize the original boundary and surfaces.

was observed for both island size measurements made, the Cary-Hanson method and the width of the flattened section of the rotational transform profile, as well as visually from the puncture plots. We also found that while smaller perturbations, relatively speaking, still opened islands in SIESTA, they could only be resolved to the size of the SIESTA grid. While not shown, these islands were difficult to see in the puncture plots, if at all. It was also noted that the radial location of the O-points and X-points changed with increasing perturbation size as well. Furthermore, we observed overall trends in the two cases regarding the island width's dependence on the helical perturbation. One shot, 12092031, showed the island width being approximately proportional to the square root of the perturbation, whereas the other, 14092626, showed a linear relationship between the two. A possible explanation for this was attributed to the initial point where the island formed, with the island that formed near the plasma edge was possibly restricted in its ability to expand because it could not deform the plasma boundary. Although, it was also noted that the perturbations located closer to the plasma edge in shot 12092031 resulted in larger islands than those in shot 14092626 with the same perturbation magnitude. It was also noted that the O-points moved radially inwards, while the X-points moved radially outwards with increasing perturbation size for both cases, likely allowing the islands to expand.

Additionally, to investigate further the relationship between the location of the resonance relative to the plasma boundary, we performed a set of equilibrium calculations were several radial surfaces were removed prior to calculating the equilibrium. This was done to simulate the resonance occurring closer to the last closed flux surface. We found that the magnetic islands became larger and moved inwards as the plasma boundary moved closer to the resonance location. The cause for this behavior is unknown, but we believe that free-boundary calculations would be required to investigate if this behavior is physical, or a result of calculating fixed-boundary equilibria.

Chapter 4

Linear Stability Studies

Some text and figures in this chapter are reproduced from,

Gabriel S. Woodbury Saudeau, Riccardo Betti, Luca Guazzotto; Linear stability analysis of compressible Kelvin–Helmholtz and Rayleigh–Taylor instability and the effect of a flow-aligned magnetic field. Phys. Plasmas 1 February 2026; 33 (2): 022107. https://doi.org/10.1063/5.0301956

with the permission of AIP Publishing.

4.1 Introduction

The Kelvin-Helmholtz instability (KHI) [7, 8] and the Rayleigh-Taylor instability (RTI) [9, 10] are widely studied fluid/plasma instabilities that are known to occur in several physical phenomena, such as inertial confinement fusion [114–116] in the case of the RTI and astrophysical settings [117–121] or magnetic confinement fusion [122, 123] in the case of the KHI. The KHI is an instability driven by shear flow in a fluid or plasma [124, 125], while the RTI is an instability driven by gravity or a gravitational-like force in the presence of a density gradient oriented in the opposite direction.[124, 125]

When a linear stability analysis is conducted on either the KHI or RTI, the compressibility of the fluid must be taken into consideration. In a sizable portion of the literature, the analysis is made with the assumption that the fluid is incompressible; it is simpler and reasonably accurate in most cases. The incompressible KHI and RTI are widely studied and have analytic forms of their growth-rates, which are easy to deduce physical meaning from. [124] This is especially true in the case where both instabilities are present in the same system, as there is a known analytic form of the growth-rate in the literature.[125] The linear theory on the compressible unmagnetized KHI has been studied extensively for close to a century. Landau [126] and Miles [127] have studied the vortex sheet approximation, where the fluid velocities are discontinuous at the interface, of the homogeneous KHI and showed that compressibility stabilizes the instability. It was found that for the system to be stable, the Mach number of the relative flow must be greater than $2^{3/2}$, or $\sqrt{2}$ when the flows are equal and opposite. Plesset and Hseih [128] included gravity in their stability analysis of the vortex sheet. They showed that for supersonic flow velocities, due to the presence of gravity and the stratified fluids, the system was always unstable. There is not a consensus on this result, as Miles [129] disagreed with their results, claiming that their dispersion relation was incorrect. The case for a finite thickness shear layer has also been investigated by several authors. [130–133] The shear layer was shown to be unstable for all Mach numbers larger than one due to modes which are not present in the vortex sheet approximation.

The magnetic compressible KHI has likewise been extensively investigated. Several authors have worked on the vortex sheet approximation for this case. [134–137] Of note is the recent publication by Peyrichon et al. [137] They were able to show analytically and numerically the stabilizing effect a flow-aligned magnetic field has on the system for both homogeneous and heterogeneous flows. Additionally they validated their analytical work by comparing it to numerical simulations. The shear layer version of the problem has also been analyzed. [121, 138–140] Miura and Pritchett [121] investigated the case of compressible flows with a finite shear layer and arbitrary magnetic field orientation. In this work, the authors discuss the effect the magnetic field transverse and parallel to the flow has on the stability of the system. They find that the system is more unstable when the magnetic field is transverse to the flow as opposed to when it is parallel.

Although we will focus on analytical calculation, we note for completeness that other authors have examined both the linear and nonlinear behavior of the KHI using a computational approach. [141–144] Briard et al. [144] for example were able to recover the linear growth-rates for the MHD KHI found in Miura and Pritchett's seminal paper. [121]

The linear stability of the compressible RTI has been the subject of sustained study by various authors over time. [145–149] Livescu [148] in particular set out to resolve prior contradictory findings which stated compressibility has a stabilizing effect or a destabilizing effect on the RTI. In the case of an inviscid, infinite domain, and lack of surface tension, the author demonstrates that higher equilibrium pressures at the interface are associated with weaker compressibility effects and faster instability growth, whereas larger specific heat ratios similarly diminish compressibility but lead to a reduction in growth rate. The linear stability of the magnetic compressible RTI has also be examined in recent studies. [150–152] In these works the focus was mainly on the effects of compressibility on the system, as opposed to the stabilization effects of the magnetic field. Various numerical studies have likewise been performed over the years in regards to the nonlinear behavior, see e.g. [153–155]. Given the analytical focus of our work on the linear phase of the instability, we will not discuss them further.

The interest in the KHI and RTI comes from our work on tokamak equilibrium in the presence of highly sheared (discontinuous in the ideal magnetohydrodynamic, or MHD, model) velocities. [156, 157] In the equilibrium first described in Ref. [156], a contact discontinuity exists between two regions of the plasma with a finite jump in plasma density, pressure, and velocity. This system is potentially at risk of developing a KHI due to the velocity discontinuity. Moreover, the pressure jump acts as an additional instability drive, which, for simplicity, can be approximated as a constant gravitational field pointing from the “heavy” to the “light” side of the discontinuity. In summary, a detailed analysis of the combined KHI and RTI with a magnetic field in a plasma will give the first stability model of the discontinuous equilibrium in Ref. [156].

To the authors’ knowledge, little work has been done to look at the linear stability of a compressible system where both the KHI and RTI are present. In one paper of note, [158] the authors examined the compressible KHI and RTI through both non-porous and porous-media. They considered only numerical solutions of their dispersion relation for small velocity differences. Another publication of note[159] investigated the compressible KHI in the presence of both a magnetic field and gravity. However, the derivation is done while assuming that the densities of the two fluids are constant throughout, which is not self-consistent with the equilibrium.

4.2 Kelvin-Helmholtz

4.2.1 Introduction

The KHI is an instability of sheared flows. As previously stated, the instability occurs when you have two fluids in contact with each other that are flowing at different velocities. This could be done in a variety of ways, such as setting the fluid velocities as equal and opposite, setting one fluid to be at rest, or setting them both to be arbitrary different velocities. Furthermore, there are many other considerations one must consider when studying this instability. I will proceed to briefly cover a few of these.

Perhaps the most critical aspect of the problem one must take into consideration is the compressibility of the fluid. I say this because the difficulty of the problem increases significantly when one assumes the fluid to be compressible. In simple terms, this would mean that $\nabla \cdot \mathbf{v} \neq 0$. One must take compressibility effects into account when the Mach number, M, of the fluid flows are greater than 0.3, and they become much more prevalent as the Mach number increases. The analysis of the linear stability of the incompressible KHI is relatively easy and adding on varying degrees of complexities to the problem does not impair the finding of analytic expressions for the growth-rate of the instability. The same cannot be said of the compressible case, as will be shown later on.

Another important part one must decide on when doing the analysis of this instability is the velocity profile at the interface of the two fluids. One method is to treat the velocity at the interface to be discontinuous, that is to say on one side of the interface it is a certain velocity, and on the other side it is a completely different velocity. The other velocity profile at the interface used is a sharp, but continuous, change of the velocity, using a function such as tanh(Ax), where the value of A determines the size of the interface.

Lastly, additional physics can be included in the analysis of the instability, such as the presence of gravity or a magnetic field, and fluid viscosity. Generally these are included as simple constant scalars or vector fields in the equilibrium. Depending on the configuration they could either have a stabilizing or destabilizing effect on the system.

To give the reader further background we will show two derivations of the linear growth-rate of the KHI, one assuming incompressible fluids, and the other assuming compressible fluids. The incompressible case will be performed following the derivation shown in (Chandrasekhar), whereas the compressible case will follow a process similar to the derivation shown in (Landau and Lif).

4.2.2 Incompressible Kelvin Helmholtz Instability

First, we will look at the incompressible KHI. The system will be composed of two semi-infinite fluids in a Cartesian coordinate system. The interface between the two fluids will be the xy-plane at $z = 0$, and will extend into $\pm\infty$ in both x and y. The fluids will also extend into infinity in their respective z direction, the top fluid towards positive infinity, and the bottom fluid towards negative infinity. Included in the system are a gravitational acceleration in the negative z direction, and a uniform magnetic field pointing in the positive x direction. The fluid will be assumed to be inviscid, and both fluids will flow with arbitrary velocities along x. Lastly, we will be using the ideal MHD equations to govern the system. The equilibrium equations are thus,

$$\frac{\partial \rho}{\partial t} + \mathbf{U} \cdot \nabla \rho = 0 \tag{4.1}$$

$$\rho \left(\frac{\partial}{\partial t} + \mathbf{U} \cdot \nabla \right) \mathbf{U} = -\nabla p - \rho \mathbf{g} + \frac{1}{\mu} \left(\nabla \times \mathbf{B} \right) \times \mathbf{B} \tag{4.2}$$

$$\frac{\partial \mathbf{B}}{\partial t} = \nabla \times \left(\mathbf{U} \times \mathbf{B} \right). \tag{4.3}$$

To see if the system is unstable or not we must perturb the equilibrium. Perturbing the system leads to redefining the variables as such,

$$\mathbf{U} = \mathbf{U}_0 + \delta\mathbf{U} = U_0\hat{e}_x + \left(u_x\hat{e}_x + u_y\hat{e}_y + u_z\hat{e}_z\right)$$

$$\rho = \rho_0 + \delta\rho$$

$$p = p_0 + \delta p$$

$$\mathbf{B} = \mathbf{B}_0 + \delta\mathbf{B} = B_0\hat{e}_x + \left(b_x\hat{e}_x + b_y\hat{e}_y + b_z\hat{e}_z\right)$$

where the terms with deltas or lower case (as is the case for the components of the velocity and magnetic field) are the leading order perturbation terms and those with a 0 subscript are the equilibrium quantities. Substituting these into the governing equations and dropping equilibrium terms and those of higher order leads to the following linearized equations,

$$\frac{\partial\delta\rho}{\partial t} + \mathbf{U}_0 \cdot \nabla\delta\rho = -\delta\mathbf{U} \cdot \nabla\rho_0 \tag{4.4}$$

$$\rho_0\left(\frac{\partial}{\partial t} + \mathbf{U}_0 \cdot \nabla\right)\delta\mathbf{U} = -\nabla\delta p - \delta\rho\,\mathbf{g} + \frac{1}{\mu}\left(\nabla \times \delta\mathbf{B}\right) \times \mathbf{B}_0 \tag{4.5}$$

$$\left(\frac{\partial}{\partial t} + \mathbf{U}_0 \cdot \nabla\right)\delta\mathbf{B} = \nabla \times \left(\delta\mathbf{U} \times \mathbf{B}_0\right). \tag{4.6}$$

The next step in the analysis is to assume the perturbations are normal modes and are of the following form,

$$\delta F(x, y, z, t) = \tilde{F}(z)e^{i(k_x x + k_y y) + \gamma t}$$

where δF is an arbitrary perturbed quantity. Substituting and taking all the partial derivatives with respect to x, y and t, gives,

$$\bar{\gamma}\delta\rho = -u_z D\rho_0 \implies \delta\rho = \frac{-u_z D\rho_0}{\bar{\gamma}} \tag{4.7}$$

$$\bar{\gamma}\rho_0 u_x + \rho_0 u_z DU_0 = -ik_x\delta p \tag{4.8}$$

$$\bar{\gamma}\rho_0 u_y - \frac{B_0}{\mu}\left(ik_x b_y - ik_y b_x\right) = -ik_y \delta p \tag{4.9}$$

$$\bar{\gamma}\rho_0 u_z - \frac{B_0}{\mu}(ik_x b_z - Db_x) = -D\delta p - \delta\rho g \tag{4.10}$$

$$\bar{\gamma} b_x = ik_x B_0 u_x + b_z DU_0 \tag{4.11}$$

$$\bar{\gamma} b_y = ik_x B_0 u_y \tag{4.12}$$

$$\bar{\gamma} b_z = ik_x B_0 u_z. \tag{4.13}$$

Henceforth, I will be dropping the 0 subscript that indicates the equilibrium term. Now we have 8 unknowns, the perturbed quantities, and 8 equations, the seven above and the divergence of B equation. The next step is to solve for each unknown and reduce the system to a differential equation in z of a single unknown. Solving for the components of $\delta\mathbf{B}$ gives,

$$b_z = \frac{ik_x B}{\bar{\gamma}} u_z \tag{4.14}$$

$$b_y = \frac{ik_x B}{\bar{\gamma}} u_y \tag{4.15}$$

$$b_x = \frac{ik_x B}{\bar{\gamma}}\left(u_x + \frac{u_z}{\bar{\gamma}} DU\right). \tag{4.16}$$

Substituting the components of $\delta\mathbf{B}$ into Eq. (4.9) then gives

$$\bar{\gamma}\rho u_y - \frac{B}{\mu}\left(ik_x \frac{ik_x B}{\bar{\gamma}} u_y - ik_y \frac{ik_x B}{\bar{\gamma}}\left(u_x + \frac{u_z}{\bar{\gamma}} DU\right)\right) = -ik_y \delta p$$

or

$$\bar{\gamma}\rho u_y + \frac{k_x B^2}{\mu\bar{\gamma}}\left(k_x u_y - k_y u_x - \frac{k_y u_z}{\bar{\gamma}} DU\right) = -ik_y \delta p/$$

Let $\zeta = k_x u_y - k_y u_x$. Substituting,

$$\bar{\gamma}\rho u_y + \frac{k_x B^2}{\mu\bar{\gamma}}\left(\zeta - \frac{k_y u_z}{\bar{\gamma}} DU\right) = -ik_y \delta p. \tag{4.17}$$

Doing the same as above for Eq. (4.10) and using Eq. (4.7),

$$\bar{\gamma}\rho u_z - \frac{B}{\mu}\left(ik_x\frac{ik_xB}{\bar{\gamma}}u_z - D\left(\frac{ik_xB}{\bar{\gamma}}\left(u_x + \frac{u_z}{\bar{\gamma}}DU\right)\right)\right) = -D\delta p - \frac{-u_zD\rho}{\bar{\gamma}}g$$

or

$$\bar{\gamma}\rho u_z + \frac{k_xB^2}{\mu}\left(\frac{k_x}{\bar{\gamma}}u_z + D\left(\frac{i}{\bar{\gamma}}\left(u_x + \frac{u_z}{\bar{\gamma}}DU\right)\right)\right) = -D\delta p + \frac{u_zD\rho}{\bar{\gamma}}g. \tag{4.18}$$

Now multiplying Eq. (4.8) by $-ik_y$ and Eq. (4.17) by ik_x,

$$-ik_y\bar{\gamma}\rho u_x - ik_y\rho u_zDU = -k_xk_y\delta p$$

$$ik_x\bar{\gamma}\rho u_y + i\frac{k_x^2B^2}{\mu\bar{\gamma}}\left(\zeta - \frac{k_yu_z}{\bar{\gamma}}DU\right) = k_xk_y\delta p.$$

Adding the two together,

$$-ik_y\bar{\gamma}\rho u_x - ik_y\rho u_zDU + ik_x\bar{\gamma}\rho u_y + i\frac{k_x^2B^2}{\mu\bar{\gamma}}\left(\zeta - \frac{k_yu_z}{\bar{\gamma}}DU\right) = 0.$$

Rearranging,

$$\left(1 + \frac{k_x^2B^2}{\rho\mu\bar{\gamma}^2}\right)\left(\zeta - \frac{k_yu_z}{\bar{\gamma}}DU\right) = 0.$$

Which implies that,

$$\zeta = \frac{k_yu_z}{\bar{\gamma}}DU. \tag{4.19}$$

Substituting into the Eq. (4.17) gives,

$$\bar{\gamma}\rho u_y = -ik_y\delta p. \tag{4.20}$$

Multiplying Eq. (4.8) by $-k_x$ and Eq. (4.20) by $-k_y$ then adding together gives,

$$-k_x\bar{\gamma}\rho u_x - k_x\rho u_zDU - k_y\bar{\gamma}\rho u_y = ik_x^2\delta P + ik_y^2\delta p$$

$$-\bar{\gamma}\rho(k_x u_x + k_y u_y) - k_x \rho u_z DU = iK^2 \delta p$$

$$-i\bar{\gamma}\rho D u_z - k_x \rho u_z DU = iK^2 \delta p. \tag{4.21}$$

Now multiplying Eq. (4.18) by iK^2 and solving for $D\delta p$,

$$-iK^2 \left(\bar{\gamma}\rho u_z + \frac{k_x B^2}{\mu} \left(\frac{k_x}{\bar{\gamma}} u_z + D \left(\frac{i}{\bar{\gamma}} \left(u_x + \frac{u_z}{\bar{\gamma}} DU \right) \right) \right) - \frac{u_z D\rho}{\bar{\gamma}} g \right) = iK^2 D\delta p. \tag{4.22}$$

To eliminate u_x add and subtract $ik_y^2 u_x$ and multiply all terms by k_x in the incompressible condition, $\nabla \cdot \delta \mathbf{U} = 0$, giving,

$$iK^2 u_x = -\left(k_x D u_z + ik_y \zeta\right) = -\left(k_x D u_z + \frac{ik_y^2 u_z}{\bar{\gamma}} DU \right). \tag{4.23}$$

Substituting Eq. (4.23) into Eq. (4.22), and simplifying

$$-iK^2 \bar{\gamma}\rho u_z + \frac{k_x^2 B^2}{\mu} \left(\frac{-iK^2}{\bar{\gamma}} u_z + D \left(\frac{iDu_z}{\bar{\gamma}} + \frac{k_x u_z}{\bar{\gamma}^2} DU \right) \right) + \frac{iK^2 u_z D\rho}{\bar{\gamma}} g = iK^2 D\delta p. \tag{4.24}$$

To eliminate δp, take the D of Eq. (4.21) and substitute into Eq. (4.24)

$$\begin{aligned} D\left(-i\bar{\gamma}\rho D u_z - k_x \rho u_z DU\right) = \\ - iK^2 \bar{\gamma}\rho u_z + \frac{k_x^2 B^2}{\mu} \left(\frac{-iK^2}{\bar{\gamma}} u_z + D \left(\frac{iDu_z}{\bar{\gamma}} + \frac{k_x u_z}{\bar{\gamma}^2} DU \right) \right) + \frac{iK^2 u_z D\rho}{\bar{\gamma}} g. \end{aligned} \tag{4.25}$$

And, thus, the equation is in terms of only one perturbed quantity, u_z. Until now, the analysis has been performed assuming the fluid density, ρ and the flow velocity, U to be arbitrary. Let ρ_1, ρ_2, U_1, and U_2, be the fluid density and flow velocity of the top and bottom fluid, respectively, and that $\rho_2 > \rho_1$. In each fluid, this leads to Eqs. (4.19) and (4.25) becoming

$$\zeta = 0 \tag{4.26}$$

$$-i\bar{\gamma}\rho D^2 u_z = -iK^2\bar{\gamma}\rho u_z + \frac{ik_x^2 B^2}{\mu}\left(\frac{-K^2}{\bar{\gamma}}u_z + \frac{D^2 u_z}{\bar{\gamma}}\right)$$

$$\left(\bar{\gamma}\rho + \frac{k_x^2 B^2}{\mu\bar{\gamma}}\right)\left(D^2 - K^2\right)u_z = 0. \tag{4.27}$$

The continuity equation of the perturbed interface must be satisfied,

$$\partial_t \eta + U_x \partial_x \eta\Big|_{z=\eta} = U_z\Big|_{z=\eta}. \tag{4.28}$$

Linearizing gives,

$$\bar{\gamma}_1 \delta\eta = u_{z_1}\Big|_{z=0} \quad \text{or} \quad \bar{\gamma}_2 \delta\eta = u_{z_2}\Big|_{z=0}.$$

Solving for $\delta\eta$ and equating the two gives,

$$\frac{u_{z_1}\Big|_{z=0}}{\bar{\gamma}_1} = \frac{u_{z_2}\Big|_{z=0}}{\bar{\gamma}_2} \tag{4.29}$$

which gives us the condition for the continuity of u_z. With this in mind the solutions of Eq. (4.27) are

$$u_{z_1} = A\bar{\gamma}_1 e^{-Kz} \quad \text{for} \quad z > 0 \tag{4.30}$$

$$u_{z_2} = A\bar{\gamma}_2 e^{Kz} \quad \text{for} \quad z < 0. \tag{4.31}$$

To finally get the dispersion relation, integrate Eq. (4.25) across the interface at $z = 0$ from $z = -\epsilon$ to $z = \epsilon$, and taking the limit as $\epsilon \to 0$, and using the relations above,

$$\Delta_0\left(-\bar{\gamma}\rho D u_z\right) = \frac{k_x^2 B^2}{\mu}\Delta_0\left(\frac{D u_z}{\bar{\gamma}}\right) + \frac{gK^2 u_z}{\bar{\gamma}}\Delta_0(\rho) \tag{4.32}$$

where $\Delta_0(A) = A_1 - A_2$. Simplifying,

$$\left(\bar{\gamma}_1^2\rho_1 KA + \bar{\gamma}_2^2\rho_2 KA\right) = \frac{k_x^2 B^2}{\mu}(-KA - KA) + gK^2(A\rho_1 - A\rho_2)$$

$$\bar{\gamma}_1^2\rho_1 + \bar{\gamma}_2^2\rho_2 = \frac{-2k_x^2B^2}{\mu} + gK(\rho_1 - \rho_2). \tag{4.33}$$

Expanding out the $\bar{\gamma}$ terms and dividing by $(\rho_1 + \rho_2)$,

$$(\gamma + ik_xU_1)^2\alpha_1 + (\gamma + ik_xU_2)^2\alpha_2 = \frac{-2k_x^2B^2}{\mu(\rho_1+\rho_2)} + gKA$$

$$\gamma^2 + 2ik_x(U_1\alpha_1 + U_2\alpha_2)\gamma - k_x^2(U_1^2\alpha_1 + U_2^2\alpha_2) + \frac{2k_x^2B^2}{\mu(\rho_1+\rho_2)} - gKA = 0$$

$$\gamma = -ik_x(U_1\alpha_1 + U_2\alpha_2) \pm \sqrt{(ik_x(U_1\alpha_1 + U_2\alpha_2))^2 - \left(-k_x^2(U_1^2\alpha_1 + U_2^2\alpha_2) + \frac{2k_x^2B^2}{\mu(\rho_1+\rho_2)} - gKA\right)}$$

$$\gamma = -ik_x(U_1\alpha_1 + U_2\alpha_2) \pm \sqrt{k_x^2\alpha_1\alpha_2(U_1 - U_2)^2 + gKA - \frac{2k_x^2B^2}{\mu(\rho_1+\rho_2)}}. \tag{4.34}$$

The expression above is the dispersion relation.

4.2.3 Compressible Kelvin Helmholtz Instability

Now I will derive the compressible KHI. The setup will be the same as in the incompressible case, except there will be no background magnetic field, no gravity, and we will work in only two dimensions, since there are no effects in the third dimension in this configuration. The governing equations are,

$$\frac{\partial\rho}{\partial t} + \nabla\cdot(\rho\mathbf{U}) = 0 \tag{4.35}$$

$$\rho\left(\frac{\partial\mathbf{U}}{\partial t} + \mathbf{U}\cdot\nabla\right)\mathbf{U} = -\nabla p \tag{4.36}$$

$$p = c_0^2\rho \tag{4.37}$$

where c_0 is the speed of sound inside the fluid. Perturbing the equation as done previously, and linearizing the equations gives,

$$\frac{\partial \delta\rho}{\partial t} + \mathbf{U}_0 \cdot \nabla\delta\rho + \rho_0 \left(\nabla \cdot \delta\mathbf{U}\right) = 0 \tag{4.38}$$

$$\rho_0 \left(\frac{\partial}{\partial t} + \mathbf{U}_0 \cdot \nabla\right) \delta\mathbf{U} = -\nabla\delta p \tag{4.39}$$

$$\delta p = c_0^2 \delta\rho. \tag{4.40}$$

Using the same ansatz as before for the form of the perturbations, (without the k_y component) taking the derivatives, and rearranging terms leads to,

$$\nabla \cdot \delta\mathbf{U} = -\frac{\delta\rho}{\rho_0}\bar{\gamma} \tag{4.41}$$

$$\rho_0 \bar{\gamma} \delta\mathbf{U} = -\nabla\delta p. \tag{4.42}$$

Taking the divergence of the above equation yields,

$$\rho_0 \gamma \nabla \cdot \mathbf{U} = -\nabla^2 \delta p. \tag{4.43}$$

Substituting for the divergence on the left, and our expression for the pressure

$$\bar{\gamma}^2 \delta\rho = c_0^2 \nabla^2 \delta\rho. \tag{4.44}$$

Which is then,

$$\bar{\gamma}^2 \delta\rho = c_0^2 \left(D^2 - k_x^2\right) \delta\rho. \tag{4.45}$$

Solving for the derivative,

$$D^2 \delta\rho = \left(k_x^2 + \frac{\bar{\gamma}^2}{c_0^2}\right) \delta\rho. \tag{4.46}$$

The solution to this equation is,

$$\delta\rho = Ae^{h^+ z} + Be^{h^- z}$$

where,

$$h^{\pm} = \pm\sqrt{k_x^2 + \frac{\bar{\gamma}^2}{c_0^2}}. \tag{4.47}$$

Requiring that the densities must vanish at infinity gives,

$$\delta\rho_1 = A_1 e^{h^- z} \tag{4.48}$$

$$\delta\rho_2 = A_2 e^{h^+ z} \tag{4.49}$$

where the subscripts indicate the top (1) or bottom (2) fluid. For the pressure equation substituting the expression for the density gives,

$$\delta p_1 = A_1 c_1^2 e^{h^- z} \tag{4.50}$$

$$\delta p_2 = A_2 c_2^2 e^{h^+ z}. \tag{4.51}$$

The z-component of the momentum equation is, solving for the perturbed velocity,

$$u_z = \frac{-D\delta p}{\rho\bar{\gamma}} \tag{4.52}$$

or

$$u_{z_1} = \frac{-h^- A_1 c_1^2 e^{h^- z}}{\rho_1 \bar{\gamma}_1} \tag{4.53}$$

$$u_{z_2} = \frac{-h^+ A_2 c_2^2 e^{h^+ z}}{\rho_2 \bar{\gamma}_2}. \tag{4.54}$$

With this in hand, we now look at the jump conditions and the interface equation. We require the following to be satisfied,

$$[[U_z - U_x \partial_x \eta]]\Big|_{z=\eta} = 0 \tag{4.55}$$

$$[[P]] = 0 \tag{4.56}$$

$$\partial_t \eta + U_x \partial_x \eta\Big|_{z=\eta} = U_z\Big|_{z=\eta}. \tag{4.57}$$

Linearizing the jump conditions yields,

$$[[u_z - ik_x U \delta\eta]]\Big|_{z=0} = 0$$

$$u_{z1}\Big|_{z=0} - ik_x U_1 \delta\eta = u_{z2}\Big|_{z=0} - ik_x U_2 \delta\eta$$

$$(u_{z_1} - u_{z_2})\Big|_{z=0} = (U_1 - U_2) ik_x \delta\eta \tag{4.58}$$

$$[[\delta p]]\Big|_{z=0} = 0 \implies \delta p_1\Big|_{z=0} = \delta p_2\Big|_{z=0} \implies A_1 c_1^2 = A_2 c_2^2$$

$$A_1 = \frac{c_2^2}{c_1^2} A_2 \tag{4.59}$$

$$\bar{\gamma}_1 \delta\eta = u_{z_1}\Big|_{z=0} \text{ or } \bar{\gamma}_2 \delta\eta = u_{z_2}\Big|_{z=0}.$$

Adding the two gives,

$$\left(u_{z_1} + u_{z_2}\right)\Big|_{z=0} = (\bar{\gamma}_1 + \bar{\gamma}_2)\delta\eta$$

or

$$\delta\eta = \frac{\left(u_{z_1} + u_{z_2}\right)\Big|_{z=0}}{\bar{\gamma}_1 + \bar{\gamma}_2}. \tag{4.60}$$

Substituting the expression for $\delta\eta$ into the previous equation and evaluating at $z = 0$ gives,

$$\frac{-h^{-}A_1c_1^2}{\rho_1\bar{\gamma}_1} - \frac{-h^{+}A_2c_2^2}{\rho_2\bar{\gamma}_2} = \frac{(U_1 - U_2)ik_x}{\bar{\gamma}_1 + \bar{\gamma}_2}\left(\frac{-h^{-}A_1c_1^2}{\rho_1\bar{\gamma}_1} + \frac{-h^{+}A_2c_2^2}{\rho_2\bar{\gamma}_2}\right). \tag{4.61}$$

Simplifying

$$\frac{h^{-}}{\rho_1\bar{\gamma}_1} - \frac{h^{+}}{\rho_2\bar{\gamma}_2} = \frac{(U_1 - U_2)ik_x}{\bar{\gamma}_1 + \bar{\gamma}_2}\left(\frac{h^{-}}{\rho_1\bar{\gamma}_1} + \frac{h^{+}}{\rho_2\bar{\gamma}_2}\right).$$

Substituting the expression for ρ,

$$\frac{h^{-}c_1^2}{P\bar{\gamma}_1} - \frac{h^{+}c_2^2}{P\bar{\gamma}_2} = \frac{(U_1 - U_2)ik_x}{\bar{\gamma}_1 + \bar{\gamma}_2}\left(\frac{h^{-}c_1^2}{P\bar{\gamma}_1} + \frac{h^{+}c_2^2}{P\bar{\gamma}_2}\right).$$

Simplifying and solving for $h^{\pm}$

$$\frac{h^{-}c_1^2}{\bar{\gamma}_1}\left(1 - \frac{(U_1 - U_2)ik_x}{\bar{\gamma}_1 + \bar{\gamma}_2}\right) = \frac{h^{+}c_2^2}{\bar{\gamma}_2}\left(1 + \frac{(U_1 - U_2)ik_x}{\bar{\gamma}_1 + \bar{\gamma}_2}\right)$$

$$\frac{h^{-}c_1^2}{\bar{\gamma}_1}\left(\frac{\bar{\gamma}_1 + \bar{\gamma}_2 - (U_1 - U_2)ik_x}{\bar{\gamma}_1 + \bar{\gamma}_2}\right) = \frac{h^{+}c_2^2}{\bar{\gamma}_2}\left(\frac{\bar{\gamma}_1 + \bar{\gamma}_2 + (U_1 - U_2)ik_x}{\bar{\gamma}_1 + \bar{\gamma}_2}\right)$$

$$\frac{h^{-}c_1^2}{\bar{\gamma}_1}\left(\frac{2\bar{\gamma}_2}{\bar{\gamma}_1 + \bar{\gamma}_2}\right) = \frac{h^{+}c_2^2}{\bar{\gamma}_2}\left(\frac{2\bar{\gamma}_1}{\bar{\gamma}_1 + \bar{\gamma}_2}\right)$$

$$h^{-}c_1^2\left(\frac{\bar{\gamma}_2}{\bar{\gamma}_1}\right) = h^{+}c_2^2\left(\frac{\bar{\gamma}_1}{\bar{\gamma}_2}\right). \tag{4.62}$$

Squaring both sides and substituting for $h^{\pm}$ gives,

$$\left(k_x^2 + \frac{\bar{\gamma}_1^2}{c_1^2}\right)\left(\frac{\bar{\gamma}_2}{\bar{\gamma}_1}\right)^2 c_1^4 = \left(k_x^2 + \frac{\bar{\gamma}_2^2}{c_2^2}\right)\left(\frac{\bar{\gamma}_1}{\bar{\gamma}_2}\right)^2 c_2^4. \tag{4.63}$$

Simplifying further gives,

$$\left(k_x^2c_1^2 + \bar{\gamma}_1^2\right)\bar{\gamma}_2^4c_1^2 = \left(k_x^2c_2^2 + \bar{\gamma}_2^2\right)\bar{\gamma}_1^4c_2^2 \tag{4.64}$$

which is the dispersion relation. This equation has an analytic solution, but it is so lengthy and complicated that it is difficult to gain any insight from it. However, setting the fluid densities to be equal allows for an analytic solution of the growth-rate which is straightforward to interpret. With this simplification, solving for the growth-rate gives,

$$\frac{\gamma}{kc_s} = -i\left(M_1 + M_c \pm \sqrt{1 + M_c^2 \pm \sqrt{1 + 4M_c^2}}\right). \tag{4.65}$$

The instability is then stabilized when the radical is zero, which occurs when $M_c = \sqrt{2}$.

It should be pointed out that these solutions to Eq. (4.62) are only valid on a specific domain. Equation (4.65) satisfies Eq. (4.62) when $|M_c| < \sqrt{2}$, but not when $|M_c| \geq \sqrt{2}$. The reason this occurs is twofold. The first issue is that Eq. (4.65) is a solution of the square of Eq. (4.62), and as such, a solution of that equation is not guaranteed to solve the original unsquared equation. The second reason is more physical, when $|M_c| \geq \sqrt{2}$ the perturbations no longer satisfy the boundary condition of vanishing at infinity. This can be seen in Fig. 4.3, where $h^{\pm}$ goes to 0 at $|M_c| = \sqrt{2}$. With the real component going to 0, the perturbations cannot vanish at infinity.

4.3 Rayleigh-Taylor

4.3.1 Introduction

The RTI is an instability driven by gravity. The classical set-up for this instability is a dense fluid being supported by a lighter fluid in the presence of a gravitational force. In this configuration the system has an increased amount of potential energy as compared to the case where the two fluids swap locations. Since the system would prefer to be in a lower energy state the fluids will move to attain this state. By doing so, the potential energy from the top fluid will be converted to kinetic energy which then causes the instability.

Another way to interpret this instability is to look at it in term of baroclinicity, which is a measure of how misaligned the pressure and density gradients are. Taking the curl of the momentum equation gives,

$$\frac{d\omega}{dt} = \frac{1}{\rho^2}\nabla p \times \nabla \rho \tag{4.66}$$

where ω is the fluid vorticity. Due to the fluid configuration the pressure and density gradients are not aligned causing an increase in vorticity. This leads to a positive feedback loop as the increased vorticity will increase the misalignment of the two gradients which then increases the vorticity even more.

Do note that this is not the only way this instability can occur, and other considerations can be made to study their impact on the system. Some examples of these would be fluid compressibility, the presence of a magnetic field, or fluid viscosity. To give the reader some background on this instability I will derive the linear growth-rate of the compressible RTI. The incompressible case is found by performing the same analysis as was done for the KHI, only setting the equilibrium fluid velocities to zero instead.

4.3.2 Compressible Rayleigh-Taylor Instability

As with the KHI we will be studying the stability of the RTI using ideal MHD. The set up will be as before with two fluids superimposed on each other with the interface located on the xy-plane. The top fluid will be fluid 1 and the bottom fluid will be fluid 2. Assuming an inviscid, isothermal, ideal gas with no dissipation, the governing equations are

$$\frac{\partial \rho}{\partial t} + \nabla \cdot (\rho \mathbf{U}) = 0 \tag{4.67}$$

$$\rho\left(\frac{\partial}{\partial t} + \mathbf{U} \cdot \nabla\right)\mathbf{U} = -\nabla p - \rho \mathbf{g} \tag{4.68}$$

$$P = \rho c_0^2. \tag{4.69}$$

The equilibrium quantities here are,

$$\mathbf{U}_0 = 0 \tag{4.70}$$

$$\frac{dp_0}{dz} = -\rho_0 g \tag{4.71}$$

$$p_0 = \rho_0 c_0^2. \tag{4.72}$$

Using the above equations to solve for ρ_0 gives,

$$\frac{d(\rho_0 c_0^2)}{dz} = -\rho_0 g \implies \rho_0 = \hat{\rho}_0 e^{-\frac{gz}{c_0^2}} = \hat{\rho}_0 e^{-\frac{z}{L_0}}$$

where $L_i = c_i^2/g$ is the stratification length and $\hat{\rho}_0$ is the density at the interface. Thus in the two fluids we have,

$$\rho_{0_1} = \rho_1 = \hat{\rho}_1 e^{-\frac{z}{L_1}}, \quad z > 0 \tag{4.73}$$

$$\rho_{0_2} = \rho_2 = \hat{\rho}_2 e^{-\frac{z}{L_2}}, \quad z < 0 \tag{4.74}$$

$$p_{0_1} = P_1 = \hat{\rho}_1 c_1^2 e^{-\frac{z}{L_1}}, \quad z > 0 \tag{4.75}$$

$$p_{0_2} = P_2 = \hat{\rho}_2 c_2^2 e^{-\frac{z}{L_2}}, \quad z < 0. \tag{4.76}$$

This also implies,

$$\hat{\rho}_1 c_1^2 = \hat{\rho}_2 c_2^2.$$

The next step in the derivation is to perturb the equilibrium and linearize the equations. Perturbing the system leads to redefining the variables as such,

$$\mathbf{U} = \mathbf{U}_0 + \delta\mathbf{U} = u_x\hat{e}_x + u_y\hat{e}_y + u_z\hat{e}_z$$

$$\rho = \rho_0 + \delta\rho$$

$$p = p_0 + \delta p$$

where the terms with deltas or lower case (as is the case for the components of the velocity) are the leading order perturbation terms and those with a 0 subscript are the equilibrium quantities.

Assuming the perturbation are normal modes and have the form,

$$\delta F(x,z,t) = \tilde{F}(z)e^{ik_x x+\gamma t}$$

the linearized equations are,

$$\gamma\delta\rho + \delta\mathbf{U}\cdot\nabla\rho_0 + \rho_0\nabla\cdot\delta\mathbf{U} = 0 \tag{4.77}$$

$$\rho_0\gamma\delta\mathbf{U} = -\nabla\delta p - \delta\rho g\hat{e}_z \tag{4.78}$$

$$\delta p = \delta\rho c_0^2. \tag{4.79}$$

The next step is to manipulate the system of equations until we have a differential equation of a single unknown. In this case we will solve for the density. Substituting the expressions for the equilibrium density into Eq. (4.77) gives,

$$\gamma\delta\rho - u_z\frac{\hat{\rho}_0 e^{-\frac{z}{L_0}}}{L_0} + \hat{\rho}_0 e^{-\frac{z}{L_0}}\nabla\cdot\delta\mathbf{U} = 0.$$

Let us now define the following,

$$\delta n = \frac{\delta\rho}{\hat{\rho}_0 e^{-\frac{z}{L_0}}}. \tag{4.80}$$

Dividing the equation by $\hat{\rho}_0 e^{-\frac{z}{L_0}}$ then gives,

$$\gamma\delta n - \frac{u_z}{L_0} + \nabla\cdot\delta\mathbf{U} = 0. \tag{4.81}$$

We can do the same for Eq. (4.78),

$$\gamma\delta\mathbf{U} = \frac{-\nabla\delta p}{\hat{\rho}_0 e^{-\frac{z}{L_0}}} - \delta n g\hat{e}_z = -\frac{c_0^2\nabla\delta\rho}{\hat{\rho}_0 e^{-\frac{z}{L_0}}} - \delta n g\hat{e}_z.$$

Now, note that,

$$\nabla \delta n = \nabla \left(\frac{\delta \rho}{\hat{\rho}_0 e^{-\frac{z}{L_0}}} \right) = \frac{\nabla \delta \rho}{\hat{\rho}_0 e^{-\frac{z}{L_0}}} + \delta \rho \nabla \frac{e^{\frac{z}{L_0}}}{\hat{\rho}_0}.$$

And thus,

$$\frac{\nabla \delta \rho}{\hat{\rho}_0 e^{-\frac{z}{L_0}}} = \nabla \delta n - \delta \rho \nabla \frac{e^{\frac{z}{L_0}}}{\hat{\rho}_0}.$$

Substituting the above gives,

$$\gamma \delta \mathbf{U} = -c_0^2 \left(\nabla \delta n - \delta \rho \nabla \frac{e^{\frac{z}{L_0}}}{\hat{\rho}_0} \right) - \delta n g \hat{e}_z.$$

Expanding and taking the gradient of the exponential gives,

$$\gamma \delta \mathbf{U} = -c_0^2 \nabla \delta n + \frac{\delta \rho}{\hat{\rho}_0 e^{-\frac{z}{L_0}}} \frac{c_0^2}{L_0} \hat{e}_z - \delta n g \hat{e}_z.$$

Note that the two terms on the right cancel, thus giving,

$$\gamma \delta \mathbf{U} = -c_0^2 \nabla \delta n. \tag{4.82}$$

Taking the divergence of Eq. (4.82) gives,

$$\nabla \cdot \delta \mathbf{U} = -\frac{c_0^2}{\gamma} \nabla^2 \delta n. \tag{4.83}$$

The z-component of Eq. (4.82) gives,

$$u_z = \frac{c_0^2}{\gamma} \frac{\partial}{\partial z} \delta n. \tag{4.84}$$

Substituting both of these into Eq. (4.81) and simplifying yields,

$$\gamma^2 \delta n + g \frac{\partial}{\partial z} \delta n - c_0^2 \nabla^2 \delta n = 0.$$

Taking the Laplacian and rearranging gives us the differential equation of the normalized density,

$$\frac{\partial^2}{\partial z^2} \delta n - \frac{1}{L_0} \frac{\partial}{\partial z} \delta n - \frac{\gamma^2 + c_0^2 k^2}{c_0^2} \delta n = 0. \tag{4.85}$$

Requiring that the perturbations vanish at infinity leads to the following solutions for each fluid,

$$\delta n_1 = \delta \hat{n}_1 e^{\alpha_1^- z}, \quad z > 0 \tag{4.86}$$

$$\delta n_2 = \delta \hat{n}_2 e^{\alpha_2^+ z}, \quad z < 0 \tag{4.87}$$

where,

$$\alpha_i^{\pm} = \frac{1}{2L_i} \left(1 \pm \sqrt{1 + 4L_i k(\hat{\gamma}^2 + kL_i)} \right) \tag{4.88}$$

and

$$\hat{\gamma}^2 = \frac{\gamma^2}{kg}. \tag{4.89}$$

Now that we have an expression for the normalized density, the next step is to apply the jump conditions at the interface and then form an equation that consists solely of constants and the growth-rate. The interface equations are,

$$\gamma \delta \eta = u_z \big|_{z=0} \tag{4.90}$$

$$u_{z_1} \big|_{z=0} = u_{z_2} \big|_{z=0} \tag{4.91}$$

$$(\delta p_1 + D p_1 \delta \eta) \big|_{z=0} = (\delta p_2 + D p_2 \delta \eta) \big|_{z=0} \tag{4.92}$$

where $\delta\eta$ is the location of the perturbed interface in z, and D is a partial derivative in z. Using Eq. (4.84) to eliminate u_z and Eqs. (4.71), (4.79), and (4.80) to eliminate the pressures, some straightforward algebra leads to the following dispersion relation,

$$\alpha_1^- L_1 - \alpha_2^+ L_2 = \left(\frac{\rho_1 - \rho_2}{\rho_1}\right) \frac{(\alpha_1^- - L_1)(\alpha_2^+ L_2)}{\hat{n}^2 k L_1}. \tag{4.93}$$

4.4 Combined Compressible System

With both the KHI and RTI derivations done, we can now work on the most complicated case so far, the compressible KHRTI with a magnetic field. In this section, we derive an analytic dispersion relation for the growth rate of the compressible Kelvin–Helmholtz instability (KHI) in the presence of gravity, under the assumption of a continuous density profile at the interface. On this basis, we analyze the asymptotic behavior of the growth rate in the limit of large velocity differences, as well as the spatial structure of the associated eigenfunctions. The analysis is then extended to the compressible KHRTI, where we present the asymptotic expansion of the growth rate with respect to the velocity difference and characterize the dependence of its peak value on the same parameter. Finally, we investigate the effect of a uniform flow-aligned magnetic field, identifying the approximate field strength required for stabilization and comparing the result with the incompressible case.

The rest of the chapter is organized as follows. In Sec. 4.4.1, we define the system and the geometry of the problem. In Sec. 4.4.2, we introduce the governing equations and perform the linear stability analysis, obtaining dispersion relations for both the case with and without a magnetic field. In Sec. 4.4.3, we discuss the results obtained for both cases studied. Our analytic approximations for various quantities of interest are presented, such as expressions for the growth-rate or for the magnetic field required to stabilize the instability. Lastly, in Sec. 4.4.4, we summarize our results.

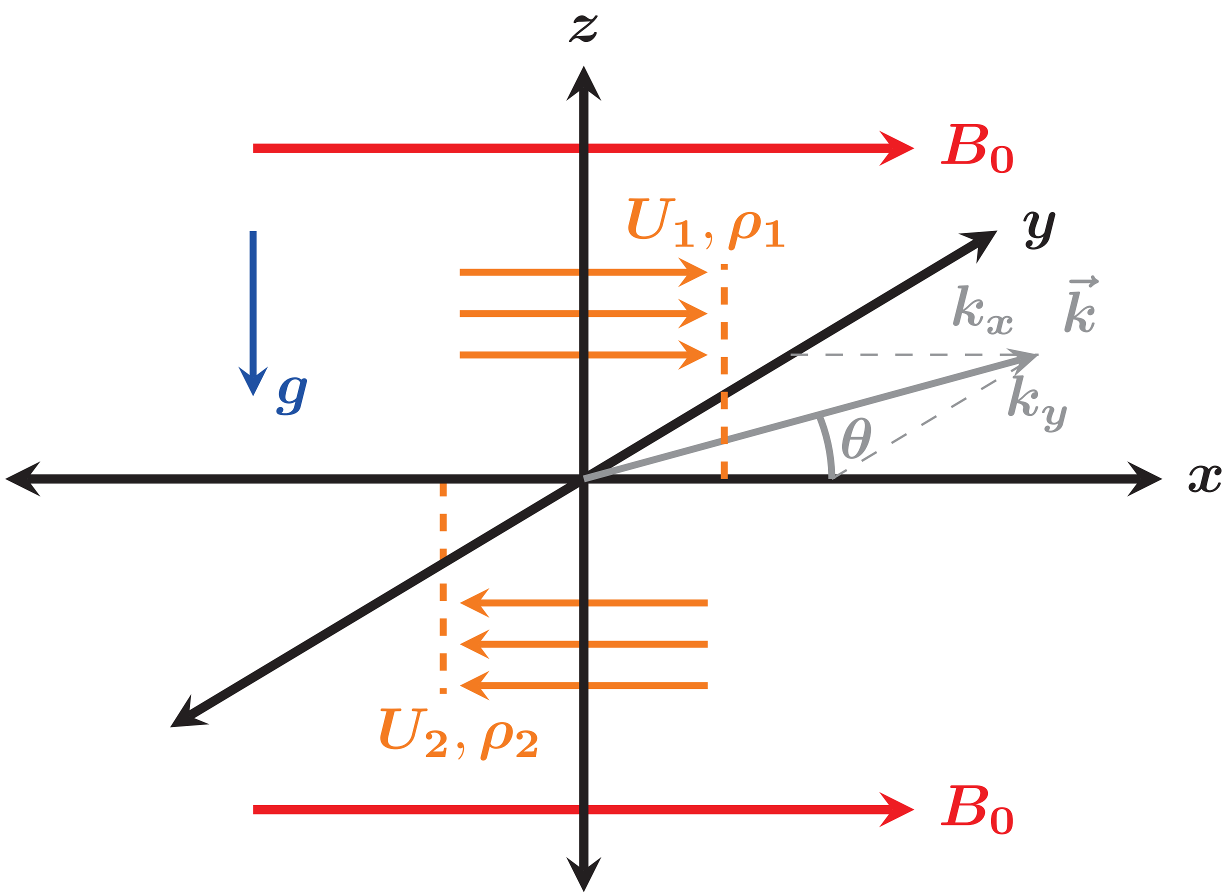

Figure 4.1: 3D representation of the system studied. ρ_i is the fluid density in kg/m^3, U_i is the fluid flow velocity in m/s, B_0 is the equilibrium magnetic field in T, g is the gravitational acceleration in m/s^2, and the axes all are measured in meters. Not pictured is the pressure which is measured in pascals.

4.4.1 Defining the System

We assume the simple slab geometry shown in Fig. 4.1. We use Cartesian coordinates, and the interface of the two fluids is the xy plane at $z = 0$. The letters in the image have the following meanings: ρ is the density of the fluid, U is the fluid's streaming velocity, g is the gravitational acceleration, k is the wave vector and its components, and B_0 is the uniform magnetic field present throughout the plasma. The magnetic field and streaming velocities point in the x direction (i.e. $\mathbf{B} = B_0\hat{e}_x$), while the gravitational force points in the negative z direction (i.e. $\mathbf{g} = -g\hat{e}_z$). The subscripts 1 and 2 differentiate quantities for the top and bottom fluids, respectively. The 0 subscript indicates that the parameter is an equilibrium quantity.

The fluids are assumed to be ideal (i.e., inviscid) and compressible. For simplicity, we use an isothermal closure condition and ignore surface tension for the stability analysis. As a consequence of the isothermal assumption, the equilibrium pressure is governed by the equation

$$p_0 = \rho_0^\Gamma c_0^2 \rightarrow \rho_0 c_0^2$$

where P is the pressure, ρ is the plasma density, Γ is the adiabatic index, and c_0 is the speed of sound in the plasma and the subscript indicates that they are the equilibrium quantities. From Bernoulli's equation we see that the only spacial dependence is in P and ρ and thus have,

$$\frac{dp_0}{\mathrm{dz}} = -\rho_0 g. \tag{4.94}$$

Substituting the previous definition for P and rearranging terms gives,

$$\frac{d\rho_0}{\mathrm{dz}} = -\frac{g}{c_0^2}\rho_0.$$

Integrating over z gives,

$$\rho_0 = \hat{\rho}_0 e^{-\frac{g}{c_0^2}z} = \hat{\rho}_0 e^{-\frac{z}{L_0}}.$$

Where we have defined the following stratification length,

$$L_0 \equiv \frac{c_0^2}{g}.$$

Thus we have the following results,

$$\rho_{0_1} = \hat{\rho}_1 e^{-\frac{g}{c_1^2}z} = \hat{\rho}_1 e^{-\frac{z}{L_1}}, \quad z > 0 \tag{4.95}$$

$$\rho_{0_2} = \hat{\rho}_2 e^{-\frac{g}{c_2^2}z} = \hat{\rho}_1 e^{-\frac{z}{L_2}}, \quad z < 0 \tag{4.96}$$

$$p_{0_1} = \hat{\rho}_1 c_1^2 e^{-\frac{g}{c_1^2}z} = \hat{\rho}_1 c_1^2 e^{-\frac{z}{L_1}}, \quad z > 0 \tag{4.97}$$

$$p_{0_2} = \hat{\rho}_2 c_2^2 e^{-\frac{g}{c_2^2}z} = \hat{\rho}_2 c_2^2 e^{-\frac{z}{L_2}}, \quad z < 0 \tag{4.98}$$

$$\hat{\rho}_1 c_1^2 = \hat{\rho}_2 c_2^2. \tag{4.99}$$

Henceforth, ρ_1 and ρ_2 without the hats will refer to the equilibrium fluid density of the top and bottom fluids respectively, while the version with a hat will refer to the fluid density at the interface. A polytropic relation, $P \propto \rho^{\Gamma}$, with arbitrary Γ is more general, but makes the two fluids finite in z, thus complicating the boundary conditions significantly. Setting $\Gamma = 1$ allows for the two fluids to be infinite in z.

4.4.2 Linear Stability

The governing equations for our system are the compressible ideal MHD equations, plus our closure condition,

$$\frac{\partial \rho}{\partial t} + \nabla \cdot (\rho \mathbf{U}) = 0 \tag{4.100}$$

$$\rho \left(\frac{\partial}{\partial t} + \mathbf{U} \cdot \nabla \right) \mathbf{U} = -\nabla p - \rho \mathbf{g} + \frac{1}{\mu} (\nabla \times \mathbf{B}) \times \mathbf{B} \tag{4.101}$$

$$\frac{\partial \mathbf{B}}{\partial t} = \nabla \times (\mathbf{U} \times \mathbf{B}) \tag{4.102}$$

$$p = \rho c^2. \tag{4.103}$$

Now we will assume the system is in equilibrium and then slightly perturb it from this equilibrium. The variables will now have the following form,

$$\mathbf{U} = \mathbf{U}_0 + \delta\mathbf{U} = U_0\hat{e}_x + \left(u_x\hat{e}_x + u_y\hat{e}_y + u_z\hat{e}_z\right)$$
$$\rho = \rho_0 + \delta\rho$$
$$p = p_0 + \delta p$$
$$\mathbf{B} = \mathbf{B}_0 + \delta\mathbf{B} = B_0\hat{e}_x + \left(b_x\hat{e}_x + b_y\hat{e}_y + b_z\hat{e}_z\right).$$

Where the terms with a 0 subscript represent the equilibrium quantities, and the terms with deltas or lower case (as is the case for the components of the velocity and magnetic field) are the 1st order perturbation terms. Substituting these into our governing equations, dropping zeroth and second order terms, and derivatives of constant quantities leads to the following linearized equations,

$$\left(\frac{\partial}{\partial t} + \mathbf{U}_0 \cdot \nabla\right)\delta\rho + \nabla \cdot (\delta\rho_0\mathbf{U}) = 0 \tag{4.104}$$

$$\rho\left(\frac{\partial}{\partial t} + \mathbf{U}_0 \cdot \nabla\right)\delta\mathbf{U} = -\nabla\delta p - \delta\rho\mathbf{g} + \frac{1}{\mu}(\nabla \times \delta\mathbf{B}) \times \mathbf{B}_0 \tag{4.105}$$

$$\left(\frac{\partial}{\partial t} + \mathbf{U}_0 \cdot \nabla\right)\delta\mathbf{B} = \nabla \times (\delta\mathbf{U} \times \mathbf{B}_0) \tag{4.106}$$

$$\delta p = \delta\rho c_0^2. \tag{4.107}$$

Analyzing the perturbations into normal modes, we take our perturbed quantities to have the general form,

$$\delta F(x,y,z,t) = \tilde{F}(z)e^{i(k_x x + k_y y) + \gamma t}$$

where k_x and k_y are the components of the wave vector $\mathbf{K}$ and γ is the growth-rate of the perturbed quantity. Our end goal is to get a dispersion relation that shows us how γ behaves. Using the new form of the perturbations we can take the derivatives in Eqs. (4.104)-(4.107) and get the following equations. Note that the vector equations are now separated into their component equations and derivative with respect to z will be represented with a 'D'.

$$\overline{\gamma}\delta\rho - \frac{u_z}{L_0}\rho_0 + \rho_0\nabla\cdot\delta\mathbf{U} = 0 \tag{4.108}$$

$$\rho_0\overline{\gamma}u_x = -ik_x\delta p \tag{4.109}$$

$$\rho_0\overline{\gamma}u_y = -ik_y\delta p + \frac{B_0}{\mu}\left(ik_xb_y - ik_yb_x\right) \tag{4.110}$$

$$\rho_0\overline{\gamma}u_z = -D\delta p - \delta\rho g + \frac{B_0}{\mu}\left(ik_xb_z - Db_x\right) \tag{4.111}$$

$$b_x\overline{\gamma} + B_0\nabla\cdot\delta\mathbf{U} = B_0ik_xu_x \tag{4.112}$$

$$b_y\overline{\gamma} = B_0ik_xu_y \tag{4.113}$$

$$b_z\overline{\gamma} = B_0ik_xu_z, \tag{4.114}$$

where $\overline{\gamma} = \gamma + ik_xU_0$. Henceforth the 0 subscript that indicates the equilibrium terms will be dropped.

The next step is to reduce this system of equations into a single differential equation with a single unknown which can then be solved. The unknown of interest is u_z, the perturbed velocity in the z direction. The general process will be to express every perturbed quantity in terms of u_z and $\delta n = \frac{\delta\rho}{\rho}$, the normalized density, and then convert all the δn terms into terms with u_z. First let us divide out the density from Eqs.(4.108)-(4.111) and, in the case of the momentum equations, isolate the perturbed density.

$$\overline{\gamma}\delta n - \frac{u_z}{L} + \nabla\cdot\delta\mathbf{U} = 0 \tag{4.115}$$

$$u_x = -\frac{ik_xc^2}{\overline{\gamma}}\delta n \tag{4.116}$$

$$u_y - \frac{B}{\rho\mu\overline{\gamma}}\left(ik_xb_y - ik_yb_x\right) = -\frac{ik_yc^2}{\overline{\gamma}}\delta n \tag{4.117}$$

$$u_z - \frac{B}{\rho\mu\overline{\gamma}}\left(ik_x b_z - Db_x\right) = -\frac{c^2}{\overline{\gamma}} D\delta n. \tag{4.118}$$

Now solving Faraday's Law for the components of the magnetic field,

$$b_x = -\frac{B}{\overline{\gamma}}\left(ik_y u_y + Du_z\right) \tag{4.119a}$$

$$b_x = \frac{B}{\overline{\gamma}}\left(ik_x u_x - \nabla \cdot \delta\mathbf{U}\right) \tag{4.119b}$$

$$b_y = \frac{Bik_x}{\overline{\gamma}} u_y \tag{4.120}$$

$$b_z = \frac{Bik_x}{\overline{\gamma}} u_z. \tag{4.121}$$

With all of these in hand we can now begin reducing our system of equations. First let us combine Eqs.(4.116)-(4.117) by multiplying the former by ik_x, the latter by ik_y and adding them together to get,

$$\nabla \cdot \delta\mathbf{U} - Du_z + \frac{B}{\mu\rho\overline{\gamma}}\left(b_y k_x k_y - b_x k_y^2\right) = \frac{c^2 K^2}{\overline{\gamma}} \delta n. \tag{4.122}$$

Then using the previous equations we can eliminate all the variables except u_z and δn and solve for δn,

$$\delta n = \frac{\overline{\gamma}\left(u_z\left(\overline{\gamma}^2 + K^2 V^2\right) - L\mathrm{Du}_z\left(\overline{\gamma}^2 + V^2 k_x^2\right)\right)}{L\left(c^2 V^2 K^2 k_x^2 + K^2 \overline{\gamma}^2\left(c^2 + V^2\right) + \overline{\gamma}^4\right)} \tag{4.123}$$

where $K^2 = k_x^2 + k_y^2$, and $V = B^2/\mu\rho$. We can do a similar process for $D\delta n$ in Eq.(4.118) to get,

$$D\delta n = \frac{\overline{\gamma}\left(V^2 \mathrm{Du}_z - Lu_z\left(\overline{\gamma}^2 + V^2 k_x^2\right)\right)}{L\left(c^2 V^2 k_x^2 + \overline{\gamma}^2\left(c^2 + V^2\right)\right)}. \tag{4.124}$$

Then taking the z derivative of Eq. (4.123), taking note that the V terms have a z dependency from the density, and then equating it to the above equation yields a differential equation in u_z,

$$\mathcal{A}\, u_z''(z) + \mathcal{B}\, u_z'(z) + \mathcal{C}\, u_z(z) = 0 \tag{4.125}$$

whose solution is then,

$$u_z(z) = \Phi_1 e^{h^- z} + \Phi_2 e^{h^+ z} \tag{4.126}$$

where,

$$h^{\pm} = \frac{\mathcal{B} \pm \sqrt{\mathcal{B}^2 + 4\mathcal{A}\mathcal{C}}}{2\mathcal{A}} \tag{4.127}$$

$$\mathcal{A} = L_i^2 \left(\overline{\gamma}_i^2 + V_i^2 k_x^2\right)\left(c_i^2 \overline{\gamma}_i^2 + V_i^2 \overline{\gamma}_i^2 + c_i^2 V_i^2 k_x^2\right)\left(c_i^2 K^2 \overline{\gamma}_i^2 + \overline{\gamma}_i^4 + K^2 V_i^2 \overline{\gamma}_i^2 + c_i^2 K^2 V_i^2 k_x^2\right) \tag{4.128a}$$

$$\begin{aligned}\mathcal{B} = L_i \overline{\gamma}_i^2 \big(&2c_i^4 V_i^2 \overline{\gamma}_i^2 k_x^4 + 2c_i^4 V_i^2 \overline{\gamma}_i^2 k_x^2 k_y^2 + c_i^4 \overline{\gamma}_i^4 k_x^2 + c_i^4 \overline{\gamma}_i^4 k_y^2 + c_i^2 \overline{\gamma}_i^6 + c_i^2 V_i^4 \overline{\gamma}_i^2 k_x^4 + 3c_i^2 V_i^4 \overline{\gamma}_i^2 k_x^2 k_y^2 \\ &+ 2c_i^2 V_i^2 \overline{\gamma}_i^4 k_x^2 + 3c_i^2 V_i^2 \overline{\gamma}_i^4 k_y^2 + 2V_i^4 \overline{\gamma}_i^4 k_y^2 + c_i^4 K^2 V_i^4 k_x^4\big)\end{aligned} \tag{4.128b}$$

$$\begin{aligned}\mathcal{C} = c_i^2 K^2 V_i^4 \overline{\gamma}_i^2 k_x^2 &\left(k_y^2 \left(L_i^2 \left(3c_i^2 + 2V_i^2\right) k_x^2 + 2c_i^2\right) + L_i^2 \left(3c_i^2 + 2V_i^2\right) k_x^4\right) \\ &+ L_i^2 \overline{\gamma}_i^8 \left(\left(2c_i^2 + 3V_i^2\right) k_x^2 + 2\left(c_i^2 + V_i^2\right) k_y^2\right) \\ &+ K^2 L_i^2 \overline{\gamma}_i^6 \left(\left(c_i^2 + V_i^2\right)^2 k_y^2 + \left(c_i^4 + 6c_i^2 V_i^2 + 3V_i^4\right) k_x^2\right) \\ &+ K^2 V_i^2 \overline{\gamma}_i^4 \big(\left(c_i^2 + V_i^2\right) k_y^2 \left(L_i^2 \left(3c_i^2 + V_i^2\right) k_x^2 + 2c_i^2\right) \\ &+ L_i^2 \left(3c_i^4 + 6c_i^2 V_i^2 + V_i^4\right) k_x^4\big) + L_i^2 \overline{\gamma}_i^{10} + c_i^4 K^4 L_i^2 V_i^6 k_x^6\end{aligned} \tag{4.128c}$$

with the i subscript indicating the value is from either fluid 1 or 2, and $\Phi_{1,2}$ are constants. The perturbation must go to zero at positive and negative infinity; as such, the solution that is valid in the top fluid is the term with h^-, and for the bottom fluid the term with h^+.

Now that u_z is known, the last steps of the derivation can proceed. At the boundary between the two fluids certain linearized conditions must be satisfied. These are known as the jump conditions or the interface equations. ([160]) The location of the perturbed interface in z is defined as $\delta\eta(\mathbf{x}, t)$. Since there is no mixing occurring between the two fluids, their displacements must match. Another requirement is that the total pressure and magnetic field normal to the interface are continuous across the interface. This then yields the following equations that must be satisfied,

$$\left(u_{z_1} - U_1 \frac{\partial(\delta\eta)}{\partial x}\right)\bigg|_{z=0} = \left(u_{z_2} - U_2 \frac{\partial(\delta\eta)}{\partial x}\right)\bigg|_{z=0} \tag{4.129}$$

$$u_{z_1}\big|_{z=0} = \left(U_1 \frac{\partial(\delta\eta)}{\partial x} + \frac{\partial(\delta\eta)}{\partial t}\right)\bigg|_{z=0} \tag{4.130}$$

$$u_{z_2}\big|_{z=0} = \left(U_2 \frac{\partial(\delta\eta)}{\partial x} + \frac{\partial(\delta\eta)}{\partial t}\right)\bigg|_{z=0} \tag{4.131}$$

$$\left(\delta p_1 + Dp_1 \delta\eta + \frac{Bb_{x_1}}{\mu}\right)\bigg|_{z=0} = \left(\delta p_2 + Dp_2 \delta\eta + \frac{Bb_{x_2}}{\mu}\right)\bigg|_{z=0} \tag{4.132}$$

$$b_{z_1}\big|_{z=0} = b_{z_2}\big|_{z=0}. \tag{4.133}$$

Assuming the same normal mode as before for the perturbed quantity, taking the derivatives and substituting Eq. (4.121) into Eq. (4.133) we have that,

$$\delta\eta\big|_{z=0} = \frac{\left(u_{z_1} + u_{z_2}\right)\big|_{z=0}}{\overline{\gamma}_1 + \overline{\gamma}_2} \tag{4.134}$$

$$u_{z_1}\big|_{z=0} = \frac{\overline{\gamma}_1}{\overline{\gamma}_2} u_{z_2}\big|_{z=0} \tag{4.135}$$

$$\Phi_1 = \frac{\overline{\gamma}_1}{\overline{\gamma}_2}\Phi_2. \tag{4.136}$$

Now we will begin to substitute into the pressure balance equation, Eq. (4.132), and this will yield the dispersion relation. We will use Eq. (4.107) to eliminate the δp terms, Eq. (4.94) to eliminate Dp, Eq. (4.119a) to eliminate b_x, and Eq. (4.134) to eliminate $\delta\eta$. Henceforth, the evaluated at $z = 0$ will be dropped, but addressed later. After substituting, we have,

$$c_1^2 \delta\rho_1 - \delta\eta g \rho_1 - \frac{B^2\left(Du_{z_1} + ik_y u_{y_1}\right)}{\mu\overline{\gamma}_1} = c_2^2 \delta\rho_2 - \delta\eta g \rho_2 - \frac{B^2\left(Du_{z_2} + ik_y u_{y_2}\right)}{\mu\overline{\gamma}_2}.$$

Next, we change the $\delta\rho$ terms into δn, and use Eqs. (4.116)-(4.117) to eliminate u_x and u_y, giving,

$$c_1^2\delta n_1\rho_1 + \delta\eta g\rho_2 + \frac{B^2}{\mu\overline{\gamma}_2}\left(\frac{k_y^2\left(c_2^2\delta n_2\overline{\gamma}_2 - V_2^2 Du_{z_2}\right)}{\overline{\gamma}_2^2 + K^2V_2^2} + Du_{z_2}\right) =$$
$$c_2^2\delta n_2\rho_2 + \delta\eta g\rho_1 + \frac{B^2}{\mu\overline{\gamma}_2}\left(\frac{k_y^2\left(c_1^2\delta n_1\overline{\gamma}_1 - V_1^2 Du_{z_1}\right)}{\overline{\gamma}_1^2 + K^2V_1^2} + Du_{z_1}\right).$$

Next we use Eq. (4.134) to replace $\delta\eta$, and Eq. (4.123) to eliminate δn. Using Eq. (4.136) to evaluate at $z = 0$, simplifying and rearranging terms leads to the full dispersion relation,

$$g\left(\frac{\overline{\gamma}_2^2\left(B^2k_y^2 + K^2\mu P\right) + K^2\mu P V_2^2k_x^2}{K^2\overline{\gamma}_2^2\left(c_2^2 + V_2^2\right) + \overline{\gamma}_2^4 + c_2^2K^2V_2^2k_x^2} - \frac{\overline{\gamma}_1^2\left(B^2k_y^2 + K^2\mu P\right) + K^2\mu P V_1^2k_x^2}{K^2\overline{\gamma}_1^2\left(c_1^2 + V_1^2\right) + \overline{\gamma}_1^4 + c_1^2K^2V_1^2k_x^2}\right)$$
$$- \frac{h^-\left(\overline{\gamma}_1^2 + V_1^2k_x^2\right)\left(\overline{\gamma}_1^2\left(B^2 + \mu P\right) + B^2c_1^2k_x^2\right)}{K^2\overline{\gamma}_1^2\left(c_1^2 + V_1^2\right) + \overline{\gamma}_1^4 + c_1^2K^2V_1^2k_x^2}$$
$$+ \frac{h^+\left(\overline{\gamma}_2^2 + V_2^2k_x^2\right)\left(\overline{\gamma}_2^2\left(B^2 + \mu P\right) + B^2c_2^2k_x^2\right)}{K^2\overline{\gamma}_2^2\left(c_2^2 + V_2^2\right) + \overline{\gamma}_2^4 + c_2^2K^2V_2^2k_x^2} = 0. \quad (4.137)$$

In the limit of no magnetic field the dispersion relation is,

$$2\overline{\gamma}_1^2\left(g + \sqrt{4c_2^2\left(\overline{\gamma}_2^2 + c_2^2\left(k_x^2 + k_y^2\right)\right) + g^2}\right) - 2\overline{\gamma}_2^2\left(g - \sqrt{4c_1^2\left(\overline{\gamma}_1^2 + c_1^2\left(k_x^2 + k_y^2\right)\right) + g^2}\right)$$
$$- \left(\frac{1}{c_2^2} - \frac{1}{c_1^2}\right)g\left(g - \sqrt{4c_1^2\left(\overline{\gamma}_1^2 + c_1^2\left(k_x^2 + k_y^2\right)\right) + g^2}\right)$$
$$\times\left(g + \sqrt{4c_2^2\left(\overline{\gamma}_2^2 + c_2^2\left(k_x^2 + k_y^2\right)\right) + g^2}\right) = 0. \quad (4.138)$$

4.4.3 Results and Discussion

Results Without Magnetic Field and $A = 0$

In the specific case of the two fluids being of equal density at the interface Eq. (4.138) has an analytic solution for γ. The normalized growth-rate is as follows,

$$\hat{\gamma} = -\left(M_1 + M_c\right) i + i\sqrt{\left(1 \mp \frac{i}{2\overline{L}}\right) + M_c^2 - \sqrt{\left(1 \mp \frac{i}{2\overline{L}}\right)^2 + 4M_c^2}} \tag{4.139a}$$

$$\hat{\gamma} = -\left(M_1 + M_c\right) i - i\sqrt{\left(1 \pm \frac{i}{2\overline{L}}\right) + M_c^2 - \sqrt{\left(1 \pm \frac{i}{2\overline{L}}\right)^2 + 4M_c^2}} \tag{4.139b}$$

where, $\hat{\gamma} = \frac{\gamma}{kc}$ $\overline{L} = \frac{c^2 k}{g}$, $M_1 = \frac{U_1}{c}\cos(\theta)$, and $M_c = \frac{U_2 - U_1}{2c}\cos(\theta)$. The two sets of equations represent the solution depending on the sign of M_c. When $M_c > 0$ the growth-rate follows Eq. (4.139a), and when $M_c < 0$ it follows Eq. (4.139b). The two sets of plus-minuses or minus-pluses dictate the sign of the real component of γ. In both cases, when the top signs are chosen the real component is positive, and the opposite configuration gives a negative real component. It is important to note that, since the density gradient is aligned with the gravitational acceleration, the system is RT stable. Also note that here and moving forward g will be assumed to be positive, as switching the sign of g effectively switches the sign of M_c. To the authors' knowledge, this analytic result is not found in the literature. Since these modes satisfy the boundary conditions, namely that the perturbations vanish at $z \to \pm\infty$, we conclude these are physical solutions of the dispersion relation.

The key insight from this result is that, due to the presence of gravity, there are now imaginary terms in the radicals, as opposed to the pure compressible KHI. These new terms cause the system to always be unstable, beyond even where the case without gravity would stabilize, $M_c > \sqrt{2}$. For simplicity, we will work in the frame where the fluid velocities are equal and opposite. This removes the terms outside the radical and changes the M_c terms to M. Setting the square root equal to zero and solving for M in Eqs. (4.139a)-(4.139b) gives, $M = 0$ and either $M = \pm\sqrt{2 + i/\overline{L}}$ or $M = \pm\sqrt{2 - i/\overline{L}}$ depending on the flow orientation. The first solution is physically valid, when there is no flow and thus no KHI. The second set of solutions are not physically valid as the Mach number is a real quantity. As such, because of the gravitational term, there is no non-zero value of the Mach number that allows the system to be stable.

We will examine asymptotic behavior in the rest of this section. We found in our calculations that the asymptotic regime occurs for $M_c \gtrapprox 2$ (not necessarily $M_c \gg 1$) as long as $M_c \gg \overline{L}^{-1}$. Different asymptotics are found for $\overline{L}^{-1} \gg M_c$, which will be mentioned later on. In the limit of $M_c \to \infty^+$ Eq. (4.139a) has the following expansion,

$$\hat{\gamma} = \pm\frac{1}{4\overline{L}M_c} - i(1 + M_1) + \mathcal{O}\left(\frac{1}{M_c^2}\right) \tag{4.140}$$

where the plus minus sign accounts for the positive and negative real components from Eq. (4.139a). We see from the expansion that the real component of the growth-rate is inversely proportional to M_c, indicating that the instability persists even with increasing velocity differences.

Another notable aspect of the instability is the behavior of the eigenfunctions. In the region beyond $M_c > \sqrt{2}$ the value of the growth-rate is several orders of magnitude smaller than the peak value, see Fig. 4.2 for an example of this. While the growth-rate is small, the resulting eigenfunctions are very broad and impact large portions of the plasma. As defined earlier, the perturbed z-velocity, u_z, is proportional to e^{zh^-} or e^{zh^+} depending on the fluid chosen. Fig. 4.3 shows the behavior of the real component of the h terms in the exponentials for the case with and without gravity. We see that for $M_c > \sqrt{2}$ the terms with gravity are nonzero and flatten out significantly. This occurs because the real parts of the coefficients in the exponential are small. An example of this is shown in Fig. 4.4 which plots $e^{\overline{z}\overline{h}^-}$ as a function of $\overline{z} = zk$ for different values of $\overline{L}$ at $M_c = 2$.

We remark that we are now considering a system in a region of instability where the growth-rate has decreased by over nine orders of magnitude from its peak. While one may

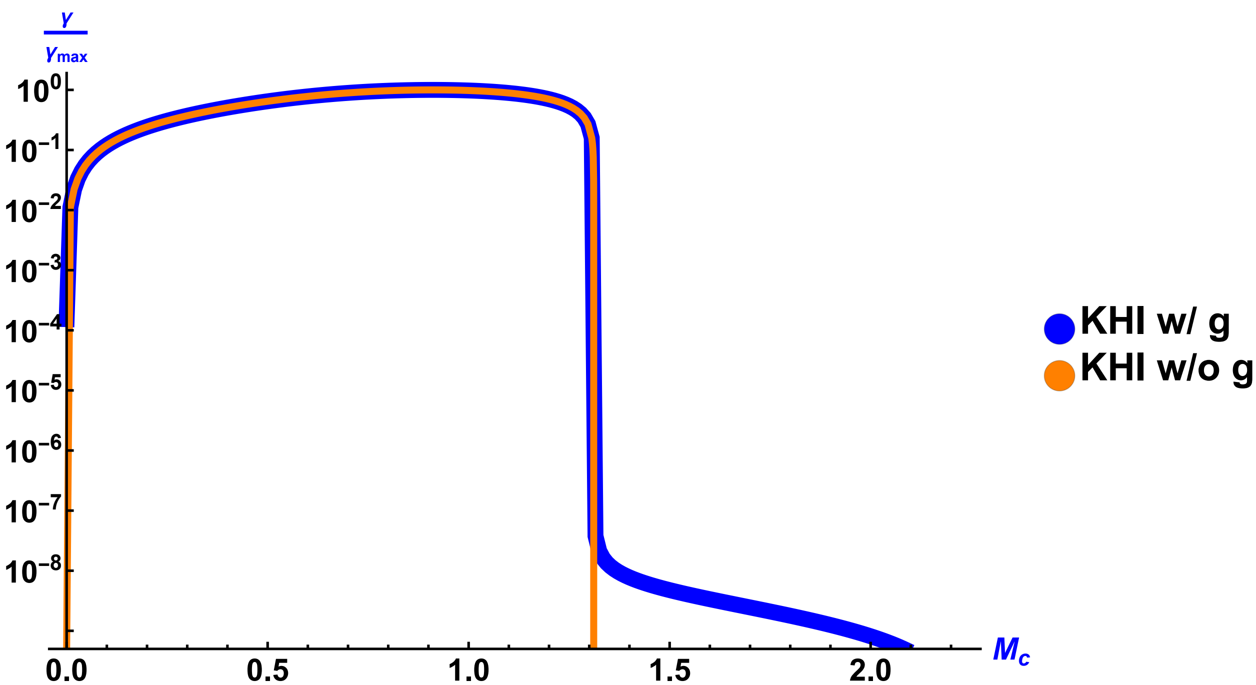

Figure 4.2: The real component of the growth-rate obtained from the numerical solution of Eq. (4.138) together with the growth-rate for the compressible KHI without gravity (also computed numerically) for $A = 0.9$ is plotted versus the convective Mach number, $M_c = \frac{U_2 - U_1}{c_1 + c_2}$. Here we have normalized the growth-rates to lie between 0 and 1 for both cases by dividing the values by the maximal growth-rates respectively.

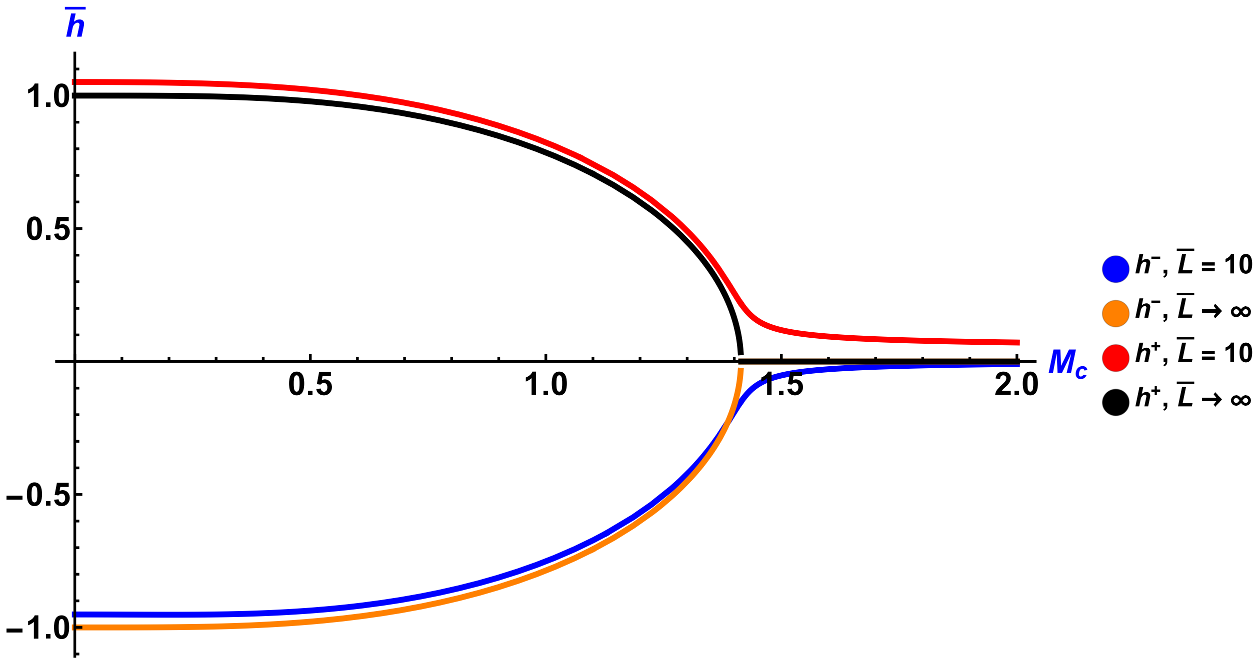

Figure 4.3: The real component of $\overline{h}^{\pm} = h^{\pm}/k$ found by evaluating Eq. (4.127) with and without gravity and eliminating the magnetic field terms is plotted versus the convective Mach number, $M_c = \frac{U_2 - U_1}{2c}$. Here $\overline{L} = \frac{c^2 k}{g}$.

reasonably think that the mode is at this point stabilized for all practical purposes, we observe that systems in a strongly, but not fully, stabilized regime can still be very important areas of study.

One such example, and one of the major concerns and constraints in tokamak physics and operation, in particular for the multi-billion dollar ITER experiment and for other experiments aiming to reach breakeven, is the Resistive Wall Mode (RWM). An uncontrolled RWM can cause a disruption, i.e. a sudden termination of the plasma discharge, which has the potential to severely damage the experiment for high performance discharges. What makes this relevant to our point is that the RWM is a resistively stabilized external kink mode. The external kink mode is a fast-growing tokamak instability that develops over Alfvén time scales, $\sim 10^{-6}$s for tokamak relevant parameters. An ideal (superconductive) wall close enough to the plasma stabilizes the external kink mode. If the wall has a finite resistivity the external kink is only partially stabilized and transforms into a mode now growing on scales of the order of the resistive diffusion timescale of

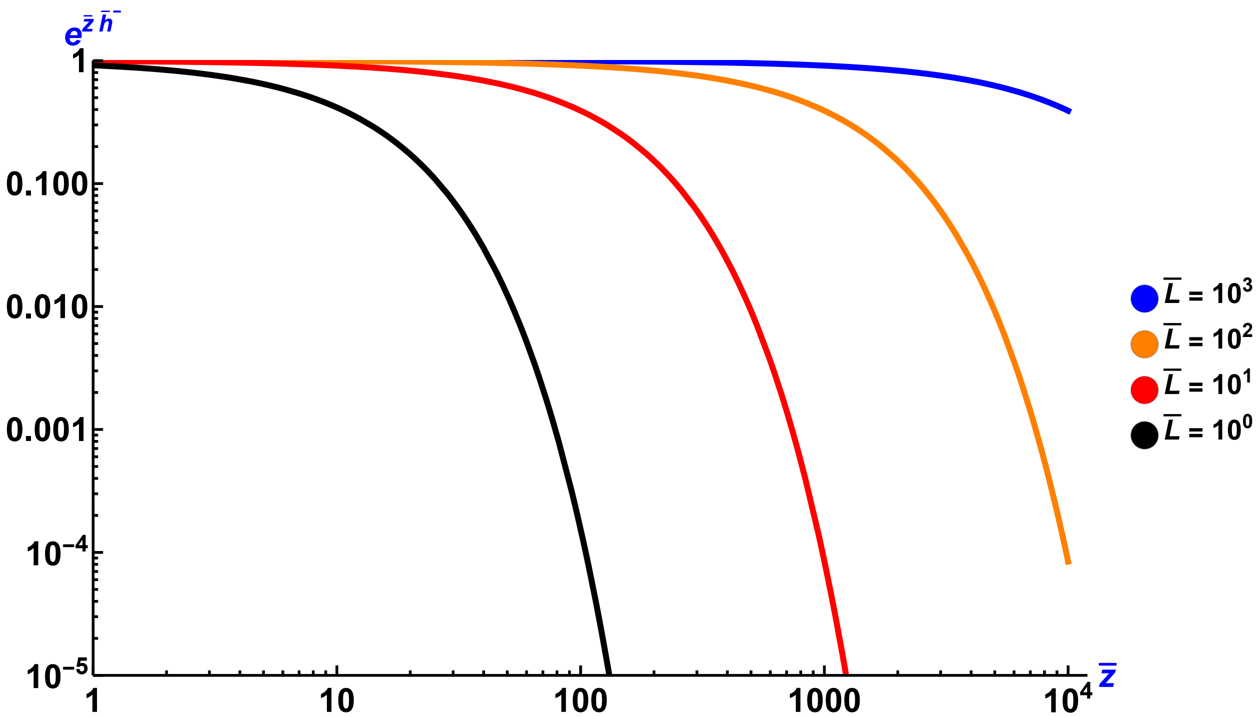

Figure 4.4: The value of the real component of the exponential part of the perturbed z-velocity, u_z, in the top fluid, $e^{\bar{z}\bar{h}^-}$ is plotted versus a normalized length, $\bar{z} = zk$. In this plot we are also only plotting the envelope of the oscillating function.

the wall, $\sim 10^{-1}$–$\mathcal{O}(1)$s, depending on the resistivity and thickness of the wall and the geometry of the machine.

In short, all of the previous discussion is to bring to the attention of the reader that in other cases a change in growth rate of several orders of magnitude transforms an intractable instability into one that can be controlled in real time in an experiment. Papers rarely show plots of growth rates in the external kink and resistive wall regimes on the same figure, but some examples can be found for instance in Ref. [161, 162].

Coming back to our work, our aim is to obtain general results rather than focus on a specific problem such as the RWM one. A direct application of our results is in fact beyond the scope of this paper.

Results Without Magnetic Field and $A \neq 0$

We start our analysis of the results considering solutions of Eq. (4.138) for large convective Mach numbers, with the convective Mach number being defined as, $M_c = \frac{U_2 - U_1}{c_1 + c_2}$. [137] The region where $M_c > \sqrt{2}$ is of interest because in the standard two-dimensional compressible KH problem, the instability is stabilized by the increasing velocity difference. [132, 163] This is shown in Fig. 4.2. In the case where the densities are equal in both fluids, the compressible KHI without gravity is stabilized at $M_c = \sqrt{2}$. The stabilization point is dependent on the densities of the two fluids. That is the reason why in Fig. 4.2 the stabilization occurs for a slightly different value of M_c , approximately 1.3. This behavior has been shown previously in the literature. [137]

We find that for $U_2 - U_1 \gg 1$, or $M_c \gg 1$, the growth-rate can be expressed to leading-order in $1/(U_2 - U_1)$ or $1/M_c$ as,

$$\gamma \approx \pm \frac{g c_2}{2 c_1 (U_2 - U_1) \cos(\theta)} - ik(c_1 + U_1 \cos(\theta)) \tag{4.141}$$

or in non-dimensional form,

$$\hat{\gamma} \approx \pm \frac{c_2^+}{2\overline{L}_1 M_c \cos(\theta)} - i(1 + M_1 \cos(\theta)) \tag{4.142}$$

where, $\hat{\gamma} = \frac{\gamma}{kc_1}, \overline{L}_1 = \frac{c_1^2 k}{g}, c_i^+ = \frac{c_i}{c_1+c_2}, \theta \neq \pi/2$, and the $\pm$ indicates that there are two sets of roots which have different signs in their real component. Setting the sound speeds to be equal in Eq. (4.142) recovers the result in Eq. (4.140) as one would expect. The next terms in the expansion for both the real and imaginary components are second-order in the expansion parameters and only cause small changes in the numerical values of γ as given by Eqs. (4.141) and (4.142). We include them to emphasize that the growth-rate can, in principle, be expanded to arbitrary order, and the continued dependence on gravity. Letting the right-hand side of Eq. (4.141) be γ_1 then,

$$\gamma \approx \gamma_1 \pm \frac{gc_2}{2(U_2 - U_1)^2 \cos^2(\theta)} - i\frac{g^2(c_2^2 - 2c_1^2) + 4c_1^4 c_2^2 k^2}{8c_1^3 k (U_2 - U_1)^2 \cos^2(\theta)}. \tag{4.143}$$

When we compare Eqs. (4.141) and (4.142) to the numerical result, they exhibit good agreement when M_c becomes sufficiently large, as seen in Figs. (4.7)-(4.8). We also note that the approximation is more accurate when the Atwood number is closer to 1. Furthermore, the numerical solutions of Eq. (4.138) match well with the incompressible solutions at low M_c. This indicates that our dispersion relation behaves correctly when compressibility effects are negligible. This is seen clearly in Figs. (4.5)-(4.6).

Equations (4.141)-(4.142) show that the growth-rate of the instability is inversely proportional to the convective Mach number, and also proportional to the gravitational acceleration the system experiences. Therefore, the velocity difference still has a stabilizing effect at high M_c as in the compressible pure KHI, and gravity has a destabilizing effect. It is also worth noting that Eqs. (4.141)-(4.142) still hold when the system is RT stable, i.e. $c_1 > c_2$ or $\rho_1 < \rho_2$. This means that there is still an instability present due to the presence of gravity, as opposed to the incompressible case where gravity would have a stabilizing effect. We emphasize that this is

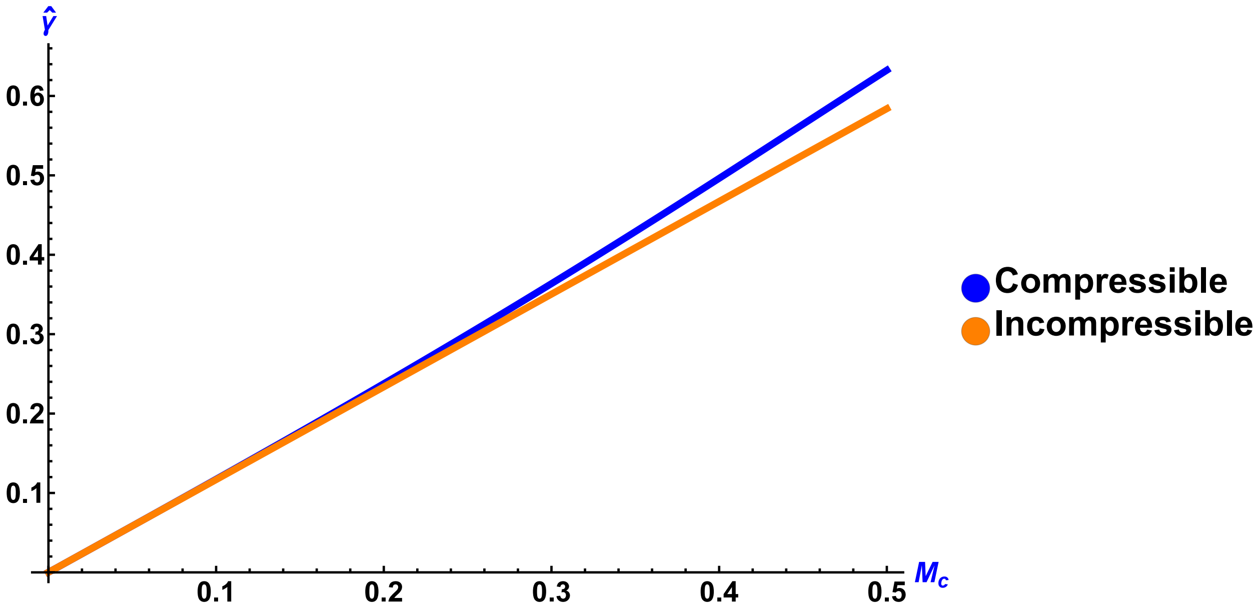

Figure 4.5: The normalized real component of the growth-rate, $\hat{\gamma} = \frac{Re(\gamma)}{kc_1}$, obtained from the numerical solution of Eq. (4.138) and from the analytic expression of the incompressible KHI growth-rate for $A = 0.9$ is plotted versus the convective Mach number, $M_c = \frac{U_2 - U_1}{c_1 + c_2}$.

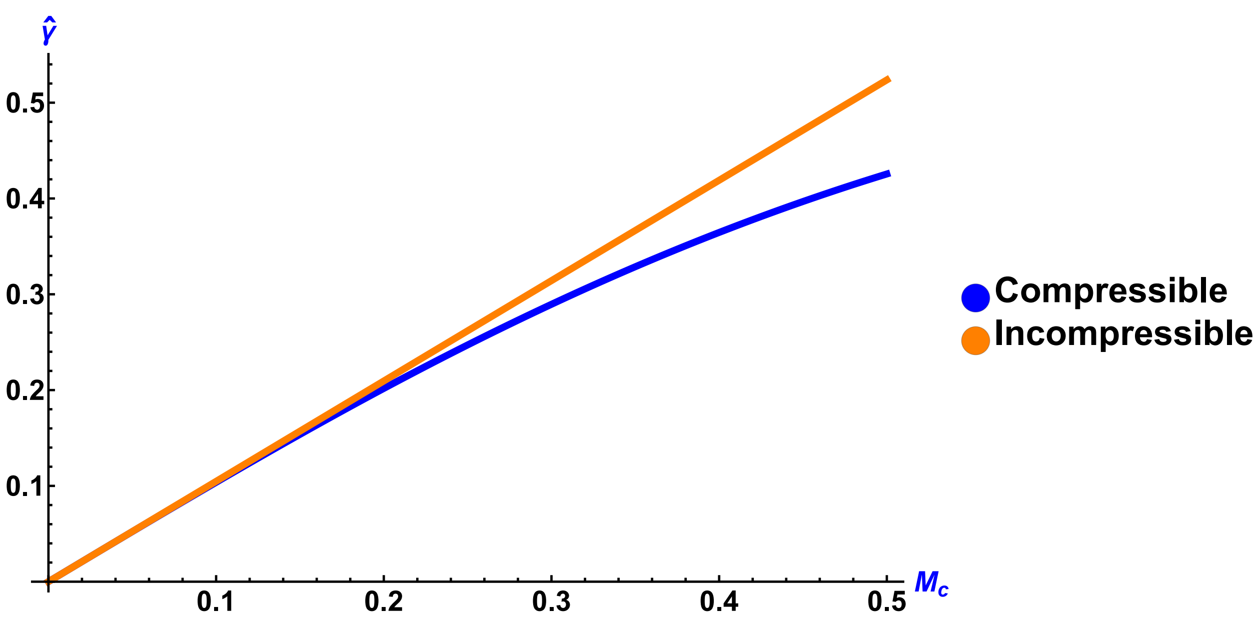

Figure 4.6: The normalized real component of the growth-rate, $\hat{\gamma} = \frac{Re(\gamma)}{kc_1}$, obtained from the numerical solution of Eq. (4.138) and from the analytic expression of the incompressible KHI growth-rate for $A = 0.1$ is plotted versus the convective Mach number, $M_c = \frac{U_2 - U_1}{c_1 + c_2}$.

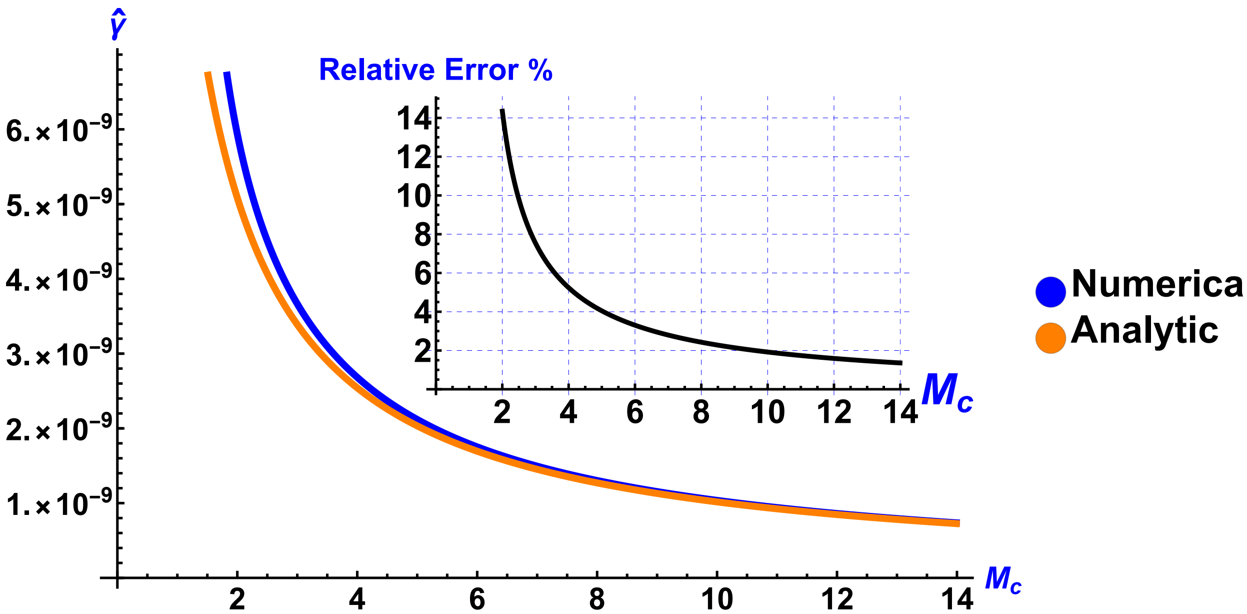

Figure 4.7: The normalized real component of the growth-rate, $\hat{\gamma} = \frac{Re(\gamma)}{kc_1}$, obtained from the numerical solution of Eq. (4.138) and from the approximate analytic expression described in Eq. (4.142) for $A = 0.9$ is plotted versus the convective Mach number, $M_c = \frac{U_2 - U_1}{c_1 + c_2}$. Also inlaid is a plot of the relative error, defined as the absolute value of the difference between the numerical and analytic values divided by the numerical value, as a function of M_c.

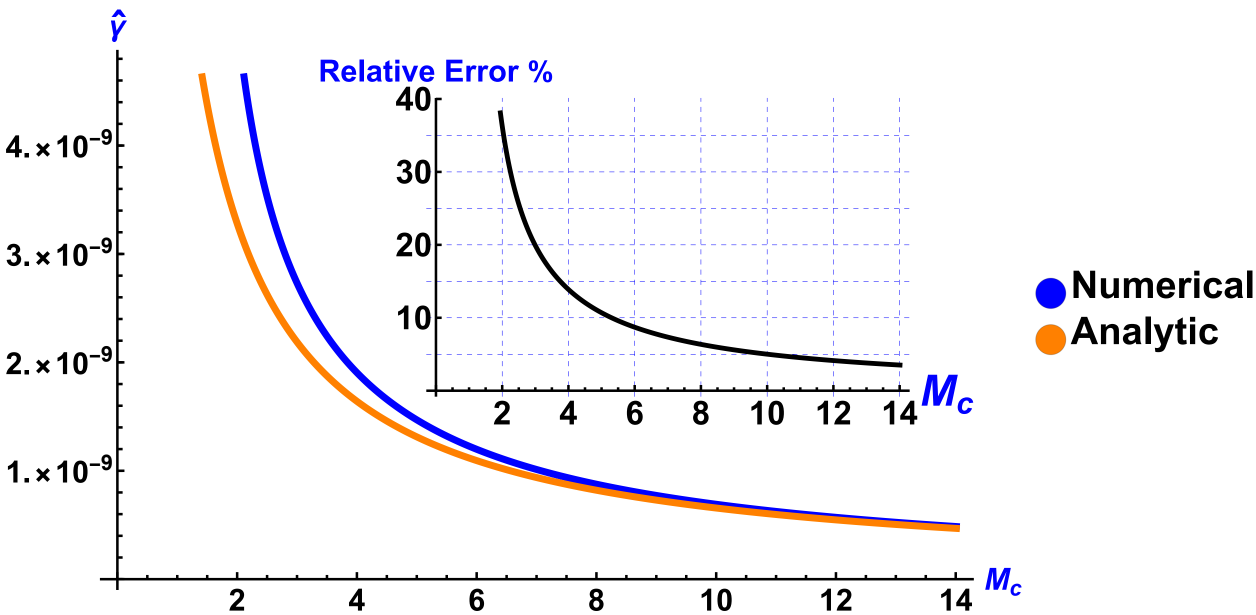

Figure 4.8: The normalized real component of the growth-rate, $\hat{\gamma} = \frac{Re(\gamma)}{kc_1}$, obtained from the numerical solution of Eq. (4.138) and from the approximate analytic expression given in Eq. (4.142) for $A = 0.1$ is plotted versus the convective Mach number, $M_c = \frac{U_2 - U_1}{c_1 + c_2}$. Also inlaid is a plot of the relative error, defined as the absolute value of the difference between the numerical and analytic values divided by the numerical value times 100, as a function of M_c.

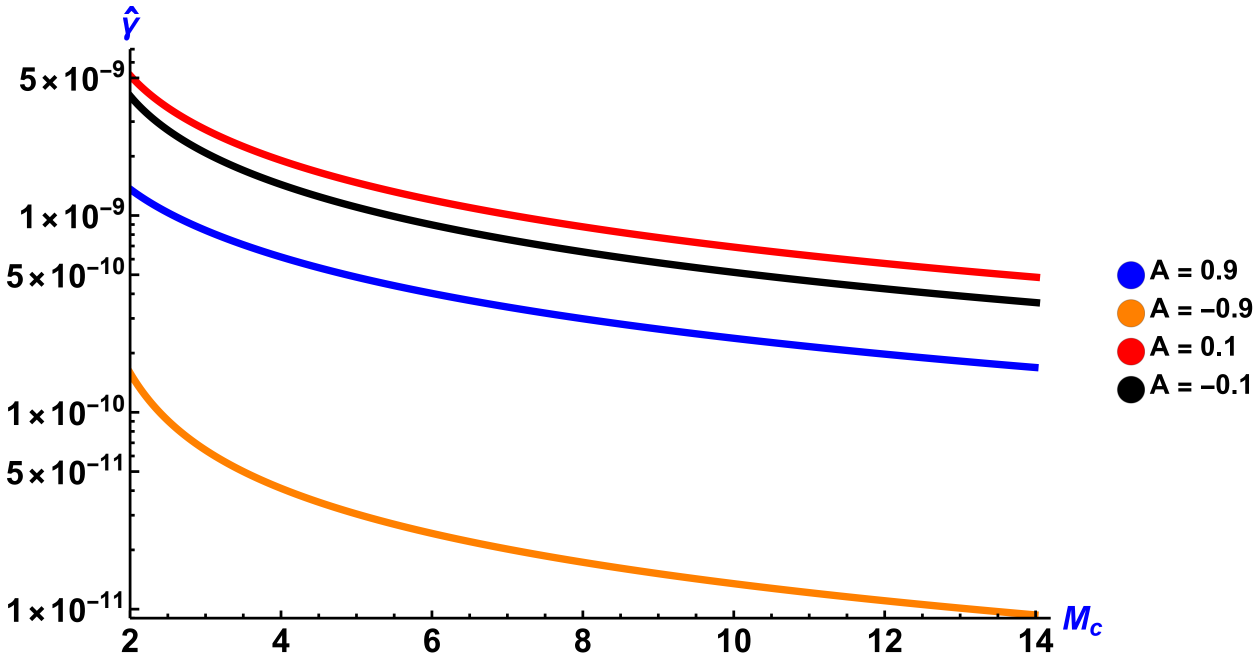

Figure 4.9: The normalized real component of the growth-rate, $\hat{\gamma} = \frac{Re(\gamma)}{kc_1}$, obtained from the numerical solution of Eq. (4.138) for different Atwood numbers, $A = \frac{\hat{\rho_1}-\hat{\rho_2}}{\hat{\rho_1}+\hat{\rho_2}}$, with and without an RTI present is plotted versus the convective Mach number, $M_c = \frac{U_2-U_1}{c_1+c_2}$. Here a negative Atwood number indicates the system is RT stable and a positive one indicates the system is RT unstable.

only true in the large M_c region, as in the low M_c region, $M_c < 0.2$, the growth-rate behaves like the incompressible solution found in the literature, as seen in Figs. (4.5)-(4.6), where gravity can stabilize the system when the system is RT stable. The differences in the magnitude of the growth-rate between the RT stable configuration and the unstable one are most notable when there is no velocity difference — thus there only being an RTI present — and at high velocities, which is shown in Fig. 4.9. This can also be seen from Eq. (4.141) where $\gamma \propto c_2/c_1$. When the system is RT stable, $c_2/c_1 < 1$ which leads to a smaller growth-rate. In comparison, when the system is RT unstable, $c_2/c_1 > 1$ causes the growth-rate to be larger.

It is also of interest to investigate the position (i.e., the value of M_c) for which the growth-rate of the compressible KHI reaches its largest value with respect to the difference in velocities or the convective Mach number, see Fig. 4.2. Since the main driver of the instability is the difference in the fluid velocities, $d = U_2 - U_1$, there will be a value of d which will maximize the growth-rate. We find the following first order in c_1 and c_2 approximation of the peak's position,

$$d_{peak} \approx 0.37c_1 + 0.48c_2 \tag{4.144}$$

or in non-dimensional form dividing every term by $(c_1 + c_2)$,

$$M_{c_{Peak}} \approx 0.37c_1^+ + 0.48c_2^+ \tag{4.145}$$

where c_i^+ is defined after Eq. (4.142). We find that this expression is within approximately 5% of the actual peak. For reference when comparing to the homogeneous compressible KHI without gravity [132, 163] one finds it to be, $d_{peak} = \frac{\sqrt{3}}{2}c$. In the limit when the sound speeds are equal the constants in Eqs. (4.144)-(4.145) add to 0.85, which is less than $\sqrt{3} \approx 0.87$. This discrepancy may be caused by the observed increased contribution of higher order effects when the sound speeds approach the same value.

Another source of error is the lack of a gravity term in the expression, as a very small linear dependence was observed. The above results were found with $g \sim \mathcal{O}(10)$, or in terms of the normalized stratification length, $\overline{L}_1 \sim \mathcal{O}(10^7)$. In this regime gravity has a minor impact on the peak. That is no longer true when gravity is much larger, or $\overline{L}_1 \sim \mathcal{O}(1)$ or smaller. In fact, when using such parameters one finds that not only is the location of the peak shifted to higher values of M_c, the actual peak value increases as well. Plotting the real component of Eq. (4.139a) for different values of $\overline{L}$ in Fig. 4.10 showcases this behavior. Furthermore, in the case where $\overline{L}^{-1} \gg M_c$ in Eqs. (4.139a)-(4.139b), the growth-rate's leading order behavior is as such,

$$\hat{\gamma} = \pm 2M_c\overline{L} - iM_1 + \mathcal{O}(\overline{L}^{2}). \tag{4.146}$$

Which is quite different that the large M_c behavior seen in Eq. (4.140).

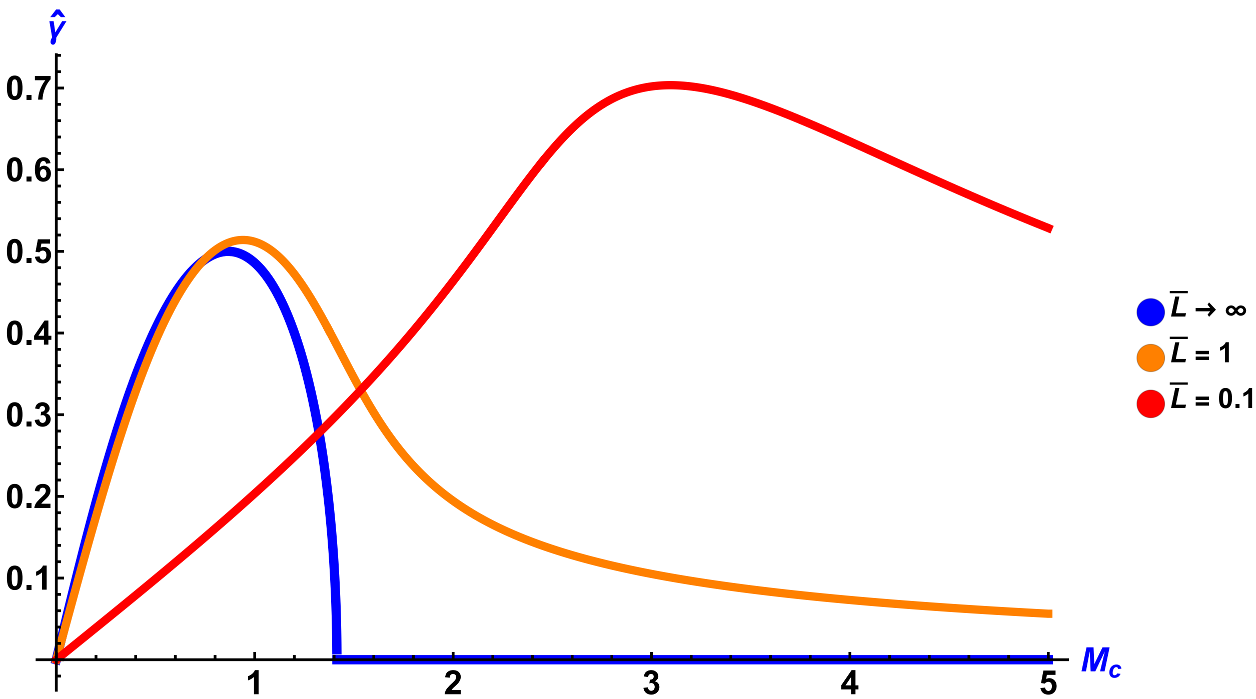

Figure 4.10: The normalized real component of the growth-rate, $\hat{\gamma} = \frac{Re(\gamma)}{kc}$, obtained by evaluating Eq. (4.139a) for different values of $\overline{L} = \frac{c^2 k}{g}$ is plotted versus the convective Mach number, $M_c = \frac{U_2 - U_1}{2c}$.

Results With Magnetic Field

The last case we consider is the more challenging one, including the presence of a magnetic field. For this problem, the dispersion relation becomes considerably more complex than the one considered so far, see Eq. (4.137). Solving the dispersion relation presents a non-trivial challenge. Without setting an exceptionally high numerical precision, approximately 200 to 300 digits, it becomes arduous to obtain accurate results. The unusual need for such high precision stems from the fact that the solution of the dispersion relation requires various operations involving very large and very small numbers, which cannot be completed accurately with standard precision.

Another numerical issue to note occurs because of the method that was used to find the roots of Eq. 4.137. We clarify the issue by describing the process used to study the effect of B on the system. In that case, we initially solve the equation using a very small value for B with an initial guess of the growth-rate obtained from Eq. 4.141. Then we progressively increase B by small amounts, using the previous results as initial guess for the numerical solver. It was found that the numerical solver may fail if the initial guess has inaccuracies as small as a fraction of a percentage point. The problem is exacerbated by the fact that there are many roots to Eq. 4.137, with only a specific one being the one of interest. Moreover, some roots can be very close to one another, either in their real or imaginary part. This can occasionally lead the solver to converge to a root different from the desired one. Fortunately, the behaviors of the various roots are noticeably different from one another, either the plots would be discontinuous or a kink would appear, thus it was straightforward to determine when the solver switched from one root to another. For all of the reasons above, high accuracy and precision are required for the solver to keep track of the roots we are interested in.

In the ensuing results, unless the specific parameter is being varied or otherwise specified, we have used the following input parameters: $\rho_1 = 3 * 10^{-7}\, kg\, m^{-3}$, $\rho_2 = 8 * 10^{-8}\, kg\, m^{-3}$, $P = 200\, Pa$, $g = 10\, m/s^2$, $k_x = 1\, m^{-1}$, $U_2 - U_1 = 5 \times 10^5\, m/s$.

First, we will mention the effect the magnetic field has at low M_c. At low convective Mach number, $M_c < 0.2$, the system behaves as the incompressible one does. In this regime, the flow aligned magnetic field acts as an effective surface tension, stabilizing the system. [124] In the incompressible case, the expression for the growth-rate of the magnetic KHRTI is, [124, 125]

$$\gamma_{inc} = \sqrt{gk_xA + k_x^2\rho_1^+\rho_2^+\left(U_2 - U_1\right)^2 - \frac{2k_x^2B_x^2}{\mu_0(\rho_1+\rho_2)}} \\ -ik_x\left(\rho_1^+U_1 + \rho_2^+U_2\right) \tag{4.147}$$

where $\rho_i^+ = \frac{\rho_i}{\rho_1+\rho_2}$. Setting the radical in Eq. 4.147 to zero and solving for B gives,

$$B_{crit_{inc}} = \sqrt{\frac{\mu_0\left(g\left(\rho_1^2 - \rho_2^2\right) + k_x\rho_1\rho_2(U_2 - U_1)^2\right)}{2k_x\left(\rho_1 + \rho_2\right)}}. \tag{4.148}$$

Since $k_x\rho_1\rho_2(U_2 - U_1)^2 \gg g\left(\rho_1^2 - \rho_2^2\right)$ we can approximate the expression to be,

$$B_{crit_{inc}} \approx \sqrt{\frac{\mu_0\rho_1\rho_2}{2(\rho_1 + \rho_2)}}(U_2 - U_1) \tag{4.149}$$

or as,

$$\frac{V_{A_{12}crit}}{\Delta U} \approx \sqrt{\frac{\rho_1^+\rho_2^+}{2}} \tag{4.150}$$

where $V_{A_{12}} = \frac{B}{\sqrt{\mu_0(\rho_1+\rho_2)}}$. With the given parameters the right hand side of the above equation is approximately 0.29.

As previously stated, the growth-rates found from Eq. (4.137) should match with those from Eq. (4.147) at low convective Mach numbers. A result of this is that they should both show the same stabilizing behavior regarding a flow aligned magnetic field. This exact behavior is seen, for example, in Fig. 4.11.

Now we will discuss the effect the magnetic field has on the system in the region where the convective Mach number is between 0.2 and 1.4. Here compressibility effects have a larger impact on the growth-rate of the instability, and as a result the incompressible solution is no longer valid. In this regime of M_c, the work of Peyrichon, et al. [137] serves as a good benchmark.

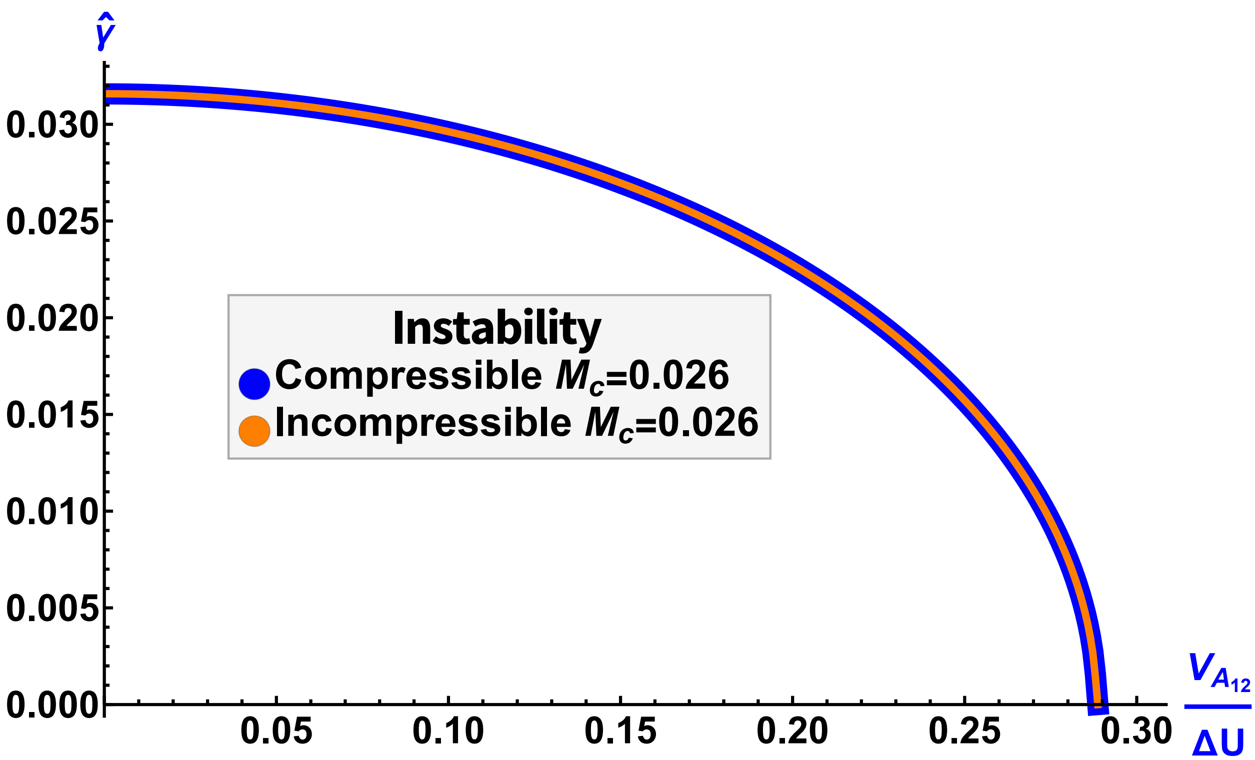

Figure 4.11: The real component of the normalized growth-rate, $\hat{\gamma} = \frac{Re(\gamma)}{kc_1}$ obtained from the numerical solution of Eq. (4.137) as well as from Eq. (4.147) plotted versus $\frac{V_{A_{12}}}{\Delta U}$, where $V_{A_{12}} = \frac{B}{\sqrt{\mu_0(\rho_1+\rho_2)}}$, for $M_c = 0.026$.

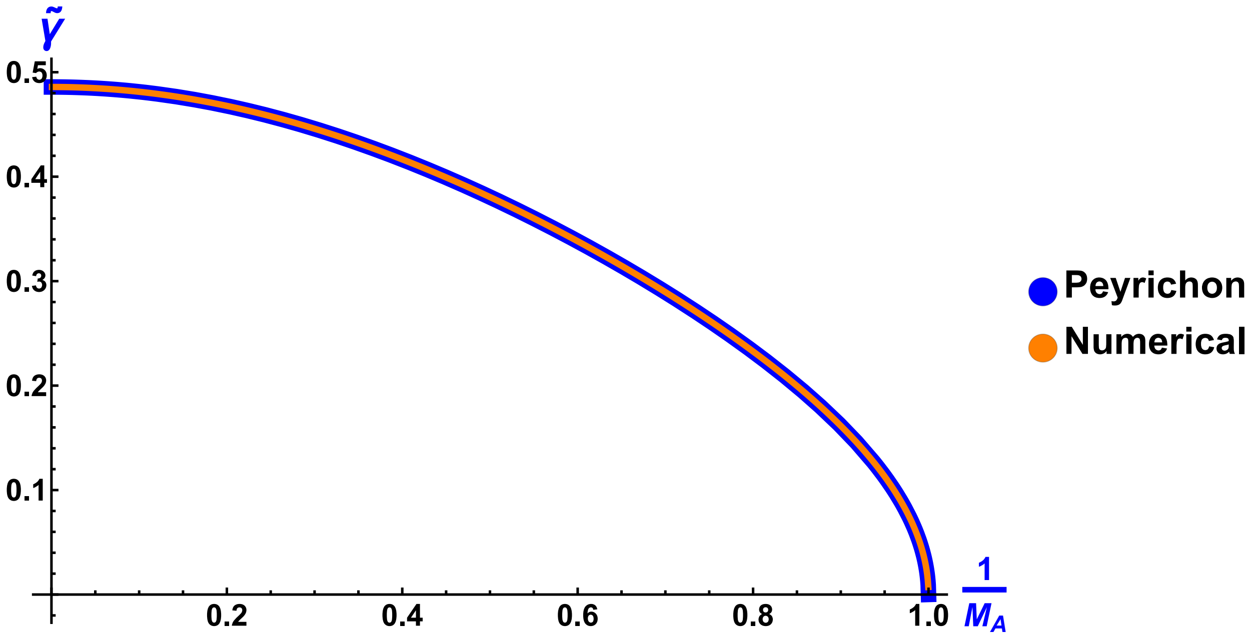

Figure 4.12: The real component of the normalized growth-rate, $\tilde{\gamma} = \frac{Re(\gamma)}{k\Delta U}$ obtained from Eq. (13) from Ref. [137], and numerical solutions of Eq. (4.137) plotted versus $\frac{1}{M_A} = \frac{V_A}{\Delta U}$. Here $V_A = \frac{B}{\sqrt{\mu\rho}}$ is the Alfvén velocity. Also note that $A = 0$ and $M_c = 1$ for this plot.

For $M_c < 1.5$ their results and ours should align well, even if there are some differences in the two systems.

We will proceed to compare our results and the ones of Ref. [137] for the parameters listed previously, except we set $M_c = 1$ and $A = 0$ to make use of their Eq. (13). In this regime $\overline{L} \sim \mathcal{O}(10^7)$, meaning that gravitational effects will be minimal and should not contribute meaningful discrepancies between the two results. Furthermore, Ref. [137] uses an adiabatic index, $\Gamma = 5/3$. This causes differences in the results, such as discrepancies in the required field for stabilization of approximately $\mathcal{O}(\sqrt{\Gamma})$ when plotted versus the magnetic field strength. However, we expect good numerical agreement when dimensionless quantities are used and the polytropic index is absorbed into the convective Mach number. This is confirmed in Fig. 4.12, where the two curves are indistinguishable.

Lastly, we will now discuss the effects of the magnetic field on the system in the high M_c regime. We designate this region with $M_c > 2$. $M_c = 2$ was chosen as the limit of the region

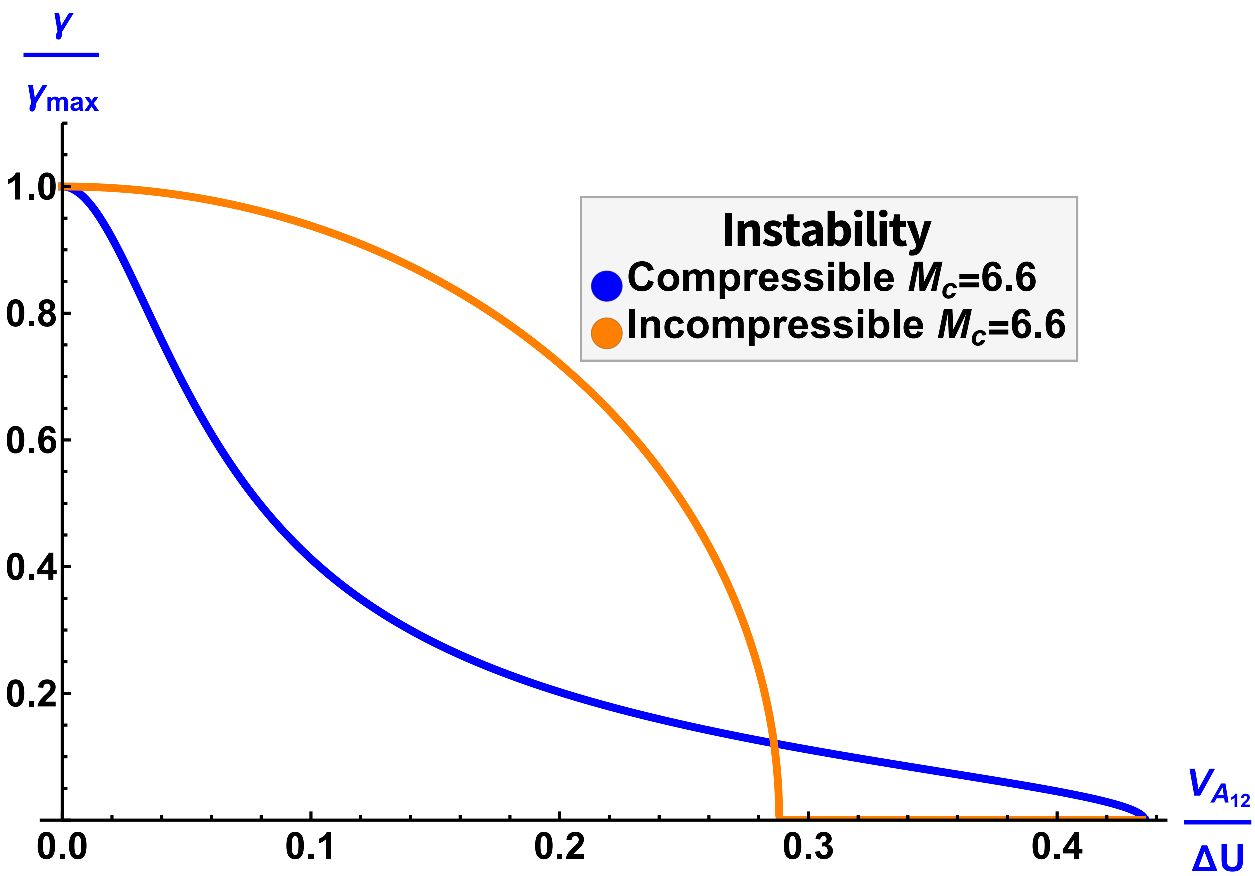

Figure 4.13: Qualitative comparison of the normalized compressible and incompressible KHRTI growth-rates, real component only, vs $\frac{V_{A_{12}}}{\Delta U}$ at $M_c = 6.6$. Where $V_{A_{12}} = \frac{B}{\sqrt{\mu_0(\rho_1+\rho_2)}}$. Here we have normalized the growth-rates to lie between 0 and 1 for all cases by dividing the values by the maximal growth-rates respectively. The maximum growth-rate of the incompressible case is approximately, $\mathcal{O}(10^5)$, while the compressible case's growth-rate is approximately, $\mathcal{O}(10^{-5})$.

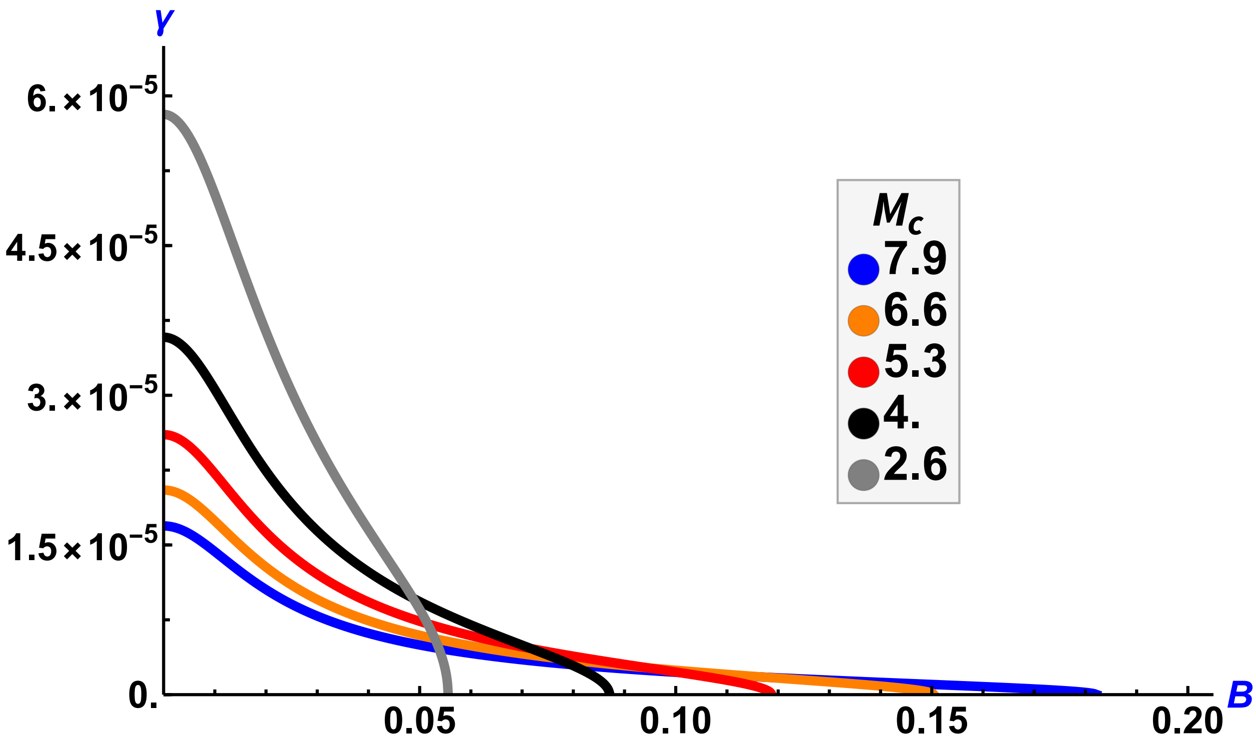

Figure 4.14: The real component of the growth-rate, γ, in s^{-1} plotted versus the magnitude of the magnetic field, B, in Tesla, obtained from the numerical solution of Eq. (4.137) for different convective Mach numbers, $M_c = \frac{U_2 - U_1}{c_1 + c_2}$.

for convenience, since for $M_c \gtrapprox 2$ the numerical solution approaches the asymptotic solution more and more closely, as seen in Figs. 4.7 and 4.8. In this highly compressible domain, the magnetic field should have a weaker stabilizing effect than in the less compressible case as has been shown previously. [137]

We can qualitatively show this by making the same comparison made in Fig. 4.11 but at a higher value of M_c. While the incompressible result is inaccurate at $M_c \gg 1$, this comparison is meant to emphasize the change in the stabilization due to the magnetic field. Fig. 4.13 shows this difference in behavior. It is important to note the normalization used in this plot. For both cases, the largest value of γ is found when the magnetic field is 0. The growth-rate of the incompressible case is approximately, $\mathcal{O}(10^5)$, while the compressible case's growth-rate is approximately, $\mathcal{O}(10^{-5})$. Fig. 4.13 shows that a stronger magnetic field is required to suppress a less unstable system.

Looking further into the effect the magnetic field has on the system we were able to find a noticeable pattern. As mentioned earlier in this section we solved Eq. (4.137) numerically for increasing B until the system reached a point where the growth-rate decreased rapidly with approximately 1% increments in B and the solver was no longer able to find a solution. The increment in B was generally $\mathcal{O}(10^{-5})$. A plot of the growth-rate versus the magnitude of the magnetic field is shown in Fig. 4.14.

From this plot we can see that the growth-rate's dependence on the magnetic field has changed significantly compared to the previous cases. While the growth-rate decreases for increasing M_c, as it should given Eq. (4.142), the necessary field required to suppress the instability increases. This further shows that the increased dominance of compressibility effects lessens the stabilizing ability of the magnetic field.

Another aspect of Fig. 4.14 that was noteworthy was the B field required to stabilize the instability. While it may not be immediately obvious, the points where the curves in Fig. 4.14 go to zero are evenly spaced with the evenly spaced values of M_c. Note that we used evenly spaced, round values of the difference in velocity as input rather than round values for the Mach numbers. The Mach numbers are themselves evenly spaced. A plot of the critical magnetic field versus the difference in fluid velocities (not shown) confirms that the relation between the two quantities is linear. Using unit analysis and the quantities we were using for the calculation we were able to obtain an approximate expression for this critical magnetic field,

$$B_{crit_{KH}} \approx \sqrt{\mu_0 \rho_2}\left((U_2 - U_1) - c_1\right). \tag{4.151}$$

Expressing it solely in terms of velocities we also have,

$$V_{A_2} \approx (U_2 - U_1) - c_1 \tag{4.152}$$

where $V_{A_2} = \frac{B}{\sqrt{\mu_0 \rho_2}}$ is the Alfvén velocity of the bottom fluid.

This expression was tested for various densities and convective Mach numbers, and it

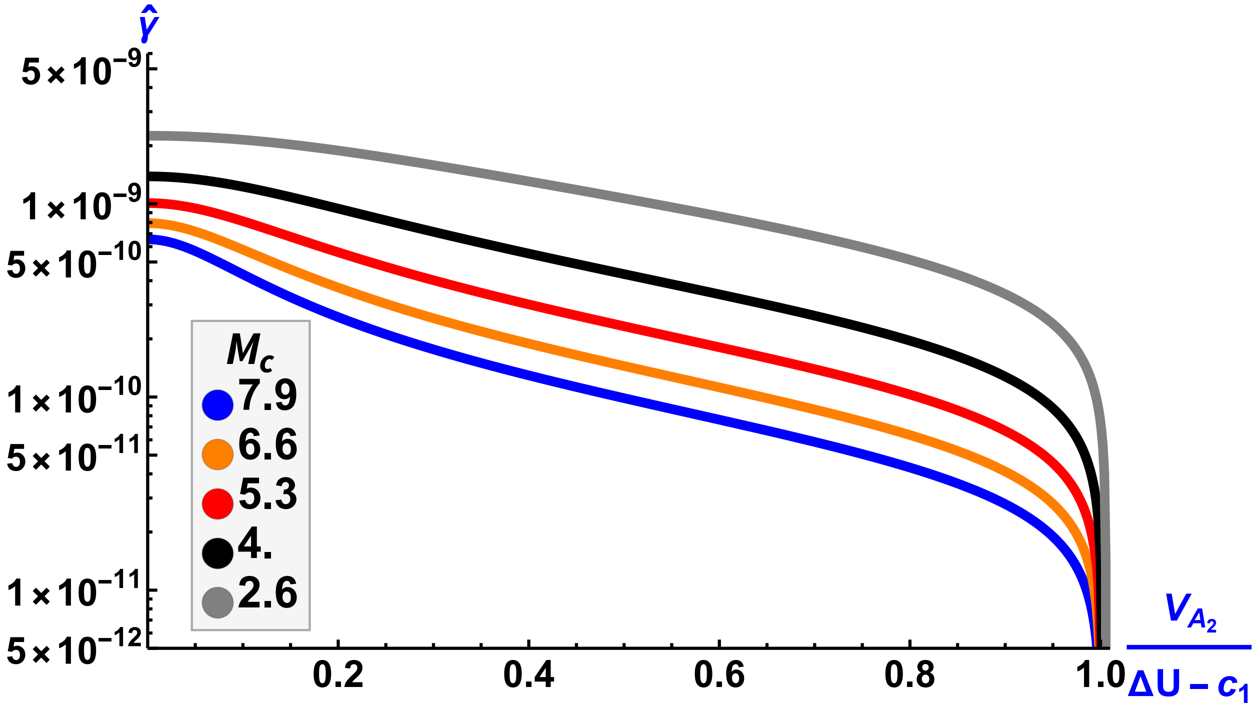

Figure 4.15: The real component of the normalized growth-rate, $\hat{\gamma} = \frac{Re(\gamma)}{kc_1}$ obtained from the numerical solution of Eq. (4.137) plotted versus the Alfvén velocity of the bottom fluid, in m/s, divided by the difference of the fluid velocities minus the speed of sound of the top fluid, both in m/s for different convective Mach numbers, $M_c = \frac{U_2 - U_1}{c_1 + c_2}$.

was found to be accurate. Rescaling the horizontal axis in Fig. 4.14 as the ratio of the two sides of Eq. (4.152), it is easy to show that all the curves go to zero when Eq. (4.152) is approximately satisfied. This is shown in Fig. 4.15. It is worth noting that the approximation is more accurate as the convective Mach number increases, though it is still accurate for lower values, as the curve for $M_c = 2.6$ goes to zero at approximately 1.05 in Fig. 4.15. At velocity differences where the asymptotic behavior is not as prevalent, $M_c < 2$, we noted this expression to be overestimating the required field for stabilization by over 50%.

An aspect of Eq. (4.151) that needs to be emphasized is its independence of the value of g or $\overline{L}_1$ for the values tested, $10^3 < \overline{L}_1 < 10^7$. Increasing the value of g by orders of magnitude only increased the magnitude of the growth-rate by similar orders of magnitude, and had no impact on the stabilization of the instability. After further investigation we found that, in this regime of $M_c \gg \overline{L}_1^{-1}$, $Re(\gamma) \propto g/c_1$, or $\hat{\gamma} \propto \overline{L}_1^{-1}$, as found in the case without a magnetic field in Eqs. (4.141)-(4.142). This can be seen in Fig. 4.16. The linear dependence on gravity is anticipated as without its presence there would be no instability; the continued inverse dependence on c_1 is unexpected although in line with the previous findings.

4.4.4 Conclusion

In this study we have investigated the stability of the compressible KHI and RTI both with and without a magnetic field. In the case without a magnetic field, an analytic expression for the growth-rate of the instability, Eqs. (4.139a)-(4.139b) was found for the case where there was no density discontinuity at the interface. This then allowed us to find the asymptotic behavior of the instability for large M_c, as well as show how deep into the fluid the eigenfunctions persist. In the case where $A \neq 0$ an approximate analytic expression for the growth-rate of the KHRTI for large M_c was obtained. This expression, Eq. 4.141, shows that the real part of the growth-rate is proportional to gravity times the speed of sound of the bottom fluid, and inversely proportional to the speed of sound of the top fluid times the difference in fluid velocities. This expression matches the one found for the case of equal densities at the interface in the proper limit. Furthermore,

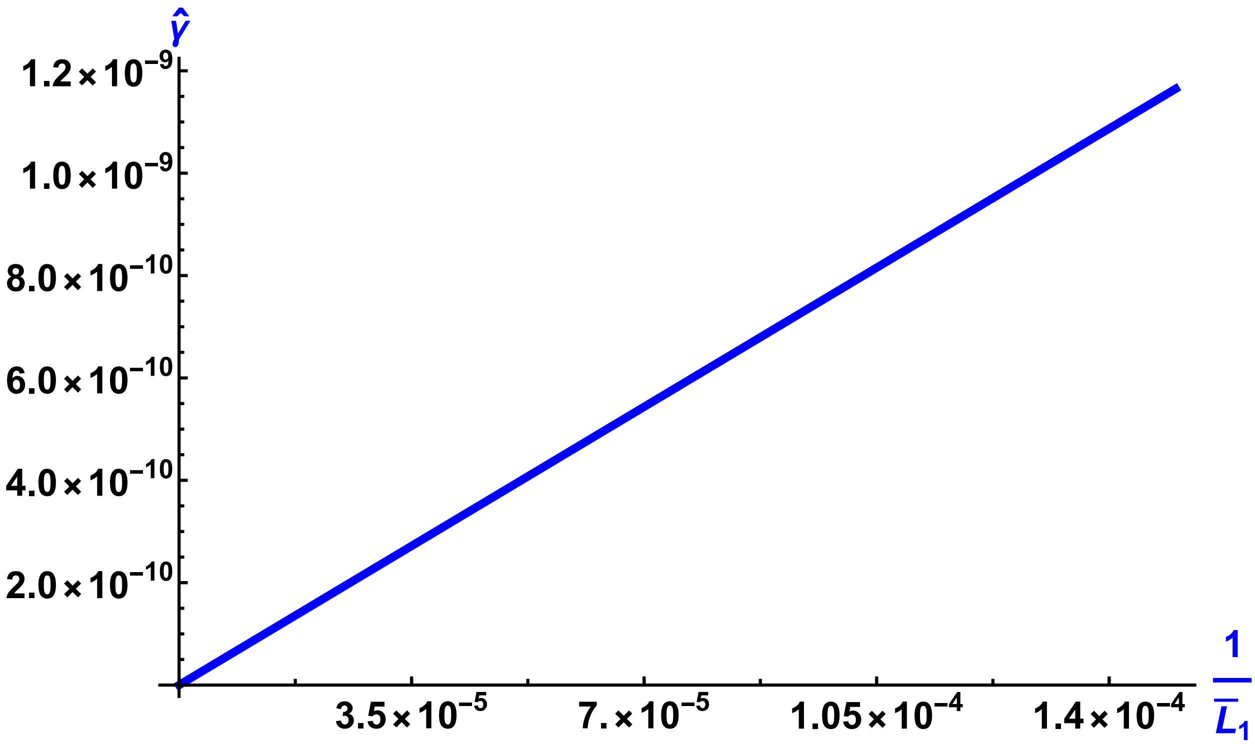

Figure 4.16: The real component of the normalized growth-rate, $\hat{\gamma} = \frac{Re(\gamma)}{kc_1}$ obtained from the numerical solution of Eq. (4.137) plotted versus $\bar{L}_1^{-1} = \frac{g}{c_1^2 k}$.

we found an expression that estimates the location of the point of maximum growth-rate with respect to the flow shear with low error, when gravity is small. The equation shows that the peak occurs at a value of the difference in velocities that is equal to a linear combination of the fluid sound speeds. When gravity is large, or $\overline{L}$ is small, we show that the peak of the instability shifts upwards in magnitude and towards larger values of M_c.

In the case where a magnetic field aligned with the fluid flow is present, the field has a stabilizing effect like in the incompressible case. However, the stabilizing behavior is quite different. The growth-rate's dependence on B is non-linear, and there is a critical value of B where the system rapidly stabilizes. We found an accurate expression for the critical point, Eq. 4.151, which implies that the mode is stabilized when the Alfvén velocity of the bottom fluid plus the sound speed of the top fluid equals the difference in fluid velocities. We compared our numerical results qualitatively to that of the incompressible case and showed that for low shear they match well. At high shear the behaviors diverge, and increased compressibility diminishes the magnetic field's ability to stabilize the system. In addition, we show that our results qualitatively match those found in Ref. [137].

Chapter 5

Conclusion

In this thesis, we have undertaken the task to study magnetically confined plasmas from two different, yet related approaches. First we studied the equilibria of 3D magnetically confined plasmas, with both an idealized case and a case from experimental reconstructions. The former was done to facilitate the comparison and verification of different computational models used to find stellarator equilibria against one another. These codes are routinely used by the community and as such it is important to ensure that, while they use different formulations or models of MHD, given the same system they all reach the same of close to the same solution. For the latter, we took reconstructions of equilibria which were known to have magnetic islands and used them as a vehicle to further investigate how the SIESTA code handles magnetic islands, as well as develop methods to detect and characterize them. Since magnetic islands naturally arise in non-axisymmetric toroidal plasmas, improving our understanding of these structures requires a deeper understanding of the computational framework used to model them. These investigations comprise the totality of the work presented in Chapter 3.

There we presented the results of both the qualitative and quantitative comparisons performed for the validation study. We were able to show that the equilibria found by the solvers for both the vacuum and finite pressure cases matched well across all the codes. Consistency in the resulting flux surfaces and magnetic axis locations among the different equilibria provided confidence that the computational codes were identifying the same equilibrium solution.

Then we performed a systematic study on the impact the helical perturbation input parameter has on the magnetic islands present in the calculated equilibrium. For this we used reconstructions of two shots from the Compact Toroidal Hybrid which were known to have islands. We were able to show that increasing the magnitude of the perturbation parameter increased the island size, but that the behavior was not uniform across the two cases. A possible explanation for this was the location of the resonant surface relative to the edge. To further investigate this we performed another analysis were we artificially moved the boundary closer to the resonance. This was done by removing the outer surfaces from the initial problem. We found that as the resonance was brought closer to the edge of the plasma, the effect of the perturbation became more pronounced, and as a result a larger island formed in the equilibrium. This specific interplay was unexpected and bears future investigation to better understand the mechanisms which are causing the effects seen.

The second approach we used to study magnetically confined plasmas was though a linear stability analysis. Once a system is in equilibrium, it becomes important to know if it has beneficial properties, for say use in reactor design. One of the most important properties of the equilibrium is whether is stable or not, as ideally the system would stay in equilibrium for extended periods of time. In the work presented in Chapter 4 we investigate the stability of a compressible fluid system that is subject to two instabilities, the Kelvin-Helmholtz and Rayleigh-Taylor instabilities, with and without a magnetic field. Motivated by the work presented in Ref. [156] we investigated the linear stability of a similar system. This allowed for a simpler geometry to be used, slab rather than toroidal, while still being able to investigate the important physics present.

While the problem was quite complex, we were able to find out a great deal about the system. In the case where there was no magnetic field we were able to find an analytic expression for the growth-rate of the instability when the fluids had the same density. In the case where the densities were different we were able to find the asymptotic behavior of the growth-rate for very large flow velocities. In the case of a flow aligned magnetic field we were able to show that at very high flow rates, beyond the point where the standard KHI is stabilized, the magnetic field's ability to suppress the instability is lessened. Regardless, it still does suppress it, and we were able to find an accurate approximate expression for the critical field required for this.

5.1 Future Work

The work presented in this thesis motivates several directions for future research. Below, a number of potential projects are outlined that would build upon the present results and constitute natural continuations of this work.

5.1.1 Additional Free-Boundary Verification Studies

The verification study performed in this thesis was done with an idealized design to ensure the different codes would be able to adequately resolve their equilibrium. For example SPEC can be fragile due to how it was implemented. Regardless, it would be worthwhile to extend the study to more complex and realistic designs. Performing the analysis on devices with torsion, non-zero toroidal plasma current, or stellarator asymmetric geometries would allow for more robust verification between the various codes.

A possible starting point for this could be running vacuum and finite pressure cases of CTH equilibria, as it has a non-zero toroidal plasma current being driven during its operation. This should be straightforward for VMEC and SIESTA since there is extensive experience running both to calculate CTH equilibria. DESC should also be relatively easy to run since VMEC already is used and converting the VMEC inputs is not difficult. Free-boundary SPEC may pose a greater challenge, as initial forays into running it were performed previously. The difficulty arose from getting the vacuum magnetic fields from the coils using FOCUS. It struggled with this task, and we were unable to diagnose the exact cause of this.

5.1.2 Additional Magnetic Island Studies

In the work investigating magnetic islands in SIESTA, all the equilibria were calculated with a fixed boundary. It would be valuable to extend the analysis by repeating these equilibrium calculations using free-boundary formulations. This would be especially insightful to understand how large islands near the edge are resolved by the code, as well as how they would deform the boundary, if at all. This analysis was not pursued because, at the time, uncertainty remained regarding the accuracy of free-boundary SIESTA equilibria computed in sparse mode. Additional work is therefore required to verify that free-boundary calculations in sparse mode are performed reliably and accurately.

We were able to demonstrate the relationship between magnetic island size and the proximity of the resonant surface to the plasma boundary. This was done by forcing the boundary closer to the resonance by removing outer surfaces and fixing the new last closed flux surface. It would be worth performing an analysis where instead of moving the surface, one changes the rotational transform profile. One could calculate various equilibria of the same system, except the iota profile is shifted so that the location of the resonant surface of interest is located at different points in the plasma. This would allow for further investigation on the relationship between of the resonant surface's proximity to the boundary and the island size.

5.1.3 Additional KHRTI Studies

The linear stability analysis performed in this thesis was for a slab geometry. While it is a valid geometry to study, it is a simplified one. The problem as presented is very complicated and adding any further complexities will only increase the complexity of the problem. Regardless, it would be worthwhile to perform the analysis with more realistic geometries. A possible first step would be to calculate the growth rate of the instability again using a cylinder rather than a slab, and thus make the fluids rotate rather than only move in a specific direction. This would allow for rotational effects to be accounted for and see how they impact the stability of the system. The magnetic field could be set as having only an angular component like in a z pinch. If results with the cylinder are found the next step would be to attempt the analysis with a toroidal geometry. Although, at that point an analytic solution may no longer be feasible and a numerical one may be required.

References

[1] U.S. Energy Information Administration, *Annual Energy Outlook 2026*, tech. rep. (U.S. Government Printing Office, Washington, DC, 2026).

[2] J. P. Freidberg, *Plasma physics and fusion energy* (Cambridge University Press, 2007).

[3] J. P. Freidberg, *Ideal mhd* (Cambridge University Press, 2014).

[4] M. Kikuchi and M. Azumi, “Steady-state tokamak research: core physics,” Rev. Mod. Phys. **84**, 1807–1854 (2012).

[5] J. Wesson, “Hydromagnetic stability of tokamaks,” Nuclear Fusion **18**, 87 (1978).

[6] A. H. Boozer, “Theory of tokamak disruptions,” Physics of Plasmas **19**, 058101 (2012).

[7] W. Thomson, *Mathematical and Physical Papers: Volume 4: Hydrodynamics and General Dynamics*, edited by S. J. Larmor, Vol. 4, Cambridge Library Collection - Physical Sciences (Cambridge University Press, Cambridge, 2011).

[8] H. Hermann, “On Discontinuous Movements of Fluids,” The London, Edinburgh, and Dublin Philosophical Magazine and Journal of Science **36**, 337–346 (1868).

[9] J. W. Strutt, “Investigation of the Character of the Equilibrium of an Incompressible Heavy Fluid of Variable Density,” in *Scientific Papers: Volume 2: 1881–1887*, Vol. 2, Cambridge Library Collection - Mathematics (Cambridge University Press, Cambridge, 2009), pp. 200–207.

[10] G. I. Taylor, “The instability of liquid surfaces when accelerated in a direction perpendicular to their planes. I,” Proceedings of the Royal Society of London. Series A. Mathematical and Physical Sciences **201**, Publisher: Royal Society, 192–196 (1950).

[11] P. Helander, “Theory of plasma confinement in non-axisymmetric magnetic fields,” Reports on Progress in Physics **77**, 087001 (2014).

[12] L.-M. Imbert-Gérard, E. J. Paul, and A. M. Wright, *An introduction to stellarators: from magnetic fields to symmetries and optimization* (Society for Industrial and Applied Mathematics, Philadelphia, PA, 2024).

[13] W. D. D’haeseleer, W. N. Hitchon, J. D. Callen, and J. L. Shohet, *Flux coordinates and magnetic field structure* (Springer Berlin, Heidelberg, 2012).

[14] S. Hirshman and J. T. Hogan, “ORMEC: A Three-Dimensional MHD Spectral Inverse Equilibrium Code,” Journal of Computational Physics **63**, tex.ids= hirshman_ormec_1985, 329–352 (1986).

[15] D. W. Dudt and E. Kolemen, “Desc: a stellarator equilibrium solver,” Physics of Plasmas **27**, 102513 (2020).

[16] S. P. Hirshman and J. C. Whitson, “Steepest-descent moment method for three-dimensional magnetohydrodynamic equilibria,” The Physics of Fluids **26**, 3553–3568 (1983).

[17] R. Morris, J. Glowienka, G. Neilson, S. Hirshman, and P. Merkel, “Finite-beta equilibrium magnetic field perturbations in stellarator plasmas,” Nuclear Fusion **29**, 2115 (1989).

[18] H. YAMADA, K. IDA, H. IGUCHI, S. MORITA, O. KANEKO, H. ARIMOTO, M. HOSOKAWA, H. IDEI, S. KUBO, K. MATSUOKA, K. NISHIMURA, S. OKAMURA, Y. TAKEIRI, Y. TAKITA, C. TAKAHASHI, K. HANATANI, H. HOWE, S. Hirshman, and D. LEE, “Shafranov shift in the low aspect ratio heliotron torsatron compact helical system,” Nucl. Fusion **32**, 25–32 (1992).

[19] J. JOHNSON, D. Monticello, A. Reiman, A. SALAS, A. FRAGUAS, and S. Hirshman, “Comparison of atf and tj-ii stellarator equilibria as computed by the 3-d vmec and pies codes,” Computer Phys. Commun. **77**, 1–10 (1993).

[20] S. Besshou, K. Ogata, K. Kondo, T. Mizuuchi, K. Nagasaki, H. Okada, F. Sano, H. Zushi, and T. Obiki, “Detection of the free boundary plasma shift in a toroidal helical plasma on heliotron-e,” Nuclear Fusion **35**, 173 (1995).

[21] S. Besshou, N. Fujita, K. Ogata, K. Kondo, Y. Kurimoto, T. Mizuuchi, K. Nagasaki, H. Okada, F. Sano, and T. Obiki, “Dipole moment of the pfirsch-schluter current in a finite beta stellarator plasma in heliotron e,” Nuclear Fusion **37**, 13 (1997).

[22] S. Arndt, P. Merkel, D. Monticello, and A. Reiman, “Finite-beta equilibria for wendelstein 7-x configurations using the princeton iterative equilibrium solver code,” Phys. Plasmas **6**, 1246–1252 (1999).

[23] J. D. Hanson, S. P. Hirshman, S. F. Knowlton, L. L. Lao, E. A. Lazarus, and J. M. Shields, “V3fit: a code for three-dimensional equilibrium reconstruction,” Nucl. Fusion **49** (2009).

[24] J. D. Hanson, D. T. Anderson, M. Cianciosa, P. Franz, J. H. Harris, G. H. Hartwell, S. P. Hirshman, S. F. Knowlton, L. L. Lao, E. A. Lazarus, L. Marrelli, D. A. Maurer, J. C. Schmitt, A. C. Sontag, B. A. Stevenson, and D. Terranova, “Non-axisymmetric equilibrium reconstruction for stellarators, reversed field pinches and tokamaks,” Nucl. Fusion **53** (2013).

[25] G. R. Dennis, S. R. Hudson, D. Terranova, P. Franz, R. L. Dewar, and M. J. Hole, “Minimally constrained model of self-organized helical states in reversed-field pinches,” Phys. Rev. Lett. **111** (2013).

[26] D. Terranova, L. Marrelli, J. D. Hanson, S. P. Hirshman, M. Cianciosa, and P. Franz, "Helical equilibrium reconstruction with v3fit in the rfx-mod reversed field pinch," Nucl. Fusion **53** (2013).

[27] J. C. Schmitt, J. N. Talmadge, D. T. Anderson, and J. D. Hanson, "Modeling, measurement, and 3-d equilibrium reconstruction of the bootstrap current in the helically symmetric experiment," Phys. Plasmas **21** (2014).

[28] S. A. Lazerson and D.-D. Team, "Three-dimensional equilibrium reconstruction on the diii-d device," Nucl. Fusion **55** (2015).

[29] A. Reiman, N. M. Ferraro, A. Turnbull, J. K. Park, A. Cerfon, T. E. Evans, M. J. Lanctot, E. A. Lazarus, Y. Liu, G. McFadden, D. Monticello, and Y. Suzuki, "Tokamak plasma high field side response to an $n = 3$ magnetic perturbation: a comparison of 3d equilibrium solutions from seven different codes," Nucl. Fusion **55** (2015).

[30] M. Cianciosa, A. Wingen, S. P. Hirshman, S. K. Seal, E. A. Unterberg, R. S. Wilcox, P. Piovesan, L. Lao, and F. Turco, "Helical core reconstruction of a diii-d hybrid scenario tokamak discharge," Nucl. Fusion **57** (2017).

[31] Y. Suzuki, "Hint modeling of three-dimensional tokamaks with resonant magnetic perturbation," Plasma Phys. Control. Fusion **59** (2017).

[32] A. Wingen, R. S. Wilcox, M. R. Cianciosa, S. K. Seal, E. A. Unterberg, J. M. Hanson, S. P. Hirshman, L. L. Lao, N. C. Logan, C. Paz-Soldan, and M. W. Shafer, "Use of reconstructed 3d vmec equilibria to match effects of toroidally rotating discharges in diii-d," Nucl. Fusion **57** (2017).

[33] M. Cianciosa, S. P. Hirshman, S. K. Seal, and M. W. Shafer, "3d equilibrium reconstruction with islands," Plasma Phys. Control. Fusion **60** (2018).

[34] X. Ma, M. R. Cianciosa, D. A. Ennis, J. D. Hanson, G. J. Hartwell, J. L. Herfindal, E. C. Howell, S. F. Knowlton, D. A. Maurer, and P. J. Traverso, "Determination of current and rotational transform profiles in a current-carrying stellarator using soft x-ray emissivity measurements," Phys. Plasmas **25** (2018).

[35] K. Aleynikova, S. R. Hudson, P. Helander, A. Kumar, J. Geiger, M. Hirsch, J. Loizu, C. Nuehrenberg, K. Rahbarnia, Z. Qu, Y. Gao, H. Thomsen, Y. Turkin, M. Zanini, and W.-X. Team, "Model for current drive induced crash cycles in w7-x," Nucl. Fusion **61** (2021).

[36] S. A. Lazerson, S. Sakakibara, and Y. Suzuki, "A magnetic diagnostic code for 3d fusion equilibria," Plasma Phys. Control. Fusion **55**, 025014 (2013).

[37] R. Koeberl, U. von Toussaint, H.-J. Bungartz, J. G. Schilling, C. Albert, and W.-X. Team, "Uncertainty quantification in three-dimensional magnetohydrodynamic equilibrium reconstruction via surrogate-assisted bayesian inference," Contrib. Plasma Phys. **63** (2023).

[38] S. A. Lazerson, O. P. Ford, C. Nuehrenberg, S. Aekaeslompolo, P. Z. Poloskei, M. Machielsen, P. McNeely, L. Vano, N. Rust, S. Bozhenkov, T. W. C. Neelis, J. P. Graves, D. Pfefferle, A. Spanier, D. Hartmann, N. Marushchenko, Y. Turkin, M. Hirsch, N. Chaudhary, U. Hoefel, T. Stange, G. Weir, N. Pablant, A. Langenberg, P. Traverso, P. Valson, J. Knauer, K. J. Brunner, E. Pasch, M. Beurskens, H. Damm, G. Fuchert, P. Nelde, E. Scott, U. Hergenhahn, A. Pavone, K. Rahbarnia, T. Andreeva, J. Schilling, C. Brandt, U. Neuner, H. Thomsen, M. Jakubowski, A. Ali, Y. Gao, H. Niemann, A. P. Sitjes, R. Koenig, R. C. Wolf, and W.-X. Team, "Validation of the beams3d neutral beam deposition model on wendelstein 7-x," Nucl. Fusion **60** (2020).

[39] Y. Nakamura, T. Matsumoto, M. Wakatani, S. Galkin, V. Drozdov, A. Martynov, Y. Poshekhonov, K. Ichiguchi, L. Garcia, B. Carreras, C. Nuhrenberg, W. Cooper, and J. Johnson, "Comparison of the calculations of the stability properties of a specific stellarator equilibrium with different mhd stability codes," JOURNAL OF COMPUTATIONAL PHYSICS **128**, 43–57 (1996).

[40] A. D. Turnbull, N. M. Ferraro, V. A. Izzo, E. A. Lazarus, J. .-. Park, W. A. Cooper, S. P. Hirshman, L. L. Lao, M. J. Lanctot, S. Lazerson, Y. Q. Liu, A. Reiman, and F. Turco, "Comparisons of linear and nonlinear plasma response models for non-axisymmetric perturbations," Phys. Plasmas **20**, 54th Annual Meeting of the APS Division of Plasma Physics, Province, RI, 2012 (2013).

[41] J. Loizu, S. R. Hudson, and C. Nuehrenberg, "Verification of the spec code in stellarator geometries," Phys. Plasmas **23** (2016).

[42] J. Loizu, S. R. Hudson, C. Nuehrenbergi, J. Geiger, and P. Helander, "Equilibrium β-limits in classical stellarators," J. Plasma Phys. **83** (2017).

[43] S. R. Hudson, R. L. Dewar, G. Dennis, M. J. Hole, M. McGann, G. Von Nessi, and S. Lazerson, "Computation of multi-region relaxed magnetohydrodynamic equilibria," Physics of Plasmas **19**, 112502 (2012).

[44] S. P. Hirshman, R. Sanchez, and C. R. Cook, "SIESTA: A scalable iterative equilibrium solver for toroidal applications," Physics of Plasmas **18**, 062504 (2011).

[45] R. Dewar and S. Hudson, "Stellarator symmetry," Physica D: Nonlinear Phenomena **112**, Proceedings of the Workshop on Time-Reversal Symmetry in Dynamical Systems, 275–280 (1998).

[46] M. Cianciosa, "Modeling symmetry breaking islands in the Compact Toroidal Hybrid (CTH) using SIESTA," 67th Annual Meeting of the APS Division of Plasma Physics (2025).

[47] M. D. Pandya, M. C. ArchMiller, M. R. Cianciosa, D. A. Ennis, J. D. Hanson, G. J. Hartwell, J. D. Hebert, J. L. Herfindal, S. F. Knowlton, X. Ma, S. Massidda, D. A. Maurer, N. A. Roberds, and P. J. Traverso, "Low edge safety factor operation and passive disruption avoidance in current carrying plasmas by the addition of stellarator rotational transform," Physics of Plasmas **22**, 110702 (2015).

[48] D. W. Dudt, R. Conlin, D. Panici, and E. Kolemen, “The DESC stellarator code suite Part 3: Quasi-symmetry optimization,” Journal of Plasma Physics **89**, Publisher: Cambridge University Press, 955890201 (2023).

[49] D. Panici, R. Conlin, D. Dudt, K. Unalmis, and E. Kolemen, “The DESC stellarator code suite. Part 1. Quick and accurate equilibria computations,” Journal of Plasma Physics **89**, 955890303 (2023).

[50] R. Conlin, D. W. Dudt, D. Panici, and E. Kolemen, “The desc stellarator code suite. part 2. perturbation and continuation methods,” Journal of Plasma Physics **89**, 955890305 (2023).

[51] F. Zernike and F. J. M. Stratton, “Diffraction Theory of the Knife-Edge Test and its Improved Form, The Phase-Contrast Method,” Monthly Notices of the Royal Astronomical Society **94**, 377–384 (1934).

[52] Z. S. Qu, D. Pfefferle, S. R. Hudson, A. Baillod, A. Kumar, R. L. Dewar, and M. J. Hole, “Coordinate parameterisation and spectral method optimisation for beltrami field solver in stellarator geometry,” Plasma Phys. Control. Fusion **62** (2020).

[53] V. L. Genberg, G. J. Michels, and K. B. Doyle, “Orthogonality of Zernike polynomials,” in Optomechanical design and engineering 2002, Vol. 4771, edited by A. E. Hatheway (International Society for Optics and Photonics, 2002), pp. 276–286.

[54] A. Yen, “Straightforward path to Zernike polynomials,” Journal of Micro/Nanopatterning, Materials, and Metrology **20** (2021).

[55] K. Niu and C. Tian, “Zernike polynomials and their applications,” Journal of Optics **24**, 123001 (2022).

[56] R. Conlin, J. Schilling, D. W. Dudt, D. Panici, R. Jorge, and E. Kolemen, *High Order Free Boundary MHD Equilibria in DESC*, arXiv:2412.05680 [physics], Dec. 2024.

[57] W. Dommaschk, “Representations for vacuum potentials in stellarators,” Computer Physics Communications **40**, 203–218 (1986).

[58] S. A. Lazerson, J. Loizu, S. Hirshman, and S. R. Hudson, “Verification of the ideal magnetohydrodynamic response at rational surfaces in the vmec code,” Physics of Plasmas **23**, 012507 (2016).

[59] G. R. Dennis, S. R. Hudson, R. L. Dewar, and M. J. Hole, “The infinite interface limit of multiple-region relaxed magnetohydrodynamics,” Physics of Plasmas **20**, 032509 (2013).

[60] J. M. Greene and J. L. Johnson, “Determination of hydromagnetic equilibria,” The Physics of Fluids **4**, 875–890 (1961).

[61] D. GARREN and A. BOOZER, “Finite beta-effects in quasi-helical stellarators,” PHYSICS OF PLASMAS **1**, 139–149 (1994).

[62] D. GARREN and A. BOOZER, “Magnetic-field strength of toroidal plasma equilibria,” PHYSICS OF FLUIDS B-PLASMA PHYSICS **3**, 2805–2821 (1991).

[63] D. GARREN and A. BOOZER, “Existence of quasihelically symmetrical stellarators,” PHYSICS OF FLUIDS B-PLASMA PHYSICS **3**, 2822–2834 (1991).

[64] G. G. Plunk, M. Landreman, and P. Helander, “Direct construction of optimized stellarator shapes. part 3. omnigenity near the magnetic axis,” JOURNAL OF PLASMA PHYSICS **85** (2019).

[65] R. Jorge, W. Sengupta, and M. Landreman, “Near-axis expansion of stellarator equilibrium at arbitrary order in the distance to the axis,” JOURNAL OF PLASMA PHYSICS **86** (2020).

[66] R. Jorge, W. Sengupta, and M. Landreman, “Construction of quasisymmetric stellarators using a direct coordinate approach,” NUCLEAR FUSION **60** (2020).

[67] M. Landreman and R. Jorge, “Magnetic well and mercier stability of stellarators near the magnetic axis,” JOURNAL OF PLASMA PHYSICS **86** (2020).

[68] M. Landreman, “Figures of merit for stellarators near the magnetic axis,” JOURNAL OF PLASMA PHYSICS **87** (2021).

[69] W. Sengupta, E. Rodriguez, R. Jorge, M. Landreman, and A. Bhattacharjee, “Stellarator equilibrium axis-expansion to all orders in distance from the axis for arbitrary plasma beta,” JOURNAL OF PLASMA PHYSICS **90** (2024).

[70] W. Sengupta, N. Nikulsin, R. Gaur, and A. Bhattacharjee, “Asymptotic quasisymmetric high-beta three-dimensional magnetohydrodynamic equilibria near axisymmetry,” JOURNAL OF PLASMA PHYSICS **90** (2024).

[71] E. Rodriguez, W. Sengupta, and A. Bhattacharjee, “Constructing the space of quasisymmetric stellarators through near-axis expansion,” PLASMA PHYSICS AND CONTROLLED FUSION **65** (2023).

[72] E. Rodriguez, “Magnetohydrodynamic stability and the effects of shaping: a near-axis view for tokamaks and quasisymmetric stellarators,” JOURNAL OF PLASMA PHYSICS **89** (2023).

[73] M. Landreman, “Mapping the space of quasisymmetric stellarators using optimized near-axis expansion,” JOURNAL OF PLASMA PHYSICS **88** (2022).

[74] N. Duignan and J. D. Meiss, “Normal forms and near-axis expansions for beltrami magnetic fields,” PHYSICS OF PLASMAS **28** (2021).

[75] M. Hirsch, J. Baldzuhn, C. Beidler, R. Brakel, R. Burhenn, A. Dinklage, H. Ehmler, M. Endler, V. Erckmann, Y. Feng, J. Geiger, L. Giannone, G. Grieger, P. Grigull, H.-J. Hartfuss, D. Hartmann, R. Jaenicke, R. Koenig, H. P. Laqua, H. Maassberg, K. McCormick, F. Sardei, E. Speth, U. Stroth, F. Wagner, A. Weller, A. Werner, H. Wobig, S. Zoletnik, and W. A. Team, "Major results from the stellarator wendelstein 7-as," PLASMA PHYSICS AND CONTROLLED FUSION **50** (2008).

[76] H. Wobig, "Theory of advanced stellarators," PLASMA PHYSICS AND CONTROLLED FUSION **41**, 25th EPS Conference on Controlled Fusion and Plasma Physics / International Congress on Plasma Physics, PRAGUE, CZECH REPUBLIC, JUN 29-JUL 03, 1998, A159–A173 (1999).

[77] J. Chen, N. Nakajima, and M. Okamoto, "Global mode analysis of ideal magnetohydrodynamic modes in a heliotron/torsatron system: i. mercier-unstable equilibria," PHYSICS OF PLASMAS **6**, 40th Annual Meeting of the Division of Plasma Physics of the American-Physical-Society, NEW ORLEANS, LA, NOV 16-20, 1998, 1562–1574 (1999).

[78] N. Nakajima, S. R. Hudson, and C. C. Hegna, "Properties of ballooning modes in the planar axis heliotron configurations with a large shafranov shift," FUSION SCIENCE AND TECHNOLOGY **51**, 15th International Stellarator Workshop, Lab Nacl Fus, CIEMAT, Madrid, SPAIN, OCT 03-07, 2005, 79–91 (2007).

[79] A. KATO, Y. NAKAMURA, and M. WAKATANI, "Trapped-particle confinement studies in l=2 torsatrons for additional helical-coils, radial electric-field and finite beta-effect," JOURNAL OF THE PHYSICAL SOCIETY OF JAPAN **60**, 494–511 (1991).

[80] C. Fuchs, J. Geiger, H. Hartfuss, H. Maassberg, and W.-A. Team, "Shafranov shift in the 'electron root' feature at the w7-as stellarator," FUSION ENGINEERING AND DESIGN **53**, IAEA TCM on ECRH Physics and Technology for Fusion Devices and the 11th Joint Workshop on Electron Cyclotron Emission and Electron Cyclotron Heating, OH, JAPAN, OCT 04-08, 1999, 309–314 (2001).

[81] C. Zhu, S. R. Hudson, Y. Song, and Y. Wan, "New method to design stellarator coils without the winding surface," Nuclear Fusion **58**, 016008 (2017).

[82] S. R. Hudson, D. Panici, C. Zhu, G. S. Woodbury Saudeau, A. Baillod, M. Cianciosa, and A. S. Ware, "Verification of the Shafranov shift in free-boundary VMEC, DESC, and SPEC calculations with elliptical geometry," Physics of Plasmas **32**, 043906 (2025).

[83] H. Yamada, K. Ida, H. Iguchi, S. Morita, O. Kaneko, H. Arimoto, M. Hosokawa, H. Idei, S. Kubo, K. Matsuoka, K. Nishimura, S. Okamura, Y. Takeiri, Y. Takita, C. Takahashi, K. Hanatani, H. Howe, S. Hirshman, and D. Lee, "Shafranov shift in the low aspect ratio heliotron/torsatron compact helical system," Nuclear Fusion **32**, 25 (1992).

[84] C. Fuchs, J. Geiger, H. Hartfuß, and H. Maaßberg, "Shafranov shift in the 'electron root' feature at the w7-as stellarator," Fusion Engineering and Design **53**, 309–314 (2001).

[85] A. H. Boozer, "What is a stellarator?" Physics of Plasmas **5**, 1647–1655 (1998).

[86] J. D. Hanson and J. R. Cary, "Elimination of stochasticity in stellarators," The Physics of Fluids **27**, 767–769 (1984).

[87] J. R. Cary and J. D. Hanson, "Stochasticity reduction," The Physics of Fluids **29**, 2464–2473 (1986).

[88] S. R. Hudson, D. A. Monticello, A. H. Reiman, A. H. Boozer, D. J. Strickler, S. P. Hirshman, and M. C. Zarnstorff, "Eliminating islands in high-pressure free-boundary stellarator magnetohydrodynamic equilibrium solutions," Phys. Rev. Lett. **89**, 275003 (2002).

[89] M. Landreman, B. Medasani, and C. Zhu, "Stellarator optimization for good magnetic surfaces at the same time as quasisymmetry," Physics of Plasmas **28**, 092505 (2021).

[90] A. Baillod, J. Loizu, J. P. Graves, and M. Landreman, "Stellarator optimization for nested magnetic surfaces at finite beta and toroidal current," Physics of Plasmas **29**, 042505 (2022).

[91] C. B. Smiet, J. Loizu, E. Balkovic, and A. Baillod, "Efficient single-stage optimization of islands in finite- β stellarator equilibria," Physics of Plasmas **32**, 012504 (2025).

[92] E. Ascasíbar, D. López-Bruna, F. Castejón, V. I. Vargas, V. Tribaldos, H. Maassberg, C. D. Beidler, R. Brakel, A. Dinklage, J. Geiger, J. H. Harris, A. Kus, T. Mizuuchi, S. Murakami, S. Okamura, R. Preuss, F. Sano, U. Stroth, Y. Suzuki, J. Talmadge, Y. Turkin, K. Y. Watanabe, H. Yamada, and M. Yokoyama, "Effect of rotational transform and magnetic shear on confinement of stellarators," Plasma and Fusion Research **3**, S1004–S1004 (2008).

[93] K. H. Burrell, "Effects of E×B velocity shear and magnetic shear on turbulence and transport in magnetic confinement devices," Physics of Plasmas **4**, 1499–1518 (1997).

[94] J. M. Greene, "Two-Dimensional Measure-Preserving Mappings," Journal of Mathematical Physics **9**, 760–768 (1968).

[95] J. M. Greene, "A method for determining a stochastic transition," Journal of Mathematical Physics **20**, 1183–1201 (1979).

[96] M. Landreman, B. Medasani, F. Wechsung, A. Giuliani, R. Jorge, and C. Zhu, "SIMSOPT: A flexible framework for stellarator optimization," Journal of Open Source Software **6**, 3525 (2021).

[97] D. Lee, J. Harris, and G. Lee, "Magnetic island widths due to field perturbations in toroidal stellarators," Nuclear Fusion **30**, 2177 (1990).

[98] J. R. Cary and J. D. Hanson, "Simple method for calculating island widths," Physics of Fluids B: Plasma Physics **3**, 1006–1014 (1991).

[99] T. S. Pedersen, J. P. Kremer, R. G. Lefrancois, Q. Marksteiner, N. Pomphrey, W. Reiersen, F. Dahlgren, and X. Sarasola, "Construction and initial operation of the columbia nonneutral torus," Fusion Science and Technology **50**, 372–381 (2006).

[100] L. B. Centurión and J. J. Martinell, "MHD equilibria with magnetic islands in the TJ-II heliac," Radiation Effects and Defects in Solids **174**, 9–18 (2019).

[101] J. D. Hanson, S. P. Hirshman, S. F. Knowlton, L. L. Lao, E. A. Lazarus, and J. M. Shields, "V3FIT: a code for three-dimensional equilibrium reconstruction," Nuclear Fusion **49**, 075031 (2009).

[102] M. Cianciosa, S. P. Hirshman, S. K. Seal, and M. W. Shafer, "3D equilibrium reconstruction with islands," Plasma Physics and Controlled Fusion **60**, 044017 (2018).

[103] J. Brackbill and D. Barnes, "The effect of nonzero $\nabla \cdot$ B on the numerical solution of the magnetohydrodynamic equations," Journal of Computational Physics **35**, 426–430 (1980).

[104] G. Tóth, "The $\nabla \cdot \mathbf{B} = 0$ constraint in shock-capturing magnetohydrodynamics codes," Journal of Computational Physics **161**, 605–652 (2000).

[105] G. Tóth and P. Roe, "Divergence- and curl-preserving prolongation and restriction formulas," Journal of Computational Physics **180**, 736–750 (2002).

[106] D. S. Balsara, "Second-order-accurate schemes for magnetohydrodynamics with divergence-free reconstruction," The Astrophysical Journal Supplement Series **151**, 149 (2004).

[107] F. Mackay, R. Marchand, and K. Kabin, "Divergence-free magnetic field interpolation and charged particle trajectory integration," Journal of Geophysical Research: Space Physics **111** (2006).

[108] P. Probert, "High-Performance Interpolation of Stellarator Magnetic Fields," IEEE Transactions on Plasma Science **39**, 1051–1054 (2011).

[109] D. Pfefferlé, W. Cooper, J. Graves, and C. Misev, "VENUS-LEVIS and its spline-Fourier interpolation of 3D toroidal magnetic field representation for guiding-centre and full-orbit simulations of charged energetic particles," Computer Physics Communications **185**, 3127–3140 (2014).

[110] B. Ravu, M. Rudman, G. Metcalfe, D. R. Lester, and D. V. Khakhar, "Creating analytically divergence-free velocity fields from grid-based data," Journal of Computational Physics **323**, 75–94 (2016).

[111] M. Yang, D. del-Castillo-Negrete, G. Zhang, and M. T. Beidler, "A divergence-free constrained magnetic field interpolation method for scattered data," Physics of Plasmas **30**, 033901 (2023).

[112] G. J. Hartwell, S. F. Knowlton, J. D. Hanson, D. A. Ennis, and D. A. Maurer, “Design, construction, and operation of the compact toroidal hybrid,” Fusion Science and Technology **72**, 76–90 (2017).

[113] K. Elsasser, “Magnetic field line flow as a Hamiltonian problem,” Plasma Physics and Controlled Fusion **28**, 1743–1752 (1986).

[114] J. D. Kilkenny, S. G. Glendinning, S. W. Haan, B. A. Hammel, J. D. Lindl, D. Munro, B. A. Remington, S. V. Weber, J. P. Knauer, and C. P. Verdon, “A review of the ablative stabilization of the Rayleigh–Taylor instability in regimes relevant to inertial confinement fusion,” Physics of Plasmas **1**, 1379–1389 (1994).

[115] Y. Zhou, B. A. Remington, H. F. Robey, A. W. Cook, S. G. Glendinning, A. Dimits, A. C. Buckingham, G. B. Zimmerman, E. W. Burke, T. A. Peyser, W. Cabot, and D. Eliason, “Progress in understanding turbulent mixing induced by Rayleigh–Taylor and Richtmyer–Meshkov instabilities,” Physics of Plasmas **10**, 1883–1896 (2003).

[116] R. Betti, V. N. Goncharov, R. L. McCrory, and C. P. Verdon, “Growth rates of the ablative Rayleigh–Taylor instability in inertial confinement fusion,” Physics of Plasmas **5**, 1446–1454 (1998).

[117] J. H. Hunter and R. W. Whitaker, “Kelvin-Helmholtz Instabilities in the Interstellar Medium,” Annals of the New York Academy of Sciences **497**, 144–153 (1987).

[118] M. Faganello and F. Califano, “Magnetized Kelvin–Helmholtz instability: theory and simulations in the earth’s magnetosphere context,” Journal of Plasma Physics **83**, 535830601 (2017).

[119] Q. Chen, A. Otto, and L. C. Lee, “Tearing instability, Kelvin-Helmholtz instability, and magnetic reconnection,” Journal of Geophysical Research: Space Physics **102**, 151–161 (1997).

[120] Z.-Y. Pu and M. G. Kivelson, “Kelvin-Helmholtz instability at the magnetopause: solution for compressible plasmas,” Journal of Geophysical Research: Space Physics **88**, 841–852 (1983).

[121] A. Miura and P. L. Pritchett, “Nonlocal stability analysis of the MHD Kelvin-Helmholtz instability in a compressible plasma,” Journal of Geophysical Research: Space Physics **87**, 7431–7444 (1982).

[122] X. Garbet, C. Fenzi, H. Capes, P. Devynck, and G. Antar, “Kelvin–helmholtz instabilities in tokamak edge plasmas,” Physics of Plasmas **6**, 3955–3965 (1999).

[123] J. R. Myra, D. A. D’Ippolito, D. A. Russell, M. V. Umansky, and D. A. Baver, “Analytical and numerical study of the transverse kelvin–helmholtz instability in tokamak edge plasmas,” Journal of Plasma Physics **82**, 905820210 (2016).

[124] S. Chandrasekhar, *Hydrodynamic and Hydromagnetic Stability*, Dover Books on Physics Series (Dover Publications, 1981).

[125] A. Hillier, "Ideal MHD Instabilities, with a focus on the Rayleigh–Taylor and Kelvin–Helmholtz Instabilities," in *Topics in magnetohydrodynamic topology, reconnection and stability theory*, edited by D. MacTaggart and A. Hillier (Springer International Publishing, Cham, 2020), pp. 1–36.

[126] L. D. Landau, "On the Problem of Turbulence," Compt. Rend. Acad. Sci. URSS **44** (1944).

[127] J. W. Miles, "On the disturbed motion of a plane vortex sheet," Journal of Fluid Mechanics **4**, 538–552 (1958).

[128] M. S. Plesset and D.-Y. Hsieh, "General analysis of the stability of superposed fluids," The Physics of Fluids **7**, 1099–1108 (1964).

[129] J. W. Miles, "Comments on "general analysis of the stability of superposed fluids"," The Physics of Fluids **8**, 1754–1755 (1965).

[130] W. Blumen, "Shear layer instability of an inviscid compressible fluid," Journal of Fluid Mechanics **40**, 769–781 (1970).

[131] W. Blumen, P. G. Drazin, and D. F. Billings, "Shear layer instability of an inviscid compressible fluid. part 2," Journal of Fluid Mechanics **71**, 305–316 (1975).

[132] S. R. Choudhury and R. V. E. Lovelace, "On the Kelvin-Helmholtz instabilities of supersonic shear layers," The Astrophysical Journal **283**, 331 (1984).

[133] T. P. Ray, "The effects of a simple shear layer on the growth of kelvin–helmholtz instabilities," Monthly Notices of the Royal Astronomical Society **198**, 617–625 (1982).

[134] J. A. Fejer, "Hydromagnetic stability at a fluid velocity discontinuity between compressible fluids," The Physics of Fluids **7**, 499–503 (1964).

[135] A. K. Sen, "Effect of compressibility on Kelvin–Helmholtz instability in a plasma," The Physics of Fluids **7**, 1293–1298 (1964).

[136] A. G. Gonzalez and J. Gratton, "The Kelvin–Helmholtz instability in a compressible plasma: the role of the orientation of the magnetic field with respect to the flow," Journal of Plasma Physics **51**, 43–60 (1994).

[137] G. Peyrichon, H. El-Rabii, J.-F. Ripoll, A. Casner, A. Michael, V. G. Merkin, and O. A. Hurricane, "Kelvin–Helmholtz instability under stabilizing parallel magnetic field in nonhomogeneous compressible MHD flows," Physics of Plasmas **32**, 042112 (2025).

[138] T. P. Ray and A. I. Ershkovich, "Kelvin–Helmholtz instabilities in a sheared compressible plasma," Monthly Notices of the Royal Astronomical Society **204**, 821–831 (1983).

[139] I. B. Bernstein and D. L. Book, “Effect of compressibility on the Rayleigh–Taylor instability,” The Physics of Fluids **26**, 453–458 (1983).

[140] S. Roy Choudhury and R. V. E. Lovelace, “On the Kelvin-Helmholtz Instabilities of High-Velocity Magnetized Shear Layers,” The Astrophysical Journal **302**, 188 (1986).

[141] T. Tajima and J. N. Leboeuf, “Kelvin–Helmholtz instability in supersonic and super–Alfvénic fluids,” The Physics of Fluids **23**, 884–888 (1980).

[142] S. Choudhury, “Nonlinear evolution of the kelvin–helmholtz instability of supersonic tangential velocity discontinuities,” Journal of Mathematical Analysis and Applications **214**, 561–586 (1997).

[143] A. Shimony, W. C. Wan, S. R. Klein, C. C. Kuranz, R. P. Drake, D. Shvarts, and G. Malamud, “Construction and validation of a statistical model for the nonlinear kelvin-helmholtz instability under compressible, multimode conditions,” Physics of Plasmas **25**, 122112 (2018).

[144] A. Briard, J.-F. Ripoll, A. Michael, B.-J. Gréa, G. Peyrichon, M. Cosmides, H. El-Rabii, M. Faganello, V. G. Merkin, K. A. Sorathia, A. Y. Ukhorskiy, J. G. Lyon, A. Retino, V. Bouffetier, L. Ceurvorst, H. Sio, O. A. Hurricane, V. A. Smalyuk, and A. Casner, “The inviscid incompressible limit of kelvin–helmholtz instability for plasmas,” Frontiers in Physics **Volume 12 - 2024** (2024).

[145] M. Mitchner and R. K. M. Landshoff, “Rayleigh–Taylor instability for compressible fluids,” The Physics of Fluids **7**, 862–866 (1964).

[146] W. G. Mathews and G. R. Blumenthal, “Rayleigh-Taylor Stability of Compressible and Incompressible Radiation-Supported Surfaces and Slabs: Application to QSO Clouds,” The Astrophysical Journal **214**, 10 (1977).

[147] L. Baker, “Compressible rayleigh–taylor instability,” The Physics of Fluids **26**, 950–952 (1983).

[148] D. Livescu, “Compressibility effects on the Rayleigh–Taylor instability growth between immiscible fluids,” Physics of Fluids **16**, 118–127 (2004).

[149] Y. Zhou, “Rayleigh–Taylor and Richtmyer–Meshkov instability induced flow, turbulence, and mixing. I,” Physics Reports **720-722**, Rayleigh-Taylor and Richtmyer-Meshkov instability induced flow, turbulence, and mixing. I, 1–136 (2017).

[150] S. Liberatore and S. Bouquet, “Analytical modeling of magnetic rayleigh–taylor instabilities in compressible fluids,” Physics of Fluids **20**, 116101 (2008).

[151] S. Liberatore, S. Jaouen, E. Tabakhoff, and B. Canaud, “Compressible magnetic rayleigh–taylor instability in stratified plasmas: comparison of analytical and numerical results in the linear regime,” Physics of Plasmas **16**, 044502 (2009).

[152] Díaz, A. J., Khomenko, E., and Collados, M., "Rayleigh-taylor instability in partially ionized compressible plasmas: one fluid approach," A&A **564**, A97 (2014).

[153] J. M. Stone and T. Gardiner, "The magnetic rayleigh-taylor instability in three dimensions," The Astrophysical Journal **671**, 1726 (2007).

[154] M. R. Gupta, L. Mandal, S. Roy, and M. Khan, "Effect of magnetic field on temporal development of rayleigh–taylor instability induced interfacial nonlinear structure," Physics of Plasmas **17**, 012306 (2010).

[155] A. Briard, B.-J. Gréa, and F. Nguyen, "Growth rate of the turbulent magnetic rayleigh-taylor instability," Phys. Rev. E **106**, 065201 (2022).

[156] R. Betti and J. P. Freidberg, "Radial discontinuities in tokamak magnetohydrodynamic equilibria with poloidal flow," Physics of Plasmas **7**, 2439–2448 (2000).

[157] L. Guazzotto, R. Betti, J. Manickam, and S. Kaye, "Numerical study of tokamak equilibria with arbitrary flow," Physics of Plasmas **11**, 604–614 (2004).

[158] G. A. Hoshoudy and M. K. Awasthi, "Compressibility effects on the Kelvin–Helmholtz and Rayleigh–Taylor instabilities between two immiscible fluids flowing through a porous medium," The European Physical Journal Plus **135**, 169 (2020).

[159] K. M. Srivastava, "On the Hydromagnetic Kelvin-Helmholtz Instability between Compressible Fluids," Zeitschrift für Naturforschung A **29**, 888–892 (1974).

[160] L. D. Landau and E. M. Lifshitz, "Chapter VIII - Magnetohydrodynamics," in *Electrodynamics of Continuous Media*, Vol. 8, Second, Course of Theoretical Physics (Pergamon, 1984), pp. 225–256.

[161] A. M. Garofalo, A. D. Turnbull, E. J. Strait, M. E. Austin, J. Bialek, M. S. Chu, E. Fredrickson, R. J. La Haye, G. A. Navratil, L. L. Lao, E. A. Lazarus, M. Okabayashi, B. W. Rice, S. A. Sabbagh, J. T. Scoville, T. S. Taylor, M. L. Walker, and T. D.-D. Team, "Stabilization of the external kink and control of the resistive wall mode in tokamaks," Physics of Plasmas **6**, 1893–1898 (1999).

[162] A. A. Martynov and S. Y. Medvedev, "Resistive wall modes and related sideways forces in tokamak," Physics of Plasmas **27**, 012508 (2020).

[163] L. D. Landau and E. M. Lifshitz, "Chapter IX - Shock Waves," in *Fluid mechanics*, Vol. 6, Second, Course of Theoretical Physics (Pergamon, 1987), pp. 313–360.

[164] A. Mason and C. Singh, "Helping students learn effective problem solving strategies by reflecting with peers," American Journal of Physics **78**, 748–754 (2010).

[165] S.-Y. Lin and C. Singh, "Using isomorphic problems to learn introductory physics," Phys. Rev. ST Phys. Educ. Res. **7**, 020104 (2011).

[166] B. R. Brown, A. Mason, and C. Singh, “Improving performance in quantum mechanics with explicit incentives to correct mistakes,” Phys. Rev. Phys. Educ. Res. **12**, 010121 (2016).

[167] C. Henderson and K. A. Harper, “Quiz corrections: improving learning by encouraging students to reflect on their mistakes,” The Physics Teacher **47**, 581–586 (2009).

[168] A. Mason, E. Yerushalmi, E. Cohen, and C. Singh, “Learning from mistakes: the effect of students’ written self-diagnoses on subsequent problem solving,” The Physics Teacher **54**, 87–90 (2016).

[169] J. D. Bransford and D. L. Schwartz, “Chapter 3: rethinking transfer: a simple proposal with multiple implications,” Review of research in education **24**, 61–100 (1999).

[170] D. L. Schwartz, J. M. Tsang, and K. P. Blair, *The abcs of how we learn: 26 scientifically proven approaches, how they work, and when to use them* (WW Norton & Company, 2016).

[171] K. A. Ericsson, R. T. Krampe, and C. Tesch-Römer, “The role of deliberate practice in the acquisition of expert performance.,” Psychological review **100**, 363 (1993).

[172] E. Burkholder, K. Wang, and C. Wieman, “Validated diagnostic test for introductory physics course placement,” Phys. Rev. Phys. Educ. Res. **17**, 010127 (2021).

[173] S. Salehi, S. Cotner, and C. J. Ballen, “Variation in incoming academic preparation: consequences for minority and first-generation students,” Frontiers in Education **Volume 5 - 2020** (2020).

[174] C. S. Dweck, *Self-theories: their role in motivation, personality, and development* (Psychology press, 2013).

[175] C. J. Ballen, C. Wieman, S. Salehi, J. B. Searle, and K. R. Zamudio, “Enhancing diversity in undergraduate science: self-efficacy drives performance gains with active learning,” CBE—Life Sciences Education **16**, ar56 (2017).

Appendix 1

Free-Point Friday

The appendix of this dissertation will cover an intervention performed on an algebra based introductory physics lab course during the author's first year at Auburn. Most of this appendix is reproduced from,

Nathan D. Davis, Gabriel S. Woodbury Saudeau, Spencer H. Johnson, Eric W. Burkholder; Free-Point Friday: An Intervention Model for Introductory Physics. Phys. Teach. 1 February 2024; 62 (2): 84–86. `https://doi.org/10.1119/5.0094456`

with the permission of AIP Publishing.

A1.1 Background

Before the intervention, the course teaching assistants (TAs) noticed that students were getting on average, below 50% on their weekly lab quizzes. To help students resolve deficiencies in understanding and facilitate a greater understanding of the concepts covered in lecture, the TAs saw a need for an intervention. The concept for FPF originated from previous work in physics education research. It has been shown that interventions can reinforce a student's cognitive understanding and bolster their overall skills related to problem-solving, and that these skills could have far greater benefits even outside of the physics classroom [164]. Specifically, the application of isomorphic problems for practice to reinforce relevant concepts and explicit incentives like grade-recovery can have positive impacts on student performance [165, 166]. Wanting to leverage the potential gains from an intervention utilizing these characteristics, FPF was implemented by first-year graduate TAs to promote learning among students in an algebra-based introductory physics course while also incentivizing participation with grade recovery

Assessment	Percentage	Grades Dropped
Lecture Quizzes	10%	2 Lowest
Laboratory Quizzes	10%	2 Lowest
Laboratory Reports	15%	1 Lowest
Exams (3)	45%	1 Lowest
Final Exam	20%	N/A

Table A1.1: Course Assessment/Grading Structure

hence the name “Free-Point-Friday”.

The course studied was composed of two weekly 75-minute lectures and one 3-hour lab that met once weekly. The lab sessions typically began with a quiz on the content covered during the lecture portion of the class from the previous week. This was then followed up with review of the previous week’s quiz, which in total took approximately 1 hour of instructional time with the remaining 2 hours left for students to complete the assigned lab activity. The grading and assessment structure of the course is outlined in Table A1.1. The total enrollment in the course was 194 students; 57% of the students were women, 12% were first-generation college students, and 11% underrepresented minority students.

A1.2 Free-Point Friday Methodology

FPF had to have a flexible format that could provide multiple avenues for students to engage in the material at their comfort level. In practice, the TAs elected to schedule one day out of the week for the students to come and go at their leisure to review the incorrect items received on the previous week’s lab recitation quiz or resolve gaps in understanding. We chose Friday as there were no laboratory sections scheduled that day. While in attendance students had an option to either work on the new quiz with their peers, ask TAs questions while they circulate throughout the room, or sit amongst a group of their peers and interact with a TA as they review the material in an informal lecture format. Figure A1.1 provides a flow diagram of what a student would do when attending a typical FPF session.

This intervention required roughly 2 hours of volunteer time per week from on average

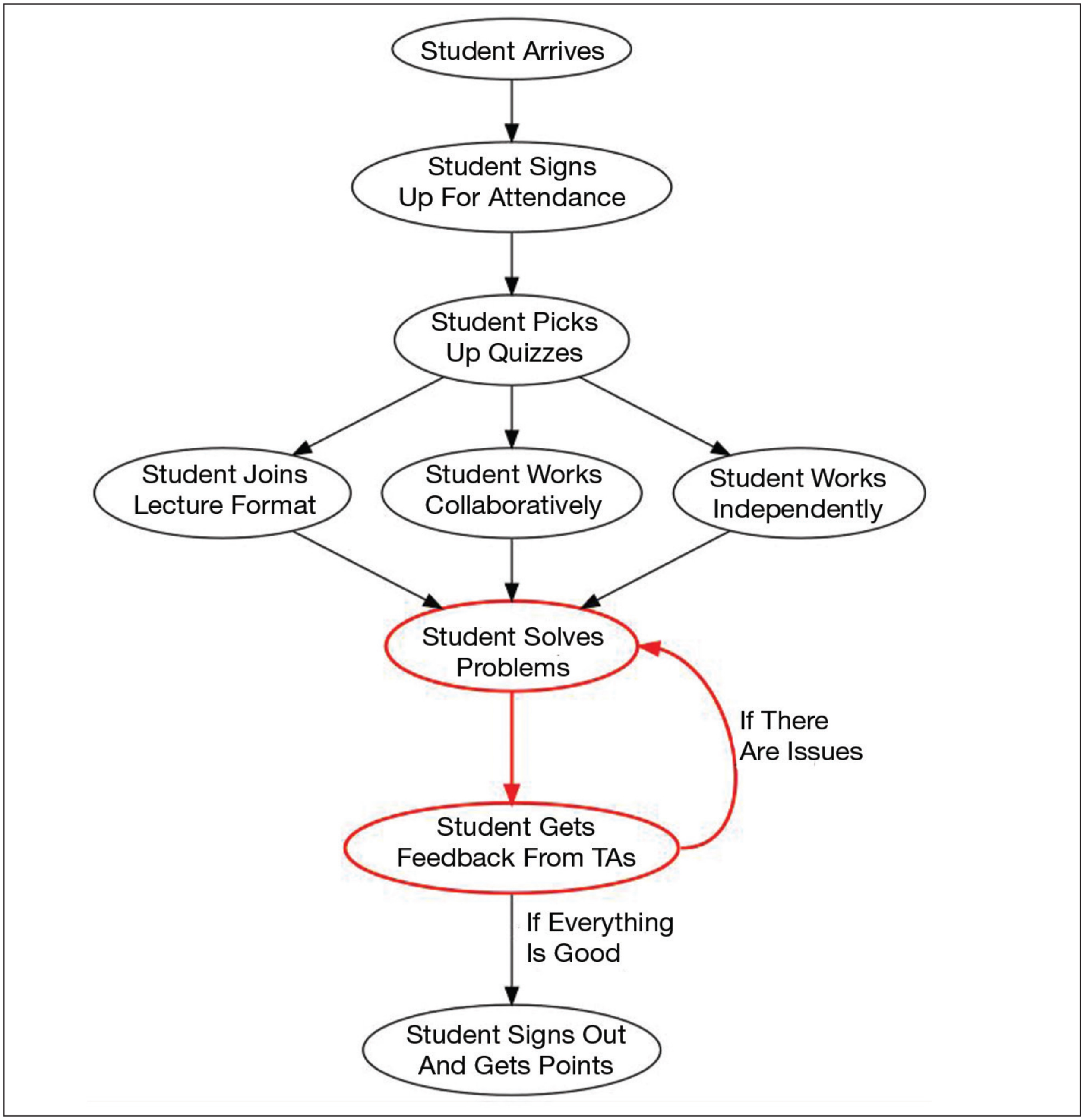

Figure A1.1: FPF Flow Diagram

4-5 TAs not necessarily associated with the course. On average, there was one TA in attendance per 3-4 students attending. It is also important to note that no extra training was provided for the TAs in preparation for the execution of FPF. While it is not replicable to always have TAs volunteer extra time, we believe the scale of the intervention is modest enough that it could easily be incorporated into existing course structures. For example, at Auburn, we are making the weekly quiz an online assignment completed before lab and then spending the recitation portion of the lab period doing an FPF-style activity with the students.

The goal behind FPF was to construct a positive and encouraging environment for students in this introductory physics class while giving students immediate feedback for them to assess their understanding of concepts. Utilizing this feedback can facilitate the student's ability to then apply skills and gain a better understanding of new problem sets to help resolve past mistakes while providing an opportunity for assessment correction to motivate practice and learning. Traditionally, assessment corrections are employed as an intervention to allow students an opportunity for grade recovery as well to take advantage of the benefits of the self-examination of mistakes. For example, some instructors have implemented forms of assessment corrections that include, but are not limited to, exam/quiz corrections to motivate students to self-assess their mistakes and hopefully correct their deficiency in understanding the topics covered [167, 168]. The first key distinction between those traditionally employed versus FPF is that FPF is wholly an interaction between students rather than between a student and a faculty member. The second difference is that the assessment correction was completed with quizzes that contained different problems than those seen on quizzes given in the lab. They covered the same material to give students a wider degree of exposure to different problems for deliberate practice on the topic of interest, while also motivating students with incentives for grade recovery and a free point. This also was designed to promote the near transfer of material [169]. The intervention was built upon two foundational principles of learning: Deliberate Practice and Motivation [170].

Deliberate Practice: Active participation in FPF inherently required deliberate practice of the material. The TAs intended to provide new questions with a slightly higher degree of difficulty than that of the quiz taken during the lab meeting. In doing this, students had exposure to more problems while having an opportunity to work through them with a sufficient level of support. The TAs provided the timely feedback that is essential for deliberate practice [171].

Motivation: The motivation piece was straightforward. Students who attended and actively participated in FPF were allowed to receive 50% of the points they had lost on the previous week's quiz or any previous quiz in case they had missed a previous session of FPF, plus an extra 1 point (quizzes were out of 10 points, so 10%) [170]. While the overall reward of points did not amount to any significant portion of the student's grade it was observed that students saw the benefit of attending FPF outside of grade recovery. So, for example, an average FPF student would receive 2.5 points on a quiz they initially received 5 out of 10 points on plus the free point for a total of 3.5 points added to their original grade. It is interesting to note that the low stakes high reward nature of the program provided sufficient motivation for students to complete the new quiz with minimal instruction as well as allowed students to examine the application and correction of previously made mistakes.

A1.3 Analysis

We collected data on the students who did and did not attend FPF from this course. For all students, we had physics diagnostic scores as well as data from a social psychological survey administered during the first lab period [172]. We also had all students' final exam scores. Only students' mindsets toward intelligence and science self-efficacy were correlated with exam performance after performing a backwards stepwise regression, so we only analyzed those factors in the final model [173]. The mindset questions were taken from Dweck, and the self-efficacy questions were taken from Ballen et al. [174, 175] We verified that the survey items loaded onto two distinct factors using confirmatory factor analysis. Finally, we had the FPF attendance records: 63 of the 154 students in the class attended FPF at least one time. Among students who attended at least once, the average attendance was 2.2 sessions (s.d = 1.5).

To analyze the effects of FPF on student performance, we conducted a multiple linear regression of their final exam grades. The model we tested was:

$$\text{Final Exam} = \beta_0 + \beta_1\text{Diagnostic} + \beta_2\text{FPF} + \beta_3\text{Social Psychological Factors}$$

The coefficient β_0 indicates the average final exam score for students with average physics preparation and self-efficacy in the control group. The coefficient β_1 measures the correlation between pre-test physics scores and final exam grades. The coefficient β_2 measures the effect of attending at least one FPF session while controlling for students' incoming physics knowledge (diagnostic score) and their social psychological factors (attitudes toward intelligence and science self-efficacy). This allows us to test whether the positive effects of FPF are due to more prepared students taking advantage of the extra points and whether the students who attended had more confidence in their ability to do science in the first place. The results are shown in Figure A1.2. The bars on the left represent the outcomes of the following regression equation:

$$\text{Final Exam} = \beta_0 + \beta_2\text{FPF}$$

which is mathematically equivalent to a t-test. The bars on the right of Figure A1.2 represent the outcomes of equation (1). The bars on the left indicate the outcomes of equation (2). In both cases, β_2 would represent the difference between the orange bar and the blue bar.

We see that students who attended at least one FPF session scored slightly better on the final exam (comparing solid orange with solid blue bars), but that effect was not statistically significant. However, once we controlled for incoming physics preparation and social-psychological factors, we saw that FPF students performed about 7% (0.42 standard deviations) better on the final exam (orange shaded bar versus blue shaded bar). This suggests that despite coming in with lower levels of physics preparation (correlation between FPF and incoming physics knowledge = -0.15, $p = 0.07$) and more negative mindsets toward science (correlation between mindset and FPF attendance = -0.14, $p = 0.07$), the FPF students were able to perform as well as some of the

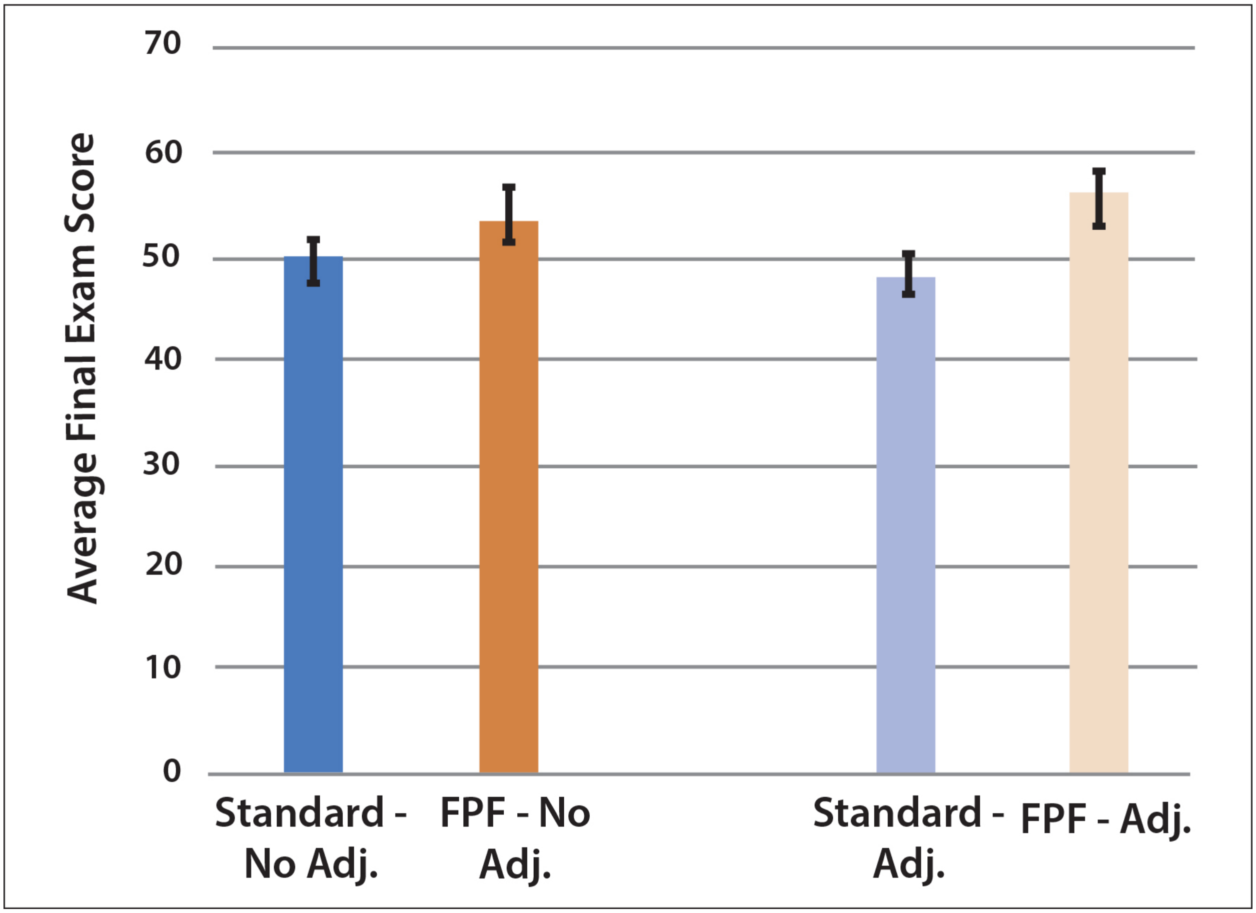

Figure A1.2: Exam scores for traditional and FPF students (left bars) as well as adjusted scores (right bars). Error bars represent the standard error on the grade estimates. Adjusted scores represent the scores for students with average diagnostic scores and incoming social psychological profiles as represented in equation 1 above.

more prepared students in the course. We will note that we measured several other dimensions of student thinking, including test anxiety, motivation to learn, interest in physics and sense of belonging, and none of these were able to explain the difference between FPF and non-FPF students.

It is important to note the limitations of a program like the FPF model discussed in this paper. The first one is the time commitment of a graduate student or instructor. Time must be considered when preparing a quiz consisting of new problems that are relevant to topics of interest along with the added 2 hours once a week to meet with students for the assessment correction and recitation. One shortcoming that was encountered was limited graduate students to accommodate approximately 45 students in attendance for the first session. This inevitably hurt students' initial perception of the activity, leading to slightly lower attendance. In our current implementation, students take the weekly quiz on WebAssign before coming to recitation. They then work in small groups on isomorphic practice problems. This requires minimal additional time from the students, but no additional TA time.

A1.4 Conclusion

We have shown how a modest intervention turning summative assessments into opportunities for deliberate practice and points recovery was correlated with improved final exam scores for roughly 40% of the students in an algebra-based physics course at Auburn University. Students were given weekly opportunities to receive supplemental instruction and work on more difficult isomorphic problems for both point-recovery and learning purposes. This shows that instructors wishing to improve learning can incorporate opportunities for isomorphic practice into their courses, and that minimal points are required to motivate students to participate.

Appendix 2

Detecting and Measuring Magnetic Islands in SIESTA Supplementary Material

A2.1 Tangent Map Calculation

To calculate the tangent map we must first define the map. The equations that define the map are the field line equations in Eq. (2.35) which we copy below for the reader,

$$\dot{s} = \frac{\partial s}{\partial v} = \frac{\mathcal{J}B^s}{\mathcal{J}B^v}$$

and,

$$\dot{u} = \frac{\partial u}{\partial v} = \frac{\mathcal{J}B^u}{\mathcal{J}B^v}$$

To advance the field-line the equations must be integrated from 0 to 2π, or $2\pi/N_{\text{fp}}$ if the system has field period symmetry. The tangent map itself cannot be directly calculated, rather it is obtained by solving the system of differential equations,

$$\frac{\partial}{\partial v}\mathbf{S} = \mathbf{C}\cdot\mathbf{S}, \quad \mathbf{S}(0) = \mathbf{I} \tag{A2.1}$$

where the matrix, $\mathbf{C}$, is defined as,

$$\mathbf{C} = \begin{pmatrix} \frac{\partial \dot{s}}{\partial s} & \frac{\partial \dot{s}}{\partial u} \\ \\ \frac{\partial \dot{u}}{\partial s} & \frac{\partial \dot{u}}{\partial u} \end{pmatrix} \tag{A2.2}$$

or in terms of the components,

$$\mathbf{C}_{1,1} = \frac{\partial \dot{s}}{\partial s} = \frac{\mathcal{J}B^v(\partial_s \mathcal{J}B^s) - \mathcal{J}B^s(\partial_s \mathcal{J}B^v)}{(\mathcal{J}B^v)^2}$$

$$\mathbf{C}_{1,2} = \frac{\partial \dot{s}}{\partial u} = \frac{\mathcal{J}B^v(\partial_u \mathcal{J}B^s) - \mathcal{J}B^s(\partial_u \mathcal{J}B^v)}{(\mathcal{J}B^v)^2}$$

$$\mathbf{C}_{2,1} = \frac{\partial \dot{u}}{\partial s} = \frac{\mathcal{J}B^v(\partial_s \mathcal{J}B^u) - \mathcal{J}B^u(\partial_s \mathcal{J}B^v)}{(\mathcal{J}B^v)^2}$$

$$\mathbf{C}_{2,2} = \frac{\partial \dot{u}}{\partial u} = \frac{\mathcal{J}B^v(\partial_u \mathcal{J}B^u) - \mathcal{J}B^u(\partial_u \mathcal{J}B^v)}{(\mathcal{J}B^v)^2}$$

The exact equations to be solved are then,

$$\begin{aligned}
\frac{\partial}{\partial v}\mathbf{S}_{1,1} &= \mathbf{C}_{1,1}\mathbf{S}_{1,1} + \mathbf{C}_{1,2}\mathbf{S}_{2,1} \\
\frac{\partial}{\partial v}\mathbf{S}_{1,2} &= \mathbf{C}_{1,1}\mathbf{S}_{1,2} + \mathbf{C}_{1,2}\mathbf{S}_{2,2} \\
\frac{\partial}{\partial v}\mathbf{S}_{2,1} &= \mathbf{C}_{2,1}\mathbf{S}_{1,1} + \mathbf{C}_{2,2}\mathbf{S}_{2,1} \\
\frac{\partial}{\partial v}\mathbf{S}_{2,2} &= \mathbf{C}_{2,1}\mathbf{S}_{1,2} + \mathbf{C}_{2,2}\mathbf{S}_{2,2}
\end{aligned} \tag{A2.3}$$

with the initial conditions, $\mathbf{S}_{1,1}(0) = \mathbf{S}_{2,2}(0) = 1$ and $\mathbf{S}_{1,2}(0) = \mathbf{S}_{2,1}(0) = 0$.

A2.2 Interpolation Method

As previously stated the divergence of the magnetic field can be expressed as,

$$\mathcal{J}(\nabla \cdot \mathbf{B}) = \frac{\partial(\mathcal{J}B^s)}{\partial s} + \frac{\partial(\mathcal{J}B^u)}{\partial u} + \frac{\partial(\mathcal{J}B^v)}{\partial v}$$

In SIESTA the magnetic field components, assuming stellarator symmetry have the following form,

$$\mathcal{J}B^s = \sum_{m,n} \mathcal{J}B^s_{mn}(s)\sin(mu + nN_{\text{fp}}v)$$

$$\mathcal{J}B^u = \sum_{m,n} \mathcal{J}B^u_{mn}(s)\cos(mu + nN_{\mathrm{fp}}v)$$

$$\mathcal{J}B^v = \sum_{m,n} \mathcal{J}B^v_{mn}(s)\cos(mu + nN_{\mathrm{fp}}v)$$

Substituting into the divergence equation then gives,

$$\begin{aligned}\mathcal{J}(\nabla \cdot B) = &\frac{\partial}{\partial s}\sum_{m,n} \mathcal{J}B^s_{mn}(s)\sin(mu + nN_{\mathrm{fp}}v)\\ &+\frac{\partial}{\partial u}\sum_{m,n} \mathcal{J}B^u_{mn}(s)\cos(mu + nN_{\mathrm{fp}}v)\\ &+\frac{\partial}{\partial v}\sum_{m,n} \mathcal{J}B^v_{mn}(s)\cos(mu + nN_{\mathrm{fp}}v)\end{aligned}$$

Putting all the terms under the same summation gives,

$$\begin{aligned}\mathcal{J}(\nabla \cdot B) = \sum_{m,n}\Bigg[&\frac{\partial}{\partial s}\mathcal{J}B^s_{mn}(s)\sin(mu + nN_{\mathrm{fp}}v)\\ &+\mathcal{J}B^u_{mn}(s)\frac{\partial}{\partial u}\cos(mu + nN_{\mathrm{fp}}v)\\ &+\mathcal{J}B^v_{mn}(s)\frac{\partial}{\partial v}\cos(mu + nN_{\mathrm{fp}}v)\Bigg]\end{aligned}$$

Now we take the derivatives with respect to u and v and simplify, yielding,

$$\mathcal{J}(\nabla \cdot B) = \sum_{m,n}\left[\left(\frac{\partial}{\partial s}\mathcal{J}B^s_{mn}(s) - (m)\mathcal{J}B^u_{mn}(s) - (n)\mathcal{J}B^v_{mn}(s)\right)\sin(mu + nN_{\mathrm{fp}}v)\right]$$

Therefore for the divergence to be equal to zero, the terms in the parenthesis must cancel. In other words we require that,

$$\frac{\partial}{\partial s}\mathcal{J}B^s_{mn}(s) = (m)\mathcal{J}B^u_{mn}(s) + (n)\mathcal{J}B^v_{mn}(s) \quad \forall\,(m,n)$$

Hence, the interpolated Fourier coefficients must satisfy the above relation.

To make interpolations of the field that satisfy the divergence free condition we use the following method. We shall make use of cubic and quartic polynomial splines for these interpolations. First we redefine some quantities. Let $\mathcal{J}B^s_{mn}(s) = X_{mn}(s)$, $\mathcal{J}B^u_{mn}(s) = Y_{mn}(s)$, and $\mathcal{J}B^v_{mn}(s) = Z_{mn}(s)$. Let each radial grid point be defined as s_i, where $i = \{1, 2, ..., N_s\}$ and N_s is the number of surfaces. Each Fourier coefficient is then represented by a set of $N_s - 1$ polynomial splines, where the radial coordinate s lies on the interval $s \in [s_i, s_{i+1}]$. Then each i^{th} spline of any particular (m, n) pair can be represented as,

$$X_i(s) = x_{i_0} + x_{i_1}(s - s_i) + x_{i_2}(s - s_i)^2 + x_{i_3}(s - s_i)^3 + x_{i_4}(s - s_i)^4 \tag{A2.4}$$

$$Y_i(s) = y_{i_0} + y_{i_1}(s - s_i) + y_{i_2}(s - s_i)^2 + y_{i_3}(s - s_i)^3 \tag{A2.5}$$

$$Z_i(s) = z_{i_0} + z_{i_1}(s - s_i) + z_{i_2}(s - s_i)^2 + z_{i_3}(s - s_i)^3 \tag{A2.6}$$

The y_i and z_i terms are calculated via interpolation, while the x_i terms are unknowns, but can be found using the divergence free condition. Substituting these equations in the divergence free relation and taking the radial derivative gives,

$$x_{i_1} + 2x_{i_2}(s - s_i) + 3x_{i_3}(s - s_i)^2 + 4x_{i_4}(s - s_i)^3 =$$

$$m(y_{i_0} + y_{i_1}(s - s_i) + y_{i_2}(s - s_i)^2 +_{i_3}(s - s_i)^3) + n(z_{i_0} + z_{i_1}(s - s_i) + z_{i_2}(s - s_i)^2 + z_{i_3}(s - s_i)^3)$$

Equating coefficients will equal powers of $(s - s_i)$ gives,

$$x_{i_1} = my_{i_0} + nz_{i_0} \tag{A2.7}$$

$$x_{i_2} = \frac{m}{2}y_{i_1} + \frac{n}{2}z_{i_1} \tag{A2.8}$$

$$x_{i_3} = \frac{m}{3}y_{i_2} + \frac{n}{3}z_{i_2} \tag{A2.9}$$

$$x_{i_4} = \frac{m}{4}y_{i_3} + \frac{n}{4}z_{i_3} \tag{A2.10}$$

The last coefficient $x_{i_0} = X_i(s = s_i)$. After interpolating the $\mathcal{J}B^u_{mn}$ and $\mathcal{J}B^v_{mn}$ Fourier coefficients, we can use Eqs. (B4)-(B7) to assign the coefficients for the $\mathcal{J}B^{s}_{mn}$ spline terms, ensuring a divergence free field.